DYNAMIC REGULATION OF INTESTINAL STEM CELL NICHE AND COLON CANCER STEM CELL DIVISION

A Dissertation

Presented to the Faculty of the Graduate School

of Cornell University

In Partial Fulfillment of the Requirements for the Degree of

Doctor of Philosophy

by

Kai-Yuan Chen

February 2016

DYNAMIC REGULATION OF INTESTINAL STEM CELL NICHE AND COLON CANCER STEM CELL DIVISION

Kai-Yuan Chen, Ph. D.

Cornell University, 2016

Tissue homeostasis requires rigorous control mechanisms for stem cell division and maintenance of a stable stem cell niche. Cancer stem cells are a subgroup of cancer cells that possess stem cell-like properties, including self-renewal and differentiation, but have subverted the control apparatus. We have identified that the tumor suppressor miR-34a, a non-coding small RNA targeting Notch, plays an important role regulating the division of colon cancer stem cells (CCSCs) and, in turn. controls the bimodality of heterogeneous population of colonic tumors. Moreover, we find out miR-34a directly suppresses the canonical cell fate determinant Numb to form an incoherent feedforward loop (iFFL) that enhances bimodality of CCSC cell fate determination. Integrative high-throughput analysis suggests that CCSCs and non-CCSCs might globally adopt reprogrammed metabolic functions leading to differential epigenetic regulation. In the normal intestine stem cell (ISC) niche, ISCs and Paneth cells form a stable pattern to control stem cell behavior. However, how the pattern manages to dynamically recover from damage is unclear. A novel optical approach integrating a high-precision femtosecond photo-ablation laser and *in vivo* imaging system revealed robust pattern recovery after local perturbation in intestine stem cell niche. Computationally and experimentally, we discovered a Notch1 positive feedback (PF) critical to regulate ISC self-renewal and regeneration. In this dissertation, the integrative engineering approaches led us to understand dynamic regulation of normal ISCs and CCSCs.

BIOGRAPHICAL SKETCH

Kai-Yuan Chen was born in Kaohsiung City, Taiwan. He earned a BS in Electrical Engineering from National Cheng Kung University in 2005 and an MS in Electrical Engineering from National Taiwan University in 2007. While studying in National Taiwan University, he received the A-class scholarship in Electrical Engineering, and was awarded the 3rd-Prize of National Innovation Award in 2006 for his research work on the development of MRI RF system. After graduation from National Taiwan University, he spent one year serving as a corporal in Marine Corps of Taiwan and was discharged in 2008. In September 2009, Kai-Yuan matriculated into the M.Eng program in Biomedical Engineering at Cornell University. After receiving his M.Eng in Biomedical Engineering, Kai-Yuan continued his MS/PhD program in Electrical and Computer Engineering at Cornell University in August 2010 under the supervision of Dr. Xiling Shen, and he was awarded Irwin M. and Joan K. Jacobs Fellowship. Kai-Yuan's project is mainly focused on using integrative approaches of systems biology and bioinformatics to investigate the intestinal stem cell-niche cell interaction, asymmetric division of colon cancer stem cells, and microRNA regulation.

To My Family

ACKNOWLEDGMENTS

It has been a privilege to work with and be under the guidance of my advisor, Dr. Xiling Shen. I have learned many valuable lessons from Xiling's lab, including research skills but also, the joy of exploring new fields and devotion for science.

I am also grateful to other members of my thesis committee, Dr. Michael Shuler and Dr. Jeffrey Varner, for their generous support and insightful comments to my research.

I also want to thank all of the past and current members of the Shen lab for their help, friendship, and collaboration.

Finally, I would like to deeply thank my family for their unconditional support and love. Without my family, I could not have overcome all of the countless obstacles during my PhD study.

TABLE OF CONTENTS

CHAPTER 1

INTRODUCTION

1.1 Regulation of Tissue Homeostasis

Tissue homeostasis and regeneration require robust regulation of stem cells, which is tightly associated with stem cell division and the stem cell niche. In normal intestinal tissue, the control of stem cells for tissue repair and maintenance is important while preventing degeneration and overgrowth. In contrast, tumors usually form from unchecked proliferation due to impaired control mechanisms. Symmetric division of stem cells favors proliferation, while asymmetric division promotes differentiation. The proper control of stem cell division is critical to tissue homeostasis for maintaining tissue size and stable heterogeneity. In higher organisms, asymmetric division is a property associated with many types of stem and progenitor cells in the embryo, nervous system, skin, mammary gland, blood, etc., in order to balance proliferation and differentiation as well as aging (Beckmann, Scheitza et al. 2007, Knoblich 2008, Bultje, Castaneda-Castellanos et al. 2009, Neumuller and Knoblich 2009, Williams, Beronja et al. 2011, Inaba and Yamashita 2012, Jackson, Waterhouse et al. 2015, Katajisto, Dohla et al. 2015). In addition to stem cell division, the stem cell niche is also critical to tissue homeostasis by regulating stem cell self-renewal and differentiation (Schofield 1978, Palmer, Willhoite et al. 2000, Calvi, Adams et al. 2003, Zhang, Niu et al. 2003, Lander, Kimble et al. 2012). Here, the stem cell niche provides the necessary conditions to support stem cell functions, including interactions between stem cells or with the surrounding differentiated cells (Pardo-Saganta, Tata et al. 2015), growth factors, metabolites, PH values, and so on (Scadden 2006). These niche factors help to either stimulate the function of stem cells or act as an external feedback to modulate the number of stem cells in the stem cell niche in response to cell loss or cell damage. These niche factors have been shown as critical to prevent stem cells from depletion or over-production leading to disease.

1.2 Cancer Stem Cells

Cancer stem cells (CSCs), or tumor initiating cells, are a subpopulation of cancer cells that are able to undergo both symmetric and asymmetric division in various cancer types (Cicalese, Bonizzi et al. 2009, Pece, Tosoni et al. 2010, Pine, Ryan et al. 2010, Dey-Guha, Wolfer et al. 2011, Lathia, Hitomi et al. 2011, Sugiarto, Persson et al. 2011, O'Brien, Kreso et al. 2012, Bajaj, Zimdahl et al. 2015). The self-renewal and differentiation ability of cancer stem cells is highly associated with tumorigenesis. Loss of tumor suppressor genes often favors increased symmetric divisions of cancer stem cells, which promote proliferation and tumor growth. It is still largely unknown how the balance between CSCs and non-CSCs is controlled.

1.3 Intestine Stem Cell Niche

The stem cell niche provides a spatial environment to regulate stem cell self-renewal and differentiation (Lander, Kimble et al. 2012). Some mammalian tissues, especially those with high regenerative potential, rely on stem cell niches rather than asymmetric division to control the number of proliferative stem cells.

One prominent example is the stem cell niche at the base of the intestinal crypt. In the niche, self-renewing LGR5+ crypt base columnar (CBC) cells and lysozyme-secreting Paneth cells form a mosaic pattern (Barker, van Es et al. 2007, Sato, van Es et al. 2010). Paneth cells provide niche factors including epidermal growth factor (EGF), Wnt ligands (WNT3A), Notch ligands, and bone morphogenetic protein (BMP) inhibitor Noggin to support CBC stem cell self-renewal, while pericryptal stromal cells underneath the niche also supply additional Wnt ligands (WNT2B) (Barker 2014). Regulation of the niche is certainly a concerted effort involving various such signaling pathways. As proliferative intestinal stem cells (ISCs), CBCs divide symmetrically, compete with each other in a neutral drift process, and regenerate the intestinal epithelium in 3 to 5 days(Lopez-Garcia, Klein et al. 2010, Snippert, van der Flier et al. 2010). Remarkably, the stem cell niche is capable of recovering from radiation or chemical damage (Buczacki, Zecchini et al. 2013, Metcalfe, Kljavin et al. 2014), which implies the importance of a robust stem cell niche in order to maintain the number of the stem cells.

1.4 miR-34a Regulation in Cancer

MicroRNAs silence gene expression by binding to the 3' untranslated regions (3' UTRs) of target mRNAs, inhibiting their translation or marking them for degradation (Pauli, Rinn et al. 2011). MicroRNAs often target genes that regulate cell-fate decisions (Ivey and Srivastava 2010, Pauli, Rinn et al. 2011). In addition, microRNA expression is globally altered in tumors relative to normal tissues, which potentially contributes to the lack of control for differentiation and arrest in cancer cells (Loboda, Nebozhyn et al. 2011).

Originally identified as a p53 target, the microRNA miR-34a acts as a tumor suppressor in many types of solid tumors (Youn, Kim et al. 2001, He, He et al. 2007, LaPointe, Dunne et al. 2008, Li, Guessous et al. 2009, Liu, Kelnar et al. 2011, Wurbel, McIntire et al. 2011). miR-34a also regulates multiple developmental cell-fate mechanisms, including the differentiation of mouse and human embryonic stem cells and somatic cell reprogramming, among others (Sikandar, Pate et al. 2010, Choi, Lin et al. 2011, Guardavaccaro and Clevers 2012, Sampieri and Fodde 2012). Among the regulatory mechanisms targeted by miR-34a, the Notch pathway plays a prominent role in cell-fate determination during development and oncogenesis (Alison, Lin et al. 2012). miR-34a binds to the 3' UTR mRNA sequences of Notch receptors, which causes reduced Notch protein levels and dampens downstream Notch signaling (Li, Guessous et al. 2009). However, despite the importance of the Notch pathway in the regulation of asymmetric division, it remains unknown whether the Notch-targeting miR-34a plays any role in determining cell-fate asymmetry in normal and cancer stem cells.

1.5 Notch Signaling Regulating Stem Cells

The Notch pathway is a critical regulator of asymmetric division in many types of normal stem cells. Asymmetric cell division is a mechanism commonly used by stem cells to generate both a daughter stem cell for self-renewal and a more differentiated daughter cell to create cellular diversity (Neumuller and Knoblich 2009). Stem cells perform asymmetric division to maintain stem cell number and tissue homeostasis in a robust and precise way (Sanchez-Tillo, de Barrios et al. 2011). Certain types of cancer cells also perform asymmetric division (Pece, Tosoni et al. 2010, Pine, Ryan et al. 2010, Dey-Guha,

Wolfer et al. 2011, Lathia, Hitomi et al. 2011, O'Brien, Kreso et al. 2012). Similar to the situation in normal stem cells, the disruption of asymmetric division can alter the balance between self-renewal and differentiation in cancer stem cells and impact tumor growth (Cicalese, Bonizzi et al. 2009, Sugiarto, Persson et al. 2011).

Moreover, Notch signaling is known to play essential roles in promoting the self-renewal of intestinal and colon stem cells (ISCs) and in specifying the choice between absorptive or secretory lineage differentiation(van Es, van Gijn et al. 2005, de Sousa, Colak et al. 2011, Taketo 2011). ISCs undergo both symmetric and asymmetric divisions, probably at different stages, during development and crypt homeostasis (Potten, Owen et al. 2002, Quyn, Appleton et al. 2010, Goulas, Conder et al. 2012, Itzkovitz, Blat et al. 2012). Colon cancer stem cells (CCSCs) from colorectal cancer (CRC) are thought to arise from, or at least share common properties with, normal colon stem cells (Dalerba, Dylla et al. 2007, O'Brien, Pollett et al. 2007, Ricci-Vitiani, Lombardi et al. 2007, Arrowsmith 2011, Clevers 2011). Tumors formed by xenotransplanted CCSCs show heterogeneity in morphology and are populated by cell types reflecting the histopathology of the parental tumor. Like ISCs, CCSCs also require Notch signaling for self-renewal (van Es, van Gijn et al. 2005, Sikandar, Pate et al. 2010).

In this thesis, we explored the intriguing aspects of dynamic regulation of stem cell divisions and stem cell niches. We found that miR-34a controls the asymmetric division of colon cancer stem cells (CCSCs) as a bimodal switch. In addition, miR-34a does not work alone; rather it forms an incoherent feedforward loop (iFFL) with Numb and Notch that cooperatively generates a more robust bimodal switch to control the balance of CCSCs. Moreover, multi-platform analysis was conducted to globally understand the transcriptomic and metabolomics difference between the CCSCs and non-CCSCs. To understand the normal stem cell niche, a novel optic approach combining femtosecond photoablation laser, multi-photon microscopy, and *in vivo* abdominal window system was developed. It was applied to directly monitor dynamics of the intestinal stem cell niche *in vivo* and administered high-precision, local single cell laser ablation in the stem cell niche. The observation from this approach led us to discover a Notch1 positive feedback that is essential to intestinal stem cell self-renewal and proliferation. By combining experimental

observations with various mathematical modeling techniques, we developed a systematic understanding of the design principles that control stem cell division and the stem cell niche.

REFERENCES

Alison, M. R., W. R. Lin, S. M. Lim and L. J. Nicholson (2012). "Cancer stem cells: in the line of fire." Cancer Treat Rev **38**(6): 589-598.

Arrowsmith, J. (2011). "Trial watch: Phase II failures: 2008-2010." Nat Rev Drug Discov **10**(5): 328-329.

Bajaj, J., B. Zimdahl and T. Reya (2015). "Fearful Symmetry: Subversion of Asymmetric Division in Cancer Development and Progression." Cancer Res **75**(5): 792-797.

Barker, N. (2014). "Adult intestinal stem cells: critical drivers of epithelial homeostasis and regeneration." Nat Rev Mol Cell Biol **15**(1): 19-33.

Barker, N., J. H. van Es, J. Kuipers, P. Kujala, M. van den Born, M. Cozijnsen, A. Haegebarth, J. Korving, H. Begthel, P. J. Peters and H. Clevers (2007). "Identification of stem cells in small intestine and colon by marker gene Lgr5." Nature **449**(7165): 1003-1007.

Beckmann, J., S. Scheitza, P. Wernet, J. C. Fischer and B. Giebel (2007). "Asymmetric cell division within the human hematopoietic stem and progenitor cell compartment: identification of asymmetrically segregating proteins." Blood **109**(12): 5494-5501.

Buczacki, S. J., H. I. Zecchini, A. M. Nicholson, R. Russell, L. Vermeulen, R. Kemp and D. J. Winton (2013). "Intestinal label-retaining cells are secretory precursors expressing Lgr5." Nature **495**(7439): 65-69.

Bultje, R. S., D. R. Castaneda-Castellanos, L. Y. Jan, Y. N. Jan, A. R. Kriegstein and S. H. Shi (2009). "Mammalian Par3 regulates progenitor cell asymmetric division via notch signaling in the developing neocortex." Neuron **63**(2): 189-202.

Calvi, L. M., G. B. Adams, K. W. Weibrecht, J. M. Weber, D. P. Olson, M. C. Knight, R. P. Martin, E. Schipani, P. Divieti, F. R. Bringhurst, L. A. Milner, H. M. Kronenberg and D. T. Scadden (2003). "Osteoblastic cells regulate the haematopoietic stem cell niche." Nature **425**(6960): 841-846.

Choi, Y. J., C. P. Lin, J. J. Ho, X. He, N. Okada, P. Bu, Y. Zhong, S. Y. Kim, M. J. Bennett, C. Chen, A. Ozturk, G. G. Hicks, G. J. Hannon and L. He (2011). "miR-34 miRNAs provide a barrier for somatic cell reprogramming." Nat Cell Biol **13**(11): 1353-1360.

Cicalese, A., G. Bonizzi, C. E. Pasi, M. Faretta, S. Ronzoni, B. Giulini, C. Brisken, S. Minucci, P. P. Di Fiore and P. G. Pelicci (2009). "The tumor suppressor p53 regulates polarity of self-renewing divisions in mammary stem cells." Cell **138**(6): 1083-1095.

Clevers, H. (2011). "The cancer stem cell: premises, promises and challenges." Nat Med **17**(3): 313-319.

Dalerba, P., S. J. Dylla, I. K. Park, R. Liu, X. Wang, R. W. Cho, T. Hoey, A. Gurney, E. H. Huang, D. M. Simeone, A. A. Shelton, G. Parmiani, C. Castelli and M. F. Clarke (2007). "Phenotypic characterization of human colorectal cancer stem cells." Proc Natl Acad Sci U S A **104**(24): 10158-10163.

de Sousa, E. M. F., S. Colak, J. Buikhuisen, J. Koster, K. Cameron, J. H. de Jong, J. B. Tuynman, P. R. Prasetyanti, E. Fessler, S. P. van den Bergh, H. Rodermond, E. Dekker, C. M. van der Loos, S. T. Pals, M. J. van de Vijver, R. Versteeg, D. J. Richel, L. Vermeulen and J. P. Medema (2011). "Methylation of cancer-stem-cell-associated Wnt target genes predicts poor prognosis in colorectal cancer patients." Cell Stem Cell **9**(5): 476-485.

Dey-Guha, I., A. Wolfer, A. C. Yeh, J. G. Albeck, R. Darp, E. Leon, J. Wulfkuhle, E. F. Petricoin, 3rd, B. S. Wittner and S. Ramaswamy (2011). "Asymmetric cancer cell division regulated by AKT." Proc Natl Acad Sci U S A.

Dey-Guha, I., A. Wolfer, A. C. Yeh, G. A. J, R. Darp, E. Leon, J. Wulfkuhle, E. F. Petricoin, 3rd, B. S. Wittner and S. Ramaswamy (2011). "Asymmetric cancer cell division regulated by AKT." Proc Natl Acad Sci U S A **108**(31): 12845-12850.

Goulas, S., R. Conder and J. A. Knoblich (2012). "The Par complex and integrins direct asymmetric cell division in adult intestinal stem cells." Cell Stem Cell **11**(4): 529-540.

Guardavaccaro, D. and H. Clevers (2012). "Wnt/beta-catenin and MAPK signaling: allies and enemies in different battlefields." Sci Signal **5**(219): pe15.

He, L., X. He, L. P. Lim, E. de Stanchina, Z. Xuan, Y. Liang, W. Xue, L. Zender, J. Magnus, D. Ridzon, A. L. Jackson, P. S. Linsley, C. Chen, S. W. Lowe, M. A. Cleary and G. J. Hannon (2007). "A microRNA component of the p53 tumour suppressor network." Nature **447**(7148): 1130-1134.

Inaba, M. and Y. M. Yamashita (2012). "Asymmetric stem cell division: precision for robustness." Cell Stem Cell **11**(4): 461-469.

Itzkovitz, S., I. C. Blat, T. Jacks, H. Clevers and A. van Oudenaarden (2012). "Optimality in the development of intestinal crypts." Cell **148**(3): 608-619.

Ivey, K. N. and D. Srivastava (2010). "MicroRNAs as regulators of differentiation and cell fate decisions." Cell Stem Cell **7**(1): 36-41.

Jackson, H. W., P. Waterhouse, A. Sinha, T. Kislinger, H. K. Berman and R. Khokha (2015). "Expansion of stem cells counteracts age-related mammary regression in compound Timp1/Timp3 null mice." Nat Cell Biol **17**(3): 217-227.

Katajisto, P., J. Dohla, C. L. Chaffer, N. Pentinmikko, N. Marjanovic, S. Iqbal, R. Zoncu, W. Chen, R. A. Weinberg and D. M. Sabatini (2015). "Stem cells. Asymmetric apportioning of aged mitochondria between daughter cells is required for stemness." Science **348**(6232): 340-343.

Knoblich, J. A. (2008). "Mechanisms of asymmetric stem cell division." Cell **132**(4): 583-597.

Lander, A. D., J. Kimble, H. Clevers, E. Fuchs, D. Montarras, M. Buckingham, A. L. Calof, A. Trumpp and T. Oskarsson (2012). "What does the concept of the stem cell niche really mean today?" BMC Biol **10**: 19.

LaPointe, L. C., R. Dunne, G. S. Brown, D. L. Worthley, P. L. Molloy, D. Wattchow and G. P. Young (2008). "Map of differential transcript expression in the normal human large intestine." Physiol Genomics **33**(1): 50-64.

Lathia, J. D., M. Hitomi, J. Gallagher, S. P. Gadani, J. Adkins, A. Vasanji, L. Liu, C. E. Eyler, J. M. Heddleston, Q. Wu, S. Minhas, A. Soeda, D. J. Hoeppner, R. Ravin, R. D. McKay, R. E. McLendon, D. Corbeil, A. Chenn, A. B. Hjelmeland, D. M. Park and J. N. Rich (2011). "Distribution of CD133 reveals glioma stem cells self-renew through symmetric and asymmetric cell divisions." Cell Death Dis **2**: e200.

Li, Y., F. Guessous, Y. Zhang, C. Dipierro, B. Kefas, E. Johnson, L. Marcinkiewicz, J. Jiang, Y. Yang, T. D. Schmittgen, B. Lopes, D. Schiff, B. Purow and R. Abounader (2009). "MicroRNA-34a inhibits glioblastoma growth by targeting multiple oncogenes." Cancer Res **69**(19): 7569-7576.

Liu, C., K. Kelnar, B. Liu, X. Chen, T. Calhoun-Davis, H. Li, L. Patrawala, H. Yan, C. Jeter, S. Honorio, J. F. Wiggins, A. G. Bader, R. Fagin, D. Brown and D. G. Tang (2011). "The microRNA miR-34a inhibits prostate cancer stem cells and metastasis by directly repressing CD44." Nat Med **17**(2): 211-215.

Loboda, A., M. V. Nebozhyn, J. W. Watters, C. A. Buser, P. M. Shaw, P. S. Huang, L. Van't Veer, R. A. Tollenaar, D. B. Jackson, D. Agrawal, H. Dai and T. J. Yeatman (2011). "EMT is the dominant program in human colon cancer." BMC Med Genomics **4**: 9.

Lopez-Garcia, C., A. M. Klein, B. D. Simons and D. J. Winton (2010). "Intestinal stem cell replacement follows a pattern of neutral drift." Science **330**(6005): 822-825.

Metcalfe, C., N. M. Kljavin, R. Ybarra and F. J. de Sauvage (2014). "Lgr5+ stem cells are indispensable for radiation-induced intestinal regeneration." Cell Stem Cell **14**(2): 149-159.

Neumuller, R. A. and J. A. Knoblich (2009). "Dividing cellular asymmetry: asymmetric cell division and its implications for stem cells and cancer." Genes Dev **23**(23): 2675-2699.

O'Brien, C. A., A. Kreso, P. Ryan, K. G. Hermans, L. Gibson, Y. Wang, A. Tsatsanis, S. Gallinger and J. E. Dick (2012). "ID1 and ID3 regulate the self-renewal capacity of human colon cancer-initiating cells through p21." Cancer Cell **21**(6): 777-792.

O'Brien, C. A., A. Pollett, S. Gallinger and J. E. Dick (2007). "A human colon cancer cell capable of initiating tumour growth in immunodeficient mice." Nature **445**(7123): 106-110.

Palmer, T. D., A. R. Willhoite and F. H. Gage (2000). "Vascular niche for adult hippocampal neurogenesis." J Comp Neurol **425**(4): 479-494.

Pardo-Saganta, A., P. R. Tata, B. M. Law, B. Saez, R. Chow, M. Prabhu, T. Gridley and J. Rajagopal (2015). "Parent stem cells can serve as niches for their daughter cells." Nature **523**(7562): 597-601.

Pauli, A., J. L. Rinn and A. F. Schier (2011). "Non-coding RNAs as regulators of embryogenesis." Nat Rev Genet **12**(2): 136-149.

Pece, S., D. Tosoni, S. Confalonieri, G. Mazzarol, M. Vecchi, S. Ronzoni, L. Bernard, G. Viale, P. G. Pelicci and P. P. Di Fiore (2010). "Biological and molecular heterogeneity of breast cancers correlates with their cancer stem cell content." Cell **140**(1): 62-73.

Pine, S. R., B. M. Ryan, L. Varticovski, A. I. Robles and C. C. Harris (2010). "Microenvironmental modulation of asymmetric cell division in human lung cancer cells." Proc Natl Acad Sci U S A **107**(5): 2195-2200.

Potten, C. S., G. Owen and D. Booth (2002). "Intestinal stem cells protect their genome by selective segregation of template DNA strands." J Cell Sci **115**(Pt 11): 2381-2388.

Quyn, A. J., P. L. Appleton, F. A. Carey, R. J. Steele, N. Barker, H. Clevers, R. A. Ridgway, O. J. Sansom and I. S. Nathke (2010). "Spindle orientation bias in gut epithelial stem cell compartments is lost in precancerous tissue." Cell Stem Cell **6**(2): 175-181.

Ricci-Vitiani, L., D. G. Lombardi, E. Pilozzi, M. Biffoni, M. Todaro, C. Peschle and R. De Maria (2007). "Identification and expansion of human colon-cancer-initiating cells." Nature **445**(7123): 111-115.

Sampieri, K. and R. Fodde (2012). "Cancer stem cells and metastasis." Semin Cancer Biol **22**(3): 187-193.

Sanchez-Tillo, E., O. de Barrios, L. Siles, M. Cuatrecasas, A. Castells and A. Postigo (2011). "beta-catenin/TCF4 complex induces the epithelial-to-mesenchymal transition (EMT)-activator ZEB1 to regulate tumor invasiveness." Proc Natl Acad Sci U S A **108**(48): 19204-19209.

Sato, T., J. H. van Es, H. J. Snippert, D. E. Stange, R. G. Vries, M. van den Born, N. Barker, N. F. Shroyer, M. van de Wetering and H. Clevers (2010). "Paneth cells constitute the niche for Lgr5 stem cells in intestinal crypts." Nature.

Scadden, D. T. (2006). "The stem-cell niche as an entity of action." Nature **441**(7097): 1075-1079.

Schofield, R. (1978). "The relationship between the spleen colony-forming cell and the haemopoietic stem cell." Blood Cells **4**(1-2): 7-25.

Sikandar, S. S., K. T. Pate, S. Anderson, D. Dizon, R. A. Edwards, M. L. Waterman and S. M. Lipkin (2010). "NOTCH signaling is required for formation and self-renewal of tumor-initiating cells and for repression of secretory cell differentiation in colon cancer." Cancer Res **70**(4): 1469-1478.

Snippert, H. J., L. G. van der Flier, T. Sato, J. H. van Es, M. van den Born, C. Kroon-Veenboer, N. Barker, A. M. Klein, J. van Rheenen, B. D. Simons and H. Clevers (2010). "Intestinal crypt homeostasis results from neutral competition between symmetrically dividing Lgr5 stem cells." Cell **143**(1): 134-144.

Sugiarto, S., A. I. Persson, E. G. Munoz, M. Waldhuber, C. Lamagna, N. Andor, P. Hanecker, J. Ayers-Ringler, J. Phillips, J. Siu, D. A. Lim, S. Vandenberg, W. Stallcup, M. S. Berger, G. Bergers, W. A. Weiss and C. Petritsch (2011). "Asymmetry-defective oligodendrocyte progenitors are glioma precursors." Cancer Cell **20**(3): 328-340.

Taketo, M. M. (2011). "Reflections on the spread of metastasis to cancer prevention." Cancer Prev Res (Phila) **4**(3): 324-328.

van Es, J. H., M. E. van Gijn, O. Riccio, M. van den Born, M. Vooijs, H. Begthel, M. Cozijnsen, S. Robine, D. J. Winton, F. Radtke and H. Clevers (2005). "Notch/gamma-secretase inhibition turns proliferative cells in intestinal crypts and adenomas into goblet cells." Nature **435**(7044): 959-963.

Williams, S. E., S. Beronja, H. A. Pasolli and E. Fuchs (2011). "Asymmetric cell divisions promote Notch-dependent epidermal differentiation." Nature **470**(7334): 353-358.

Wurbel, M. A., M. G. McIntire, P. Dwyer and E. Fiebiger (2011). "CCL25/CCR9 interactions regulate large intestinal inflammation in a murine model of acute colitis." PLoS One **6**(1): e16442.

Youn, B. S., Y. J. Kim, C. Mantel, K. Y. Yu and H. E. Broxmeyer (2001). "Blocking of c-FLIP(L)--independent cycloheximide-induced apoptosis or Fas-mediated apoptosis by the CC chemokine receptor 9/TECK interaction." Blood **98**(4): 925-933.

Zhang, J., C. Niu, L. Ye, H. Huang, X. He, W. G. Tong, J. Ross, J. Haug, T. Johnson, J. Q. Feng, S. Harris, L. M. Wiedemann, Y. Mishina and L. Li (2003). "Identification of the haematopoietic stem cell niche and control of the niche size." Nature **425**(6960): 836-841.

CHAPTER 2

A MICRORNA MIR-34A-REGULATED BIMODAL SWITCH TARGETS NOTCH IN COLON CANCER STEM CELLS

2.1 Summary

microRNAs regulate developmental cell-fate decisions, tissue homeostasis, and oncogenesis in distinct ways relative to proteins. Here, we show that the tumor suppressor microRNA miR-34a is a cell-fate determinant in early-stage dividing colon cancer stem cells (CCSCs). In pair-cell assays, miR-34a distributes at high levels in differentiating progeny, whereas low levels of miR-34a demarcate self-renewing CCSCs. Moreover, miR-34a loss of function and gain of function alter the balance between self-renewal versus differentiation both in vitro and in vivo. Mechanistically, miR-34a sequesters Notch1 mRNA to generate a sharp threshold response where a bimodal Notch signal specifies the choice between self-renewal and differentiation. In contrast, the canonical cell-fate determinant Numb regulates Notch levels in a continuously graded manner. Altogether, our findings highlight a unique microRNA-regulated mechanism that converts noisy input into a toggle switch for robust cell-fate decisions in CCSCs.

2.2 Introduction

microRNAs silence gene expression by binding to the 3' untranslated regions (3' UTRs) of target mRNAs, inhibiting their translation or marking them for degradation (Pauli et al., 2011). microRNAs often target genes that regulate cell-fate decisions (Ivey and Srivastava, 2010; Pauli et al., 2011). Recent studies show that microRNAs confer robustness to biological processes in distinct ways relative to proteins, such as suppressing fluctuations in gene regulation (Ebert and Sharp, 2012). microRNAs also frequently form feedback and feedforward loops with other microRNAs and proteins to enhance robustness (Osella et al., 2011; Tsang et al., 2007). microRNA expression is globally altered in tumors relative to normal tissues, which potentially contributes to the lack of control for differentiation and arrest in cancer cells (Loboda et al., 2011).

Originally identified as a p53 target, the microRNA miR-34a acts as a tumor suppressor in many types of

solid tumors (He et al., 2007; LaPointe et al., 2008; Li et al., 2007; Liu et al., 2011; Wurbel et al., 2011; Youn et al., 2001). miR-34a also regulates multiple developmental cell-fate mechanisms, including the differentiation of mouse and human embryonic stem cells and somatic cell reprogramming, among others (Choi et al., 2011; Guardavaccaro and Clevers, 2012; Sampieri and Fodde, 2012; Sikandar et al., 2010). Among the regulatory mechanisms targeted by miR-34a, the Notch pathway plays a prominent role in cell-fate determination during development and oncogenesis (Ali- son et al., 2012). miR-34a binds to the 3' UTR mRNA sequences of Notch receptors, which causes reduced Notch protein levels and dampens downstream Notch signaling (Li et al., 2009).

The Notch pathway is a critical regulator of asymmetric division in many types of normal stem cells. Asymmetric cell division is a mechanism commonly used by stem cells to generate both a daughter stem cell for self-renewal and a more differentiated daughter cell to create cellular diversity (Neumuller and Knoblich, 2009). Stem cells perform asymmetric division to maintain stem cell number and tissue homeostasis in a robust and precise way (Sa´nchez-Tillo´ et al., 2011). Certain types of cancer cells also perform asymmetric division (Dey-Guha et al., 2011; Lathia et al., 2011; O'Brien et al., 2012; Pece et al., 2010; Pine et al., 2010). Similar to the situation in normal stem cells, the disruption of asymmetric division can alter the balance between self- renewal and differentiation in cancer stem cells and impact tumor growth (Cicalese et al., 2009; Sugiarto et al., 2011). However, despite the importance of the Notch pathway in the regulation of asymmetric division, it remains unknown whether individual microRNAs, such as the Notch-targeting miR-34a, play any role in determining cell-fate asymmetry in normal and cancer stem cells.

Notch signaling is known to play essential roles in promoting the self-renewal of intestinal and colon stem cells (ISCs) and in specifying the choice between absorptive or secretory lineage differentiation (de Sousa E Melo et al., 2011; Taketo, 2011; van Es et al., 2005). ISCs undergo both symmetric and asymmetric divisions, probably at different stages, during development and crypt homeostasis (Goulas et al., 2012; Itzkovitz et al., 2012; Potten et al., 2002; Quyn et al., 2010). Colon cancer stem cells (CCSCs) from colorectal cancer (CRC) are thought to arise from, or at least share common properties with, normal

colon stem cells (Arrowsmith, 2011a; Clevers, 2011; Dalerba et al., 2007; O'Brien et al., 2007; Ricci-Vitiani et al., 2007). Tumors formed by xenotransplanted CCSCs show heterogeneity in morphology and are populated by cell types reflecting the histopathology of the parental tumor. Like ISCs, CCSCs also require Notch signaling for self-renewal (Sikandar et al., 2010; van Es et al., 2005).

Here, we show that, similar to ISCs, CCSCs from early-stage, well-differentiated CRC tumors can perform both self-renewing symmetric division (producing two CCSC daughter cells) and asymmetric division (producing a CCSC daughter cell and a differentiated non-CCSC daughter cell). The decision of a CCSC to perform either symmetric or asymmetric division is tightly controlled by the miR-34a level. High miR-34a levels dampen Notch signaling and promote daughter cells to become non-CCSCs, whereas low miR-34a levels upregulate Notch signaling and promote daughter cells to remain CCSCs. Investigation of regulation kinetics demonstrated a critical role for miR-34a to convert "noisy" signaling inputs into clean bimodal Notch levels that enable robust binary daughter cell-fate decisions. This role of miR-34a is distinct from that of the canonical cell- fate determinant protein Numb, which regulates Notch levels in a continuously graded manner. These studies provide new insights into asymmetric cell division mechanisms, highlighting unique regulatory roles performed by microRNAs.

2.3 Material And Methods

Isolation and Culture of CCSCs

CCSCs were isolated as described previously (Sikandar et al., 2010). For this study, CCSCs were derived from three early-stage and two late-stage CRC patient tumors (Table 2.1). In brief, after being washed with PBS, fresh human CRC tumors were dissociated with collagenase and strained with a 40 mm filter. The tumor cells were initially sorted with anti-CD133 (clone C24B9, 1:50; Cell Signaling) and anti-CD44 (clone156-3C11, 1:100; Cell Signaling) antibodies and later switched to ALDH1 with the Aldeflour kit (STEMCELL Technologies). CCSCs were cultured as spheres in ultralow-attachment flasks (Corning) in DMEM/F12 (Invitrogen) and supplemented with nonessential amino acids (Thermo Fisher), sodium pyruvate (Thermo Fisher), Penicillin- streptomycin (Thermo Fisher), N2 supplement (Invitrogen), B27 supplement (Invitrogen), 4 mg/mL heparin (Sigma-Aldrich), 40 ng/mL epidermal growth factor

(Invitrogen), and 20 ng/mL basic fibroblast growth factor (Invitrogen) at 37°C and 5% CO_2. To propagate in vitro, spheres were collected by gentle centrifugation, dissociated into single cells, and cultured for the formation of next generation spheres. All animal experiments were approved by the Cornell Center for Animal Resources and Education and followed the protocol (2009- 0071).

CCSC Differentiation and Sphere Formation Analysis

To induce differentiation, CCSCs were dissociated from spheres using trypsin-EDTA and were plated at 1.8×10^5 cells/mL on 60 mm dishes precoated with Collagen IV (BD Biosciences) in DMEM supplemented with 10% FBS and without growth factors. The cells were passaged when they reached 90% confluence. To measure tumor sphere formation, CCSC single cells were plated in 24-well ultra-low attachment plates (Corning) at 1,000 cells per well. Tumor spheres were then counted using an inverted microscope (Olympus). To quantify cell numbers per tumor sphere, tumor spheres were collected and were disassociated with trypsin-EDTA (Invitrogen) to make a single cell suspension. The viable cells were then counted using trypan blue exclusion.

Immunohistochemistry

Immunohistochemistry was performed on paraffin-embedded sections from xenografts. Sections were stained by haematoxylin-eosin after dewaxed and rehydrated.

Time-Lapse Imaging

Dissociated CCSCs were plated at 6×10^4 cells per glass bottom dish (MatTek Corp). Cells were photographed every 15 minutes with an inverted microscope harboring an Olympus 20x lens, a Lumencor Aura light engine and a Point Grey Research Chameleon CCD camera. The microscope was equipped with an incubator that maintains the temperature at 37 °C and a humidified 5% CO_2 flow. Time-lapse sequences were combined using Image J software.

Immunofluorescence

First, CCSCs were plated on an uncoated glass culture slide (BD Biosciences). After being fixed in cold methanol, the cells were blocked in 10% normal goat serum for 1 hr and incubated with antibodies against ALDH1 (clone H-4, 1:100; Santa Cruz Biotechnology), CD44 (clone156-3C11, 1:400, Cell Signaling),

CD133 (1:200, Abcam), CK20 (clone H-70, 1:100, Santa Cruz Biotechnology), CEA (1:200, Abcam), Numb (clone C44B4, 1:100 [Cell Signaling] or 1:100 [Abcam]), and NICD (1:100; R&D Systems) overnight at 4°C. Then, the cells were incubated with Rhodamine Red- or Alexa Fluor 488-labeled secondary antibody (Invitrogen) for 1 hr at room temperature. After being counterstained with DAPI (Invitrogen), the slide was observed under a fluorescent microscope (Olympus).

RNA FISH

RNA FISH was performed as described by Lu and Tsourkas (2009). CCSCs were fixed with 4% formaldehyde for 30 minutes at room temperature, followed by permeabilization in 70% ethanol at 4 °C overnight. 1-ethyl-3-(3-dimethylaminopropyl) carbodiimide (EDC) fixation was applied to prevent the loss of miRNA. After a 2 hour incubation in prehybridization buffer (25% formamide, 0.05 M EDTA, 4×SSC, 10% dextran sulfate, 1×Denhardt's solution, 0.5 mg/ml Escherichia coli tRNA and 0.5 mg/ml RVC), digoxigenin (DIG)–labeled locked nucleic acid (LNA) probe (Exiqon) was added for hybridization. The slides were then incubated with anti-DIG antibody (1:400, Roche), and the miRNA expression was detected by Rhodamine Red labeled secondary antibody (Invitrogen). DAPI (Invitrogen) was used for nucleic counterstaining. The slide was then observed under a fluorescent microscope (Olympus).

miR-34 Threshold Assay

The threshold assay was performed as described by Mukherji et al. (2011). The pTet-on-Advanced vector was transfected into CCSCs transfection Kit from Stemgent. To make the reporter construct, Notch 3`UTR and 4 repeats of bulged miR-34a binding sites were cloned into the 3`UTR of the mCherry gene in the pTRETightBI-RY-0 vector from Addgene (Mukherji et al., 2011) using ClaI and EcoRV. The constructs were then transfected into the CCSCs containing the pTet-on-Advanced vector. After induced by Doxycycline for 3 days, the cells were dissociated and plated on uncoated glass culture slides (BD Biosciences). Fluorescent and bright-field images were taken using a fluorescent microscope (Olympus). To plot the transfer function, images were analyzed using MATLAB. The raw fluorescent images were segmented to measure the fluorescence signal levels inside each segmented cell. After the subtraction of

camera background and cellular autofluorescence, pixel values in both eYFP and mCherry channels were extracted for each imaged cell. The single-cell data were then binned along the eYFP axis and the mCherry levels were averaged for cells in each bin. The mean mCherry values for each bin were then plotted for showing the transfer function.

Flow Cytometry

After dissociation by trypsin-EDTA, single CCSCs were either incubated with anti-CD133 (clone C24B9, 1:50, Cell Signaling), anti-CD44 (clone156-3C11, 1:100, Cell Signaling) antibody, or anti-Numb (clone C44B4, 1:100, Cell Signaling), anti-Notch1 (clone D6F11, 1:600, Cell signaling), anti-p53 (clone DO-1, 1:100, Calbiochem), anti-CK20 (clone H-70, 1:50, Santa Cruz) and anti-Mycn (clone NCM II 100, 1:100, Abcam) antibodies after fixed with formaldehyde and further permeabilized by methanol. The cells were then incubated with PE or FITC labeled secondary antibody (Invitrogen). The samples were analyzed using a Beckman Coulter flow cytometer. The raw FACS data were analyzed with the FlowJo software to gate cells according to their forward (FSC) and side (SSC) scatter profiles. Staining with an isotype-matched control antibody (mouse IgG or rabbit IgG) followed by PE or FITC labeled secondary antibody was used for negative control and cutoff.

Quantitative Real-Time RT-PCR Analysis

Total RNA was extracted from the cells using the TRIzol Reagent (Invitrogen). cDNA was synthesized from 500 ng of total RNA in 20 ml of reaction volume using the High Capacity cDNA Archive Kit (Applied Biosystems). Quantitative PCR was carried out using either the TaqMan MicroRNA Assay (Applied Biosystems) to detect miR-34a levels or the SYBR Green System (Applied Biosystems) to detect gene expression. All samples were run in triplicate three times. The miR-34a primer and U6 primer were purchased from Applied Biosystems. Other primer sequences include: Notch1, 5`-GTGACTGCTCCCTCAACTTCAAT-3` and 5`- CTGTCACAGTGGCCGTCACT-3`; Notch2, 5'-AACTGTCAGACCCTGGTGAAC-3' and 5`- CGACAAGTGTAGCCTCCAATC-3`; Numb, 5`-GCTGCCTCTCCAGGTCTCTTC-3` and 5`- CGCTCTTAGACACCTCTTCTAACCA-3`; CK20, 5`-AGGAGACCAAGGCCCGTTA-3` and 5`- ATCAGTTGGGCCTCCAGAGA-3`; actin, 5`-

CGCGAGAAGATGACCCAGAT-3` and 5`- ACAGCCTGGATAGCAACGTACAT-3`; The expression of each gene was defined from the threshold cycle (Ct), and the relative expression levels were calculated using the 2-ΔΔCt method after normalization to the actin expression level.

Western Blot

Whole cell lysate was prepared in a lysis buffer (20 mM Tris pH 7.5, 150 mM NaCl, 1% Nonidet P-40, 0.5% Sodium Deoxycholate, 1 mM EDTA, 0.1% SDS, protease inhibitors). Proteins were first separated by 10% SDS-PAGE and then transferred to a Hybond membrane (Amersham). The membranes were incubated with primary antibodies either anti-p53 (clone DO- 1, 1:2000, Calbiochem), anti-p21 (clone F-5, 1:1000, Santa Cruz), anti-NICD (1:1000, R&D Systems), anti-Hes1 (1:500, Millipore), anti-Notch1 (clone D6F11, 1:1000, Cell Signaling), anti- Notch2 (clone A81, 1:1000, Cell Signaling), anti-Numb (clone C44B4, 1:1000, Cell Signaling, or 1:1000, Abcam) or anti-tubulin (clone B-5-1-2, 1:4000, Sigma) in 5% milk/TBST buffer (25

mM Tris pH 7.4, 150 mM NaCl, 2.5 mM KCl, 0.1% Triton-X100) overnight, and then probed for 1 hour with secondary horseradish peroxidase (HRP)-conjugated anti-mouse or anti-rabbit IgG (Santa Cruz). After extensive wash with PBST, the target proteins were detected on membrane by enhanced chemiluminescence (Pierce).

Lentiviral Constructs and Infection

miR-34a with approximately 250 base pairs of flanking sequence was amplified from human genomic DNA and cloned into the lentiviral vector pSMPUW-miR-GFP/Puro (Cell Biolab). pHIV-D2EGFP was generated by replacing EGFP in pHIV-EGFP (Welm et al., 2008) with a destabilized variant, D2EGFP (Clontech). To construct the miR-34a sponge, 13 repeats of modified miR-34a binding sites with a bulge at position 9-12 were cloned into pHIV-D2EGFP using BamH I and Kpn I (Ebert et al., 2007). To construct the miR-34a GFP reporter, 3 repeats of miR-34a binding sites were cloned into pHIV-D2EGFP using BamH I and Kpn I (Ko et al., 2009). The Numb-GFP reporter was constructed by inserting the human Numb gene into the vector PHAGE-CMV-dsRed-UBC-GFP-W (Addgene) after the UBC promoter. The Notch EGFP reporter was ordered from Systems Biosciences and has RBPJk response

elements upstream of EGFP to report Notch signaling activity. Notch1 3`UTR Lenti-reporter-GFP construct were order from Abmgood with Notch1 3`UTR in GFP 3`UTR. miR-34a binding sequences in Notch1 3`UTR were further mutated using QuickChange Site-directed Mutagenesis Kit (Stratagene). The lentiviral constructs expressing the RBPJk shRNA were order from Sigma. The lentiviral constructs expressing the Numb shRNA were ordered from Thermo Scientific. The lentiviral vectors were then transfected into 293T cells along with helper plasmids. The viral supernatant was collected 48 hours after transfection and was used to infect CCSCs.

BrdU Incorporation Assay

CCSC sphere cells were cultured in proliferative medium (DMEM with 10% FBS) for 24 hours. Single cells were then plated and allowed to divide once in proliferative medium for 24 hours (1^{st} division). After treated with 10 mM BrdU (Sigma) for 3 hours, the cells were fixed in cold 70% ethanol, incubated in 2 M HCl for 1 hour, washed, and switched to 100 mM $Na_2B_4O_7$ for 2 minutes. After blocked in 10% normal goat serum for 1 hour, the cells were then incubated with anti-BrdU (1:200, Sigma) antibody with anti-ALDH1 (H-85, 1:100, Santa Cruz) or anti- CK20 (clone H-70, 1:100, Santa Cruz) antibody at 4 °C overnight. The cells were then incubated with Rhodamine Red or Alexa Fluor 488 labeled secondary antibody (Invitrogen) for 1 hour at room temperature. After counterstained with DAPI (Invitrogen), the slide was observed under a fluorescent microscope (Olympus).

Analysis of Proliferation, Cell Cycle, and Senescence

CCSCs were infected with either the control lentiviral vectors or lentiviral vectors expressing miR-34a. The infection efficiency was measured by the GFP expression from the vectors. The infected cells were used for cell cycle analysis with Propidium iodide (Invitrogen) staining (Hernandez-Vargas et al., 2007) and for senescence analysis using the b-Galactosidase Staining Kit (Cell Signaling). CCSC proliferation under differentiating condition was analyzed using the WST-1 Cell Proliferation Reagent (Clontech).

p53 and K-ras Mutation Detection

DNA was isolated using the DNeasy Mini kit (Qiagen). p53 mutation was detected by direct sequencing according to the IARC protocol. K-ras mutation was detected using the PNAClamp K-ras mutation

detection kit (Panagene).

In Vivo Tumor Formation

All animal experiments were approved by The Cornell Center for Animal Resources and Education (CARE) and followed the protocol (2009-0071). In brief, 4×10^6 CCSCs in 200 mL of 1:1 medium/Matrigel (BD Biosciences) solution were injected subcutaneously into the lower back region of female nude mice. Tumor sizes were measured using a caliper, and volumes were calculated using the formula: $(L\times W^2)\times0.5$, where L is the length and W is the width of each tumor.

Statistical Analysis of Xenograft Tumors

Data were expressed as mean ± SD of no smaller than three biological repeats and analyzed for statistical significance with the GraphPad Prism 5 software. Two-way ANOVA was used to compare the mean responses of different tumor sizes at different time points, followed by a Bonferroni post-hoc test to determine statistical significance.

Modeling

Mathematical Model of miR-34a Regulation

An ordinary differential equation (ODE) based simulation model was constructed to analyze miR-34a with mutual sequestration. This model consists of 3 molecular species and 7 parameters. The equations involving miR-34a are partially based on models from Osella et al (Osella et al., 2011), Xie et al (Xie et al., 2007), Levine et al (Levine et al., 2007), Khanin et al (Khanin and Vinciotti, 2008), and Vohradsky et al (Vohradsky et al., 2010). The threshold response of mircoRNA-targeted gene expression has recently be demonstrated by Mukherji et al (Mukherji et al., 2011).

ODE Equations:

$$\frac{d[miR-34a]}{dt} = \beta_1 - \alpha_1[miR-34a] - \gamma[miR-34a][NOTCH_{mRNA}]$$
$$\frac{d[NOTCH_{mRNA}]}{dt} = \beta_2 - \alpha_2[NOTCH_{mRNA}] - \gamma[miR-34a][NOTCH_{mRNA}]$$
$$\frac{d[NOTCH]}{dt} = \beta_3[NOTCH_{mRNA}] - \alpha_3[NOTCH]$$

Where:

β_1 = 0.06 molecule/minute, denoting the transcription rate of miR-34a.

β_2 = 0.09 molecule/minute, denoting the transcription rate of Notch1 mRNA.

β_3 = 0.96 molecule/minute, denoting the translation rate of Notch1.

α_1 = 0.002 /minute, denoting the degradation rate of miR-34a.

α_2 = 0.005 /minute, denoting the degradation rate of Notch1 mRNA.

α_3 = 0.02 /minute, denoting the degradation rate of Notch1 protein. γ is the binding rate of miR-34a and Notch1 mRNA.

Monte-Carlo Simulation of Notch Bimodality

We sampled the entire distribution of miR-34a levels based on FACS measurements in Figures 2.5C and S2.5A. The miR-34a levels were applied to the deterministic ODEs to calculate the steady state expression levels of NOTCH. *In silico* simulations show that the threshold response generated by miR-34a-Notch mRNA mutual sequestration can give rise to Notch bimodality (Figures S2.5D and S2.5E).

2.4 Result

2.4.1 Characterization of Early-Stage, Well-Differentiated CCSCs

Using the established CCSC markers CD133, CD44, and aldehyde dehydrogenase 1 (ALDH1) (Emmink et al., 2011; Huang et al., 2009; Ricci-Vitiani et al., 2007; Todaro et al., 2007), we isolated two CCSC lines, CCSC1 and CCSC2, from early-stage, well-differentiated CRC patient specimens (Table 2.1) (see Experimental Procedures). Consistent with previous reports (Huang et al., 2009; O'Brien et al., 2007; Sikandar et al., 2010), both CCSC1 and CCSC2 efficiently formed xenograft tumors that maintained the histopathology of their primary human CRCs upon xenografting in immunodeficient mice (Figure

S2.11A).

Both CCSC1 and CCSC2 propagate as spheres in ultralow-attachment flasks and are capable of generating cellular diversity in vitro. From dissociated spheres, fluorescence-activated cell sorting (FACS) identified a CD133+CD44+ CCSC subpopulation and a CD133-CD44- non-CCSC subpopulation (Figure S2.1B). Isolated CCSCs became heterogeneous again in spheres and reached a similar equilibrium between CCSCs (CD133+CD44+) and non-CCSCs (CD133-CD44-) as they proliferated (Figure S2.1B). Consistent with previous studies of ALDH1 and CCSCs (Huang et al., 2009), FACS analysis confirmed that CCSCs were ALDH1+, whereas non-CCSCs were ALDH1- (Figure S2.1C).

ID	Age/Sex	Stage	miR-34a[a]	Numb[a]	p53 mutation	Kras mutation	% of C/C[b]	% of C/D[b]	% of D/D[b]	% of am[b]
CCSC1	57/M	I	16.7	7.2	NO	NO	57.6	14.1	26.1	2.2
CCSC2	51/M	II	14.3	5.8	NO	NO	59.3	12.7	24.5	3.5
CCSC3	74/F	I	13.2	4.7	NO	YES	61.4	13.4	25.2	0
CCSC4	54/M	III	3.7	3.5	NO	NO	89.3	0	9.5	1.2
CCSC5	61/M	IV	1.0	1.0	YES	NO	96.3	0	3.2	0
CCSC6[c]	47/M	II	11.3	4.2	NO	NO	41.2	19	31.8	8
CCSC7[c]	87/M	III	2.5	4.1	NO	NO	82.6	0	11.3	6.1
CCSC8[c]	50/M	III	5.2	2.2	YES	YES	69.7	6.1	18.2	6
CCSC9[c]	86/M	IV	1.7	3.1	NO	NO	80.8	0	19.2	0

[a]The expression level of miR-34a and Numb were measured by qRT-PCR relative to CCSC5 sphere.
[b]The pair-cell assay was performed in CCSC spheres by coimmunofluorescence of ALDH1 and CK20. C/C, symmetric self-renewal (CCSC/CCSC); C/D, asymmetric division (CCSC/differentiated cell); D/D, symmetric differentiation (differentiated cell/differentiated cell).
[c]The cell lines are freshly isolated CCSCs from primary CRC.

Table 2.1. Colon Cancer Stem Cell Lines And Primary Human Colorectal Cancers Used In The Study

Then, we compared the tumorigenic capacity of CCSCs and non-CCSCs using the limiting dilution assay. Also consistent with previous studies of CCSCs, for both CCSC1 or CCSC2, as few as 1,000 CCSCs were sufficient to form subcutaneous xenograft tumors, whereas non-CCSCs failed to form tumors during the observed period (2 months) even when up to $1x10^6$ cells were injected (Figure S2.1D; data not shown). Sphere propagation assays confirmed that, unlike CCSCs, non-CCSCs were incapable of forming and serially propagating spheres in vitro (Figures S2.1E–S2.1G). To evaluate the differentiation potential of CCSCs, we cultured dissociated sphere cells in differentiation medium (DMEM with 10% fetal bovine serum [FBS]). After 10 days in culture, CD133 and CD44 expression significantly decreased, whereas the expression of cytokeratin 20 (CK20), a marker of mature normal colonocytes and non-CCSCs, increased (Figures S2.1H–S2.1K). Consistent with these findings, the tumorigenic ability of CCSCs cultured in differentiation medium was greatly reduced (Figure S2.1L).

2.4.2 miR-34a Inhibits CCSC Self-Renewal In Vitro

microRNA profiling previously identified miR-34a, but not miR- 34b or -34c, as being expressed in cultured CRC spheres (Jahid et al., 2012). Given that miR-34a can cause cell differentiation by inhibiting Notch signaling, we examined how miR-34a expression levels differ between CCSCs and non-CCSCs. Quantitative RT-PCR (qRT-PCR) studies showed that miR-34a expression was downregulated in CCSCs and upregulated in non-CCSCs (Figure 2.1A). Infection of CCSC1 and CCSC2 sphere cells with lentivirus driving miR-34a constitutive overexpression (miR-34a OE) increased the proportion of non-CCSCs relative to CCSCs (Figures 2.1B and 2.1C). Overall, these data are consistent with miR-34a promoting CCSC differentiation into non-CCSCs.

Then, we performed serial sphere propagation assays to examine the impact of miR-34a on self-renewal. For both CCSC1 and CCSC2 lines, we analyzed cells with the stably integrated lentiviral miR-34a OE expression cassette as described in the preceding paragraph. In addition, we also created CCSC1 and CCSC2 lines with a stably integrated miR-34a "sponge" construct (miR-34a KD). This construct drives the transcription of a decoy mRNA containing multiple tandem binding sites for miR-34a, which reduces levels of free miR-34a available to bind its endogenous mRNA targets (Ebert et al., 2007). The efficiency of the miR-34a KD construct was validated by a luciferase miR-34a reporter assay (Figure S2.2A). After selection for cells containing the miR-34a KD cassette, single cells were allowed to form spheres in vitro. Subsequently, spheres containing the miR-34a KD or control cassettes were dissociated and passaged for several generations (Figure 2.1D). Although spheres from CCSC1 and CCSC2 cells with the control sequence maintained a stable level of sphere-forming ability, miR-34a KD cells had significantly increased sphere-forming ability; in contrast, spheres from CCSC1 and CCSC2 cells with the stably integrated miR-34a OE cassette had diminished sphere-forming activity (Figures 2.1E, 2.1F, S2.2B, and S2.2C). Further- more, cells from miR-34a OE spheres lost the ability to form new spheres serially after being passaged for several generations, whereas cells from untransduced or miR-34a KD-expressing spheres could be passaged significantly longer (for at least 12 months).

Similarly, miR-34a OE sphere cells had lower proliferation rates (Figure S2.2D), which was consistent

with high miR-34a levels promoting differentiation (Figures 2.1B and 2.1C). These observations are also consistent with non-CCSCs having lower proliferative potential than CCSCs (Figure 2.2D). Finally, high miR-34a levels also increased cell-cycle arrest and senescence (Figures S2.2E and S2.2F).

2.4.3 miR-34a Suppresses CCSC Xenograft Tumor Formation

Using mouse xenograft models, we examined whether miR-34a affects tumor formation in vivo. We constructed a CCSC1 line that stably expressed a lentiviral miR-34a reporter cassette with three miR-34a binding sites cloned into the 3^0 UTR of a D2EGFP reporter gene. In this reporter line, FACS identified two distinct sphere subpopulations: miR-34a^{high} and miR-34a^{low} cells (Figure S2.2K). Of the six mice that were subcutaneously injected with miR-34a^{low} cells, all six formed tumors. In contrast, in the six mice injected in parallel with miR-34a^{high} cells, only one formed a tumor, and the volume of this tumor was much smaller than those generated by miR-34a^{high} cells (Figures 2.1I and 2.1J). Analysis of the disaggregated tumors by FACS showed that tumors developing from miR-34a^{low} cells had a higher percentage of CCSCs than those from miR-34a^{high} cells (Figure 2.1K).

Next, to confirm the inhibitory role of miR-34a in CCSC self-renewal and tumor growth, we subcutaneously injected immunodeficient mice with cells isolated from CCSC1 spheres expressing basal (control), constitutively high (miR-34a OE), or constitutively low (miR-34a KD) miR-34a levels. Only two of the six mice injected with high miR-34a-expressing sphere cells (integrated with the miR-34a OE cassette) developed tumors, whereas all six mice in the control group (injected with cells integrated with the control cassette) developed tumors (Figures 2.1L and 2.1M). Additionally, tumors that grew from injected high miR-34a-expressing cells were smaller than those arising from control cells. Consistent with these data, all six of the tumors that grew from subcutaneously injected low miR-34a-expressing cells (integrated with the miR-34a KD cassette) were consistently larger in size than those in the control group (Figures 2.1O and 2.1P). Similar results were observed from xenograft tumors arising from CCSC2 spheres with basal, high, or low miR-34a levels (Figures S2.2G and S2.2H). FACS analysis of disaggregated xenograft tumors further showed that high miR-34a levels (miR-34a OE) reduced the ratio

of CCSC to non-CCSCs, whereas low miR-34a levels (miR-34a KD) increased this ratio, suggesting that miR-34a suppressed CCSC self-renewal (Figures 2.1N and 2.1Q).

Next, to confirm these findings, we isolated CCSCs from xenograft tumors and assayed the impact of miR-34a levels on self-renewal. For both CCSC1 and CCSC2 tumors, serial sphere propagation assays confirmed that low miR-34a-expressing CCSCs from miR-34a KD tumors had increased self-renewal ability versus control CCSCs with basal miR-34a expression levels; in contrast, CCSCs with high miR-34a levels from miR- 34a OE tumors had a significantly lower self-renewal capacity than control CCSCs (Figures 2.1G, 2.1H, S2.2I, and S2.2J).

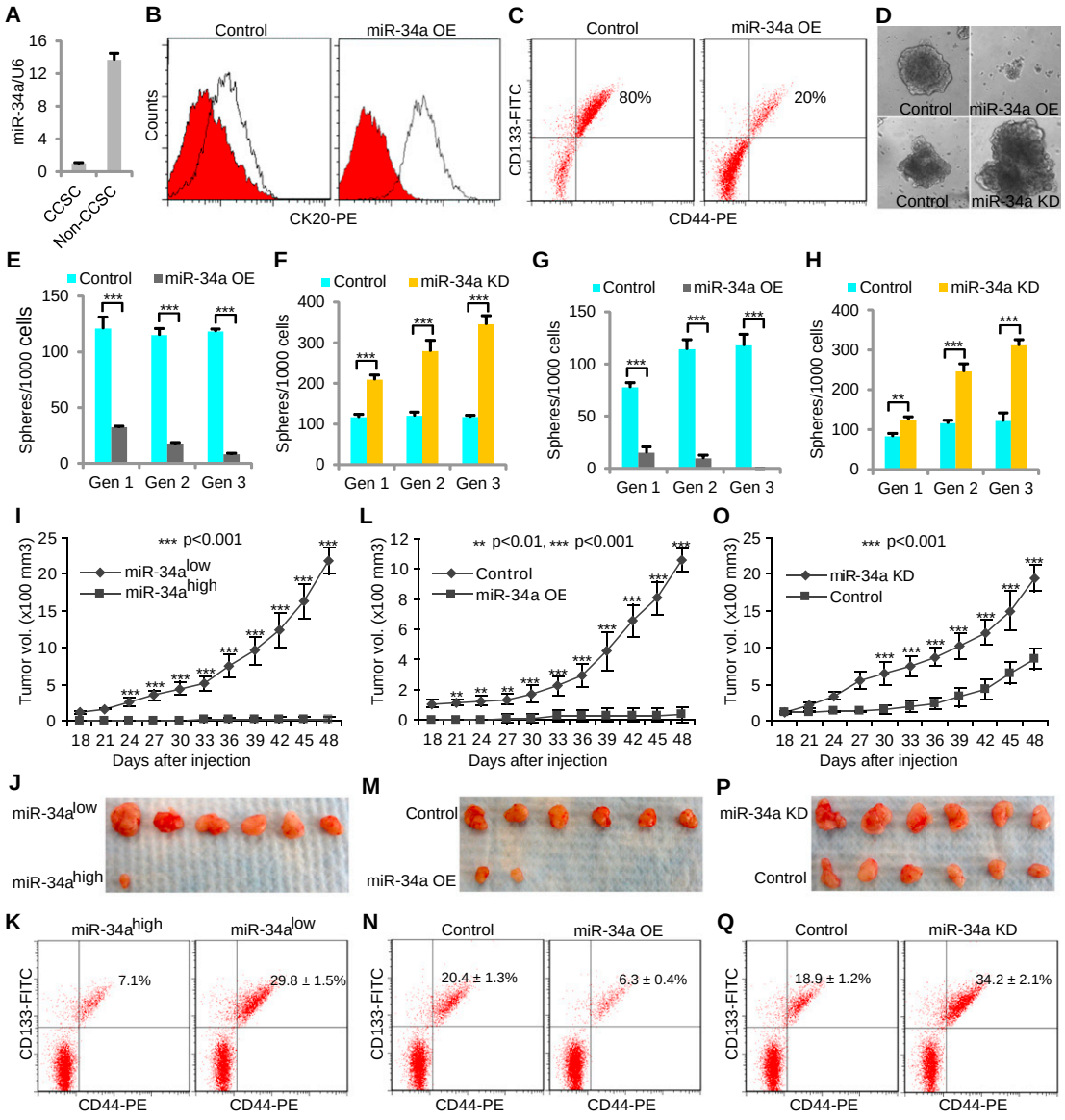

Figure 2.1 Mir-34a Regulates CCSC Self-Renewal And Tumor Formation. *(A) qRT-PCR showing miR-34a expression in CCSCs and non-CCSCs. Error bars denote the SD between triplicates. (B and C) FACS plots showing CK20, CD44, and CD133 levels in spheres after ectopic miR-34a expression (miR-34a OE). In (B), the red histograms represent isotype controls, and the blank histograms represent CK20+ cells. (D) Representative images of CCSC spheres after ectopic miR-34a expression (miR-34a OE, top) and miR-34a knockdown (miR-34a KD, bottom). (E and F) Sphere formation during serial passages after ectopic miR-34a expression (E) and miR-34a knockdown (F). Error bars denote the SD between*

*triplicates. (G and H) Serial sphere formation of CCSCs from xenografts of miR-34a OE (G) and miR-34a KD (H) cells. An equal number of cells were passaged for three generations for the formation of spheres. Error bars denote the SD between triplicates. (I and J) miR-34a^{low} sphere cells were more tumorigenic than miR-34a^{high} sphere cells in vivo, as shown by tumor growth curves (I) and images of xenograft tumors (J). Error bars denote the SD derived from six mice per group. (K) FACS showing the percentages of tumor cells that are CCSCs. (L and M) Ectopic expression of miR-34a (miR-34a OE) reduces tumorigenicity, shown by tumor growth curves (L) and images of xenograft tumors (M). Error bars denote the SD derived from six mice per group. (N) FACS showing the percentages of tumor cells that are CCSCs. (O and P) Knockdown of miR-34a (miR-34a KD) enhances tumorigenicity, shown by tumor growth curves (O) and images of xenograft tumors (P). Error bars denote the SD derived from six mice per group. (Q) FACS showing the percentages of tumor cells that are CCSCs. Gen, generation. **, $p < 0.01$; ***, $p < 0.001$. See also Figures S2.1 and S2.2.*

2.4.4 Early-Stage CCSCs Perform Both Symmetric And Asymmetric Division

To understand the mechanism of miR-34a suppression of CCSC self-renewal, we used in vitro pair-cell assay to assess how CCSCs and non-CCSCs divide (Bultje et al., 2009) (Figure S2.3A). When CCSCs were plated as single cells and allowed to progress through one cell division, coimmunofluorescence staining for ALDH1 and CK20 revealed that 65% of cell divisions were symmetrical, producing two CCSC (ALDH1+) daughter cells; whereas 28% were asymmetrical, producing one CCSC daughter cell and one non-CCSC (CK20+) daughter cell. In contrast, 87% of non-CCSCs plated in parallel divided, giving rise to two non-CCSC daughter cells (Figures 2.2A and 2.2B). The few "non-CCSCs" that produced CCSC daughter cells were presumably CCSCs with borderline CD44 and CD133 expression that were sorted into the non-CCSC population by FACS. These findings demonstrate that early-stage CCSCs can perform both symmetric and asymmetric division, whereas non-CCSCs largely divide into non-CCSCs (Figure 2.2C). This result was confirmed by additional pair-cell assays with immunofluorescence staining for other CCSC and differentiation markers, including the ISC marker Lgr5 (Arrowsmith, 2011b) (Figures S2.3B–2.3G). Furthermore, coimmunofluorescence staining for ALDH1 and CD44 or CD133 confirmed that the expression of CCSC markers in daughter cells was consistent between the two during symmetric and asymmetric division, given that the CCSC daughter cells always express CD44, CD133, and ALDH1 (Figures S2.3H and S2.3I).

To understand whether the balance between symmetric and asymmetric division changes during CRC tumor progression, we performed pair-cell assays on three other CCSC lines (CCSC3–CCSC5) and CCSCs sorted from primary cells freshly isolated from CRC tumors (CCSC6–CCSC9). Asymmetric divisions of CCSCs happen more frequently in early-stage CRC tumors than in late-stage CRC tumors (Table 2.1 and Figure S2.3J). Hence, asymmetric division is negatively correlated with tumorigenicity and invasiveness. Then, we examined whether CCSC and non-CCSC daughter cells have different proliferation rates (Sugiarto et al., 2011). After culturing CCSC1 and CCSC2 spheres in proliferative medium (DMEM with 10% FBS) for 24 hr, we plated single cells and allowed them to divide once in proliferative medium for another 24 hr (first division). Then, we treated cells with BrdU for 3 hr in order

to label the cells entering the second division before costaining for BrdU and ALDH1 and for BrdU and CK20. The CCSC (ALDH1+) daughter cells entered the second division immediately and incorporated BrdU; in contrast, the non-CCSC (CK20+) daughter cells did not immediately enter the second division and did not incorporate BrdU (Figures 2.2D and S2.3K). This experiment indicates a higher proliferative rate of CCSC versus that of non-CCSC daughter cells, similar to the rapidly dividing Lgr5+ ISCs in the intestine (Arrowsmith, 2011b).

2.4.5 Both High And Low miR-34a Levels Inhibit Asymmetric Division

Pair-cell assays with CCSC1 and CCSC2 cells showed that high miR-34a levels (miR-34a OE) decreased both symmetric CCSC- CCSC division and asymmetric division (Figures 2.2E and S2.3L), whereas low miR-34a levels (miR-34a KD) increased symmetric CCSC-CCSC division but still decreased asymmetric division (Figures 2.2F and S2.3M). To verify that miR-34a regulates primary tumor cells in the same way, we isolated CCSCs from xenografts arising from high- and low-miR-34a-expressing CCSC1 and CCSC2 spheres. These tumor-derived CCSCs were cultured as spheres and plated as single cells in the pair-cell assay. These experiments confirmed that CCSCs isolated from low miR-34a- expressing (miR-34a KD) tumors more frequently performed symmetric CCSC-CCSC division, whereas CCSCs from high miR-34a-expressing (miR-34a OE) tumors less frequently per- formed symmetric CCSC-CCSC division. Interestingly, both per- formed lower rates of asymmetric division than CCSCs isolated from basal miR-34a-expressing (i.e., control) xenografts (Figures 2.2G, 2.2H, S2.3N, and S2.3O). These data support a model in which miR-34a balances self-renewal and differentiation in CCSC as they populate growing tumors: higher miR-34a levels promote differentiation to produce non-CCSCs, whereas lower miR-34a levels promote self-renewal through symmetric CCSC-CCSC divisions.

CCSCs from late-stage CRC tumors have lower miR-34a expression levels than CCSCs from early-stage tumors, according to qRT-PCR (Table 2.1). Consistent with our data from CCSC1 and CCSC2 that miR-34a knockdown promotes symmetric CCSC-CCSC division while suppressing asymmetric division, CCSCs from late-stage CRC tumors have higher rates of symmetric CCSC-CCSC division and lower rates of asymmetric division than CCSCs from early-stage CRC tumors (Table 2.1).

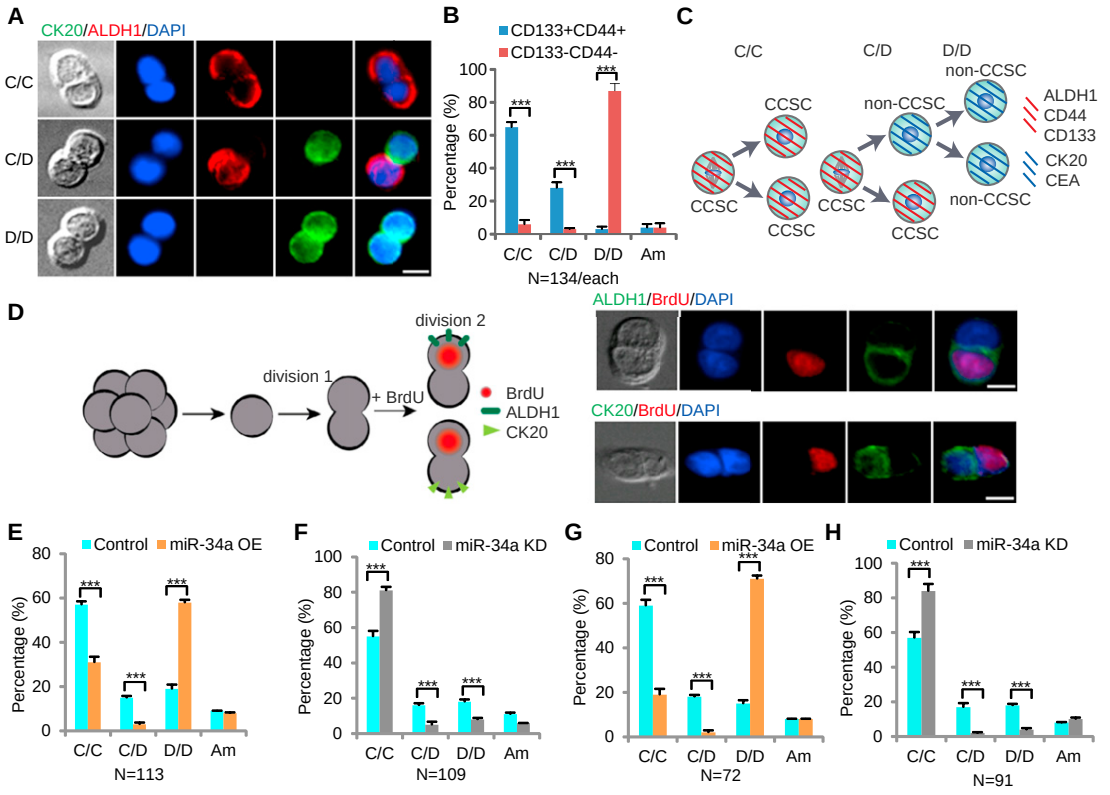

Figure 1.2. Mir-34a Regulates CCSC Division *(A) Representative images of sphere cell division. Immunofluorescence for ALDH1 (red) and CK20 (green) illustrates three types of division: CCSC/CCSC (C/C), CCSC/non-CCSC (C/D), and non-CCSC/non-CCSC (D/D). (B) Percentages of division types between the CCSC (CD133+CD44+) and non-CCSCs (CD133-CD44-) subpopulations. (C) Schematic illustration of CCSC divisions. (D) A functional assay showing that cell-fate asymmetry leads to distinct proliferation capacity. Left, a schematic representation of the experimental approach. Single sphere cells were allowed to divide once in 24 hr (first division). Then, cells were treated with BrdU for 3 hr to label cells that were entering the second division before being costained for BrdU and ALDH1 and for BrdU and CK20. Right, representative images showing that the CCSC daughter cell (ALDH1+ or CK20-) was more proliferative and incorporated BrdU. (E) Pair-cell assays with ALDH1 and CK20 coimmunofluorescence showing ectopic miR-34a expression promotes differentiation (D/D) at the expense of asymmetric division (C/D) and symmetric self-renewal (C/C). (F) Pair-cell assay with ALDH1 and CK20 coimmunofluorescence showing that miR-34a knockdown increases symmetric self-renewal*

*(C/C) at the expense of asymmetric division (C/D) and differentiation (D/D). (G and H) Immunofluorescence for ALDH1 and CK20 in pair-cell assays showing the percentages of symmetric CCSC/CCSC (C/C), asymmetric (C/D), and non- CCSC (D/D) divisions in sphere cells, which were cultured from CCSCs isolated from the xenografts of miR-34a OE (G) and miR-34a KD (H) spheres. Am, ambiguous. DAPI staining of the nucleus is shown in blue. Error bars denote the SD between triplicates. **, $p < 0.01$; ***, $p < 0.001$. See also Figure S2.3.*

2.4.6 miR-34a Levels Correlate With Cell-Fate Asymmetry

Next, we evaluated whether miR-34a levels are regulated differentially depending on whether a daughter cell adopts a CCSC or non-CCSC identity. We observed asymmetric distribution of miR-34a in pair-cell assays of early-stage CCSCs using RNA fluorescent in situ hybridization (FISH) with a miR-34a probe (Figures 2.3A and S2.4A). In contrast, the expression of miR-34c, another member of the miR-34 family, always remained low (data not shown). Asymmetric distribution of miR-34a in dividing pairs was further confirmed with the use of miR-34a D2EGFP reporter lines described previously (Figure 2.3B). Time-lapse movies of CCSCs from the reporter line showed that during division, one daughter cell started to express miR-34a, which inhibited GFP expression. In contrast, CCSCs infected with the D2GFP control vector (i.e., no 3' UTR miR-34a binding sites) always expressed GFP symmetrically during division (Figure 2.3E).

Coimmunofluorescence showed that miR-34a and ALDH1 expression were mutually exclusive in daughter cells during 88% of CCSC1 divisions (Figures 2.3C and 2.3D) and 83% of CCSC2 division (Figures S2.4B and S2.4C), consistent with miR-34a^{low} daughter cells being mostly CCSCs and miR-34a^{high} daughter cells being mostly non-CCSCs. Furthermore, pair-cell assays with CCSC1 and CCSC2 spheres incubated with BrdU showed that miR-34a^{low} daughter cells have higher proliferative rates than miR-34a^{high} daughter cells (Figures 2.3F and S2.4D). This observation is consistent with the previous finding that CCSC (ALDH1+) daughter cells have higher proliferative rates than non-CCSC (CK20+) daughter cells after asymmetric division (Figures 2.2D and S2.3K).

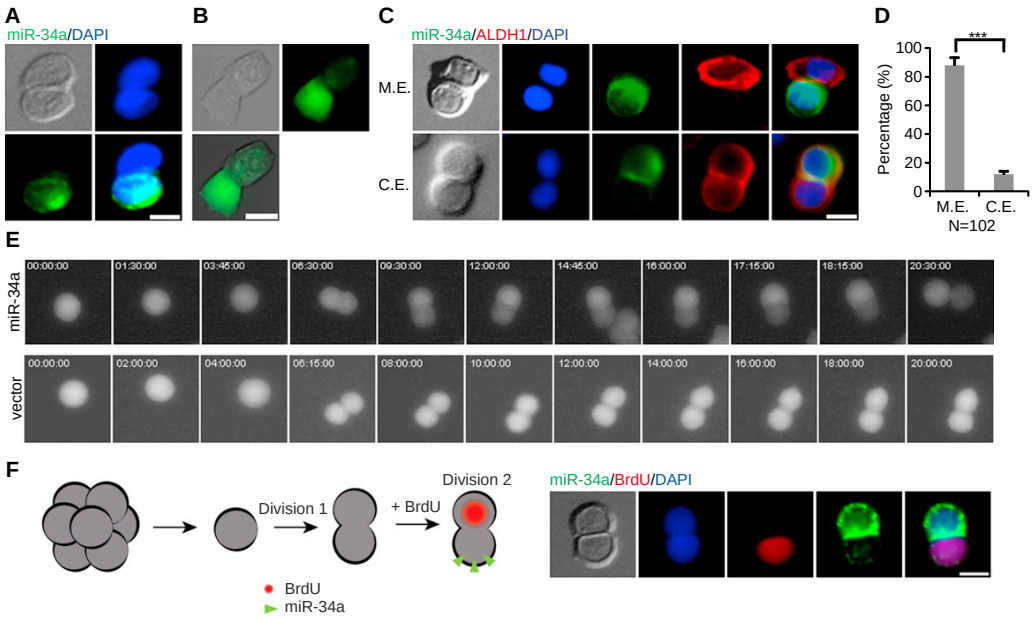

Figure 2.3. Symmetric and Asymmetric Distribution of miR-34a during Division *(A) A representative image of symmetric and asymmetric distribution of miR-34a (green) during division shown by RNA FISH. (B) A representative image of asymmetric expression of miR-34a shown by a miR-34a GFP reporter in living cells. A high-GFP fluorescent signal indicates a low miR-34a expression level. (C) Representative images showing that miR-34a (RNA FISH) and ALDH1 are mutually exclusive (M.E., top row) or are coexpressed (C.E., bottom row). (D) Percentages of CCSC divisions wherein miR-34a and ALDH1 are M.E. or C.E. (E) Top, a representative image of time-lapse images of asymmetric miR-34a expression during CCSC division with a miR-34a GFP reporter. Bottom, CCSCs infected with a D2GFP control vector divided GFP symmetrically. See also see Movie S2. (F) The miR-34a^{low} daughter cell has more proliferative potential. Left, a schematic representation of the experimental approach. Single cells were allowed to divide once in 24 hr (Division 1). Cells were then treated with BrdU for 3 hr for the labeling of cells that were entering the second division (Division 2) before being costained for BrdU and miR-34a. Right, a representative image showing that the miR-34a^{low} daughter cell was more proliferative and incorporated BrdU. DAPI staining of the nucleus is shown in blue. The scale bar represents 8 mm. Error bars denote the SD between triplicates. ***, $p < 0.001$. See also Figure S2.4.*

2.4.7 miR-34a Suppresses Notch Signaling To Promote Daughter Cell Differentiation

miR-34a has been reported to suppress Notch1 protein levels (Li et al., 2009). qRT-PCR and western blot confirmed that miR-34a downregulates Notch1 expression in early-stage CCSCs (Figures 2.4A and 2.4B). Notch signaling has been shown to promote CCSC self-renewal (Sikandar et al., 2010). CCSCs have high levels of Notch activity, expressing high levels of Notch intercellular domain (NICD) and the Notch target gene Hes1 (Figures 2.4C and 2.4D). High Notch activity is specific to CCSCs, given that depletion of CCSCs by either FACs sorting or FBS-induced differentiation significantly reduced Notch activity (Figures 2.4C and 2.4D). Inhibition of Notch by the γ-secretase inhibitor DAPT reduced the CCSC population and increased the non-CCSC population (Figures 2.4E-2.4G), confirming that Notch promotes CCSC self-renewal. Then, we constitutively expressed small hairpin RNAs (shRNAs) that targeted against the canonical Notch transcription factor RBPJk, which efficiently inhibited Notch signaling, as shown by western blot (Figure S2.5A). RBPJk knockdown and downstream Notch signaling inhibition significantly reduced the ability of CCSC to form xenograft tumors in vivo (Figures 2.4H and 2.4I). Given that miR-34a suppresses Notch, these findings are consistent with previous observations that ectopic expression of miR-34a inhibited CCSC self-renewal and tumor formation (Figures 2.1B, 2.1C, 2.1L, 2.1M, and 2.1N).

Because differential Notch signaling levels enable asymmetric division of certain normal stem cells, we asked whether Notch signaling levels are differentially regulated during CCSC asymmetric division and whether they are correlated with daughter cell-fate outcomes. Coimmunofluorescence staining of CCSCs in pair-cell assays showed that NICD was distributed asymmetrically, appearing in the CCSC (ALDH1+) daughter cell only (Figure 2.4J). The inhibition of Notch signaling by DAPT suppressed asymmetric division and reduced symmetric CCSC-CCSC division significantly (Figure 2.4K), similar to the effect of ectopic miR-34a expression on CCSC division (Figure 2.2E).

Then, we integrated a lentiviral Notch pathway EGFP reporter into CCSC spheres and performed time-lapse microscopy to visualize directly the distribution of Notch signaling during cell division. This reporter contained multiple RBPJk response elements upstream of a basal promoter that drove expression

of EGFP to measure endogenous Notch signaling activity. Notch(EGFP)+ cells either divided symmetrically into two Notch(EGFP)+ daughter cells or divided asymmetrically into a Notch(EGFP)+ daughter cell and a Notch(EGFP)- daughter cell, whereas Notch(EGFP)- cells mostly divided into two Notch(EGFP)- daughter cells (Figure 2.4L). Coimmunofluorescence staining of the same daughter pairs immediately after time-lapse imaging verified that Notch(EGFP)+ daughter cells were CCSCs (ALDH1+CK20-) and Notch(EGFP)- daughter cells were non-CCSCs (ALDH1-CK20+) (Figure 2.4L). Because differential miR-34a levels (Figures 2.3A, 2.3B, and 2.3E) can potentially contribute to differential Notch signaling levels through suppression of Notch1 expression, we examined whether the disruption of differential miR-34a levels interferes with differential Notch signaling levels. Indeed, ectopic expression of miR-34a increased Notch(EGFP)- pairs, whereas knockdown of miR-34a increased Notch(EGFP)+ pairs during cell division. In both cases, asymmetric distribution of Notch signaling was significantly reduced (Figure 2.4M). Overall, these time-lapse movies indicated that, in miR-34a^{high} daughter cells, miR-34a suppresses Notch signaling to promote differentiation.

2.4.8 Numb Localization Correlates Less Closely With Daughter Cell-Fate Outcomes Than miR-34a

A well-known mechanism for enabling asymmetric division is the cell-fate determinant Numb, which, like miR-34a, also suppresses Notch signaling (Neumu¨ller and Knoblich, 2009). During asymmetric division, Numb localizes to one side of the dividing cell and causes the degradation of membrane-bound Notch receptors and NICD (McGill and McGlade, 2003; Schweisguth, 2004). Numb protein levels are slightly upregulated in non-CCSCs relative to CCSCs (Figure 2.4N). Immunofluorescence staining of dividing pairs shows that endogenous Numb localized asymmetrically during $20% of CCSC divisions (Figure 2.4O). Analysis of a CCSC line stably expressing a Numb-GFP fusion protein from a weak ubiquitinC (UbC) promoter confirmed that, even before the completion of cell division, Numb-GFP localizes to one side of the dividing cell (Figure 2.4P). Interestingly, despite being a better-characterized cell-fate determinant, Numb and ALDH1 were mutually exclusive in only 61% of CCSC1 divisions and 55% of CCSC2 divisions, whereas, in 39% of CCSC1 divisions and 45% of CCSC2 divisions, they were coexpressed in at least one daughter cell (symmetric Numb versus asymmetric ALDH1 or vice versa)

(Figures 2.4Q, 2.4R, S2.5B, and S2.5C). miR-34a and ALDH1 expression, on the other hand, were mutually exclusive in daughter cells during 88% of CCSC1 divisions and 83% of CCSC2 divisions, as previously described (Figures 2.3C, 2.3D, S2.4B, and S2.4C). Therefore, miR-34a correlates more closely with CCSC daughter cell differentiation than Numb.

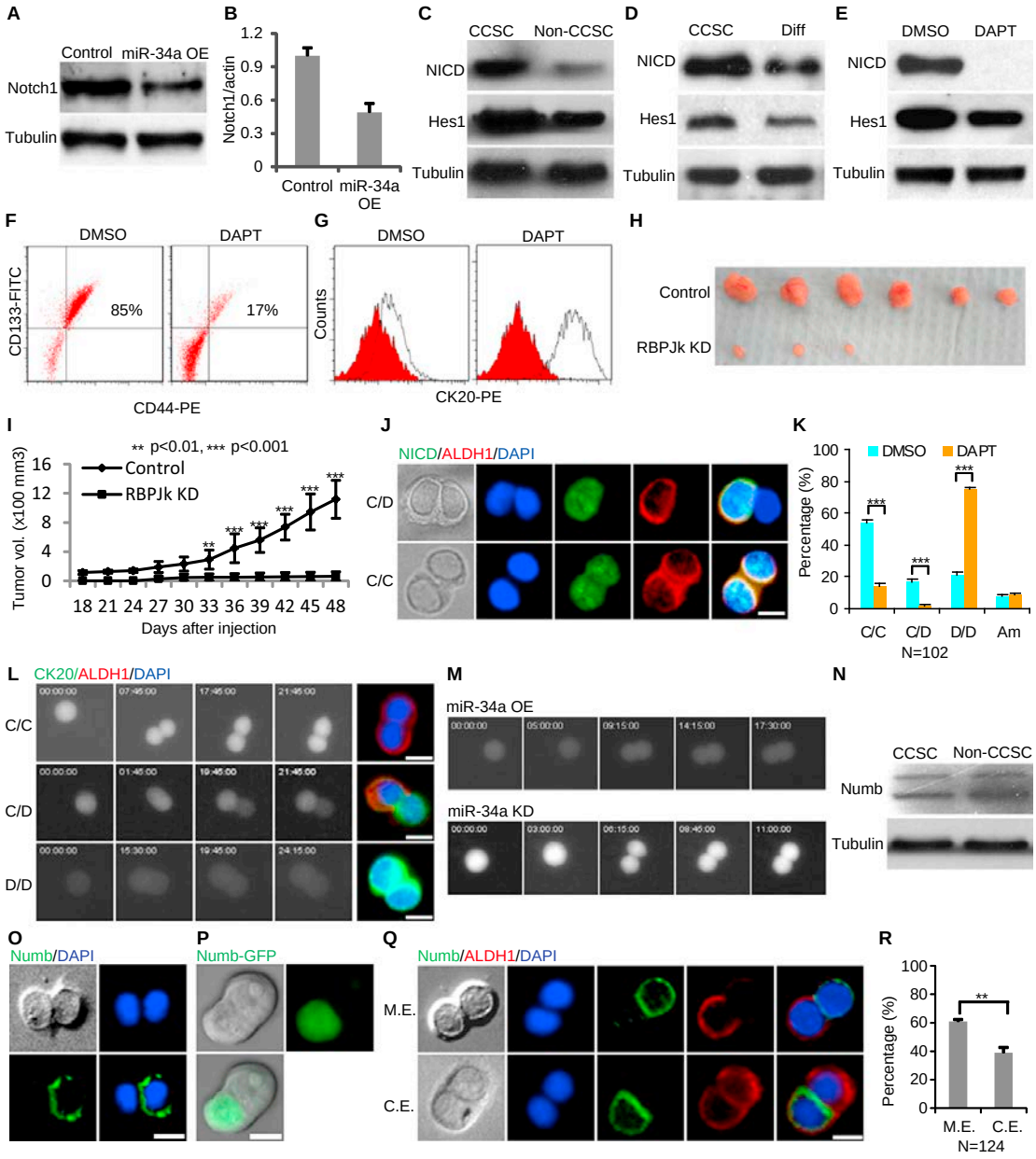

Figure 2.4. miR-34a Targets Notch to Determine Cell-fate *(A and B) Western blot (A) and qRT-PCR (B) showing that ectopic miR-34a expression (miR-34a OE) downregulates Notch1 expression. Error bars denote the SD between triplicates. (C) Notch signaling (NICD and Hes1) is upregulated in CCSCs and downregulated in non-CCSCs isolated by FACS. (D) Notch signaling (NICD and Hes1) is upregulated in CCSCs and downregulated in differentiation medium-induced differentiated cells. Diff, differentiation medium-induced differentiated cells. (E) The γ-secretase inhibitor DAPT inhibits Notch signaling (NICD*

*and HES1) in CCSCs. (F) Notch inhibition by DAPT depletes CCSCs (CD133+CD44+) from spheres compared to the control (DMSO). (G) Notch inhibition by DAPT induces differentiation. The red histograms represent isotype controls, and the blank histograms represent CK20+ cells. (H and I) Inhibition of Notch signaling by anti-RBPJk shRNA reduced tumorigenicity of the sphere cells as shown by tumor images (H) and growth curves (I). Error bars denote the SD derived from six mice per group. (J) Representative images of immunofluorescence for NICD and ALDH1. Notch signaling (NICD, green) is only expressed in ALDH1+ (red) cells. (K) DAPT inhibits asymmetric division (C/D) and increases differentiation (D/D). C/C, CCSC/CCSC daughter pair; C/D, CCSC/non-CCSC daughter pair; D/D, non-CCSC/non-CCSC daughter pair; Am, ambiguous. Error bars denote the SD between triplicates. (L) Representative time-lapse images of a Notch GFP reporter cell line showing the three types of division. Immunofluorescence of the same daughter pairs immediately after Movie S2 confirmed that the Notch+ daughter cells were ALDH1+ and the Notch_ daughter cells were CK20+. (M) Representative time-lapse images showing that ectopic miR-34a expression increases symmetric $Notch^{low}$-$Notch^{low}$ cell division (top), whereas miR-34a knockdown increases symmetric $Notch^{high}$-$Notch^{high}$ cell division (bottom). (N) Western blot showing Numb levels in CCSCs and non-CCSCs. (O) A representative image of symmetric and asymmetric segregation of endogenous Numb (green) as shown by immunofluorescence with Numb antibodies. (P) A representative image of asymmetric segregation of the Numb-GFP fusion protein in living cells. (Q) A representative image showing Numb and ALDH1 are mutually exclusive (M.E., top row) or are coexpressed (C.E) in at least one of the daughter cells (bottom row) during division. (R) Percentages of CCSC divisions wherein Numb and ALDH1 are M.E. or C.E. in daughter cells. Error bars denote the SD between triplicates. DAPI staining of the nucleus is shown in blue. The scale bar represents 8 mm. **, $p < 0.01$; ***, $p < 0.001$. See also Figure S2.5.*

2.4.9 miR-34a Generates A Bimodal Notch Distribution

To understand why miR-34a is more closely correlated with non-CCSC daughter cells than Numb after asymmetric division, we measured the distribution of endogenous Notch1, a direct target of both miR-34a and Numb. FACS of CCSC1 sphere cells showed that Notch1 displayed a bimodal distribution with well-separated peaks (Figure 2.5A, bottom). The bimodal distribution of Notch was also confirmed in other early-stage CCSC lines, including CCSCs freshly isolated from CRC tumors (Figure S2.6A). Notch1 bimodality is important for robust cell-fate decisions, because bimodal signals enable the majority of daughter cells to specify their CCSC versus non-CCSC identity unequivocally, whereas nonbimodal signals leave a substantial portion of the population undecided and are subject to stochastic variations (Figure 2.5B).

Next, we addressed whether miR-34a or Numb was responsible for Notch1 bimodality in sphere cells. FACS of sphere cells with both miR-34a FISH probes and Numb antibodies showed that both miR-34a and Numb distribution in sphere cells were semibimodal, though not to the same extent as Notch1 (Figures 2.5C and 2.5D). Given that miR-34a suppresses Notch1 posttranscriptionally whereas Numb suppresses Notch1 posttranslationally, we delineated their respective effects by constructing a cell line that stably expressed a lentiviral reporter in which the 3' UTR of Notch1 was fused to the EGFP gene. In this system, Notch 3' UTR-EGFP expression displayed a similar bimodal distribution as Notch1, confirming that a posttranscriptional mechanism acting on the Notch1 3' UTR is sufficient to generate bimodality (Figure 2.5E, top panel). Mutation of the miR-34a binding sites in the 3' UTR abolished EGFP bimodality (Figure 2.5E, bottom panel). Altogether, these data indicate that miR-34a contributes to Notch1bimodality.

Then, we tested whether knockdown of miR-34a or Numb affects Notch1 bimodality in CCSC1 and CCSC2 spheres. Two-color FACS with miR-34a FISH probes and Notch1 antibodies revealed that Numb knockdown (Numb KD) by a lentiviral shRNA vector did not completely abolish Notch1 bimodality (Figures 2.5F and S2.6B) (Numb knockdown efficiency was validated by western blot [Figure S2.6C]). In contrast, miR-34a knock-down completely abolished Notch bimodality, even though the distribution of

Numb in the population remained similar (Figures 2.5G and S2.6D). Combined, these results indicate that in CCSC miR-34a plays a more important role than Numb in causing Notch1 bimodality.

To characterize quantitatively the contribution of miR-34a and Numb to Notch bimodality, we induced miR-34a and Numb expression and monitored how they affected the distribution of Notch1 in CCSC1 and CCSC2 spheres. First, we constructed a CCSC line integrated with a Tet-inducible lentiviral vector that can incrementally increase miR-34a expression levels (Figure 2.5H). Instead of gradually reducing Notch1 levels in all cells, an incremental increase of miR-34a levels (confirmed by qRT-PCR) switched off Notch1 expression sharply in individual cells, thus maintaining Notch1 bimodality (Figures 2.5J and S2.6E). Furthermore, FACS with FISH probes showed that the induced miR-34a levels do not need to be bimodal to cause Notch bimodality (Figures 2.5J and S2.6F). Next, we generated CCSC lines that stably expressed Tet-inducible Numb (Figure 2.5I). In contrast to the effect of miR-34a overexpression, increasing Numb levels reduced Notch1 levels in all cells gradually and shifted the entire Notch1 distribution in a continuously graded manner without creating two separate populations (Figures 2.5K and S2.6G). Furthermore, after we knocked down miR-34a to remove potential crosstalk between Numb and miR-34a, Notch1 remained unimodal throughout the induction of Numb (Figures 2.5L and S2.6H).

Collectively, these experiments support a model in which both Numb and miR-34a regulate Notch1, but miR-34a has an intrinsic ability to cause Notch1 bimodality. This role is consistent with our previous findings that miR-34a correlates with cell-fate asymmetry more strongly than Numb does.

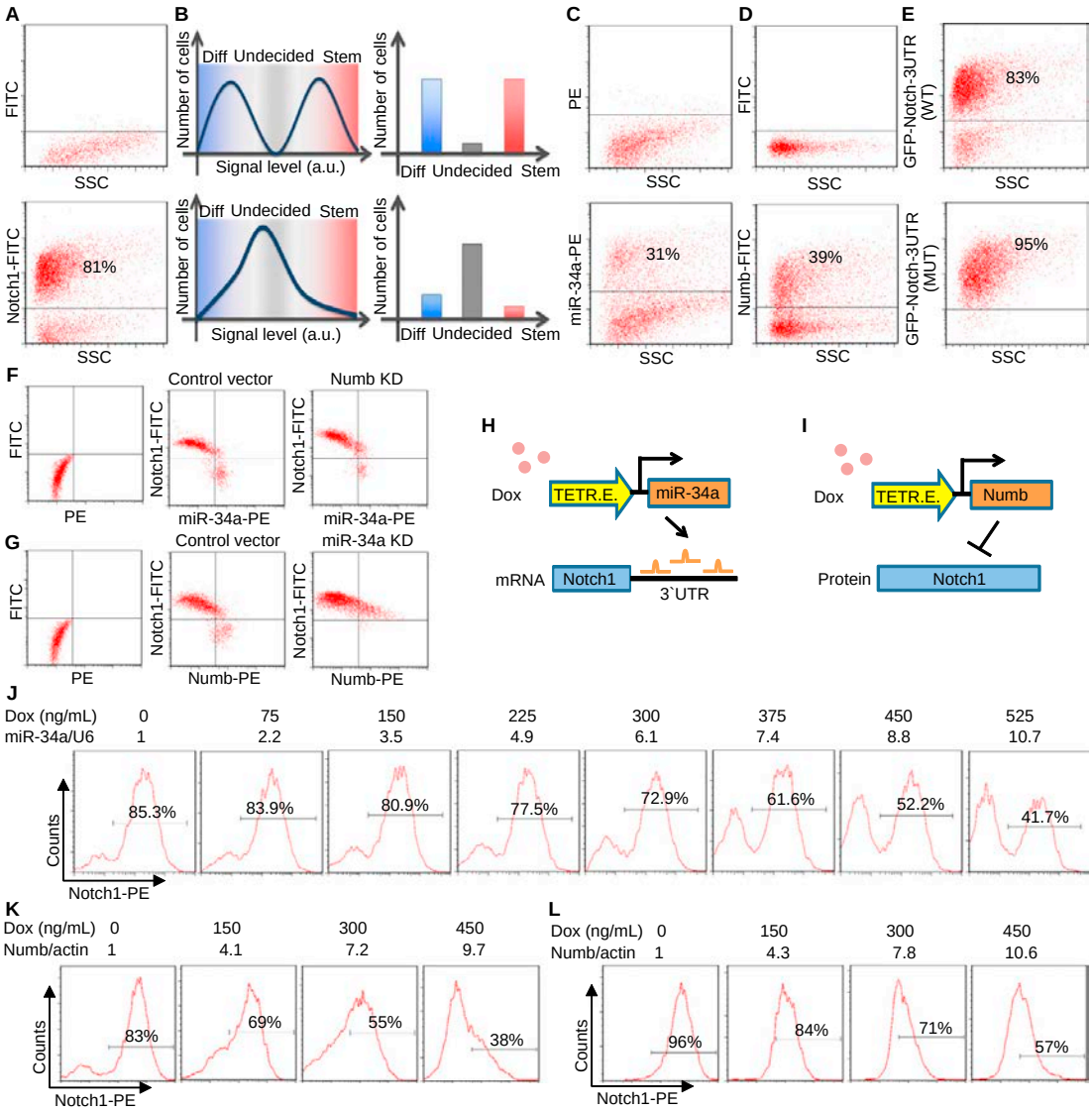

Figure 2.5. miR-34a Generates Bimodal Notch Levels *(A) FACS plots of sphere cells showing bimodal Notch in CCSC sphere cells. The cutoff threshold was determined by the negative control in the top panel with isotype-matched IgG followed by FITC- or PE-conjugated secondary antibodies. Cutoff thresholds for the remaining FACs plots in Figure 5 were determined in a similar way. (B) A schematic representation showing that signaling bimodality is important for robust cell-fate decision. Bimodal signals enable the majority of cells to determine their fate unequivocally, whereas unimodal signals leave a big portion of the population undecided and subject to stochastic variations. (C and D) FACS plots showing miR-34a (C) and Numb (D) distribution in CCSC sphere cells. (E) A FACS plot showing GFP*

levels from Notch1 3' UTR reporters with native (top) and mutated (bottom) miR-34a binding sites. (F) FACS plots showing the distribution of miR-34a and Notch levels in Numb knockdown (KD) and control CCSC sphere cells. Numb was knocked down by an shRNA vector. (G) FACS plots showing the distribution of Numb and Notch levels in miR-34a KD and control CCSC sphere cells. miR-34a was knocked down by microRNA sponges. (H) A schematic illustrating the inducible miR-34a construct used in the experiments shown in (J). (I) A schematic illustrating the inducible Numb construct used in the experiments shown in (K) and (L). (J) Notch1 displayed a bimodal on/off response when miR-34a expression was incrementally induced by doxycycline, as shown by FACS. The miR-34a levels were measured by qRT-PCR and are shown on top of the FACs plots. (K and L) FACS plots showing Notch1 distribution in wild-type CCSC sphere cells (K) and miR-34a KD CCSC sphere cells (L) when Numb expression was incrementally induced by doxycycline. The Numb levels were measured by qRT-PCR and are shown on top of the FACs plots.

2.4.10 Mutual Sequestration Between miR-34a And Notch1 Creates A Sharp Threshold Response

To understand how miR-34a generates Notch1 bimodality, we constructed a mathematical model of miR-34a regulation based on published measurements and equations of microRNA regulation (Osella et al., 2011; Vohradsky et al., 2010) (see Supplemental Information). This analysis revealed a potential mechanism for microRNAs to generate bimodality without feedback.

Incorporated in the RNA-induced silencing complex (RISC), a given microRNA and its target mRNA sequesters each other when they bind together (Levine et al., 2007; Liu et al., 2005) (Figure 2.6A). The strength of this mutual sequestration is dependent on kinetic factors, including binding and disassociation rates, degradation rates, the number and matching sequences of microRNA binding sites, and the recycling time of the microRNA. If the mutual sequestration is sufficiently strong, microRNAs will quickly turn off target genes when the activity level of microRNAs exceeds the target mRNA level (Figure 2.6B). This leads to a threshold response of target gene expression to the microRNA level, which has been demonstrated with synthetic constructs in HeLa cells (Mukherji et al., 2011).

Using a similar experimental approach as Mukherji et al. (2011), we tested specifically whether miR-34a generates a threshold response in Notch1 expression in CCSC1 and CCSC2 spheres. Briefly, we generated CCSC lines that stably express a two-color fluorescent reporter. This reporter contains a bidirectional Tet-inducible promoter that drives the expression of two genes encoding the fluorescent proteins mCherry and enhanced yellow fluorescent protein (eYFP) (Figure 2.6C). The 3' UTR of mCherry contains either the Notch1 3' UTR sequence or four repeats of miR-34a binding sites. The eYFP fluorescence indicates baseline transcriptional activity and the mCherry fluorescence reflects the level of a miR-34a target gene (such as Notch1 or a miR-34a reporter). By normalizing the mCherry fluorescence with the eYFP fluorescence, the effect of miR-34a regulation in single cells can be compared.

After induction by Doxycycline, the levels of eYFP and mCherry in individual cells were measured with fluorescence microscopy. Without miR-34a binding sites in its 3' UTR, the expression level of mCherry was proportional to the level of eYFP expression. When the mCherry 3' UTR contained either the Notch1 3' UTR or tandem miR-34a binding sites, the mCherry level initially showed no significant increase in

comparison to increasing eYFP levels until a threshold was reached. After this point, the mCherry level increased rapidly (Figures 2.6D and S2.7A). This threshold behavior was quantitatively characterized by plotting the transfer function between the mCherry and eYFP levels (Mukherji et al., 2011) (Figure 2.6E). The transfer function confirmed the threshold response of miR-34a target genes, because of the level of mCherry, which represents the target gene expression, does not significantly rise until a threshold level of eYFP is reached.

Stochastic simulations confirmed that the threshold response can generate the observed Notch1 bimodality from the measured miR-34a distribution (Figures S2.7B and S2.7C). Hence, the data collectively support a model that mutual sequestration between miR-34a and Notch1 mRNA generates a sharp response with a threshold, which separates the bimodal Notch+ and miR-34a- CCSC and the Notch- and miR-34a+ non-CCSC subpopulations (Figure 2.6F).

A caveat is that microRNA regulation does not always generate such thresholds. As mentioned previously, the strength of mutual inhibition depends on multiple factors. Mukherji et al. (2011) showed that the existence of a threshold depends on both the number and affinity of the microRNA binding sites in the target mRNA. For example, Mycn, another target of miR-34a (Choi et al., 2011), does not display a bimodal distribution (Figure S2.6I). Therefore, miR-34a may selectively target a subset of genes for bimodal outputs.

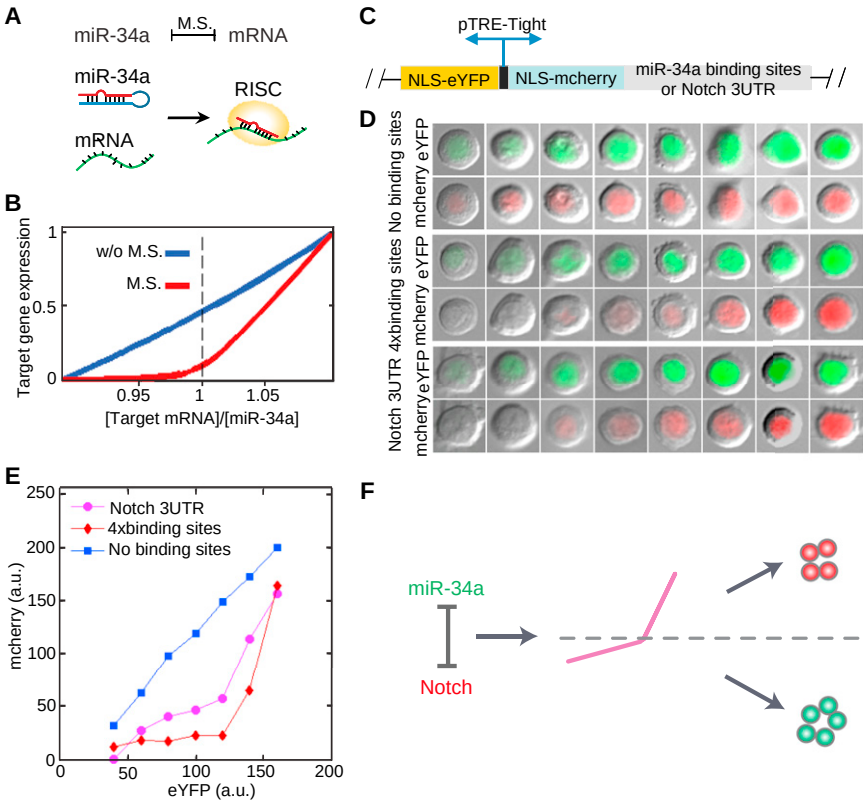

Figure 6. miR-34a Generates Notch1 Threshold Response *(A) A cartoon illustration of the mutual sequestra- tion between miR-34a and Notch1 mRNA. (B) Mutual sequestration leads to a sharp threshold response in simulation. M.S., mutual sequestration. (C) A schematic of a two-color fluorescent reporter. The reporter contains a bidirectional Tet-inducible promoter driving the expression of nuclear localization sequences (NLS)-tagged mCherry and enhanced yellow fluorescent protein (eYFP). Notch 3' UTR or four repeats of the bugled miR-34a binding sequence were cloned into the 3' UTR of mCherry. (D) Representative images of single cells expressing eYFP and mCherry. Their two-color reporters contain Notch 3' UTR (bottom), miR-34a binding sequence (middle), or neither (top). The reporters containing Notch 3' UTR or miR-34a binding sites show a sharper turn-on response with a threshold-like response. (E) Transfer function relating eYFP to mCherry generated by binning the imaged cells according to eYFP intensity and plotting the mean mCherry level in each bin (a.u., arbitrary units). (F) A schematic illustration of the model. Mutual sequestration generates a threshold response that separates bimodal populations. See also Figure S2.7.*

2.5 Discussion

By analyzing the properties of cultured human CRC cells, we determined that the microRNA miR-34a acts as a bimodal switch to target Notch in early-stage CCSCs. This switch controls the choice of daughter cells to self-renew or to differentiate during division. The ability of miR-34a to generate robust binary signals may contribute to its stronger correlation with cell-fate markers during CCSC division than Numb. However, the extent of correlation between Numb and cell-fate markers may be confounded by other factors. First, the phosphorylation state of Numb plays a major role in its localization during asymmetric cell division (Neumu¨ller and Knoblich, 2009), so the level of active Numb, rather than the total level of Numb, may be a better indicator of its function. Second, our characterization of CCSC differentiation may be simplistic. Normal ISCs first differentiate into trans-amplifying (TA) progenitor cells, which then become more terminally differentiated cells. It is possible that there is a progenitor cell population in the CCSC spheres as well, although, to date, there is no identified marker that can distinguish this progenitor subgroup. Alternatively, CRC cells may have "lost" this intermediate state, unlike normal ISCs. If distinct CRC TA progenitors do exist, it is conceivable that these cells might have distinct Numb levels that affect the correlation between Numb and CCSC markers.

Our studies demonstrate that miR-34a's ability to generate a threshold response in its target genes allows it to regulate Notch as a bimodal switch. This switch determines cell-fate asymmetry in a robust and precise way during CCSC division. In addition, miR-34a most likely targets multiple targets besides Notch to further enforce cell-fate determination. Given that various microRNAs are expressed in different types of stem cells, it will not be surprising if some of those microRNAs also act as bimodal switches like miR-34a. Important parameters to generate these switches will include the number and sequence matching of the microRNA binding sites in target mRNAs. In electrical circuit design, switches are widely used because they can function in the presence of environmental and intrinsic noises. The fact that cells and electrical circuits share a similar design principle even though regulatory networks and electronic devices are vastly different illustrates the fundamental importance of mechanisms that convert noisy signals into unambiguous signals for robust decision making.

The miR-34a switch is necessary and sufficient for Notch bimodality. However, the bimodality of miR-34a and Numb levels may further contribute to Notch bimodality. In fact, their mutual correlation with Notch suggests that miR-34a and Numb are not independent regulators. Instead, they most likely share common upstream regulators or crosstalk with each other to determine cell fate synergistically. Hence, the miR-34a switch is probably part of a complex mechanism to ensure robust cell-fate decisions.

Pair-cell assays with early-stage CCSC showed that (a) high miR-34a levels decreased both symmetric CCSC-CCSC division and asymmetric division, resulting in fewer CCSC daughter cells and more non-CCSC daughter cells, and (b) low miR-34a levels increased symmetric CCSC-CCSC division but still decreased asymmetric division, resulting in more CCSC daughter cells and fewer non-CCSC daughter cells. Given that CCSC daughter cells have higher proliferation rates than non-CCSC daughter cells, low miR-34a levels promote proliferation as well as self-renewal and symmetric division. Interestingly, asymmetric division in this system requires miR-34a levels to reside in a “sweet spot” in the middle: either too much or too little miR-34a abolishes asymmetric division. These data support a model where a single microRNA can regulate three distinct cell division outcome “states”: symmetric self-renewal, asymmetric division, and non-self-renewal. Given this ability of microRNAs to enable highly precise and nuanced regulation of the relative proportions of different cell types in a population, we anticipate that future studies will show important roles for microRNAs to regulate tissue homeostasis and pattern formation for many normal stem cell systems that use microRNAs’ ability to “fine-tune” the balance between asymmetric and symmetric stem cell division. Restoration of such roles for microRNAs in cancer cells may represent an important therapeutic strategy for future cancer treatment.

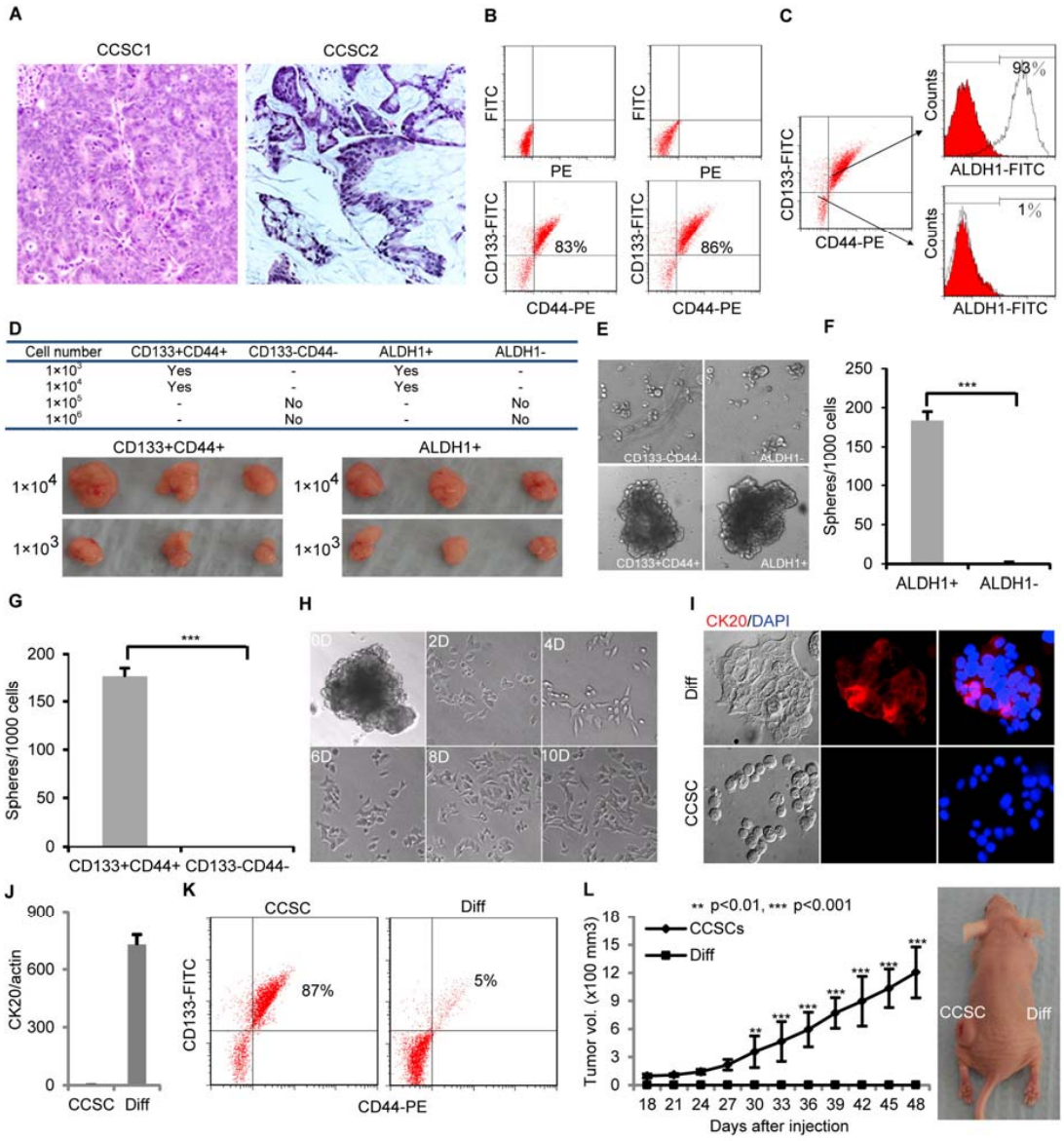

Figure S2.1. Characterization of Early-Stage CCSCs, Related to Figure 2.1 (A) Representative images of xenograft CCSC tumors stained with H&E. CCSC1 and CCSC2 were derived from stage I, II CRC patient tumors (see Table 1). (B) Left panels: FACS plots showing the CD44+CD133+ CCSCs and the CD44-CD133- non- CCSCs subpopulations in colonospheres. Right panels: FACS plots showing isolated CD133+CD44+ cells became heterogeneous and reached a similar equilibrium between CD133+CD44+ CCSCs and CD133-CD44- non-CCSCs as before in spheres. The cutoff thresholds are provided by the negative controls in the top panels with isotype-matched IgG followed by FITC or PE

*conjugated secondary antibodies. (C) FACS showing CD133+CD44+ cells are largely ALDH1+ whereas CD133-CD44- cells are ALDH1-. (D) Top: Tumor formation capability of CD133+CD44+, CD133-CD44-, ALDH1+ and ALDH1- sphere cells in immunodeficient mice. The numbers of injected cells are indicated on the left. Bottom: Representative images of xenograft tumors. (E–G) Sphere forming ability of CD133+CD44+, CD133-CD44-, ALDH1+ and ALDH1- cells. The error bars denotes the s.d. between triplicates. (H) Representative images of CCSC morphology after cultured in differentiation medium (DMEM with 10% FBS) for 2, 4, 6, 8 and 10 days. (I and J) Immunofluorescence (I) and RT-qPCR (J) showing upregulation of CK20 in CCSCs after cultured in differentiation medium for 10 days. The error bars denotes the s.d. between triplicates. (K) FACS plots showing the reduced CD133+CD44+ population in the differentiating culture. (L) Growth curves and representative images of xenograft tumors showing differentiation medium-induced differentiated cells lost the ability to form xenograft tumors. *, $p<0.05$; **, $p<0.01$; ***, $p<0.001$. Error bars denote the s.d. derived from 6 mice per group.*

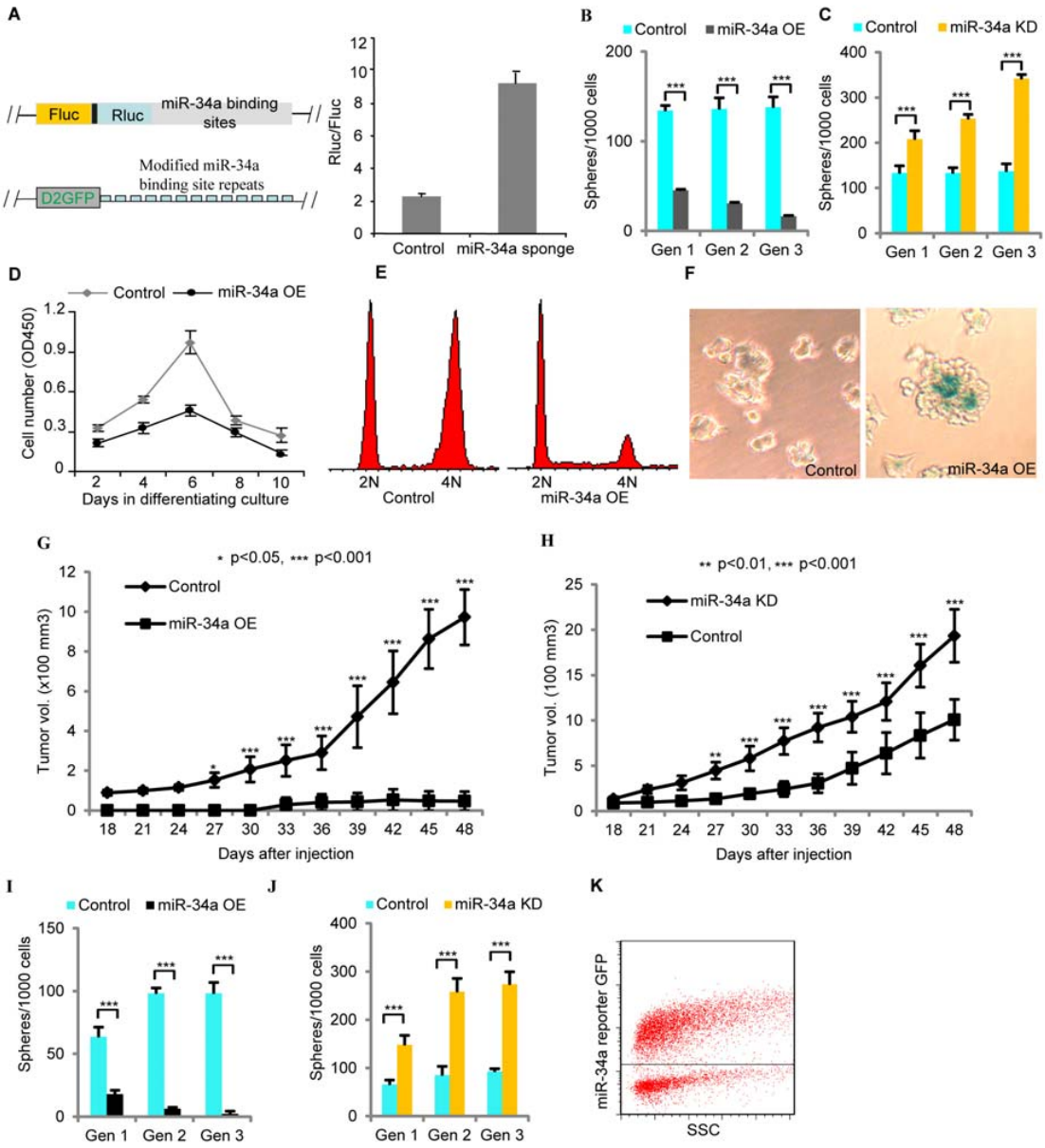

Figure S2.2. miR-34a Regulates CCSC Self-Renewal and Tumor Formation, Related to Figure 2.1 (A) miR-34a knockdown using a miR-34a sponge. Left top, schematic representation of a miR- 34a luciferase reporter. Left bottom, schematic representation of a miR-34a sponge construct, in which 13 repeats of miR-34a binding sequences were cloned into the 3`UTR of D2GFP. Right, the luciferase reporter showing the suppression efficiency by the sponge. Error bars denote the s.d. between triplicates. (B and C) Sphere formation of CCSC2 during serial passages after ectopic miR-34a expression (B) and miR-34a knockdown (C). Error bars denote the s.d. between triplicates. (D) Ectopic miR-34a expression reduces

*CCSCs proliferation in proliferative culture. Error bars denote the s.d. between triplicates. (E and F) Ectopic miR-34a expression (miR-34a OE) induces cell cycle arrest (E) and senescence (F). (G) Ectopic expression of miR-34a (miR-34a OE) reduces CCSC2 tumorigenicity. Error bars denote the s.d. derived from 6 mice per group. (H) Knockdown of miR-34a (miR-34a KD) enhances CCSC2 tumorigenicity. Error bars denote the s.d. derived from 6 mice per group. (I and J) Serial sphere formation of CD133+CD44+ cells isolated from the control vector, miR- 34a OE (I) and miR-34a KD (J) CCSC2 xenograft tumors. Equal number of cells was passaged for 3 generation to form spheres. Error bars denote the s.d. between triplicates. (K) FACS plot showing miR-34a populations in CCSC sphere cells using a GFP reporter with miR-34a binding sites. *, $p<0.05$; **, $p<0.01$; ***, $p<0.001$.*

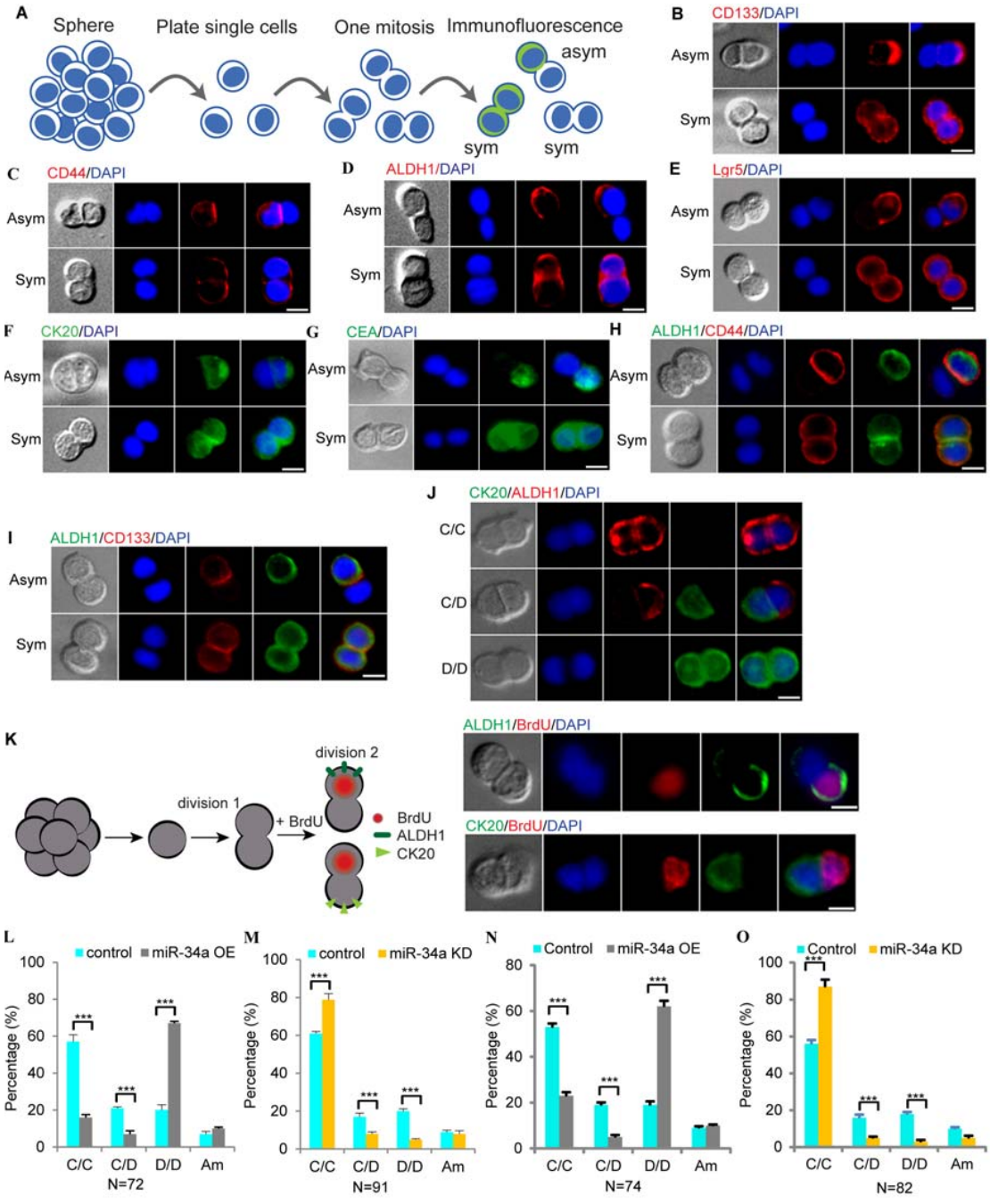

Figure S2.3. miR-34a Regulates CCSC Division, Related to Figure 2.2 (A) Schematic representation of the pair-cell assay for assessing the mode of cell division. (B–G) Representative images of asymmetric and symmetric expression cancer stem cell markers CD133 (B), CD44 (C), ALDH1 (D) and Lgr5 (E), and the differentiation markers CK20 (F) and CEA (G) during sphere cell division. (H) Representative images

*of co-immunofluorescence for ALDH1 (green) and CD44 (red). (I) Representative images of co-immunofluorescence for ALDH1 (green) and CD133 (red). (J) Representative images of co-immunofluorescence for ALDH1 (red) and CK20 (green) in CCSCs isolated from early stage CRC tumors (CCSC6). (K) A functional assay showing cell fate asymmetry leads to distinct proliferation capacity during CCSC2 division. Left, schematic representation of the experimental approach. Single cells were allowed to divide once in 24 hours (1st division). Cells were then treated with BrdU for 3 hours to label cells that were entering the 2nd division before co-staining for BrdU/ALDH1, BrdU/CK20 and Brdu/miR-34a. Right, representative images showing that the CCSC daughter (ALDH1+ or CK20-) was more proliferative and incorporated BrdU. (L) Pair-cell assays with ALDH1 and CK20 co-immunofluorescence showing ectopic miR-34a expression increases symmetric differentiation (D/D) at the expense of asymmetric division (C/D) and symmetric self-renewal (C/C) during CCSC sphere cell division. (M) Pair-cell assay with ALDH1 and CK20 co-immunofluorescence showing miR-34a knockdown increases symmetric self-renewal (C/C) at the expense of asymmetric division (C/D) and symmetric differentiation (D/D) during CCSC2 sphere cell division. (N and O) Immunofluorescence for ALDH1 and CK20 in pair-cell assays showing the percentages of symmetric CCSC-CCSC (C/C), asymmetric (C/D), and symmetric non-CCSC (D/D) divisions in sphere cells, which were cultured from CD133+CD44+ cells isolated from the control vector, miR-34a OE (N) and miR-34a KD (O) CCSC2 xenograft tumors. Am, ambiguous. Blue is DAPI staining of the nucleus. Scale bar, 8 mm. Error bars denote the s.d. between triplicates. ***, $p<0.001$.*

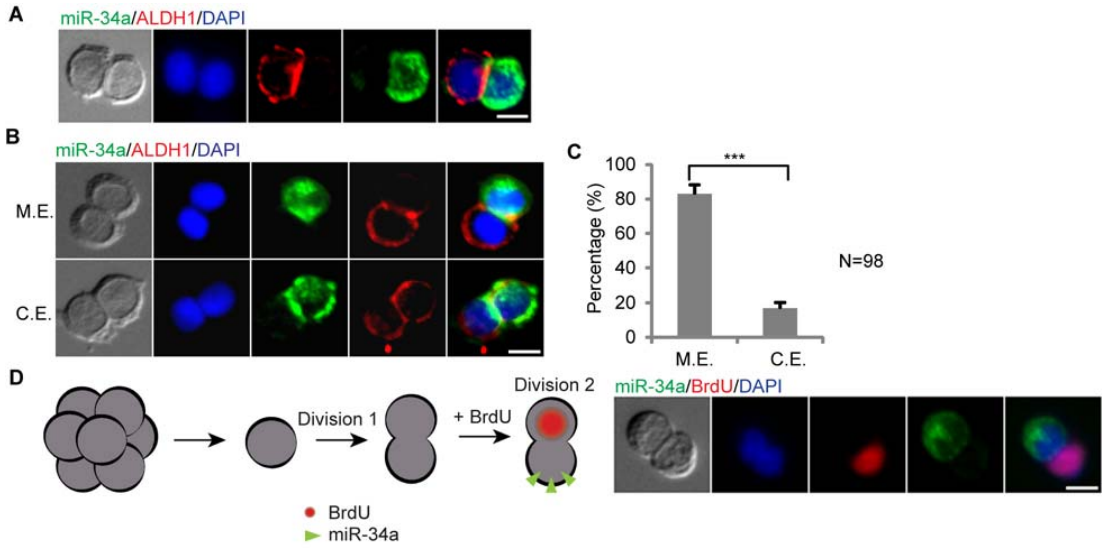

*Figure S2.4. Asymmetric miR-34a Distribution, Related to Figure 2.3. (A) Representative images of co-immunofluorescence for ALDH1 (red) and miR-34a (green) in CCSCs freshly isolated from early stage CRC tumors (CCSC6). (B) Representative images showing miR-34a (RNA FISH) and ALDH1 are mutually exclusive (M.E., top row) or are co-expressed (C.E., bottom row) during CCSC2 division. (C) Percentages of CCSC2 divisions wherein miR-34a and ALDH1 are M.E. or C.E.. (D) A functional assay showing cell fate asymmetry leads to distinct proliferation capacity during CCSC2 division. Left, schematic representation of the experimental approach. Single cells were allowed to divide once in 24 hours (1st division). Cells were then treated with BrdU for 3 hours to label cells that were entering the 2nd division before co-staining for BrdU/ALDH1, BrdU/CK20 and Brdu/miR-34a. Right, representative images showing that miR-34a- daughter cell was more proliferative and incorporated BrdU. Blue is DAPI staining of the nucleus. Scale bar, 8 mm. Error bars denote the s.d. between triplicates. ***, $p<0.001$.*

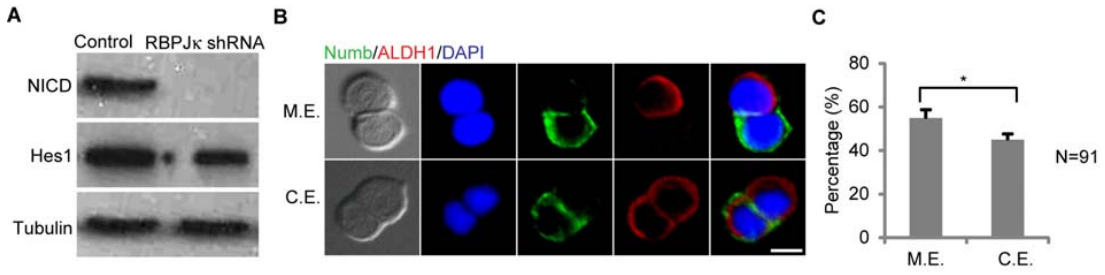

*Figure S2.5. Asymmetric Numb Distribution, Related to Figure 2.4 (A) Western blot showing RBPJk knockdown downregulates Notch signaling (NICD, HES1) in CCSC sphere cells. (B) Representative image showing Numb and ALDH1 are mutually exclusive (M.E., top row) or are co-expressed (C.E) in at least one of the daughter cells (bottom row) during CCSC2 sphere cell division. (C) Percentages of CCSC2 sphere cell divisions wherein Numb and ALDH1 are M.E. or C.E. in daughter cells. Blue is DAPI staining of the nucleus. Scale bar, 8 mm. Error bars denote the s.d. between triplicates. *, $p<0.05$.*

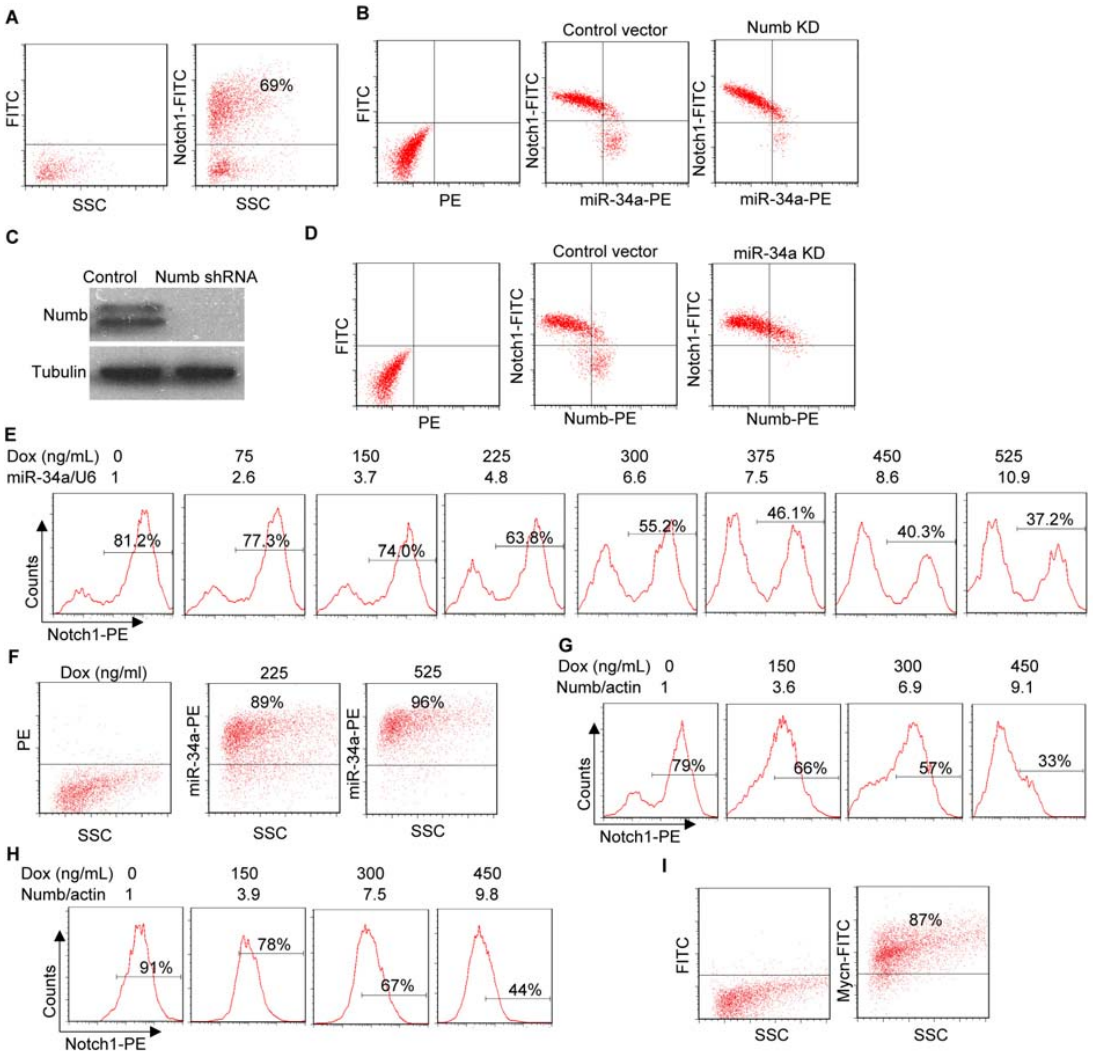

Figure S2.6. miR-34a Generates Bimodal Notch Levels, Related to Figure 2.5 (A) FACS plots of sphere cells showing bimodal Notch distribution in CCSC sphere cells freshly isolated from early stage CRC tumors (CCSC6). The top panel is the negative control with isotype-matched IgG, followed by FITC conjugated secondary antibody. (B) FACS plots showing the distribution of miR-34a and Notch1 levels in Numb knockdown (KD) and control CCSC2 sphere cells. Numb was knocked down by a shRNA vector. (C) Western blot showing Numb was efficiently knocked down by the shRNA construct. (D) FACS plots showing the distribution of Numb and Notch1 levels in miR-34a KD and control CCSC2 sphere cells. miR-34a is knocked down by microRNA sponges.). (E) Notch1 displayed a binary, on-off response in CCSC2 sphere cells when miR-34a expression was incrementally induced by doxycycline, as shown by

FACS. The miR-34a levels were measured by RT-qPCR and shown on top of the FACs plots. (F) FACS plots with RNA FISH showing miR-34a levels during doxycycline induction. The left panel is the negative control with isotype-matched IgG, followed by FITC conjugated secondary antibody. (G and H) FACS plots showing Notch1 distribution in wild-type CCSC2 sphere cells (G) and miR-34a KD CCSC2 sphere cells (H) when Numb expression was incrementally induced by doxycycline. The Numb levels were measured by RT-qPCR and shown on top of the FACs plots. (I) FACs showing Mycn levels in CCSC sphere cells. The top panel is the negative control with isotype-matched IgG, followed by FITC conjugated secondary antibody.

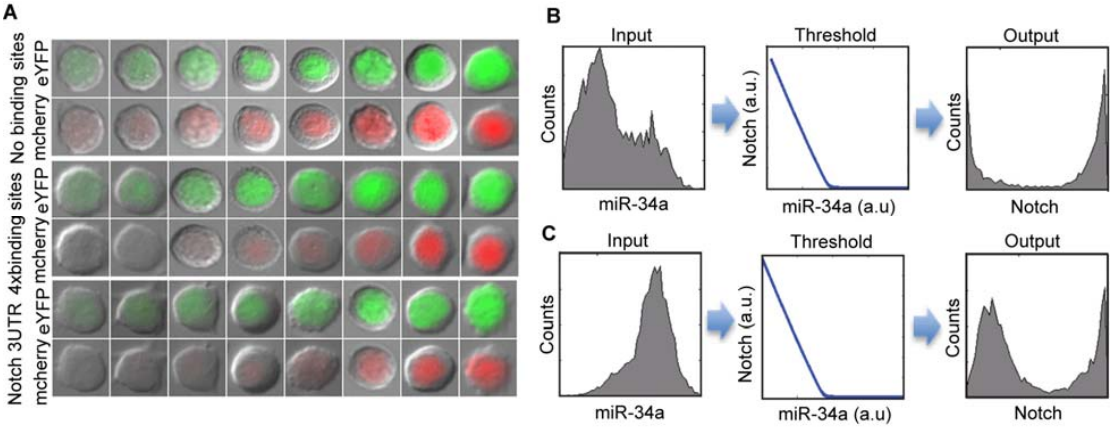

Figure S2.7. miR-34a Generates Notch1 Threshold Response, Related to Figure 2.6 (A) Representative images of single cells from CCSC2 sphere cells expressing YFP and mCherry. Their 2 color reporters contain Notch1 3'UTR (bottom), miR-34a binding sequence (middle) or neither (top). The reporters containing Notch1 3`UTR or miR-34a binding sites show a sharper turn-on with a threshold-like response. (B) In silico simulation showing that threshold enhances Notch1 bimodality in wild-type sphere cells. Left, distribution of miR-34a levels in wild-type sphere cells measured by FACS (Figure 2.5C). Middle, the threshold response. Right, simulated Notch1 distribution. (C) In silico simulation showing that threshold enables unimodal miR-34a to generate Notch1 bimodality. Left, Doxycycline induced miR-34a level measured by FACS (Figure S2.6F). Middle, the threshold response. Right, simulated Notch1 distribution.

REFERENCES

Alison, M.R., Lin, W.R., Lim, S.M., and Nicholson, L.J. (2012). Cancer stem cells: in the line of fire. Cancer Treat. Rev. *38*, 589–598.

Arrowsmith, J. (2011a). Trial watch: Phase II failures: 2008-2010. Nat. Rev. Drug Discov. *10*, 328–329.

Arrowsmith, J. (2011b). Trial watch: phase III and submission failures: 2007- 2010. Nat. Rev. Drug Discov. *10*, 87.

Bultje, R.S., Castaneda-Castellanos, D.R., Jan, L.Y., Jan, Y.N., Kriegstein, A.R., and Shi, S.H. (2009). Mammalian Par3 regulates progenitor cell asym- metric division via notch signaling in the developing neocortex. Neuron *63*, 189–202.

Choi, Y.J., Lin, C.P., Ho, J.J., He, X., Okada, N., Bu, P., Zhong, Y., Kim, S.Y., Bennett, M.J., Chen, C., et al. (2011). miR-34 miRNAs provide a barrier for somatic cell reprogramming. Nat. Cell Biol. *13*, 1353–1360.

Cicalese, A., Bonizzi, G., Pasi, C.E., Faretta, M., Ronzoni, S., Giulini, B., Brisken, C., Minucci, S., Di Fiore, P.P., and Pelicci, P.G. (2009). The tumor suppressor p53 regulates polarity of self-renewing divisions in mammary stem cells. Cell *138*, 1083–1095.

Clevers, H. (2011). The cancer stem cell: premises, promises and challenges. Nat. Med. *17*, 313–319.

Dalerba, P., Dylla, S.J., Park, I.K., Liu, R., Wang, X., Cho, R.W., Hoey, T., Gurney, A., Huang, E.H., Simeone, D.M., et al. (2007). Phenotypic character- ization of human colorectal cancer stem cells. Proc. Natl. Acad. Sci. USA *104*, 10158–10163.

de Sousa E Melo, F., Colak, S., Buikhuisen, J., Koster, J., Cameron, K., de Jong, J.H., Tuynman, J.B., Prasetyanti, P.R., Fessler, E., van den Bergh, S.P., et al. (2011). Methylation of cancer-stem-cell-associated Wnt target genes predicts poor prognosis in colorectal cancer patients. Cell Stem Cell *9*, 476–485.

Dey-Guha, I., Wolfer, A., Yeh, A.C., Albeck, J.G., Darp, R., Leon, E., Wulfkuhle, J., Petricoin, E.F., 3rd, Wittner, B.S., and Ramaswamy, S. (2011). Asymmetric cancer cell division regulated by AKT.

Proceedings of the National Academy of Sciences of the United States of America.

Ebert, M.S., and Sharp, P.A. (2012). Roles for microRNAs in conferring robust- ness to biological processes. Cell *149*, 515–524.

Ebert, M.S., Neilson, J.R., and Sharp, P.A. (2007). MicroRNA sponges: competitive inhibitors of small RNAs in mammalian cells. Nat. Methods *4*, 721–726. Emmink, B.L., Van Houdt, W.J., Vries, R.G., Hoogwater, F.J., Govaert, K.M., Verheem, A., Nijkamp, M.W., Steller, E.J., Jimenez, C.R., Clevers, H., et al. (2011). Differentiated human colorectal cancer cells protect tumor-initiating cells from irinotecan. Gastroenterology *141*, 269–278.

Goulas, S., Conder, R., and Knoblich, J.A. (2012). The Par complex and integ- rins direct asymmetric cell division in adult intestinal stem cells. Cell Stem Cell *11*, 529–540. Guardavaccaro, D., and Clevers, H. (2012). Wnt/b-catenin and MAPK signaling: allies and enemies in different battlefields. Sci. Signal. *5*, pe15.

He, L., He, X., Lim, L.P., de Stanchina, E., Xuan, Z., Liang, Y., Xue, W., Zender, L., Magnus, J., Ridzon, D., et al. (2007). A microRNA component of the p53 tumour suppressor network. Nature *447*, 1130–1134.

Huang, E.H., Hynes, M.J., Zhang, T., Ginestier, C., Dontu, G., Appelman, H., Fields, J.Z., Wicha, M.S., and Boman, B.M. (2009). Aldehyde dehydrogenase 1 is a marker for normal and malignant human colonic stem cells (SC) and tracks SC overpopulation during colon tumorigenesis. Cancer Res. *69*, 3382–3389.

Itzkovitz, S., Blat, I.C., Jacks, T., Clevers, H., and van Oudenaarden, A. (2012). Optimality in the development of intestinal crypts. Cell *148*, 608–619.

Ivey, K.N., and Srivastava, D. (2010). MicroRNAs as regulators of differentia- tion and cell fate decisions. Cell Stem Cell *7*, 36–41. Jahid, S., Sun, J., Edwards, R.A., Dizon, D., Panarelli, N.C., Milsom, J.W., Sikandar, S.S., Gumus, Z.H., and Lipkin, S.M. (2012). miR-23a Promotes the Transition from Indolent to Invasive Colorectal Cancer. Cancer discovery. LaPointe, L.C., Dunne, R., Brown, G.S., Worthley, D.L., Molloy, P.L., Wattchow, D., and Young, G.P. (2008). Map of differential transcript

expression in the normal human large intestine. Physiol. Genomics *33*, 50–64. Lathia, J.D., Hitomi, M., Gallagher, J., Gadani, S.P., Adkins, J., Vasanji, A., Liu, L., Eyler, C.E., Heddleston, J.M., Wu, Q., et al. (2011). Distribution of CD133 reveals glioma stem cells self-renew through symmetric and asymmetric cell divisions. Cell Death Dis *2*, e200.

Levine, E., McHale, P., and Levine, H. (2007). Small regulatory RNAs may sharpen spatial expression patterns. PLoS Comput. Biol. *3*, e233. Li, X., Madison, B.B., Zacharias, W., Kolterud, A., States, D., and Gumucio, D.L. (2007). Deconvoluting the intestine: molecular evidence for a major role of the mesenchyme in the modulation of signaling cross talk. Physiol. Genomics *29*, 290–301.

Li, Y., Guessous, F., Zhang, Y., Dipierro, C., Kefas, B., Johnson, E., Marcinkiewicz, L., Jiang, J., Yang, Y., Schmittgen, T.D., et al. (2009). MicroRNA-34a inhibits glioblastoma growth by targeting multiple oncogenes. Cancer Res. *69*, 7569–7576.

Liu, J., Valencia-Sanchez, M.A., Hannon, G.J., and Parker, R. (2005). MicroRNA-dependent localization of targeted mRNAs to mammalian P-bodies. Nat. Cell Biol. *7*, 719–723.

Liu, C., Kelnar, K., Liu, B., Chen, X., Calhoun-Davis, T., Li, H., Patrawala, L., Yan, H., Jeter, C., Honorio, S., et al. (2011). The microRNA miR-34a inhibits prostate cancer stem cells and metastasis by directly repressing CD44. Nat. Med. *17*, 211–215.

Loboda, A., Nebozhyn, M.V., Watters, J.W., Buser, C.A., Shaw, P.M., Huang, P.S., Van't Veer, L., Tollenaar, R.A., Jackson, D.B., Agrawal, D., et al. (2011). EMT is the dominant program in human colon cancer. BMC Med. Genomics *4*, 9.

Lu, J., and Tsourkas, A. (2009). Imaging individual microRNAs in single mammalian cells in situ. Nucleic Acids Res. *37*, e100.

McGill, M.A., and McGlade, C.J. (2003). Mammalian numb proteins promote Notch1 receptor ubiquitination and degradation of the Notch1 intracellular domain. J. Biol. Chem. *278*, 23196–23203.

Mukherji, S., Ebert, M.S., Zheng, G.X., Tsang, J.S., Sharp, P.A., and van Oudenaarden, A. (2011). MicroRNAs can generate thresholds in target gene expression. Nat. Genet. *43*, 854–859.

Neumuller, R.A., and Knoblich, J.A. (2009). Dividing cellular asymmetry: asym- metric cell division and

its implications for stem cells and cancer. Genes Dev. *23*, 2675–2699.

O'Brien, C.A., Pollett, A., Gallinger, S., and Dick, J.E. (2007). A human colon cancer cell capable of initiating tumour growth in immunodeficient mice. Nature *445*, 106–110.

O'Brien, C.A., Kreso, A., Ryan, P., Hermans, K.G., Gibson, L., Wang, Y., Tsatsanis, A., Gallinger, S., and Dick, J.E. (2012). ID1 and ID3 regulate the self-renewal capacity of human colon cancer-initiating cells through p21. Cancer Cell *21*, 777–792.

Osella, M., Bosia, C., Cora, D., and Caselle, M. (2011). The role of incoherent microRNA-mediated feedforward loops in noise buffering. PLoS Comput. Biol. *7*, e1001101.

Pauli, A., Rinn, J.L., and Schier, A.F. (2011). Non-coding RNAs as regulators of embryogenesis. Nat. Rev. Genet. *12*, 136–149.

Pece, S., Tosoni, D., Confalonieri, S., Mazzarol, G., Vecchi, M., Ronzoni, S., Bernard, L., Viale, G., Pelicci, P.G., and Di Fiore, P.P. (2010). Biological and molecular heterogeneity of breast cancers correlates with their cancer stem cell content. Cell *140*, 62–73.

Pine, S.R., Ryan, B.M., Varticovski, L., Robles, A.I., and Harris, C.C. (2010). Microenvironmental modulation of asymmetric cell division in human lung cancer cells. Proc. Natl. Acad. Sci. USA *107*, 2195–2200.

Potten, C.S., Owen, G., and Booth, D. (2002). Intestinal stem cells protect their genome by selective segregation of template DNA strands. J. Cell Sci. *115*, 2381–2388.

Quyn, A.J., Appleton, P.L., Carey, F.A., Steele, R.J., Barker, N., Clevers, H., Ridgway, R.A., Sansom, O.J., and Na¨thke, I.S. (2010). Spindle orientation bias in gut epithelial stem cell compartments is lost in precancerous tissue. Cell Stem Cell *6*, 175–181.

Ricci-Vitiani, L., Lombardi, D.G., Pilozzi, E., Biffoni, M., Todaro, M., Peschle, C., and De Maria, R. (2007). Identification and expansion of human colon- cancer-initiating cells. Nature *445*, 111–115.

Sampieri, K., and Fodde, R. (2012). Cancer stem cells and metastasis. Semin. Cancer Biol. *22*, 187–193.

Sa´ nchez-Tillo´ , E., de Barrios, O., Siles, L., Cuatrecasas, M., Castells, A., and Postigo, A. (2011). b-catenin/TCF4 complex induces the epithelial-to-mesen- chymal transition (EMT)-activator ZEB1 to

regulate tumor invasiveness. Proc. Natl. Acad. Sci. USA *108*, 19204–19209.

Schweisguth, F. (2004). Regulation of notch signaling activity. Curr. Biol. *14*, R129–R138.

Sikandar, S., Edwards, R., Lyles, K., Waterman, M., and Lipkin, S.M. (2010). NOTCH signaling is required for formation and self-renewal of tumor-initiating cells and for repression of secretory cell differentiation in colon cancer. Cancer Res. *70*, 1469–1478.

Sugiarto, S., Persson, A.I., Munoz, E.G., Waldhuber, M., Lamagna, C., Andor, N., Hanecker, P., Ayers-Ringler, J., Phillips, J., Siu, J., et al. (2011). Asymmetry-defective oligodendrocyte progenitors are glioma precursors. Cancer Cell *20*, 328–340.

Taketo, M.M. (2011). Reflections on the spread of metastasis to cancer prevention. Cancer Prev. Res. (Phila.) *4*, 324–328.

Todaro, M., Alea, M.P., Di Stefano, A.B., Cammareri, P., Vermeulen, L., Iovino, F., Tripodo, C., Russo, A., Gulotta, G., Medema, J.P., and Stassi, G. (2007). Colon cancer stem cells dictate tumor growth and resist cell death by produc- tion of interleukin-4. Cell Stem Cell *1*, 389–402.

Tsang, J., Zhu, J., and van Oudenaarden, A. (2007). MicroRNA-mediated feed- back and feedforward loops are recurrent network motifs in mammals. Mol. Cell *26*, 753–767.

van Es, J.H., van Gijn, M.E., Riccio, O., van den Born, M., Vooijs, M., Begthel, H., Cozijnsen, M., Robine, S., Winton, D.J., Radtke, F., and Clevers, H. (2005). Notch/gamma-secretase inhibition turns proliferative cells in intestinal crypts and adenomas into goblet cells. Nature *435*, 959–963.

Vohradsky, J., Panek, J., and Vomastek, T. (2010). Numerical modelling of microRNA-mediated mRNA decay identifies novel mechanism of microRNA controlled mRNA downregulation. Nucleic Acids Res. *38*, 4579–4585.

Wurbel, M.A., McIntire, M.G., Dwyer, P., and Fiebiger, E. (2011). CCL25/CCR9 interactions regulate large intestinal inflammation in a murine model of acute colitis. PLoS ONE *6*, e16442.

Youn, B.S., Kim, Y.J., Mantel, C., Yu, K.Y., and Broxmeyer, H.E. (2001). Blocking of c-FLIP(L)—independent cycloheximide-induced apoptosis or Fas-mediated apoptosis by the CC chemokine receptor 9/TECK interaction. Blood *98*, 925–933.

CHAPTER 3

MIR-34A AND NUMB SYNERGIZE FOR ASYMMETRIC CELL FATE DETERMINATION TO CONTROL STEM CELL PROLIFERATION

3.1 Summary

Asymmetric cell division relies on spatial imbalance of cell fate determinant proteins to break symmetry. Emerging evidence suggests that microRNAs can also act as cell fate determinants, but whether microRNA and protein cell fate determinants coordinate with each other remains unclear. Here we show that miR-34a directly suppresses Numb in early-stage colon cancer stem cells (CCSCs), although both target Notch to promote differentiation. Mathematical modeling and quantitative analyses revealed that an incoherent feedforward loop (IFFL) synergizes the two cell fate determinants to create a unique regulatory scheme in order to separate stem and non-stem cell fates robustly. Perturbation of the IFFL leads to a new intermediate cell population with plastic and ambiguous identity. Lgr5+ mouse intestinal stem cells (ISCs) normally undergo symmetric division, but turn on asymmetric division to curb the number of ISCs when proinflammatory stress causes excessive proliferation. Deletion of miR-34a inhibits asymmetric division and exacerbates Lgr5+ ISC proliferation under such stress. Collectively, our data indicate that microRNA and protein cell fate determinants coordinate to enhance robustness of cell fate decision, and they provide a safeguard mechanism against stem cell proliferation induced by inflammation or oncogenic mutation.

3.2 Introduction

Cells usually divide symmetrically, producing two identical daughter cells. However, there are prokaryotic and eukaryotic cells that can divide asymmetrically, giving rise to daughter cells with different characteristics (Li 2013). In higher organisms, asymmetric division is a property associated with many types of stem and progenitor cells in embryo, nervous system, skin, mammary gland, blood, etc, in order to balance proliferation and differentiation as well as aging (Beckmann, Scheitza et al. 2007, Knoblich 2008, Bultje, Castaneda-Castellanos et al. 2009, Neumuller and Knoblich 2009, Williams,

Beronja et al. 2011, Inaba and Yamashita 2012, Jackson, Waterhouse et al. 2015, Katajisto, Dohla et al. 2015). Asymmetric division manages differentiation and self-renewal simultaneously while keeping the number of stem cells constant, making it an attractive mechanism for tissue homeostasis. On the other hand, symmetric division expands the number of stem cells, and often occurs during early embryonic development, tissue regeneration and repair (Morrison and Kimble 2006). These are certainly not fixed rules, because stem cells often rely on a spatial niche to regulate their number and behavior (Lander, Kimble et al. 2012). For example, Lgr5+ crypt base columnar (CBC) cells in the intestine predominantly undergo symmetric division, and rely on a neutral drift process in the niche to stabilize their number (Lopez-Garcia, Klein et al. 2010, Snippert, van der Flier et al. 2010).

Cancer stem cells, or tumor initiating cells, of various cancer types, undergo both symmetric and asymmetric division (Cicalese, Bonizzi et al. 2009, Pece, Tosoni et al. 2010, Pine, Ryan et al. 2010, Dey-Guha, Wolfer et al. 2011, Lathia, Hitomi et al. 2011, Sugiarto, Persson et al. 2011, O'Brien, Kreso et al. 2012, Bajaj, Zimdahl et al. 2015). Loss of tumor suppressor genes often favors increased symmetric divisions of cancer stem cells, which promote proliferation and tumor growth.

Asymmetric cell division usually relies on imbalance of cell fate determinant proteins in the two cellular compartments to break symmetry, resulting in daughter cells with distinct cell fates. A canonical cell fate determinant in Drosophila neuroblasts and various mammalian stem cells, Numb targets membrane-bound Notch receptors for degradation (McGill and McGlade 2003, Schweisguth 2004). Furthermore, Numb is a cell fate determinant for various cancer stem cells, and has been used as a marker for distinguishing symmetric vs. asymmetric division (O'Brien, Kreso et al. 2012).

Recently, emerging evidence suggests that asymmetric distribution of microRNAs can also give rise to asymmetric cell fates (Bu, Chen et al. 2013, Hwang, Jiang et al. 2014). For example, we have shown that miR-34a directly targets Notch to form a cell fate determination switch in colon cancer stem cells (CCSCs). A tumor suppressor in many cancer types, miR-34a regulates differentiation of embryonic and neural stem cell, somatic cell reprogramming, and cardiac aging (He, He et al. 2007, Choi, Lin et al. 2011,

Liu, Kelnar et al. 2011, Boon, Iekushi et al. 2013). miR-34a mimics such as MRX34 are among the first microRNA mimics to reach clinical trial for cancer therapy (Bader 2012, Bouchie 2013).

However, this raises the question as to whether microRNA and protein cell fate determinants act independently or coordinate with each other to determine cell fate. The relationship between miR-34a and Numb is intriguing, because both target Notch in CCSCs. Here we show that miR-34a directly bind to the 3`UTR of Numb mRNA to suppress Numb expression, so that miR-34a, Numb, and Notch form an incoherent feedforward loop (IFFL). Combination of computational analysis and quantitative experiments revealed that the unique regulatory kinetics among miR-34a, Numb, and Notch enables a robust binary switch, so that Notch level is steady and insensitive to precise miR-34a level except for a sharp transition region. The switch enforces bimodality and cell fate bifurcation in the population. Subversion of this IFFL via Numb knockdown degrades Notch bimodality and gives rise to an intermediate subpopulation of cells with ambiguous and plastic cell fate. We further show that this cell fate determination switch plays a role in mouse intestinal stem cells (ISCs). Although Lgr5+ ISCs divide symmetrically in normal tissue homeostasis, we found that excessive proliferation caused by pro-inflammatory stress or APC deficiency triggers asymmetric division, which restrains the number of Lgr5+ ISCs. Silencing of the miR-34a-mediated switch inhibits ISC asymmetric division and contributes to CCSC-like proliferation. Hence, the cell fate determinants provide a safeguard mechanism against excessive stem cell proliferation when normal homeostasis is disrupted by inflammation or oncogenic mutation.

3.3 Material And Methods

Isolation and Culture of CCSCs

CCSCs were isolated and cultured as described previously (Bu, Chen et al. 2013). Briefly, CCSCs were isolated from patient tumors by FACS based on markers CD44, CD133 and ALDH1 and functionally validated by serial sphere formation, tumor initiation, and self-renewal assays(Bu, Chen et al. 2013). CCSCs were cultured as spheres in ultralow-attachment flasks (Corning) in DMEM/F12 (Invitrogen), supplemented with nonessential amino acids (Fisher), sodium pyruvate (Fisher), Penicillin-streptomycin (Fisher), N2 supplement (Invitrogen), B27 supplement (Invitrogen), 4 mg/mL heparin (Sigma), 40 ng/mL

epidermal growth factor (Invitrogen), and 20 ng/mL basic fibroblast growth factor (Invitrogen) at 37 °C and 5% CO_2. To propagate *in vitro*, spheres were collected by gentle centrifugation, dissociated into single cells, and then cultured to form next generation spheres.

CCSC Differentiation and Sphere Formation Analysis

To induce differentiation, CCSCs were dissociated from spheres using trypsin-EDTA and were plated at 1.8×10^5 cells/mL on 60 mm dishes pre-coated with Collagen IV (Corning) in DMEM supplemented with 10% FBS and without growth factors. To measure tumor sphere formation, single CCSCs were plated in 24-well ultra-low attachment plates (Corning) at 1,000 cells per well. Tumor spheres were counted after 2 weeks in culture by an inverted microscope (Olympus).

Transgenic Mice and DSS treatment

Lgr5-EGFP-creER^{T2}/miR-34a$^{flox/flox}$ mice were generated by interbreeding *Lgr5-EGFP-creER^{T2}* mice (Sato, Vries et al. 2009) and *miR-34a$^{flox/flox}$* mice (Concepcion, Han et al. 2012). *Lgr5-EGFP-creER^{T2}/APC$^{flox/flox}$* mice were generated by interbreeding *Lgr5-EGFP-creER^{T2}* mice with *APC$^{flox/flox}$* mice (Shibata, Toyama et al. 1997). Cre recombinase was induced by intraperitoneal injection of Tamoxifen (Sigma) dissolved in sterile corn oil for 5 consecutive days at a dose of 75mg/kg. For DSS treatment, 6-8 week old mice were treated with DSS (36,000–50,000 kDa; MP Biomedicals) in daily drinking water for 5 days, followed by plain water for 5 days. All animal experiments were approved by The Cornell Center for Animal Resources and Education (CARE) and followed the protocol (2009-0071 and 2010-0100).

Mouse intestinal organoid culture

Crypt isolation, cell dissociation, and organoid culturing were performed using previously described protocol (Sato, Vries et al. 2009). For TNFa treatment, organoid cells were cultured in medium containing 10ng/ml TNFa (R&D) for 72 hours.

Immunofluorescence

Pair-cell assay was used to investigate CCSC division. Disassociated single CCSC sphere cells were plated on an uncoated glass culture slide (Corning) and allowed to divide once. After fixed in cold methanol, the cells were blocked in 10% normal goat serum for 1 hour and then incubated with anti-

ALDH1 (clone H-4, 1:100, Santa Cruz), anti-CK20 (clone H-70, 1:100, Santa Cruz), anti-Numb (1:100, Abcam) and anti-Notch1 (1:400, Abcam) antibody overnight at 4 °C. For the BrdU incorporation assay, the tissue sections were incubated in 1M HCl for 1 hour at 37 °C after fixation. The sections were then washed, and switched to 100 mM $Na_2B_4O_7$ for 2 minutes. After blocked in 10% normal goat serum for 1 hour, the cells were then incubated with anti-BrdU (1:200, Sigma). The cells were then incubated with Rhodamine Red labeled secondary antibody (Invitrogen) for 1 hour at room temperature. After counterstained with DAPI (Invitrogen), the slides were observed under a fluorescent microscope (Olympus).

Divisions of Lgr5-EGFP ISCs were examined by three methods. First, Lgr5-GFP doublets were directly collected from intestinal organoids by FACS sorting. The cells were then immediately fixed in 4% paraformaldehyde, permeabilized in 0.5% Triton-X and stained with anti-GFP-Alexa Fluor 488 (1:500, Abcam), anti-Olfm4 (1:100, Abcam) and anti-b-Tubulin-Cy3 antibodies (1:100, Sigma). In the second method, single Lgr5-GFP cells were plated in Matrigel and allowed to divide once. The cells were then fixed, permeabilized and stained with anti-GFP, anti-Olfm4 and anti-a-tubulin (1:500, Abcam) antibodies. In the third method, intestines from *LGR5-EGFP-creER^{T2}* and *LGR5-EGFP-creER^{T2}/APC$^{flox/flox}$* mice and human colon and CRC samples were fixed in 4% paraformaldehyde. Frozen sections were then prepared and stained with anti-GFP, anti-Olfm4 and anti-a-tubulin (1:500, Abcam) antibodies. After counterstaining with DAPI (Invitrogen), the slides were observed under a fluorescent microscope (Olympus).

RNA FISH

RNA FISH was performed as described as previously (Bu, Chen et al. 2013). In brief, CCSCs were fixed with 4% formaldehyde for 30 minutes at room temperature, followed by permeabilization in 70% ethanol at 4 °C overnight. 1-ethyl-3-(3-dimethylaminopropyl) carbodiimide (EDC) fixation was applied to prevent the loss of miRNA. After a 2 hour incubation in prehybridization buffer (25% formamide, 0.05 M EDTA, 4×SSC, 10% dextran sulfate, 1×Denhardt's solution, 0.5 mg/ml Escherichia coli tRNA and 0.5 mg/ml RVC), digoxigenin (DIG)–labeled locked nucleic acid (LNA) probe (Exiqon) was added for

hybridization. The slides were then incubated with anti-DIG antibody (1:400, Roche), and the miRNA expression was detected by Rhodamine Red labeled secondary antibody (Invitrogen). DAPI (Invitrogen) was used for nucleic counterstaining. The slide was then observed under a fluorescent microscope (Olympus).

Flow Cytometry

Single CCSC sphere cells were incubated with anti-Notch1 antibody (1:100, Abcam) after fixed with formaldehyde and further permeabilized by methanol. The cells were then incubated with PE labeled secondary antibody (Invitrogen). Lgr5-GFP population was evaluated by directly measuring GFP signal from intestinal organoids. ALDH1 levels were analyzed using the Aldeflour kit. The samples were analyzed using a BD LSR II flow cytometer. The raw FACS data were analyzed with the FlowJo software to gate cells according to their forward (FSC) and side (SSC) scatter profiles.

Quantitative Real-time RT-PCR Analysis

Total RNA was extracted from the cells using the TRIzol Reagent (Invitrogen). cDNA was synthesized from 500 ng of total RNA in 20 ml of reaction volume using the High Capacity cDNA Archive Kit (Applied Biosystems). Quantitative PCR was carried out using the SYBR Green System (Applied Biosystems) to detect gene expression. All samples were run in triplicate three times. The primer sequences include: Notch1, 5`-GTGACTGCTCCCTCAACTTCAAT-3` and 5`-CTGTCACAGTGGCCGTCACT-3`; Notch2, 5'-AACTGTCAGACCCTGGTGAAC-3' and 5`-CGACAAGTGTAGCCTCCAATC-3`; Numb, 5`-GCTGCCTCTCCAGGTCTCTTC-3` and 5`-CGCTCTTAGACACCTCTTCTAACCA-3`; CK20, 5`- AGGAGACCAAGGCCCGTTA-3` and 5`-ATCAGTTGGGCCTCCAGAGA-3`; actin, 5`-CGCGAGAAGATGACCCAGAT-3` and 5`-ACAGCCTGGATAGCAACGTACAT-3`;. The expression of each gene was defined from the threshold cycle (Ct), and the relative expression levels were calculated using the 2-‥Ct method after normalization to the actin expression level.

Western Blot

Whole cell lysate was prepared in a lysis buffer (20 mM Tris pH 7.5, 150 mM NaCl, 1% Nonidet P-40, 0.5% Sodium Deoxycholate, 1 mM EDTA, 0.1% SDS, protease inhibitors). Proteins were first separated by 10% SDS-PAGE and then transferred to a Hybond membrane (Amersham). The membranes were incubated with primary antibodies either anti-Notch1 (1:1000, Abcam), anti-Numb (1:1000, Abcam), anti-NICD (1:1000, R&D Systems), anti-Hes1 (1:500, Millipore), or anti-Action (1:1000, Abcam) in 5% milk/TBST buffer (25 mM Tris pH 7.4, 150 mM NaCl, 2.5 mM KCl, 0.1% Triton-X100) overnight, and then probed for 1 hour with secondary horseradish peroxidase (HRP)-conjugated anti-mouse or anti-rabbit IgG (Santa Cruz). After extensive wash with PBST, the target proteins were detected on membrane by enhanced chemiluminescence (Pierce).

Lentiviral Vector Constructs and Infection

Lentiviral constructs expressing miR-34a or Numb shRNA have been described previously(Bu, Chen et al. 2013). The Numb luciferase reporter was generated by cloning the Numb 3`UTR into the pGL3 construct. The QuickChange Site-directed Mutagenesis Kit (Stratagene) was used to mutate the miR-34a binding sequence in Numb 3`UTR. CCSCs and intestinal organoids were infected with the vectors as described previously (Koo, Stange et al. 2012, Bu, Chen et al. 2013)

Statistical Analysis

Data were expressed as mean ± standard deviation of three biological repeats. Student t-tests were used for comparisons, with $p<0.05$ considered significant.

3.4 Results

3.4.1 miR-34a Directly Targets Numb.

Using CCSCs derived from patient tumors as we have previously described and characterized (Bu, Chen et al. 2013), we first examined whether miR-34a and Numb spatial distributions are independent or correlated in divided pairs by performing pair-cell assay with immunofluorescence (Bultje, Castaneda-Castellanos et al. 2009, Bu, Chen et al. 2013) (Figure S1A). During asymmetric CCSC division, miR-34a and Numb are mostly present in the $Notch^{low}ALDH1^{low}$ non-CCSC daughter cells (Figure S1B), consistent with their function as Notch suppressors (Figures S3.1C and S3.1D) (Bu, Chen et al. 2013).

According to co-immunofluorescence for miR-34a and Numb, miR-34a and Numb were present in the same daughter cells in 82% of the divided pairs, whereas they were present in different daughter cells in 18% of the divided pairs (Figures 3.1A and 1B). Expression of Numbl, a Numb homologue involved in neurogenesis, was not detectable in CCSC.

We then examined potential interaction between these two cell fate determinants, with the initial hypothesis that one might upregulate the other. We first expressed miR-34a in CCSCs using lentiviral infection and measured Numb expression levels by RT-qPCR and Western blot. Unexpectedly, ectopic miR-34a suppressed Numb expression (Figures 3.1C and 3.1D). To investigate whether miR-34a directly targets Numb, we used the microRNA target prediction tool RNA22 to analyze the 3`UTR sequence of Numb and found a putative miR-34a binding site (Figure 3.1E). The Numb 3`UTR was then cloned into a luciferase reporter, which showed that ectopic miR-34a expression suppressed firefly luciferase activity, whereas mutation in the putative miR-34a seed region in the Numb 3`UTRs abrogated the suppression by miR-34a (Figure 3.1F). Therefore, miR-34a directly targets Numb mRNA to silence its expression.

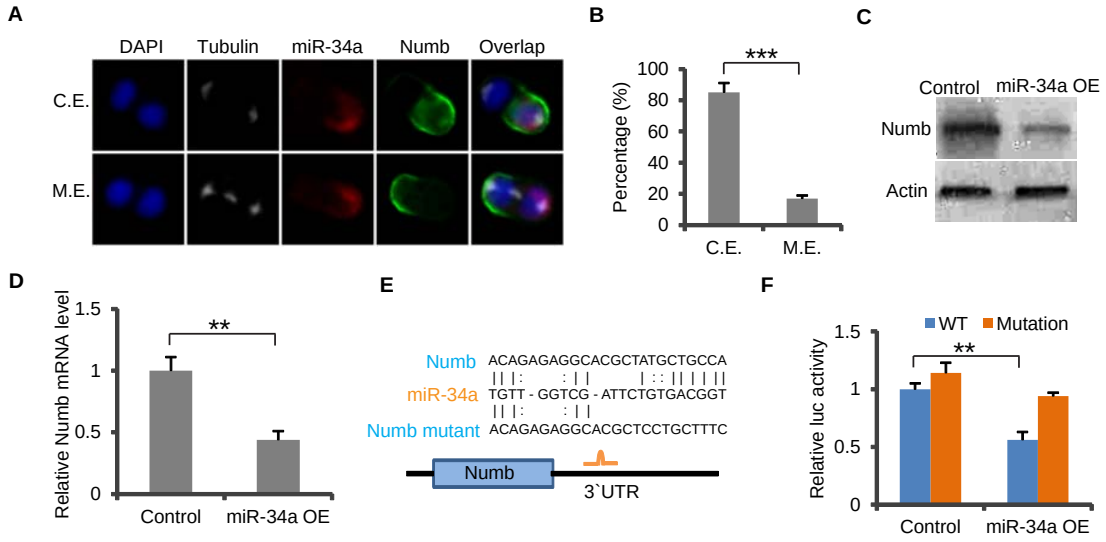

Figure 3.1. miR-34a Directly Targets Numb.

*(**A**) Representative images of miR-34a (RNA FISH, red) and Numb (green) distribution during CCSC division. miR-34a and Numb can co-exist (C.E., top row) or be mutually exclusive (M.E., bottom row) in*

*daughter cells. (**B**) Percentages of CCSC divisions wherein miR-34a and Numb are M.E. or C.E. (**C** and **D**) Western blot (C) and RT-qPCR (D) of Numb levels showing ectopic miR-34a expression (miR-34a OE) suppresses Numb expression compared to the control vector. (**E**) Schematic illustration of predicted binding between miR-34a and Numb 3` UTR, and mutation introduced to the seed region. (**F**) Luciferase reporter assay confirming the miR-34a binding site in Numb 3`UTR. Numb 3`UTR sequences containing the wild-type (Wt) or mutated (Mut) putative miR-34a binding sites were cloned into the 3`UTR of firefly luciferase (Fluc). Fluc signals were normalized by Renillar luciferase (Rluc) signals. Mutation of the binding site attenuated suppression of Numb by ectopic miR-34a expression (miR-34a OE). Scale bar, 8mm. Error bars denote s.d. of triplicates. **, p<0.01; ***, p<0.001. p-value was calculated based on Student's t-test. Also see Figure S3.1.*

3.4.2 Mir-34a, Numb, And Notch Form An Incoherent Feedforward Loop (IFFL).

It is counterintuitive that miR-34a targets Numb for suppression, considering that both cell fate determinants suppress Notch and promote differentiation. Why does miR-34a suppress Notch directly but upregulate Notch indirectly via Numb? Here, miR-34a, Numb, and Notch form a motif called incoherent feedforward loop (IFFL) (Figure 3.2A). miR-34a suppresses Notch1 and Numb translation by binding to the 3`UTRs of their mRNA, and Numb supresses Notch1 by promoting its endocytosis and degradation.

Previous studies have found that IFFL can generate non-monotonic, adaptive, or pulse-like responses in different contexts (Mangan, Itzkovitz et al. 2006, Kaplan, Bren et al. 2008, Goentoro, Shoval et al. 2009), but none of these properties seemed to be particularly relevant to cell fate determination. There have also been computational analyses suggesting that microRNA may reduce noise in IFFL, but those referred to a different topology where the microRNA is suppressed by the protein (Osella, Bosia et al. 2011).

To understand how miR-34a and Numb may synergize through this arrangement, we explored the quantitative aspects of this particular IFFL. We previously showed that miR-34a generates a threshold response from Notch due to mutual sequestration, while Numb regulates Notch in a graded, continuous way (Levine, Zhang et al. 2007, Mukherji, Ebert et al. 2011, Bu, Chen et al. 2013), raising the prospect

that this IFFL may possess unique properties. A similar setup was used to characterize the newly discovered miR-34a suppression of Numb. We incrementally increased ectopic miR-34a expression level using a Doxycycline-inducible promoter and performed Fluorescence Activated Cell Sorting (FACS) with antibody against Numb. FACS analysis revealed that incremental miR-34a induction gradually suppressed Numb levels in $Numb^{high}$ cells (Figures 3.2B and 2.2C).

A computational IFFL model was then constructed by expanding our previously published miR-34a/Notch model to include miR-34a suppression of Numb and Numb suppression of Notch (See Supplemental Information). The model assumes that miR-34a suppression of Notch1 is stronger than its suppression of Numb (which is more gradual), based on the experimental data. Simulation of the model over certain parameter ranges presented an interesting possibility that the IFFL could generate a more robust Notch switch than miR-34a alone (Figure 3.2D). With IFFL, 'high' and 'low' Notch levels are steady and insensitive to precise miR-34a level except for a narrow transition (threshold) region, which resembles a typical switch used in electronics. In contrast, Notch levels vary more with a wider transition region if there is only miR-34a but no Numb. Intuitively, when miR-34a level increases, Numb level is suppressed accordingly to offset, hence their combined suppression effect on Notch remains roughly constant until the mutual sequestration threshold is reached. Therefore, the IFFL buffers Notch level from miR-34a copy number variation and enforces a sharp transition only around the mutual sequestration threshold. Further simulations of the model suggested that the steepness of the transition is influenced by the relative strength between the direct and indirect paths (Figures S3.2A-S3.2B).

The model made a further prediction that IFFL produces better bimodality of Notch levels (and hence cell fate determination) in the population. Intuitively, the narrower transition region of the IFFL minimizes the number of cells with intermediate Notch levels (Figure 3.2D). Based on previous FACS measurements of Doxycycline-induced miR-34a level distributions in CCSC sphere cells (Bu, Chen et al. 2013), we performed stochastic simulations of IFFL and miR-34a alone (Numb knockdown). The simulations suggested that, even though miR-34a alone could generate Notch bimodality due to mutual sequestration as previously demonstrated (Bu, Chen et al. 2013), IFFL generates better Notch bimodality with more

clearly defined peaks and fewer cells in between, thanks to its more robust switching behavior (Figure 3.2E).

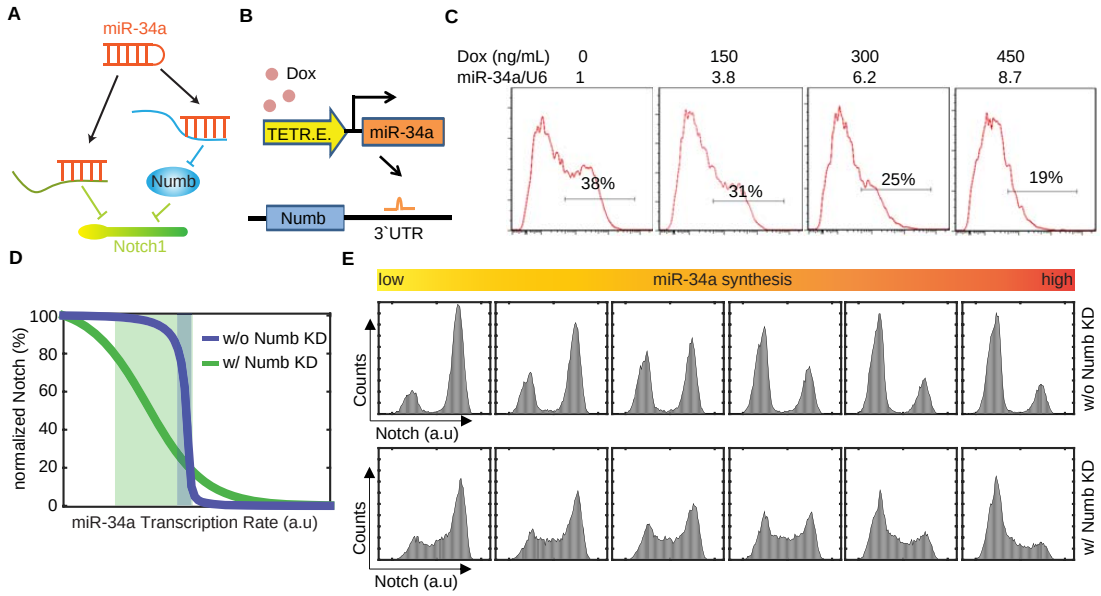

Figure 3.2. Computational analysis of the incoherent feedforward loop (IFFL).

*(**A**) Schematic of the IFFL formed by miR-34a, Numb, and Notch1. (**B**) Schematic illustration of the inducible miR-34a construct used in the experiment shown in (C). (**C**) FACS analysis of Numb expression in CCSC sphere cells when miR-34a expression was incrementally induced by Doxycycline. (**D**) Simulated Notch1 vs. miR-34a levels from the ODE-based IFFL and Numb knockdown models. Shaded areas are transition regions (80% to 20% of peak Notch level). (**E**) Simulated Notch1 distributions with IFFL and Numb knockdown models. Also see Figure S3.2.*

3.4.3 miR-34a And Numb Synergize For A Robust Notch Bimodal Switch.

Experiments were then designed to test whether the presence of Numb enhances miR-34a regulation of Notch as a cell fate switch. First, we measured the response of Notch1 level to incremental miR-34a levels with and without Numb. As previously demonstrated, we used CCSCs stably integrated with a lentiviral vector that drives ectopic miR-34a expression with a Doxycycline-inducible promoter(Bu, Chen

et al. 2013) (Figure 3.3A). CCSCs were then infected with a lentiviral vector expressing short hairpin RNAs (shRNAs) against Numb to knock down Numb. The efficiency of Numb knockdown in CCSCs was verified by western blot (Figure S2C).

CCSCs in separate wells were then treated with incremental dosages (0, 100, 200, 300, 400, and 500 ng/ml) of Doxycycline. RT-qPCR verified that induced miR-34a expression level increased linearly with Doxycycline dosage in CCSCs with or without Numb knockdown (Figures S3.2D and S3.2E). Time-series measurements indicated that it took approximately 42 hours for Notch levels to stabilize after doxycycline induction (Figures S3..2F-S3.2I), so steady-state measurements were performed 48 hours post induction. With Numb, Notch levels remained largely steady until being abruptly turned off by 400 ng/ml Doxycycline induction of miR-34a (Figures 3.3B, 3D and S3J). In contrast, Notch levels gradually decreased and slowly turned off in response to increasing miR-34a levels when Numb was knocked down (Figures 3.3C, 3D and S3K). These measurements support the computational hypothesis in Figure 3.2D that miR-34a and Numb work in synergy to generate a more robust switch. Without Numb, Notch level is more sensitive to miR-34a variation.

We then tested whether the presence of Numb enhances miR-34a regulation of Notch to be more bimodal as the computational analysis predicted. Again, we induced miR-34a at different levels and measured Notch protein levels in individual cells using flow cytometry, with antibody against Notch. In CCSCs with Numb, Notch displayed clear bimodality and individual cells were clustered around the $Notch^{high}$ or $Notch^{low}$ peaks. In contrast, in CCSCs with Numb knockdown, even though Notch level distribution was still overall bimodal due to mutual sequestration, bimodality was degraded by a subpopulation of cells with intermediate Notch levels between high and low (Figure 3.3E). This result is consistent with the computational prediction in Figure 3.2E that the IFFL improves Notch bimodality.

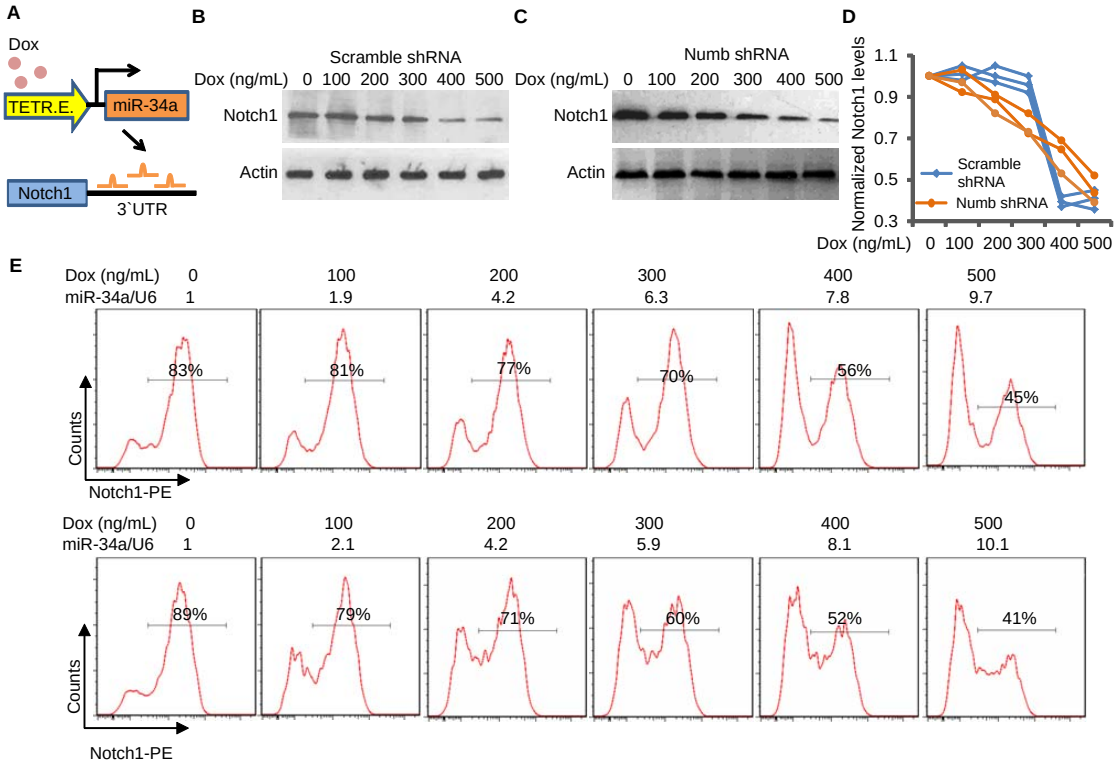

Figure 3.3. IFFL Generates A Robust Notch Switch.

*(**A**) Schematic illustration of the inducible miR-34a construct used in the experiments shown in (B to E). **(B** and **C)** Western blots of Notch levels in scramble shRNA (B) and Numb shRNA (C) infected CCSC spheres with incremental miR-34a induction by Doxycycline. (**D**) Quantification of Western blots in three independent repeats. (**E**) FACS analysis of Notch1 bimodality with incremental miR-34a induction by Doxycycline. Top row, intact IFFL; bottom row, Numb knockdown. miR-34a levels were measured by RT-qPCR and shown on top of the FACs plots. Also see Figure S3.2.*

3.4.4 Intermediate Notch Level Leads To Ambiguous And Plastic Cell Fate.

The implication of Notch bimodality on cell fate determination was then investigated. We isolated the Notch^{high}, Notch^{low} and Notch^{inter} cells by FACS (Figures 3.4A and S3.3A) and immediately performed immunofluorescence for the CCSC marker ALDH1 and differentiation marker CK20 (Figure 3.4B). Consistent with previous reports, Notch^{high} cells are ALDH1+CK20- stem cells and Notch^{low} cells are ALDH1-CK20+ differentiated cells. Interestingly, the cells with intermediate Notch levels (Notch^{inter})

expressed both ALDH1 and CK20, reflecting an intermediate state between stem cell and differentiation. RNA-seq transcriptome profiling revealed that Notch^{inter} cells have a distinct gene expression signature between those of Notch^{high} and Notch^{low} cells (Figures 3.4C and S3.3B). Notch^{inter} cells express intermediate levels of stem cell and differentiation makers, while Notch^{high} cells express high levels of stem cell markers and Notch^{low} cells express high levels of differentiation markers (Figure S3.3C). Gene Set Enrichment Analysis (GSEA) show that pathways commonly associated with CCSCs, such as Notch, Wnt, and MAPK signaling pathways, are upregulated in Notch^{high} cells (Figure S3.3D).

We then performed serial sphere propagation assay to test these cells' self-renewal ability, which is a measure of their stemness (Figures 3.4D, 3.4E, S3.3E). Notch^{high} cells efficiently formed spheres in 3D Matrigel culture and maintained their sphere formation capability, whereas Notch^{low} cells formed few spheres in the first generation and lost their sphere formation capability after serial propagation. Notch^{inter} cells could also form spheres, but the spheres were far fewer and smaller than those formed by Notch^{high} cells. We then compared tumorigenic capability by subcutaneously injecting $1x10^4$ Notch^{high}, Notch^{inter} and Notch^{low} cells respectively into Nude mice. During the observed period (6 weeks), all 6 mice injected with Notch^{high} cells grew tumors, only 2 mice injected with Notch^{inter} cells grew small tumors, and none of the mice injected with Notch^{low} cells grew tumors (Figure 3.4F). Similar results were observed in mice injected with Notch^{high}, Notch^{inter} and Notch^{low} cells sorted from a second CCSC (CCSC2) line (Figure S3.3F). Therefore, Notch^{inter} cells have intermediate self-renewal and tumorigenic capability compared to Notch^{high} and Notch^{low} cells, consistent with their intermediate gene expression signature.

Since Notch^{inter} cells seem to occupy a state between Notch^{high} CCSC and Notch^{low} non-CCSC, we next examined their plasticity, or ability to convert into CCSC or non-CCSC. When cultured in FBS-free stem cell medium and low-attachment flask, Notch^{inter} cells upregulated the CCSC marker ALDH1, while Notch^{low} cells did not express ALDH1 after 7 days (Figure 3.4G). This suggests that Notch^{inter} cells may possess the plasticity to dedifferentiate back into stem cells, in contrast to Notch^{low} cells. On the other hand, Notch^{inter} cells are more ready to differentiate than Notch^{high} cells. When cultured in differentiation medium, Notch^{inter} cells lost ALDH1 expression within 24 hours, whereas Notch^{high} cells still retained

ALDH1 expression (Figure 3.4H). It took 10 days for most Notch^{high} cells to lose ALDH1 and express CK20. Collectively, these data suggest that Notch^{inter} cells are in an intermediate state that can dedifferentiate into CCSCs or readily commit to differentiation.

We then examined how the presence of the Notch^{inter} cells affects cell division. Pair-cell assay followed by immunofluorescence for ALDH1 and CK20 revealed that Numb knockdown reduced asymmetric division and gave rise to significantly more ambiguous cell division outcomes, wherein one or both daughter cells co-expressed ALDH1 and CK20 (Figures 3.4I and 3.4J).

Altogether, the computational analysis and experimental data combined suggest that miR-34a suppresses Numb to form an IFFL, which acts as a robust switch to generate Notch bimodality. Undermining this switch by Numb knockdown results in a subpopulation of cells with intermediate Notch levels. These cells express both stem cell and differentiation markers, and show greater plasticity than Notch^{high} and Notch^{low} cells.

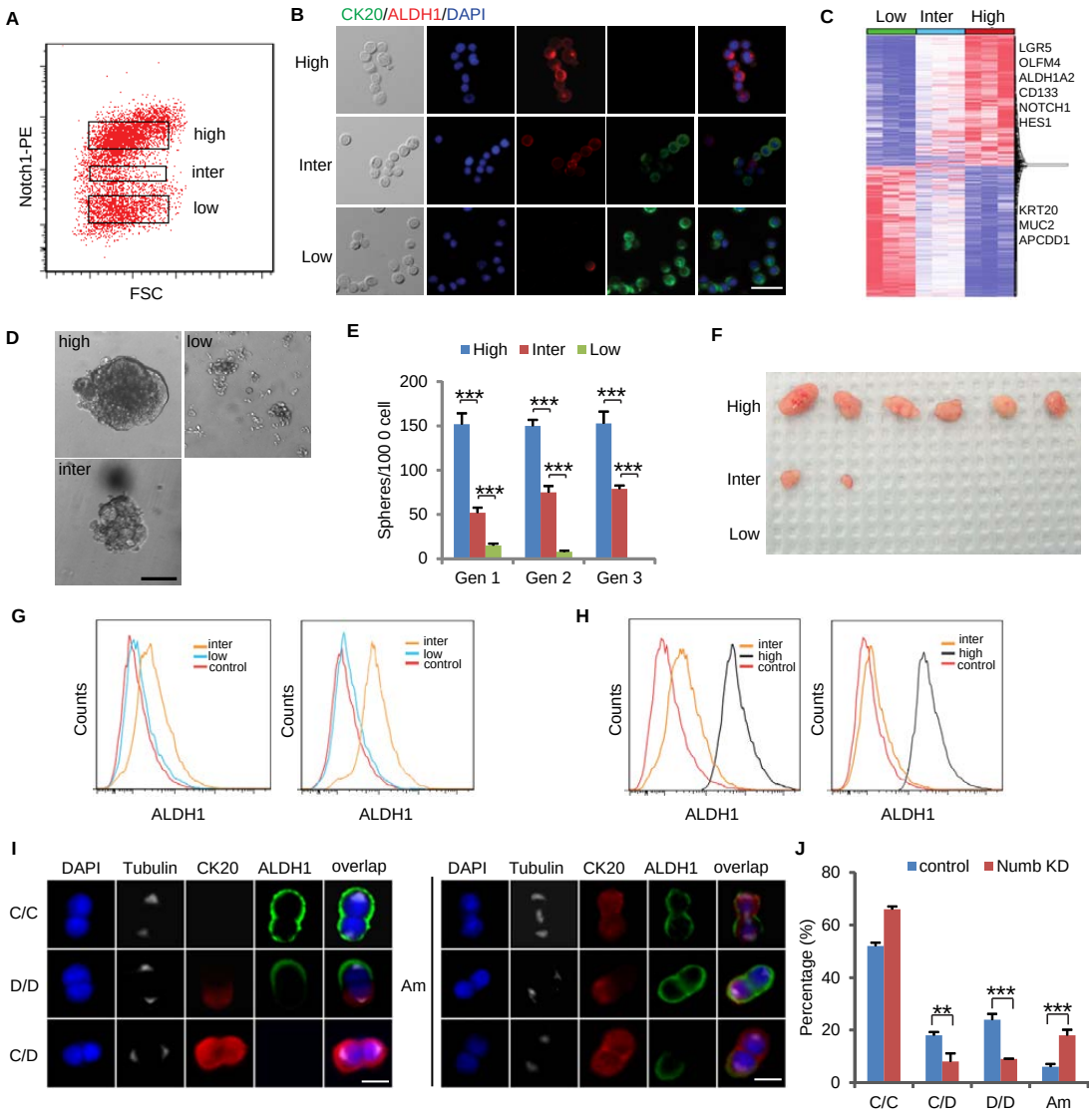

Figure 3.4. Numb Knockdown Gives Rise To An Intermediate Population.

*(**A**) FACS plot showing Notch^{high}, Notch^{inter}, and Notch^{low} subpopulations of Numb knockdown sphere cells, treated with with 200ng/ml Doxycycline. (**B**) Immunofluorescence of Notch^{high}, Notch^{inter}, and Notch^{low} cells for CK20 (green) and ALDH1 (red). Scale bar, 20mm. (**C**) Heat-map of transcriptomes of Notch^{high}, Notch^{inter}, and Notch^{low} cells measured by RNA-seq. (**D**) Representative images of spheres grown from Notch^{high}, Notch^{inter}, and Notch^{low} cells. Scale bar, 50mm. (**E**) Serial Sphere propagation of Notch^{high}, Notch^{inter}, and Notch^{low} cells isolated from Numb knockdown sphere cells. Gen, generation. (**F**) Tumor images showing tumorigenic capability of transplanted Notch^{high}, Notch^{inter}, and Notch^{low} cells. (**G**)*

*FACS analysis of Notch^{inter} and Notch^{low} cells before (left) and after (right) being under stem cell culture condition for 7 days. Notch^{inter} cells turned on ALDH1 expression under stem cell culture condition, whereas Notch^{low} cells did not. (**H**) FACS analysis of Notch^{inter} and Notch^{high} cells before (left) and after (right) being in FBS-containing medium for 24 hours. Notch^{inter} cells lost ALDH1 expression, whereas Notch^{high} cells did not. (**I**) Representative immunofluorescence images for ALDH1 (red) and CK20 (green) illustrating four types of division: CCSC/CCSC (C/C), CCSC/non-CCSC (C/D), non-CCSC/non-CCSC (D/D) and ambiguous (Am). Scale bar, 8mm. (**J**) Numb knockdown significantly increased Am divisions besides reducing C/D and D/D. Error bars denote s.d. of triplicates. **, p<0.01; ***, p<0.001. p-value was calculated based on Student's t-test. Also see Figure S3.3.*

3.4.5 miR-34a And Numb Are Associated With Differentiation of Mouse Intestinal Stem Cells.

We have previously shown that miR-34a mediated asymmetric cell fate determination is mostly active in CCSCs isolated from early-stage CRC patient specimens, and tends to be silenced in CCSCs isolated from late-stage CRC specimens. CCSCs from early-stage specimens form xenograft tumors in mice that maintain histopathology of their primary human CRCs, which still retain reminiscent features of original colon tissue (Bu, Chen et al. 2013). This raised the possibility that miR-34a and Numb perform cell fate-related functions in normal tissues, which was initially inherited by early-stage CCSCs but eventually subverted in late-stage CCSCs.

To test this possibility, we first performed immunofluorescence for miR-34a and Numb in cryosectioned mouse intestinal crypts harvested from *Lgr5-EGFP-IRES-CreER^{T2}* transgenic mice (Sato, Vries et al. 2009). miR-34a and Numb expression are low in GFP-labeled Lgr5+ intestinal stem cells (ISCs), but becomes higher in more differentiated cells above the stem cell niche (Figures 3.5A and 3.5B). On the other hand, Notch1, the target of miR-34a and Numb suppression, was more expressed in Lgr5+ ISCs (Figure 3.5C), consistent with previous reports that Notch is expressed in ISC and essential for ISC self-renewal (Fre, Hannezo et al. 2011, VanDussen, Carulli et al. 2012).

To compare Numb and miR-34a expression levels between ISCs and more differentiated cells, we cultured mouse intestinal cells from *Lgr5-EGFP-IRES-CreER*^{T2} mice in 3D Matrigel, where they grew into crypt-villus like organoids (Sato, Vries et al. 2009) (Figure 3.5D). The Lgr5+ ISCs (also called CBCs) are capable of both self-renewal and generating other intestinal cell lineages in these organoids. RT-qPCR showed that both Numb and miR-34a expression levels are lower in Lgr5-GFP+ cells than in Lgr5-GFP- cells (Figures 3.5E and 3.5F). The difference in expression levels between Lgr5-GFP+ and Lgr5-GFP- cells is greater for miR-34a than for Numb. Flow analysis with RNA FISH probes confirmed low miR-34a expression in Lgr5-GFP+ cells (Figure S4A). Together, the immunofluorescence and RT-qPCR data suggest that miR-34a and Numb expression are associated with more differentiated cells, whereas Notch1 is associated with Lgr5+ ISC.

To validate whether miR-34a and Numb suppress Notch1 in intestinal cells, we infected organoids with lentiviral vectors that express miR-34a or Numb. Transduction and knockdown efficiency was validated by RT-qPCR and Western blot (Figures S3.4B-S3.4C). Western blot confirmed that ectopic miR-34a and Numb suppressed Notch1 expression in organoid cells (Figures 3.5G and 3.5H). Moreover, ectopic miR-34a expression also downregulated Numb expression, consistent with the IFFL (Figure 3.5I).

We then investigated how miR-34a, Numb and Notch impact ISC cell fate decision. Inhibition of Notch by treating the organoids with the g-secretase inhibitor DAPT significantly reduced the Lgr5-GFP+ ISC population in the organoids (Figures 3.5J and S3.4D). Ectopic expression of miR-34a or Numb via lentiviral infection of organoid cells had a similar effect of reducing Lgr5-GFP+ ISCs, consistent with their role of Notch suppression (Figures 3.5K-5L). Next, we used a lentiviral vector to express shRNA against Numb in organoids in order to examine whether knockdown of Numb would impact intestinal cell fate bimodality as it does to early-stage CCSCs. The efficiency of Numb knockdown was validated by Western blot (Figure S4E). Indeed, a subpopulation of cells with intermediate Lgr5 expression levels between Lgr5^{high} ISCs and Lgr5^{low} non-ISCs emerged, and the Lgr5-GFP distribution was no longer bimodal (Figure 3.5M). The effects on ISCs were further validated by measuring the levels of Olfm4, an alternative marker for Lgr5+ ISC (Yan, Chia et al. 2012, Schuijers, van der Flier et al. 2014).

Consistently, inhibition of Notch signaling by DAPT, ectopic miR-34a or Numb expression reduced Olfm4 levels, whereas Numb knockdown increased Olfm4 levels in organoids (Figures 3.5N-5Q). Notch inhibition by DAPT, ectopic miR-34a, or Numb expression also increased apoptotic cells shed into the lumen, a process reminiscent of the shedding of terminally differentiated cells *in vivo* (Figures S3.5F-S.3.5I) (Sato, Vries et al. 2009).

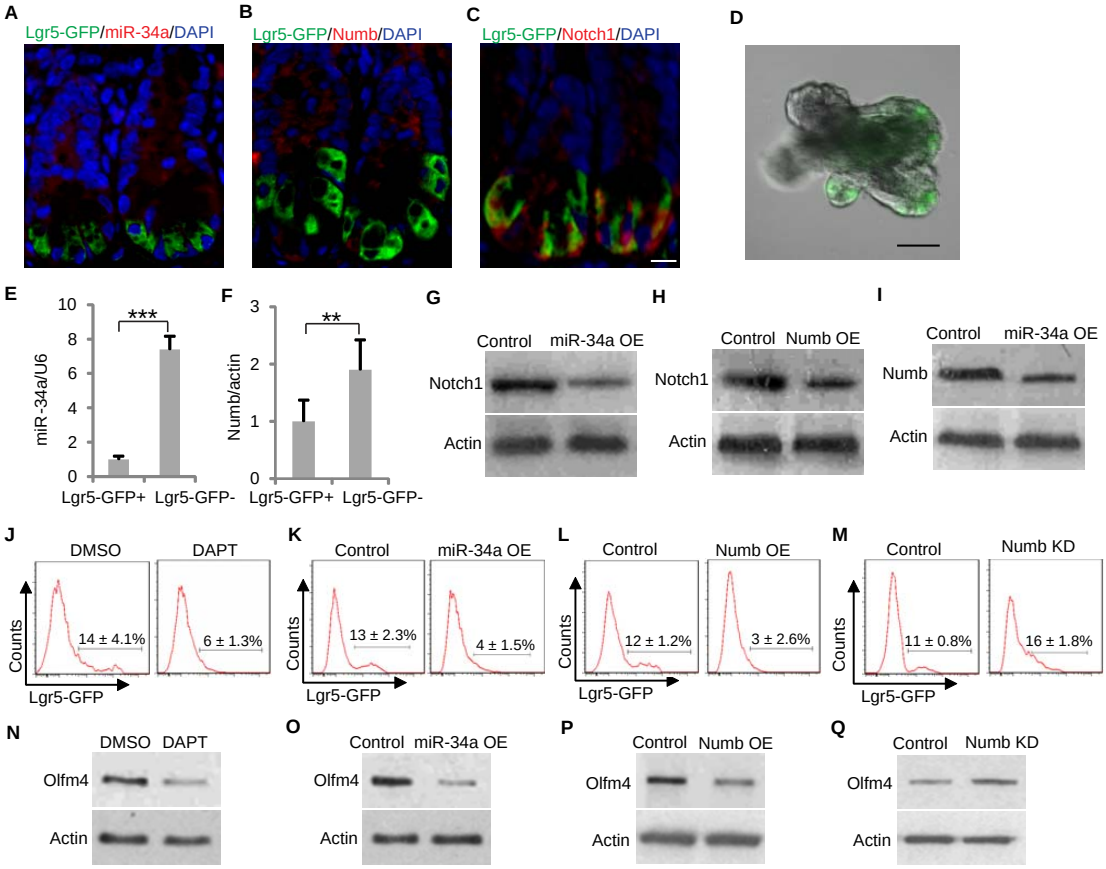

Figure 3.5. Mir-34a And Numb Expression In Mouse Intestinal Cells.

(**A** to **C**) Immunofluorescence images of intestinal crypts from an *Lgr5-EGFP-CreER*^{T2} transgenic mouse. Scale bar, 20mm. (**D**) A representative image of an intestinal organoid with Lgr5-GFP labeled ISCs. Scale bar, 50mm. (**E** and **F**) miR-34a (E) and Numb (F) expression levels in Lgr5-GFP+ and Lgr5-GFP- cells isolated from *Lgr5-EGFP-CreER*^{T2} intestinal organoids, measured by RT-qPCR. (**G** and **H**) Western blot showing that ectopic miR-34a (G) or Numb (H) expression decreased Notch1 level in organoid cells. (**I**) Western blot showing that ectopic miR-34a expression decreased Numb level in organoid cells. (**J**) DAPT

treatment decreased the Lgr5-GFP cell population in *Lgr5-EGFP-CreER^{T2}* organoids. (**K** and **L**) Ectopic miR-34a (K) or Numb (L) expression decreased the Lgr5-GFP cell population in *Lgr5-EGFP-CreER^{T2}* organoids. (**M**) Numb knockdown gave rise to a subpopulation with intermediate Lgr5-GFP expression. (N to Q) Western blot of Olfm4 levels in conditions corresponding to J to M. Error bars denote s.d. of triplicates. **, p<0.01; ***, p<0.001. p-value was calculated based on Student's t-test. Also see Figure S3.4

3.4.6 Inflammatory Stress Induced miR-34a-Dependent Asymmetric Division.

To investigate how loss of the miR-34a-mediated switch may specifically impact ISC cell fate decision, we crossed *miR-34a$^{flox/flox}$* mice (Concepcion, Han et al. 2012) with *Lgr5-EGFP-IRES-CreER^{T2}* mice and then intraperitoneally administered Tamoxifen, which activated Cre to knock out miR-34a in Lgr5+ ISC specifically. miR-34a knockout in Lgr5+ ISCs did not cause noticeable changes to the crypt morphology or the number of Lgr5-GFP ISCs *in vivo* or in derived organoids (Figures S3.5A-S3.5B). To confirm that miR-34a is not essential for crypt homeostasis, we examined the intestinal crypts from a constitutive miR-34a knockout (miR-34a$^{-/-}$) model (Choi, Lin et al. 2011), and stained ISCs with antibody against Olfm4. The crypt morphology and Olfm4+ ISCs again seem normal (Figures S3.5C-S3.5D). This suggests that the miR-34a-mediated switch is not essential for Lgr5+ ISC mediated intestinal homeostasis under normal physiological conditions.

TNFa, a pro-inflammatory cytokine associated with chronic colitis, has been linked to risk of colorectal carcinogenesis (Coussens and Werb 2002, Popivanova, Kitamura et al. 2008). A low dosage (10ng/ml) treatment of TNFa for 3 days caused modest proliferation of Lgr5-GFP+ ISCs, increasing their number from 12% to 19% of the total organoid cell population. The effect of TNFa treatment was amplified by miR-34a knockout. TNFa-induced ISC proliferation became more excessive in organoids derived from *miR-34a$^{flox/flox}$* mice/*Lgr5-GFP-IRES-CreER^{T2}* mice after miR-34a knockout was induced, causing proliferating Lgr5-GFP+ ISCs to comprise 38% of the organoid cell population (Figure 3.6A). Consistent with the flow analyses, TNFa and loss of miR-34a greatly increased the expression of Olfm4, the marker

for Lgr5+ ISCs (Figure 3.6B). Moreover, miR-34a knockout caused TNFa-treated organoids to grow into undifferentiated spheres that resemble CCSC spheres, with enrichment of Lgr5-GFP+ ISCs (Figure 3.6C). BrdU incorporation assay showed that loss of miR-34a led to excessive proliferation in TNFa-treated organoids (Figure 3.6D). Therefore, despite being non-essential for normal tissue homeostasis, the miR-34a-mediated cell fate switch provides a safeguard against excessive ISC proliferation when stem cells regenerate under pro-inflammatory stress.

Lgr5+ ISCs are thought to divide symmetrically in normal conditions (Lopez-Garcia, Klein et al. 2010, Snippert, van der Flier et al. 2010). We explored whether the presence of miR-34a has the capability to promote asymmetric division and differentiation to counter excessively proliferating Lgr5+ ISCs. We first examined the division of intestinal organoid cells using both the pair-cell assay and direct immunofluorescence on Lgr5-GFP+ doublets freshly isolated by FACS, with antibodies against a- or b-tubulin to mark mitotic cells (Figures 3.6E and 3.6G). Under normal organoid culture condition, only 4.6% of the Lgr5-GFP+ cells or 4.2% of Olfm4+ cells from *Lgr5-EGFP-CreER^{T2}* organoids divided asymmetrically, while asymmetric division was barely observed in miR-34a deficient Lgr5-GFP+ or Olfm4+ cells from *Lgr5-EGFP-CreER^{T2}/miR-34a$^{flox/flox}$* organoids. Remarkably, 3-day treatment of 10ng/ml TNFa caused 19% of Lgr5-GFP+ cells or 14.5% Olfm4+ cells from *Lgr5-EGFP-CreER^{T2}* organoids to divide asymmetrically. In contrast, miR-34a deficiency reduced such asymmetric division to less than 2% in *Lgr5-EGFP-CreER^{T2}/miR-34a$^{flox/flox}$* organoids (Figures 3.6F and 3.6H).

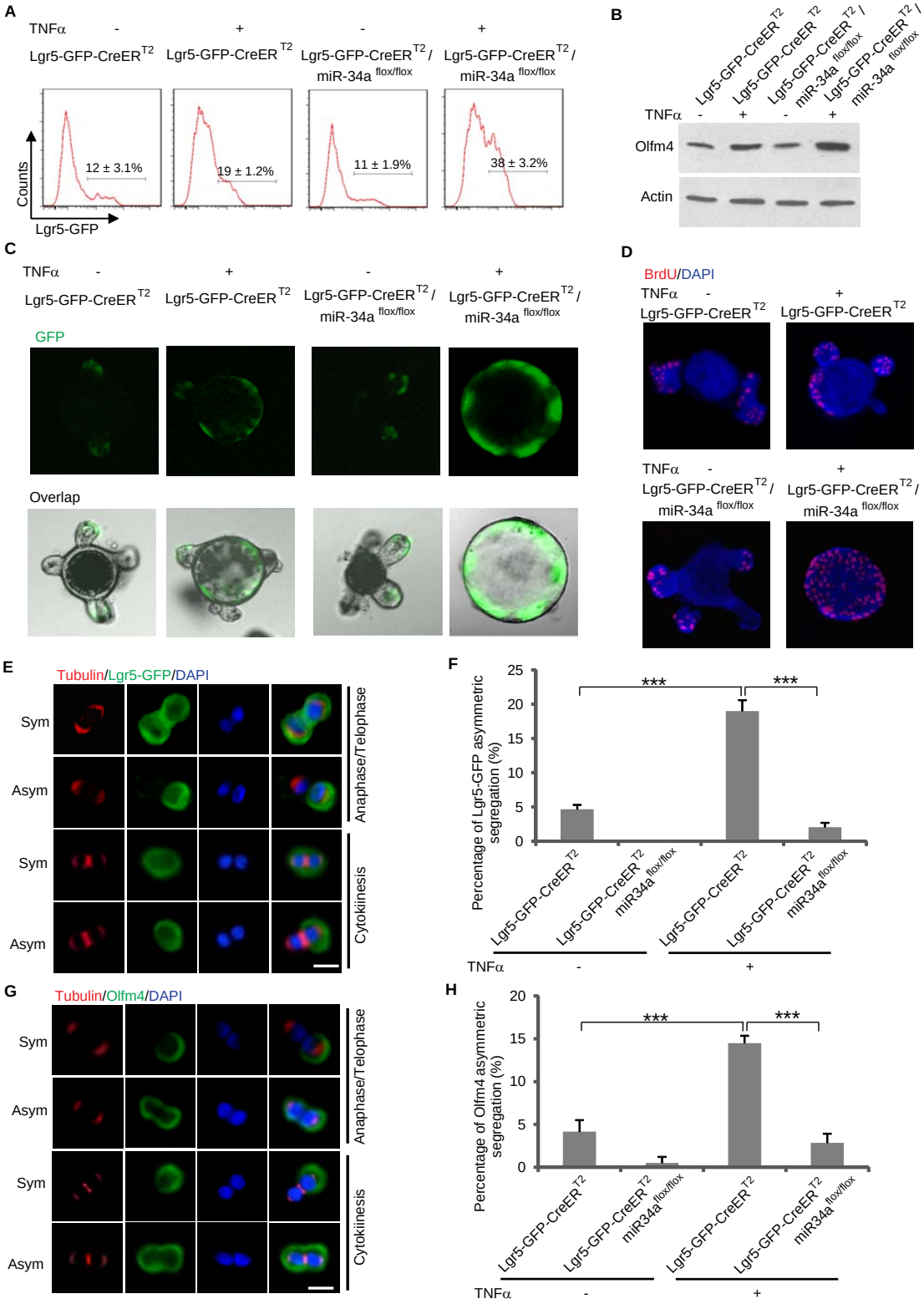

Figure 3.6. Loss Of Mir-34a Inhibits Asymmetric Division And Promotes ISC Proliferation In

Organoids Treated With TNFa.

*(**A**) FACS analysis of Lgr5-EGFP-CreER^{T2} and Lgr5-EGFP-CreER^{T2}/miR-34a$^{flox/flox}$ organoids with or without TNFa treatment. Percentage of Lgr5-GFP ISCs increased more dramatically in organoids from Lgr5-EGFP-CreER^{T2}/miR-34a$^{flox/flox}$ mice. (**D**) Western blot of Olfm4 levels. (**C**) Representative images of organoids. Intestinal organoids from Lgr5-EGFP-CreER^{T2}/miR-34a$^{flox/flox}$ mice grew into CCSC-like, undifferentiated spheres with high level of Lgr5-GPF upon TNFa treatment. (**D**) Cell proliferation measured by BrdU incorporation. (**E**) Representative images of symmetric and asymmetric division of Lgr5-GFP ISCs in intestinal organoids. Tubulin staining indicates stages of mitosis. The anaphase/telophase images were taken from FACS-sorted Lgr5-GFP+ doublets that were fixed and stained immediately without recovery. The cytokinesis images were taken from the pair-cell assay. Scale bar, 8mm. (**F**) Frequency of asymmetric division of Lgr5-GFP stem cells from Lgr5-EGFP-CreER^{T2} and Lgr5-EGFP-CreER^{T2}/miR-34a$^{flox/flox}$ intestinal organoids with or without TNFa treatment. (**G**) Representative images of symmetric and asymmetric division of Olfm4+ ISCs in intestinal organoids. Tubulin staining indicates stages of mitosis. The anaphase/telophase images were taken from FACS-sorted doublets that were fixed and stained immediately without recovery. The cytokinesis images were taken from the pair-cell assay. Scale bar, 8mm. (**H**) Frequency of asymmetric division of Olfm4+ stem cells from Lgr5-EGFP-CreER^{T2} and Lgr5-EGFP-CreERT2/miR-34a$^{flox/flox}$ intestinal organoids with or without TNFa treatment. Scale bar, 20mm. Error bars denote s.d. of triplicates. ***, p<0.001. p-value was calculated based on Student's t-test. Also see Figure S3.7.*

3.4.7 miR-34a Dependent Asymmetric Division In Vivo

To examine whether inflammation also activates ISC asymmetric division in a miR-34a dependent manner *in vivo*, *Lgr5-EGFP-CreER^{T2}* and *Lgr5-EGFP-CreER^{T2}/miR-34a$^{flox/flox}$* mice were treated with 3% dextran sodium sulfate (DSS) in daily drinking water for 5 days, followed by 5 days of plain water supply for recovery. Tissues were then harvested and stained. Consistent with the observation in organoids, regeneration after DSS-induced tissue damage caused the number of Lgr5-GFP+ ISCs to increase in the

intestine, which was further amplified by loss of miR-34a (Figures 3.7A-3.7B). DSS treatment caused more proliferation in miR-34a deficient crypts, as shown by the number of cells incorporating BrdU (Figures S3.5E-S3.5F). Crypts were then stained for tubulin to identify dividing cell pairs with microtubule configuration consistent with telophase (the final phase of mitosis) – the midbody at the division plane during cytokiensis and asters at the poles. Under stress, more ISCs switch to asymmetric division, from 2% to 13% of all Lgr5-GFP+ divisions and from 1.6% to 9.3% of all Olfm4+ divisions. Asymmetric division was remarkably decreased to 4% in miR-34a deficient mice (Figures 3.7C-3.7F). Co-immunofluorescence confirmed that Lgr5-GFP+ cells are Olfm4+ and their expression patterns are consistent during asymmetric division *in vivo* (Figure S3.5G). Notably, colon stem cells follow the same trend. During recovery from DSS treatment, Lgr5-GFP and Olfm4+ colon stem cells underwent more asymmetric division in a miR-34a dependent manner (Figures S3.6A-S3.6D).

We then tested whether asymmetric division can also be triggered by ISC proliferation due to genetic mutation. APC deficiency causes ISC proliferation and is an initiation step for adenomas and 90% of CRC (Schepers, Snippert et al. 2012). We crossed transgenic mice carrying *Lgr5-EGFP-CreER*^{T2} and *APC*$^{flox/flox}$ alleles, and co-immunofluorescence for Lgr5-GFP and Tubulin confirmed that APC$^{-/-}$ intestinal tissues derived from *Lgr5-EGFP-CreER*^{T2}*/APC*$^{flox/flox}$ mice induced with Tamoxifen *in vivo* contain asymmetric LGR5+/LGR5- or Olfm4+/Olfm4- division pairs (Figures S3.6E-S3.6H). Hence ISC proliferations in APC-deficient mouse adenomas can trigger asymmetric division.

To further validate the presence of asymmetric division in clinical samples, we examined 12 pairs of human normal colon and CRC samples. 10.6% of the Lgr5+ and 8.2% of the Olfm4+ dividing pairs were undergoing asymmetric division in CRC samples, in contrast to less than 1% in normal colon samples (Figures 3.7G-3.7J).

Taken together, the *in vitro* and *in vivo* data indicate that, despite being rare in normal tissue, the frequency of asymmetric division can be increased to rein in excessive stem cell proliferation during inflammation-induced regeneration/repair. Loss of miR-34a inhibits asymmetric division and promotes symmetric division that exacerbates stem cell proliferation (Figure S3.7).

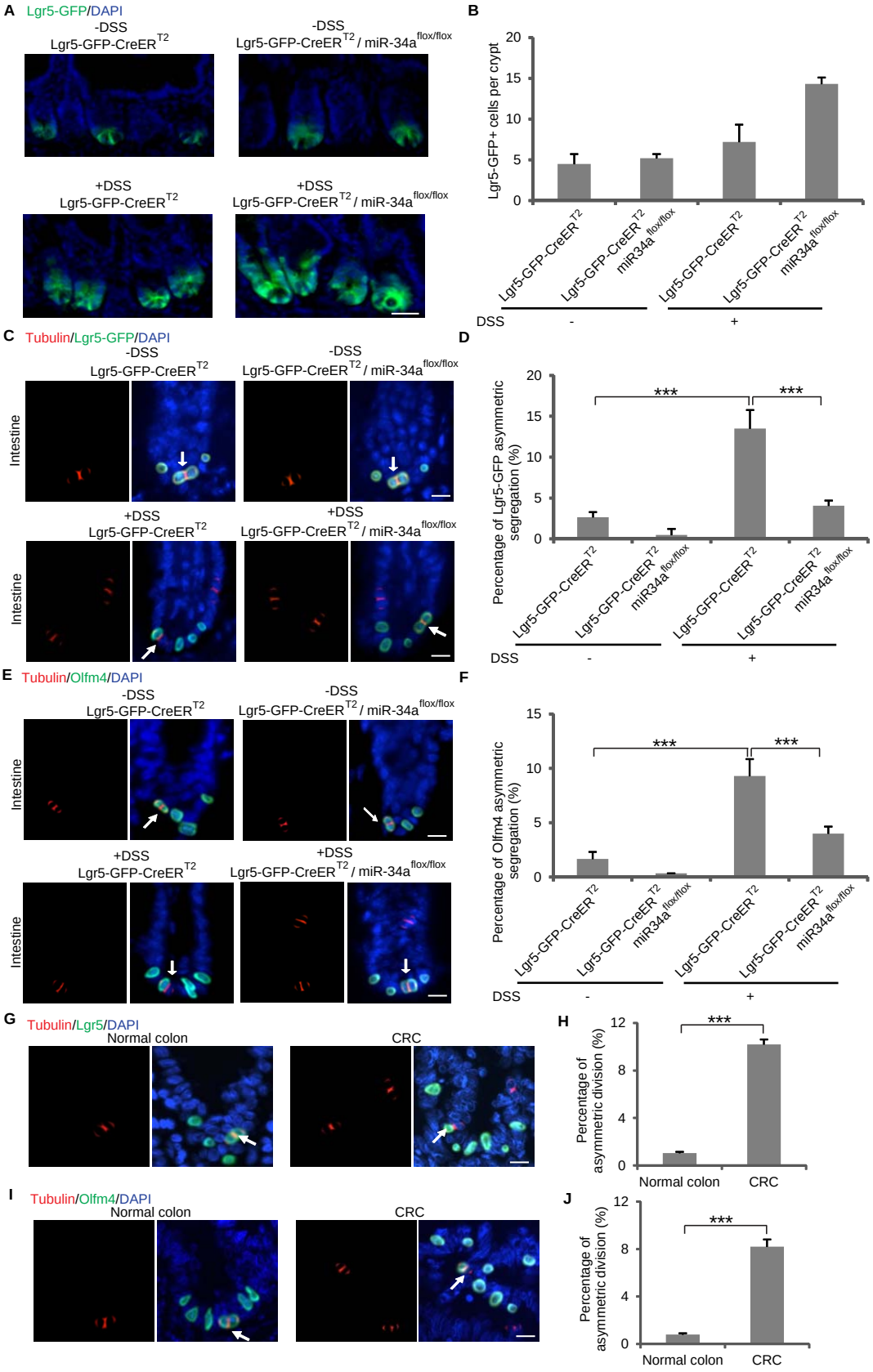
A
Lgr5-GFP/DAPI
-DSS
Lgr5-GFP-CreER^T2
-DSS
Lgr5-GFP-CreER^T2 / miR-34a^flox/flox
+DSS
Lgr5-GFP-CreER^T2
+DSS
Lgr5-GFP-CreER^T2 / miR-34a^flox/flox
B
Lgr5-GFP+ cells per crypt
0
5
10
15
20
Lgr5-GFP-CreER^T2
Lgr5-GFP-CreER^T2 miR34a^flox/flox
Lgr5-GFP-CreER^T2
Lgr5-GFP-CreER^T2 miR34a^flox/flox
DSS
-
+
C
Tubulin/Lgr5-GFP/DAPI
-DSS
Lgr5-GFP-CreER^T2
-DSS
Lgr5-GFP-CreER^T2 / miR-34a^flox/flox
Intestine
+DSS
Lgr5-GFP-CreER^T2
+DSS
Lgr5-GFP-CreER^T2 / miR-34a^flox/flox
Intestine
D
Percentage of Lgr5-GFP asymmetric segregation (%)
0
5
10
15
20
***
***
Lgr5-GFP-CreER^T2
Lgr5-GFP-CreER^T2 miR34a^flox/flox
Lgr5-GFP-CreER^T2
Lgr5-GFP-CreER^T2 miR34a^flox/flox
DSS
-
+
E
Tubulin/Olfm4/DAPI
-DSS
Lgr5-GFP-CreER^T2
-DSS
Lgr5-GFP-CreER^T2 / miR-34a^flox/flox
Intestine
+DSS
Lgr5-GFP-CreER^T2
+DSS
Lgr5-GFP-CreER^T2 / miR-34a^flox/flox
Intestine
F
Percentage of Olfm4 asymmetric segregation (%)
0
5
10
15
***
***
Lgr5-GFP-CreER^T2
Lgr5-GFP-CreER^T2 miR34a^flox/flox
Lgr5-GFP-CreER^T2
Lgr5-GFP-CreER^T2 miR34a^flox/flox
DSS
-
+
G
Tubulin/Lgr5/DAPI
Normal colon
CRC
H
Percentage of asymmetric division (%)
0
4
8
12
***
Normal colon
CRC
I
Tubulin/Olfm4/DAPI
Normal colon
CRC
J
Percentage of asymmetric division (%)
0
4
8
12
***
Normal colon
CRC

Figure 3.7. Loss Of Mir-34a Inhibits Asymmetric Division And Promotes ISC Proliferation In Crypts Recovering From DSS Treatment.

*(**A**) Representative images of intestinal crypts from Lgr5-EGFP-CreER^{T2} and Lgr5-EGFP-CreER^{T2}/miR-34a$^{flox/flox}$ mice administrated with DSS or plain water. DSS treatment followed by recovery increased Lgr5-GFP ISCs in the intestine. (**B**) Quantification of Lgr5-GFP+ cells per crypt of (A). (**C** and **D**) Representative images (C) and quantification (D) of symmetric and asymmetric division of Lgr5-GFP ISCs in Lgr5-EGFP-CreER^{T2} and Lgr5-EGFP-CreERT2/miR-34a$^{flox/flox}$ mice with (+DSS) or without (-DSS) treatment. (**E** and **F**) Representative images (E) and quantification (F) of symmetric and asymmetric division of Olfm4+ ISCs in Lgr5-EGFP-CreER^{T2} and Lgr5-EGFP-CreER^{T2}/miR-34a$^{flox/flox}$ mice with (+DSS) or without (-DSS) treatment. (**G** and **H**) Representative images (G) and quantification (H) of symmetric and asymmetric division of Lgr5+ cells in human normal colon and CRC tissue. (**I** and **J**) Representative images (I) and quantification (J) of symmetric and asymmetric division of Olfm4+ cells in human normal colon and CRC tissue. Scale bar, 20mm. Error bars denote s.d. of triplicates. ***, $p<0.001$. p-value was calculated based on Student's t-test. Also see Figure S3.7.*

3.5 Discussion

Spatial imbalance of cell fate determinants can break symmetry and force bifurcation of cell fate. Here we show that the microRNA cell fate determinant miR-34a and canonical protein cell fate determinant Numb synergize to regulate self-renewal vs. differentiation of early-stage CCSC. miR-34a directly suppresses Numb to form an IFFL, which generates a robust binary switch response from Notch. This switch enhances bimodality of the population and separates CCSCs from non-CCSCs. Undermining this switch via Numb knockdown degrades bimodality and gives rise to an intermediate population of cells that have more ambiguous and plastic cell fate. We further showed that this cell fate determination switch likely provides a safeguard against excessive ISC self-renewal and proliferation in normal tissues. This safeguard mechanism can be triggered during tissue regeneration and repair after inflammation-induced damage, and its inactivation by miR-34a deletion exacerbates Lgr5+ ISC proliferation. The miR-34a-

mediated asymmetric division is active in early-stage CCSCs, likely triggered by their excessive proliferation, and is eventually subverted by miR-34a silencing in late-stage CCSCs.

Like most microRNAs, miR-34a targets multiple genes. The level of free miR-34a available to bind Notch1 mRNA is subject to variation due to the expression of other miR-34a target genes. The IFFL may provide an additional benefit of buffering Notch and cell fate decision from such miR-34a copy number variation, because binary Notch level and its resulting bimodality is largely insensitive to precise miR-34a concentration as long as it does not cross the transition threshold.

miR-34a and Numb are lower in mouse Lgr5+ ISCs and higher in more differentiated non-ISCs, consistent with their roles of suppressing Notch. However, the fact that miR-34a deletion generates no obvious intestinal phenotype was puzzling initially. Why loss of miR-34a is so significant to CCSCs? The observation that miR-34a curbs excessive ISC proliferation under pro-inflammatory stress provides a potential answer: normal tissues possess seemingly non-essential or redundant mechanisms for robustness (Shen, Collier et al. 2008, Ebert and Sharp 2012), and the importance of such mechanisms can become more prominent under stress or disease conditions. CCSCs in late-stage tumors eventually remove this barrier by silencing miR-34a and asymmetric division, contributing to more undifferentiated tumors (Bu, Chen et al. 2013, Bu, Chen et al. 2013). The concept of robustness may also provide insights into other microRNAs that are important tumor suppressors but not essential for normal tissue homeostasis.

The subject of ISC division symmetry has been intensely studied, which transformed our view of adult stem cell in mammalian tissue (McHale and Lander 2014). Previously, ISCs were thought to undergo asymmetric division exclusively to protect their number and genomic integrity (Potten, Owen et al. 2002, Quyn, Appleton et al. 2010, Goulas, Conder et al. 2012). However, Lgr5+ CBC cells were identified as actively cycling ISCs, and they perform symmetric division while competing with each other in a neutral drift process (Lopez-Garcia, Klein et al. 2010, Snippert, van der Flier et al. 2010).

Intriguingly, asymmetric division has been consistently observed in CCSCs, and its abrogation in favor of symmetric division increases their tumor initiating and proliferative capacity (O'Brien, Kreso et al. 2012, Bu, Chen et al. 2013, Hwang, Jiang et al. 2014). Similar observations have been made in other types of

cancer stem cells as well (Cicalese, Bonizzi et al. 2009, Pece, Tosoni et al. 2010, Pine, Ryan et al. 2010, Dey-Guha, Wolfer et al. 2011, Lathia, Hitomi et al. 2011, Sugiarto, Persson et al. 2011, Bajaj, Zimdahl et al. 2015). Why do CCSCs activate asymmetric division, seemingly *de novo*, which curbs proliferation and promotes differentiation? Our data provide a potential explanation to this paradox: the mechanism of asymmetric division exists in ISC, but is largely silent during normal tissue homeostasis. The rate of asymmetric division is increased to rein in the number of proliferating Lgr5+ stem cells during tissue regeneration after inflammatory damages. It is plausible that asymmetric division may be activated to counter stem cell proliferation at the onset of oncogenesis and remains active in early-stage CCSCs, until being eventually silenced (e.g., through silencing miR-34a) by tumor progression.

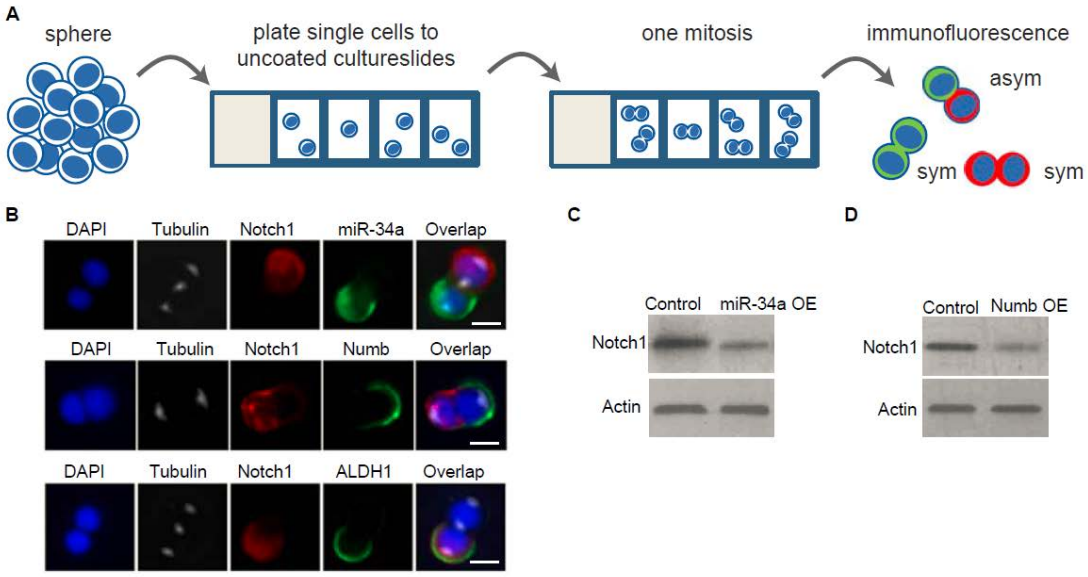

Fig. S3.1. Asymmetric distribution of Notch-targeting miR-34a and Numb during CCSC division.

*(**A**) Schematic illustration of the pair-cell assay. (**B**) Representative images of pair-cell assay with staining for miR-34a (green) and Notch1 (red), Numb (green) and Notch1 (red), and ALDH1 (green) and Notch1 (red). Tubulin staining indicates dividing pairs in telophase. (**C** and **D**) Western blot of Notch1 levels with ectopic miR-34a (B) or Numb (C) expression. Scale bar, 8μm.*

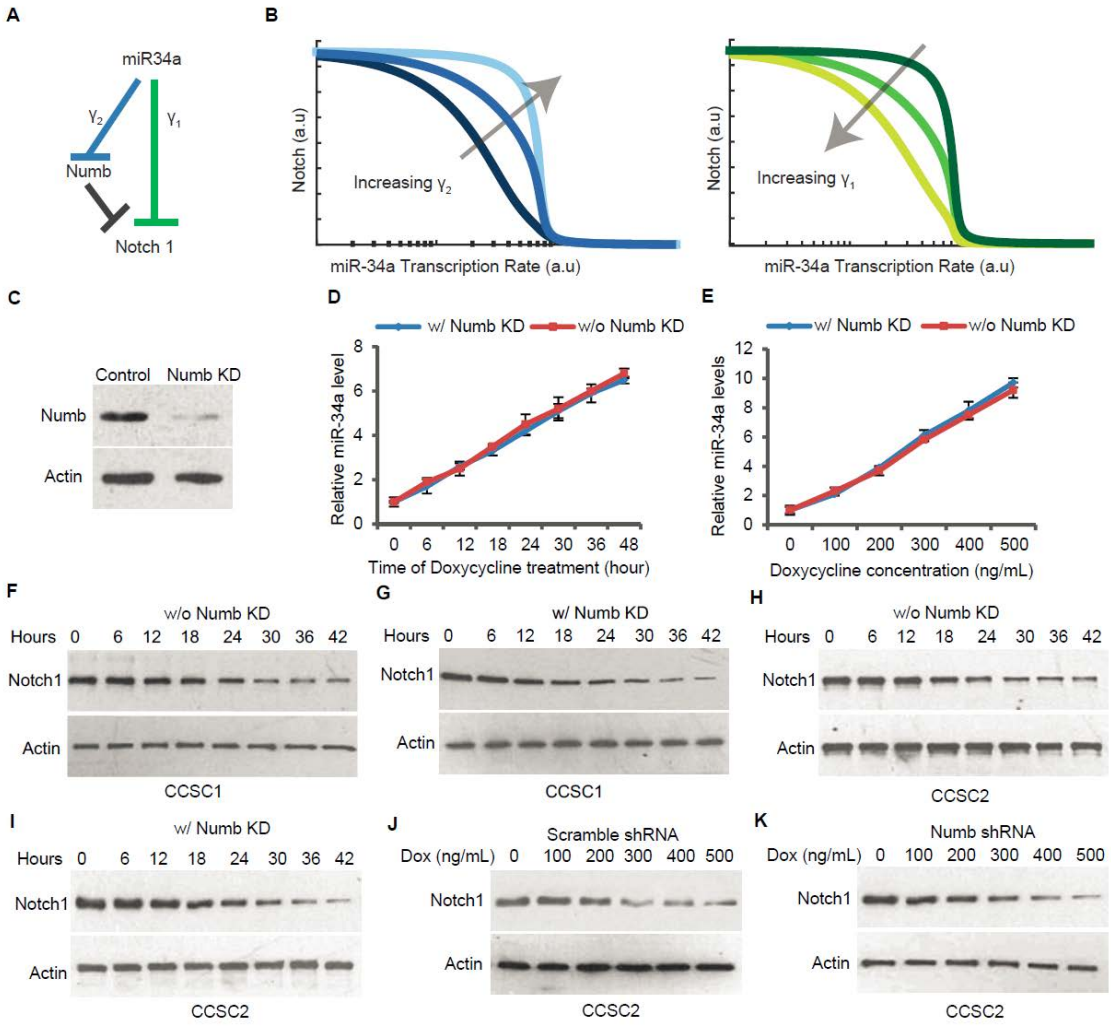

Fig. S3.3. IFFL generates a robust Notch switch.

(A) *Schematic of the IFFL.* ***(B)*** *Computational simulation shows the transition (threshold and slope) of the IFFL switch is influenced by the strength of miR-34a suppression of Notch (γ_1) and Numb (γ_2).* ***(C)*** *Western blot showing shRNA knockdown of Numb in CCSCs.* ***(D)*** *Time-series RT-qPCR measurements of induced miR-34a levels after addition of Doxycycline.* ***(E)*** *RT-qPCR measurements of miR-34a levels induced by different Doxycycline concentrations.* ***(F*** *and* ***G)*** *Time-series Western blot measurements of Notch1 levels without (F) or with (G) Numb knockdown after miR-34a expression in CCSC1 was induced*

*by 400ng/ml Doxycycline. (**H** and **I**) Time-series Western blot measurements of Notch1 levels without (H) or with (I) Numb knockdown after miR-34a expression in CCSC2 was induced by 400ng/ml Doxycycline. **(J** and **K)** Western blots of Notch levels in scramble shRNA (J) and Numb shRNA (K) infected CCSC2 spheres with incremental miR-34a induction by Doxycycline.*

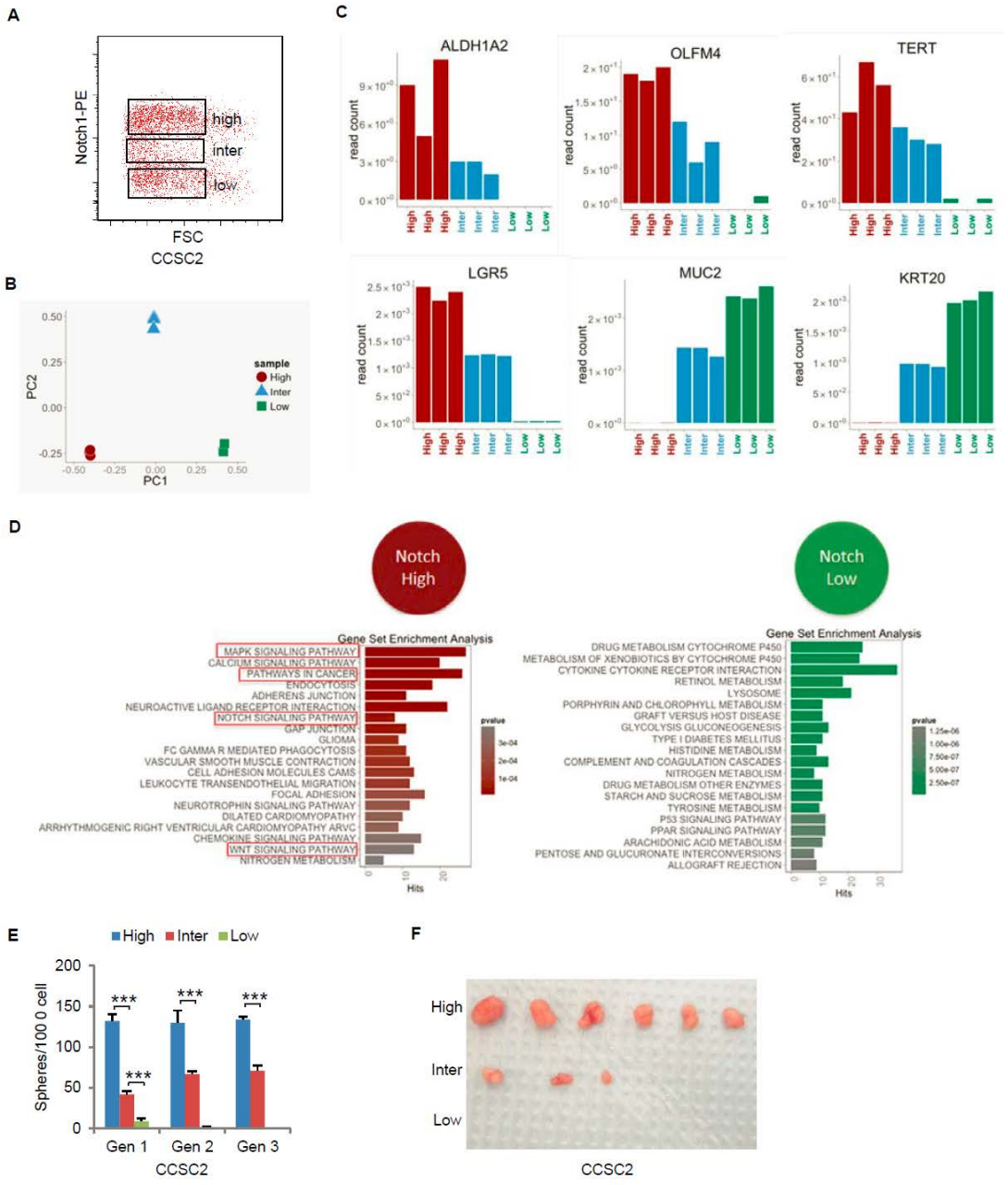

Fig. S3.3. Characterizations of Notch intermediate population in CCSCs generated by Numb

knockdown.

*(**A**) FACS plot showing Notch^{high}, Notch^{inter}, and Notch^{low} subpopulations of Numb knockdown CCSC2 sphere cells, treated with 200ng/ml Doxycycline. (**B**) Principle component analysis (PCA) of transcriptomic profiles of Notch^{high}, Notch^{inter}, and Notch^{low} cells. (**C**) Marker expression in Notch^{high}, Notch^{inter}, and Notch^{low} cells. (**D**) Pathways identified by Gene Set Enrichment Analysis (GSEA). (**E**) Serial Sphere propagation of Notch^{high}, Notch^{inter}, and Notch^{low} cells isolated from Numb Knockdown CCSC2 sphere cells. Gen, generation. (**F**) Tumor images showing tumorigenic capability of transplanted Notch^{high}, Notch^{inter}, and Notch^{low} cells. Error bars denote s.d. of triplicates. ***, p<0.001. p-value was calculated based on Student's t-test.*

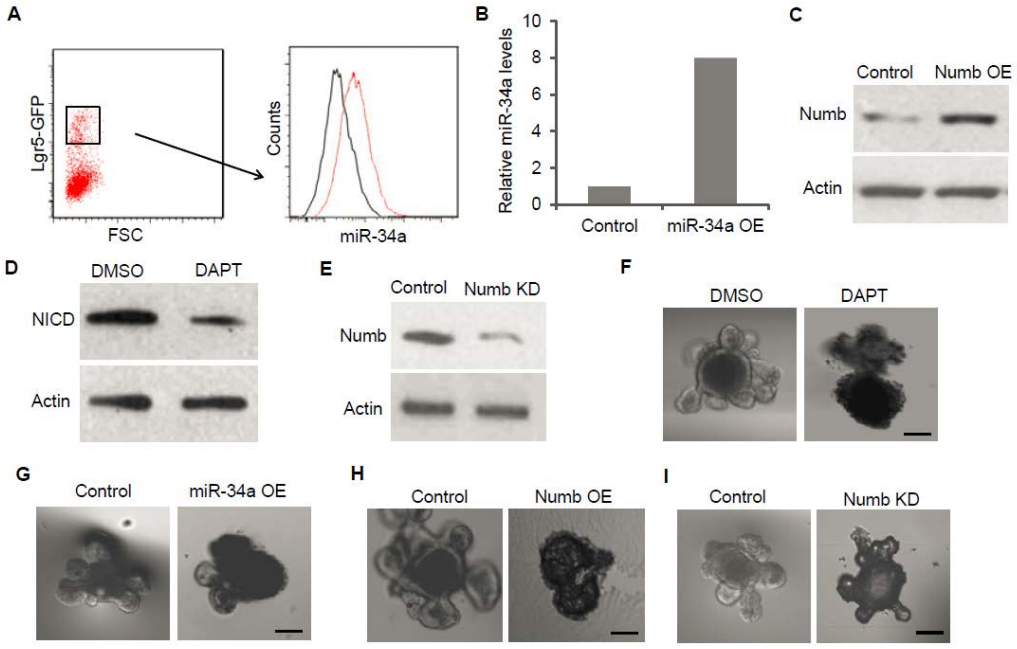

Fig. S3.4. Perturbation of Notch, miR-34a, and Numb in mouse intestinal organoids

*(**A**) miR-34a expression in Lgr5-GFP+ cells by FACS with miR-34a FISH probes. (**B**) RT-qPCR showing ectopic miR-34 expression. (**C**) Western blot showing ectopic Numb expression. (D) Western blot showing inhibition of Notch by DAPT. (**E**) Western blot showing Numb knockdown efficiency. (**F-I**) Representative images of organoids with DAPT treatment (F), ectopic miR-34a (G) or Numb (H) expression, and with*

Numb knockdown (I).

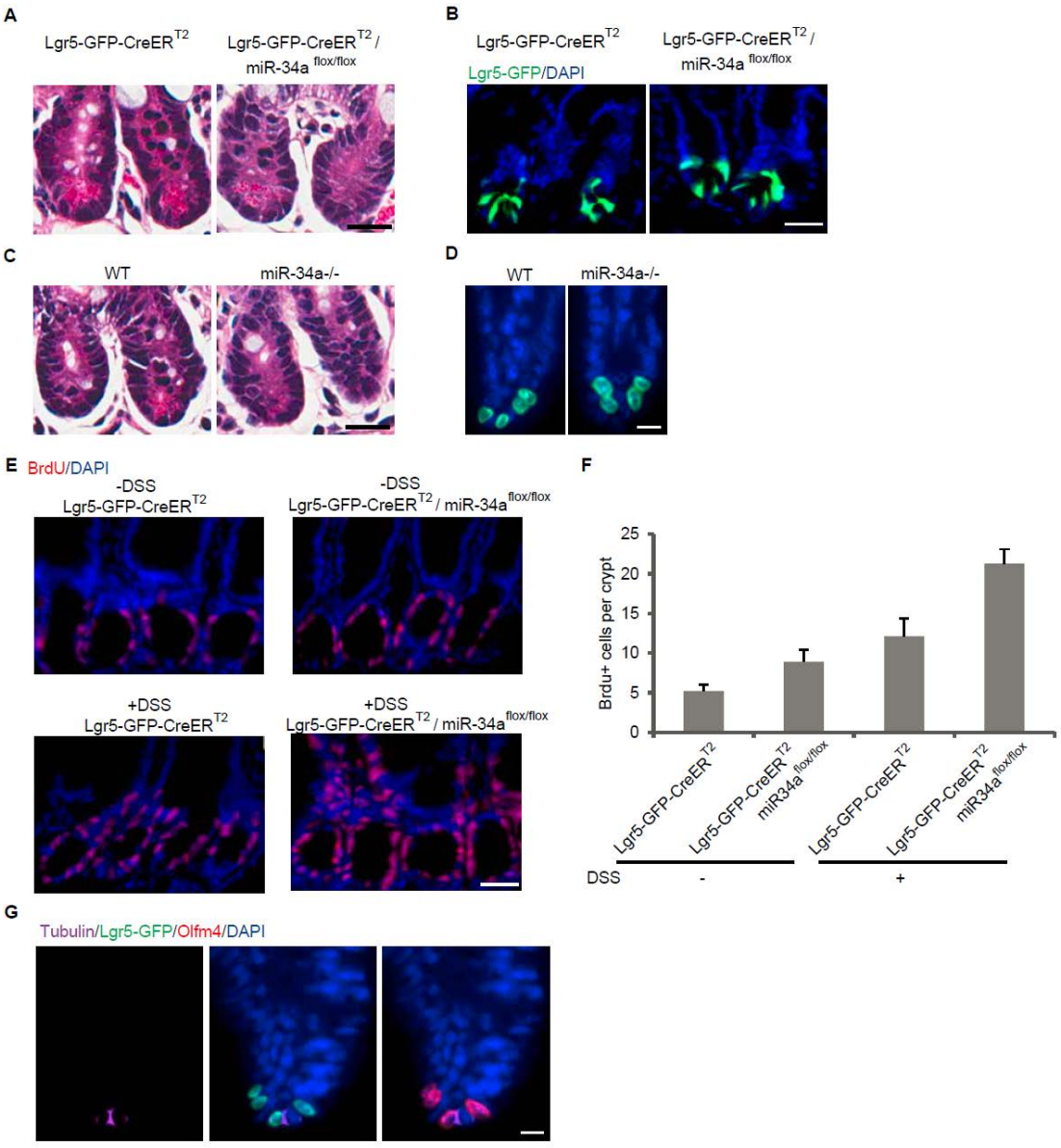

Fig. S3.5. Loss of miR-34a increases DSS-induced proliferation in mouse intestinal crypts.

*(**A** and **B**) H&E staining (A) and immunofluorescence (B) of intestinal crypts from Lgr5-EGFP- CreER^{T2} and Lgr5-EGFP-CreER^{T2}/miR-34a$^{flax/flax}$ transgenic mice after Tamoxifen induction. No obvious phenotypes in terms of morphology or Lgr5-GFP (green) ISCs were observed. Scale bar, 50μm. (**C** and **D**) H&E staining (C) and immunofluorescence (D) of intestinal crypts from wild type and miR-34a whole-*

*body knockout mice. No obvious phenotypes in terms of morphology or Olfm4 (green) ISCs were observed. Scale bar, 50μm. (**E**) Representative images of cell proliferation identified by the BrdU incorporation assay in mouse intestine. Scale bar, 50μm. (**F**) Quantification of (E). DSS and loss-of miR-34a increases proliferation. (**G**) Co- immunofluorescence confirming Lgr5-GFP cells are Olfm4+. Tubulin staining indicates a dividing pair, which was undergoing asymmetric division as shown by both Lgr5-GFP and Olfm4 staining. Scale bar, 20μm.*

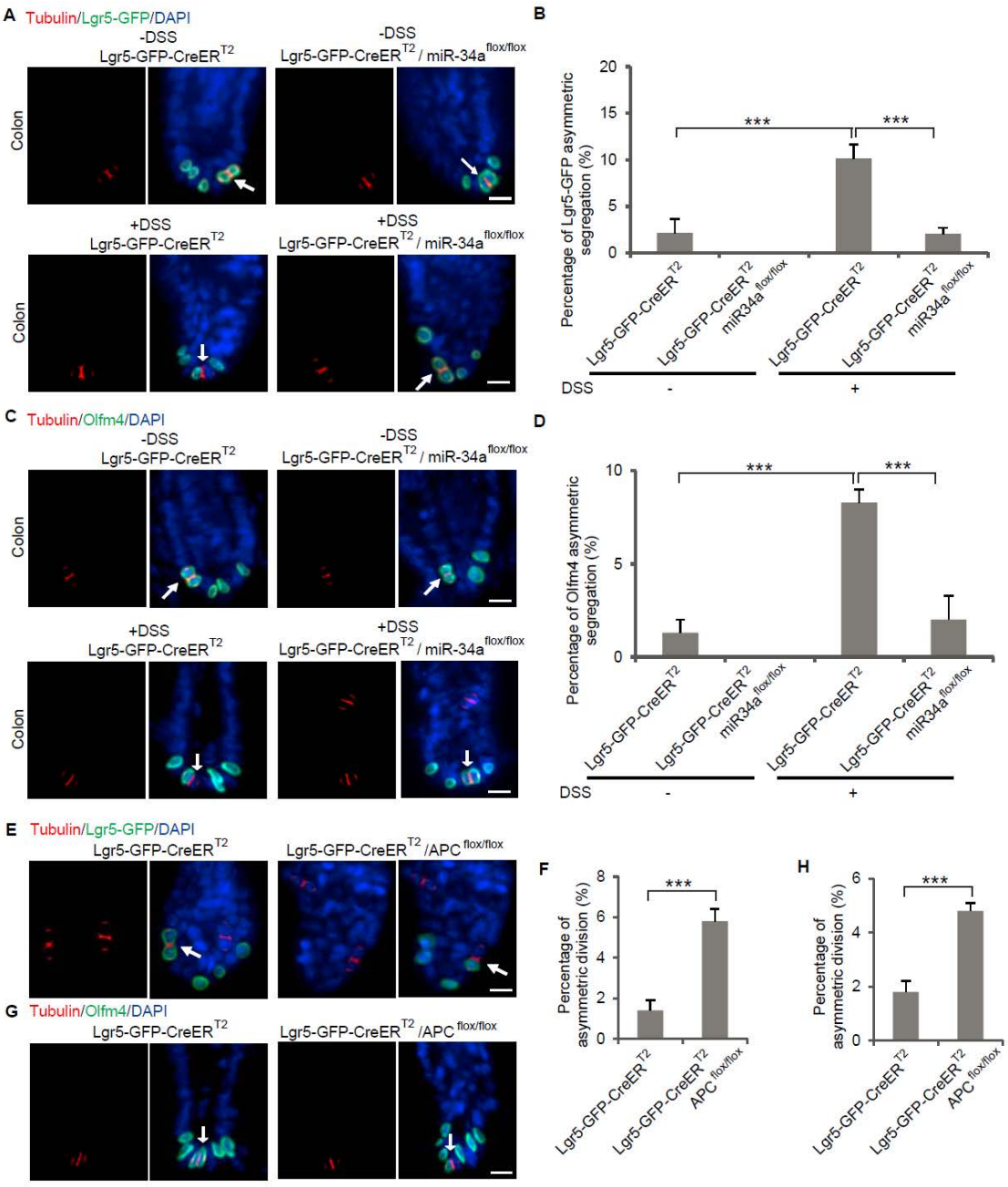

Fig. S3.6. DSS treatment increases asymmetric division and loss-of-miR-34a abrogates asymmetric division in mouse intestine and colon.

*(**A**) Representative images of symmetric and asymmetric division of Lgr5-GFP colon stem cells in Lgr5-EGFP- CreER^{T2} and Lgr5-EGFP-CreER^{T2}/miR-34a$^{flax/flax}$ mice with (+DSS) or without (-DSS) treatment. (**B**) Quantification of (A). (**C**) Representative images of symmetric and asymmetric division of Olfm4+*

*colon stem cells in Lgr5-EGFP- CreER^{T2} and Lgr5-EGFP-CreER^{T2}/miR-34a$^{flax/flax}$ mice with (+DSS) or without (- DSS) treatment. (**D**) Quantification of (C). (**E**) Representative images of Lgr5-GFP ISC division in Lgr5-EGFP- CreER^{T2} mice (left panels) and Lgr5-EGFP-CreER^{T2}/miR-34a$^{flax/flax}$ mice. Tubulin staining indicates dividing cell pair. (**F**) Quantification of (E). (**G**) Representative images of Olfm4+ ISC division in Lgr5-EGFP- CreER^{T2} mice (left panels) and Lgr5-EGFP-CreER^{T2}/miR-34a$^{flax/flax}$ mice. Tubulin staining indicates dividing cell pair. (**H**) Quantification of (G). Scale bar, 20μm. Error bars denote s.d. of triplicates. ***, p<0.001. p-value was calculated based on Student's t-test.*

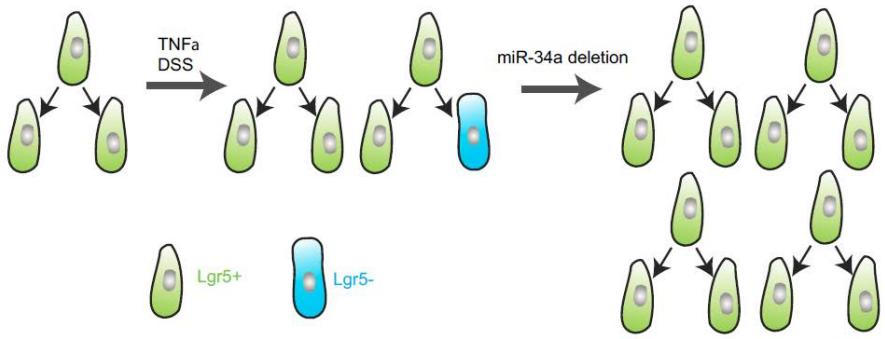

Fig. S3.7. Schematic illustrating the effect of TNF-a/DSS treatment and miR-34a loss.

TNFα or DSS treatment causes cell proliferation. Asymmetric division is increased to curb the number of Lgr5+ ISCs. Loss of miR-34a suppresses asymmetric division, contributing to Lgr5+ ISC proliferation.

REFERENCE

Bader, A. G. (2012). "miR-34 - a microRNA replacement therapy is headed to the clinic." Front Genet **3**: 120.

Bajaj, J., B. Zimdahl and T. Reya (2015). "Fearful Symmetry: Subversion of Asymmetric Division in Cancer Development and Progression." Cancer Res **75**(5): 792-797.

Beckmann, J., S. Scheitza, P. Wernet, J. C. Fischer and B. Giebel (2007). "Asymmetric cell division within the human hematopoietic stem and progenitor cell compartment: identification of asymmetrically segregating proteins." Blood **109**(12): 5494-5501.

Boon, R. A., K. Iekushi, S. Lechner, T. Seeger, A. Fischer, S. Heydt, D. Kaluza, K. Treguer, G. Carmona, A. Bonauer, A. J. Horrevoets, N. Didier, Z. Girmatsion, P. Biliczki, J. R. Ehrlich, H. A. Katus, O. J. Muller, M. Potente, A. M. Zeiher, H. Hermeking and S. Dimmeler (2013). "MicroRNA-34a regulates cardiac ageing and function." Nature **495**(7439): 107-110.

Bouchie, A. (2013). "First microRNA mimic enters clinic." Nat Biotechnol **31**(7): 577.

Bu, P., K. Y. Chen, J. H. Chen, L. Wang, J. Walters, Y. J. Shin, J. P. Goerger, J. Sun, M. Witherspoon, N. Rakhilin, J. Li, H. Yang, J. Milsom, S. Lee, W. Zipfel, M. M. Jin, Z. H. Gumus, S. M. Lipkin and X. Shen (2013). "A microRNA miR-34a-Regulated Bimodal Switch Targets Notch in Colon Cancer Stem Cells." Cell Stem Cell **12**(5): 602-615.

Bu, P., K. Y. Chen, S. M. Lipkin and X. Shen (2013). "Asymmetric division: a marker for cancer stem cells in early stage tumors?" Oncotarget **4**(7): 948-949.

Bultje, R. S., D. R. Castaneda-Castellanos, L. Y. Jan, Y. N. Jan, A. R. Kriegstein and S. H. Shi (2009). "Mammalian Par3 regulates progenitor cell asymmetric division via notch signaling in the developing neocortex." Neuron **63**(2): 189-202.

Choi, Y. J., C. P. Lin, J. J. Ho, X. He, N. Okada, P. Bu, Y. Zhong, S. Y. Kim, M. J. Bennett, C. Chen, A. Ozturk, G. G. Hicks, G. J. Hannon and L. He (2011). "miR-34 miRNAs provide a barrier for somatic cell reprogramming." Nat Cell Biol **13**(11): 1353-1360.

Cicalese, A., G. Bonizzi, C. E. Pasi, M. Faretta, S. Ronzoni, B. Giulini, C. Brisken, S. Minucci, P. P. Di Fiore and P. G. Pelicci (2009). "The tumor suppressor p53 regulates polarity of self-renewing divisions in mammary stem cells." Cell **138**(6): 1083-1095.

Concepcion, C. P., Y. C. Han, P. Mu, C. Bonetti, E. Yao, A. D'Andrea, J. A. Vidigal, W. P. Maughan, P. Ogrodowski and A. Ventura (2012). "Intact p53-dependent responses in miR-34-deficient mice." PLoS Genet **8**(7): e1002797.

Coussens, L. M. and Z. Werb (2002). "Inflammation and cancer." Nature **420**(6917): 860-867.

Dey-Guha, I., A. Wolfer, A. C. Yeh, J. G. Albeck, R. Darp, E. Leon, J. Wulfkuhle, E. F. Petricoin, 3rd, B. S. Wittner and S. Ramaswamy (2011). "Asymmetric cancer cell division regulated by AKT." Proc Natl Acad Sci U S A.

Ebert, M. S. and P. A. Sharp (2012). "Roles for microRNAs in conferring robustness to biological processes." Cell **149**(3): 515-524.

Fre, S., E. Hannezo, S. Sale, M. Huyghe, D. Lafkas, H. Kissel, A. Louvi, J. Greve, D. Louvard and S. Artavanis-Tsakonas (2011). "Notch lineages and activity in intestinal stem cells determined by a new set of knock-in mice." PLoS One **6**(10): e25785.

Goentoro, L., O. Shoval, M. W. Kirschner and U. Alon (2009). "The incoherent feedforward loop can provide fold-change detection in gene regulation." Mol Cell **36**(5): 894-899.

Goulas, S., R. Conder and J. A. Knoblich (2012). "The par complex and integrins direct asymmetric cell division in adult intestinal stem cells." Cell Stem Cell **11**(4): 529-540.

He, L., X. He, L. P. Lim, E. de Stanchina, Z. Xuan, Y. Liang, W. Xue, L. Zender, J. Magnus, D. Ridzon, A. L. Jackson, P. S. Linsley, C. Chen, S. W. Lowe, M. A. Cleary and G. J. Hannon (2007). "A microRNA component of the p53 tumour suppressor network." Nature **447**(7148): 1130-1134.

Hwang, W. L., J. K. Jiang, S. H. Yang, T. S. Huang, H. Y. Lan, H. W. Teng, C. Y. Yang, Y. P. Tsai, C. H. Lin, H. W. Wang and M. H. Yang (2014). "MicroRNA-146a directs the symmetric division of Snail-dominant colorectal cancer stem cells." Nat Cell Biol **16**(3): 268-280.

Inaba, M. and Y. M. Yamashita (2012). "Asymmetric stem cell division: precision for robustness." Cell Stem Cell **11**(4): 461-469.

Jackson, H. W., P. Waterhouse, A. Sinha, T. Kislinger, H. K. Berman and R. Khokha (2015). "Expansion of stem cells counteracts age-related mammary regression in compound Timp1/Timp3 null mice." Nat Cell Biol **17**(3): 217-227.

Kaplan, S., A. Bren, E. Dekel and U. Alon (2008). "The incoherent feed-forward loop can generate non-monotonic input functions for genes." Mol Syst Biol **4**: 203.

Katajisto, P., J. Dohla, C. L. Chaffer, N. Pentinmikko, N. Marjanovic, S. Iqbal, R. Zoncu, W. Chen, R. A. Weinberg and D. M. Sabatini (2015). "Stem cells. Asymmetric apportioning of aged mitochondria between daughter cells is required for stemness." Science **348**(6232): 340-343.

Knoblich, J. A. (2008). "Mechanisms of asymmetric stem cell division." Cell **132**(4): 583-597.

Koo, B. K., D. E. Stange, T. Sato, W. Karthaus, H. F. Farin, M. Huch, J. H. van Es and H. Clevers (2012). "Controlled gene expression in primary Lgr5 organoid cultures." Nat Methods **9**(1): 81-83.

Lander, A. D., J. Kimble, H. Clevers, E. Fuchs, D. Montarras, M. Buckingham, A. L. Calof, A. Trumpp and T. Oskarsson (2012). "What does the concept of the stem cell niche really mean today?" BMC Biol **10**: 19.

Lathia, J. D., M. Hitomi, J. Gallagher, S. P. Gadani, J. Adkins, A. Vasanji, L. Liu, C. E. Eyler, J. M. Heddleston, Q. Wu, S. Minhas, A. Soeda, D. J. Hoeppner, R. Ravin, R. D. McKay, R. E. McLendon, D. Corbeil, A. Chenn, A. B. Hjelmeland, D. M. Park and J. N. Rich (2011). "Distribution of CD133 reveals glioma stem cells self-renew through symmetric and asymmetric cell divisions." Cell Death Dis **2**: e200.

Levine, E., Z. Zhang, T. Kuhlman and T. Hwa (2007). "Quantitative characteristics of gene regulation by small RNA." PLoS Biol **5**(9): e229.

Li, R. (2013). "The art of choreographing asymmetric cell division." Dev Cell **25**(5): 439-450.

Liu, C., K. Kelnar, B. Liu, X. Chen, T. Calhoun-Davis, H. Li, L. Patrawala, H. Yan, C. Jeter, S. Honorio, J. F. Wiggins, A. G. Bader, R. Fagin, D. Brown and D. G. Tang (2011). "The microRNA miR-34a inhibits prostate cancer stem cells and metastasis by directly repressing CD44." Nat Med **17**(2): 211-215.

Lopez-Garcia, C., A. M. Klein, B. D. Simons and D. J. Winton (2010). "Intestinal stem cell replacement follows a pattern of neutral drift." Science **330**(6005): 822-825.

Mangan, S., S. Itzkovitz, A. Zaslaver and U. Alon (2006). "The incoherent feed-forward loop accelerates the response-time of the gal system of Escherichia coli." J Mol Biol **356**(5): 1073-1081.

McGill, M. A. and C. J. McGlade (2003). "Mammalian numb proteins promote Notch1 receptor ubiquitination and degradation of the Notch1 intracellular domain." J Biol Chem **278**(25): 23196-23203.

McHale, P. T. and A. D. Lander (2014). "The protective role of symmetric stem cell division on the accumulation of heritable damage." PLoS Comput Biol **10**(8): e1003802.

Morrison, S. J. and J. Kimble (2006). "Asymmetric and symmetric stem-cell divisions in development and cancer." Nature **441**(7097): 1068-1074.

Mukherji, S., M. S. Ebert, G. X. Zheng, J. S. Tsang, P. A. Sharp and A. van Oudenaarden (2011). "MicroRNAs can generate thresholds in target gene expression." Nat Genet.

Neumuller, R. A. and J. A. Knoblich (2009). "Dividing cellular asymmetry: asymmetric cell division and its implications for stem cells and cancer." Genes Dev **23**(23): 2675-2699.

O'Brien, C. A., A. Kreso, P. Ryan, K. G. Hermans, L. Gibson, Y. Wang, A. Tsatsanis, S. Gallinger and J. E. Dick (2012). "ID1 and ID3 Regulate the Self-Renewal Capacity of Human Colon Cancer-Initiating Cells through p21." Cancer Cell **21**(6): 777-792.

Osella, M., C. Bosia, D. Cora and M. Caselle (2011). "The role of incoherent microRNA-mediated feedforward loops in noise buffering." PLoS Comput Biol **7**(3): e1001101.

Pece, S., D. Tosoni, S. Confalonieri, G. Mazzarol, M. Vecchi, S. Ronzoni, L. Bernard, G. Viale, P. G. Pelicci and P. P. Di Fiore (2010). "Biological and molecular heterogeneity of breast cancers correlates with their cancer stem cell content." Cell **140**(1): 62-73.

Pine, S. R., B. M. Ryan, L. Varticovski, A. I. Robles and C. C. Harris (2010). "Microenvironmental modulation of asymmetric cell division in human lung cancer cells." Proc Natl Acad Sci U S A **107**(5): 2195-2200.

Popivanova, B. K., K. Kitamura, Y. Wu, T. Kondo, T. Kagaya, S. Kaneko, M. Oshima, C. Fujii and N. Mukaida (2008). "Blocking TNF-alpha in mice reduces colorectal carcinogenesis associated with chronic colitis." J Clin Invest **118**(2): 560-570.

Potten, C. S., G. Owen and D. Booth (2002). "Intestinal stem cells protect their genome by selective segregation of template DNA strands." J Cell Sci **115**(Pt 11): 2381-2388.

Quyn, A. J., P. L. Appleton, F. A. Carey, R. J. Steele, N. Barker, H. Clevers, R. A. Ridgway, O. J. Sansom and I. S. Nathke (2010). "Spindle orientation bias in gut epithelial stem cell compartments is lost in precancerous tissue." Cell Stem Cell **6**(2): 175-181.

Sato, T., R. G. Vries, H. J. Snippert, M. van de Wetering, N. Barker, D. E. Stange, J. H. van Es, A. Abo, P. Kujala, P. J. Peters and H. Clevers (2009). "Single Lgr5 stem cells build crypt-villus structures in vitro without a mesenchymal niche." Nature **459**(7244): 262-265.

Schepers, A. G., H. J. Snippert, D. E. Stange, M. van den Born, J. H. van Es, M. van de Wetering and H. Clevers (2012). "Lineage tracing reveals Lgr5+ stem cell activity in mouse intestinal adenomas." Science **337**(6095): 730-735.

Schuijers, J., L. G. van der Flier, J. van Es and H. Clevers (2014). "Robust cre-mediated recombination in small intestinal stem cells utilizing the olfm4 locus." Stem Cell Reports **3**(2): 234-241.

Schweisguth, F. (2004). "Regulation of notch signaling activity." Curr Biol **14**(3): R129-138.

Shen, X., J. Collier, D. Dill, L. Shapiro, M. Horowitz and H. H. McAdams (2008). "Architecture and inherent robustness of a bacterial cell-cycle control system." Proc Natl Acad Sci U S A **105**(32): 11340-11345.

Shibata, H., K. Toyama, H. Shioya, M. Ito, M. Hirota, S. Hasegawa, H. Matsumoto, H. Takano, T. Akiyama, K. Toyoshima, R. Kanamaru, Y. Kanegae, I. Saito, Y. Nakamura, K. Shiba and T. Noda (1997). "Rapid colorectal adenoma formation initiated by conditional targeting of the Apc gene." Science **278**(5335): 120-123.

Snippert, H. J., L. G. van der Flier, T. Sato, J. H. van Es, M. van den Born, C. Kroon-Veenboer, N. Barker, A. M. Klein, J. van Rheenen, B. D. Simons and H. Clevers (2010). "Intestinal crypt homeostasis results from neutral competition between symmetrically dividing Lgr5 stem cells." Cell **143**(1): 134-144.

Sugiarto, S., A. I. Persson, E. G. Munoz, M. Waldhuber, C. Lamagna, N. Andor, P. Hanecker, J. Ayers-Ringler, J. Phillips, J. Siu, D. A. Lim, S. Vandenberg, W. Stallcup, M. S. Berger, G. Bergers, W. A. Weiss and C. Petritsch (2011). "Asymmetry-defective oligodendrocyte progenitors are glioma precursors." Cancer Cell **20**(3): 328-340.

VanDussen, K. L., A. J. Carulli, T. M. Keeley, S. R. Patel, B. J. Puthoff, S. T. Magness, I. T. Tran, I. Maillard, C. Siebel, A. Kolterud, A. S. Grosse, D. L. Gumucio, S. A. Ernst, Y. H. Tsai, P. J. Dempsey and L. C. Samuelson (2012). "Notch signaling modulates proliferation and differentiation of intestinal crypt base columnar stem cells." Development **139**(3): 488-497.

Williams, S. E., S. Beronja, H. A. Pasolli and E. Fuchs (2011). "Asymmetric cell divisions promote Notch-dependent epidermal differentiation." Nature **470**(7334): 353-358.

Yan, K. S., L. A. Chia, X. Li, A. Ootani, J. Su, J. Y. Lee, N. Su, Y. Luo, S. C. Heilshorn, M. R. Amieva, E. Sangiorgi, M. R. Capecchi and C. J. Kuo (2012). "The intestinal stem cell markers Bmi1 and Lgr5 identify two functionally distinct populations." Proc Natl Acad Sci U S A **109**(2): 466-471.

CHAPTER 4

A METABOLIC SIGNATURE OF COLON CANCER INITIATING CELLS

4.1 Summary

Colon cancer initiating cells (CCICs) are more tumorigenic and metastatic than the majority of colorectal cancer (CRC) cells. CCICs have also been associated with stem cell-like properties. However, there is a lack of system-level understanding of what mechanisms distinguish CCICs from common CRC cells. We compared the transcriptomes of CD133+ CCICs and CD133- CRC cells from multiple sources, which identified a distinct metabolic signature for $CD133^{high}$ CCICs. High-resolution unbiased metabolomics was then performed to validate this CCIC metabolic signature. Specifically, levels of enzymes and metabolites involved in glycolysis, the citric acid (TCA) cycle, and cysteine and methionine metabolism are altered in CCICs. Analyses of the alterations further suggest an epigenetic link. This metabolic signature provides mechanistic insights into CCIC phenotypes and may serve as potential biomarkers and therapeutic targets for future CRC treatment.

4.2 Introduction

A rare population isolated from primary CRC tumors, CCICs play important roles in CRC tumorigenesis(O'Brien, Pollett et al. 2007, Ricci-Vitiani, Lombardi et al. 2007). CCICs also possess certain stem cell-like traits, including self-renewal, differentiation, and asymmetric division(Bu, Chen et al. 2013). CCICs were originally identified by the marker CD133(O'Brien, Pollett et al. 2007, Ricci-Vitiani, Lombardi et al. 2007, Ren, Sheng et al. 2013). Since then, they have also been associated with other markers such as CD44, ALDH1, and Lgr5(Bu, Chen et al. 2013, Medema 2013).

However, it has remained largely unclear whether CCICs isolated from different CRC tumors indeed share common mechanisms that account for their phenotype, or alternatively they are completely different cells that were categorized simply by their tumorigenic capacity.

To address this question, we first analyzed 5 GEO microarray datasets that measured the transcriptomes of CD133+ versus CD133- CRC cells(Barrett, Wilhite et al. 2013). The transcriptome analysis suggested that CD133+ cells consistently regulate certain metabolic enzymes differentially from CD133- cells.

Unbiased metabolomics by high-resolution mass spectrometry further corroborated the metabolic signature of CD133+ CCICs, which involve the glycolysis, TCA cycle, and cysteine/methionine metabolism pathways.

4.3 Material And Methods

Microarray Data From GEO

Five sets of microarray data from GEO were analyzed. These data sets include 28 FACS sorted CD133+ vs. CD133- pairs from 3 CRC patient tumors and 4 CRC cell lines (Table 4. I).

Statistical Analysis

An R-package, *Bioconductor(Gentleman, Carey et al. 2004)*, was used to extract pre-analyzed GEO data and for post-processing. Genes that were significantly (p-value <0.05) up-regulated or down-regulated in CD133+ vs. CD133- cells were identified by differential analysis using t-test and fold-change analysis. Gene frequencies and Venn diagrams were further generated by the R-packages *limma(Davis 2007)* and *vennDiagram(Chen and Boutros 2011)* to integrate analytical results from the 5 GEO datasets.

Metabolomics Data

We isolated CD133+ and CD133- populations from patient-derived CRC lines we have previously described. 6 samples were collected and FACS sorted using CD133 antibodies, and their metabolites levels were detected and measured by a high-resolution qExactive liquid chromatography–mass spectrometer (LC-MS).

Pathway Analysis

We performed pathway analyses on the CCIC-regulated genes identified from the GEO datasets using Gene Set Enrichment Analysis (GSEA)(Subramanian, Tamayo et al. 2005) and the Kyoto Encyclopedia of Genes Genomes (KEGG)(Kanehisa, Goto et al. 2004). The metabolomics and transcriptomics data were then integrated by using the KEGG Pathway Online Module (Figure 4.1, Table 4. 2).

Microarray Data List			
GEO accession number	***Bio marker***	***Cell Type***	***Sample Number***
GSE11757 (Jaksch, Múnera et al. 2008)	CD133	CACO-2	3 x CD133+ 3 x CD133-
GSE23295	CD133	SW620	2 x CD133+ 2 x CD133-
GSE24747	CD133	CACO-2	3 x CD133+ 3 x CD133-
GSE34053 (Chao, Carmical et al. 2012)	CD133	Patient specimen	3 x CD133+ 3 x CD133-
GSE38049	CD133	HCT116	3 x CD133+ 3 x CD133-

Table 4.1. GEO microarray data on CRCs

4.4 Result

4.4.1 Differential Transcriptional Profiling In CD133+ Cells

Transcriptional profiling of the five CRC sets showed that CD133+ and CD133- cells have on average 3178 significant-differential (P-value < 0.05) genes, of which 1628 genes are upregulated and 1550 genes are downregulated in CD133+ cells (Figure 4.1, Table 4. 2). To compare the gene expression profiling of the 5 sets of microarray data from 4 different platforms, we converted the probe IDs of each platform into unified Entrez format. A total of 5521 genes were identified as upregulated in CD133+ cells and 5527 genes as downregulated in CD133+ cells. Based on the frequencies of these identified genes across the 5 data sets, 946 genes were upregulated in more than one CRCs set and 718 genes were downregulated in more than one CRCs set (darker regions in Figure 4.2). However, only one gene (CD133) was consistently upregulated in all 5 datasets, and no gene was consistently downregulated in all 5 datasets.

Our differential analysis suggests that the transcriptional landscapes are consistently altered in CD133+ CCICs vs. CD133- CRC cells, and many genes are involved. However, CD133+ CCICs from different CRC tumor origins involve diverse genes, reflecting their various genetic backgrounds.

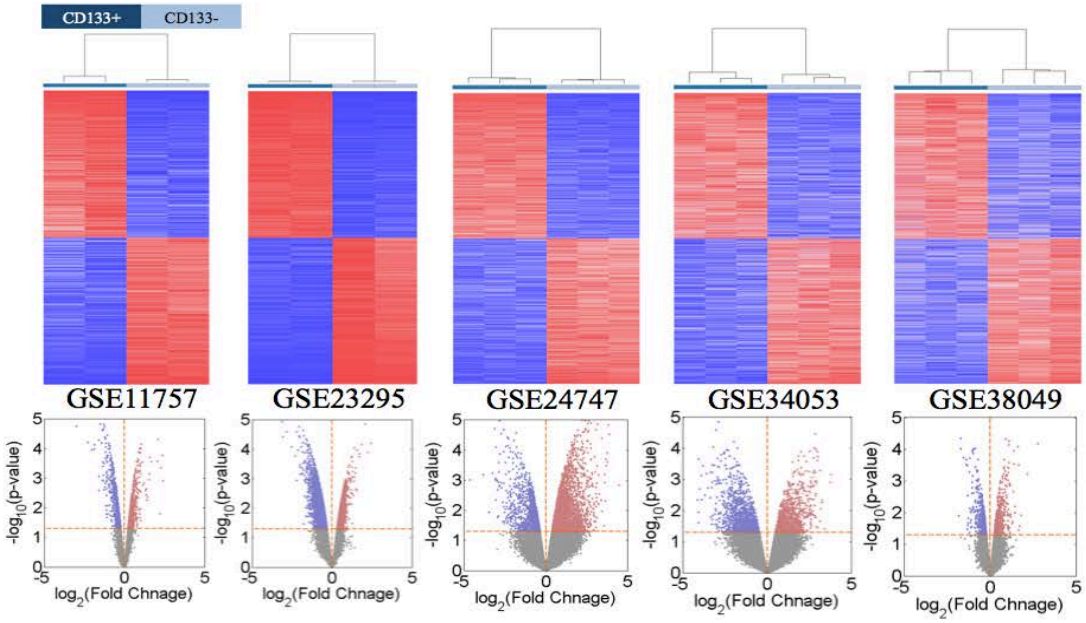

Figure 4.1. Differentially Regulated Genes In The 5 GEO Datasets*. Upper panels: Heatmaps of microarray datasets. Each row is one gene, and each colum is a sample. Red and blue colors represent high and low expression levels respectively. Lower panels: Volcano plots of differentially regulated genes calculated by p-values and fold changes, Each dot represents a gene. The red dots represent significantly upregulated genes, and the blue dots represent significantly downregulated genes.*

4.4.2 Pathway Enrichment Analysis

To find out what pathways these genes are involved with, we performed GSEA and KEGG pathway analyses on the identified list of differential genes. Pathway analyses showed that the curated gene sets of MATABOLIC PATHWAYS, PATHWAY IN CANCER, and TRANSCRIPTIONAL MISREGULATION IN CANCER are most highly enriched. KEGG identified 282 enriched pathways, among which metabolic pathways scored highest gene hit rates – 50 curated metabolic pathways involve 614 differentially regulated metabolic genes. The metabolic alterations in CD133+ CCICs are visualized in the global metabolic map shown in Figure 4.3, wherein red lines represent upregulated enzymatic reactions and blue lines represent downregulated reactions. Darker color indicates a higher frequency of the metabolic gene across the 5 datasets. The global analysis suggests that metabolic pathways are highly reprogramed in CD133+ CCICs.

GEO accession number	*Total Significant-Differential Genes*	*Significant- Differential Upregulated Genes*	*Significant- Differential Downregulated Genes*
GSE11757	1676	861	815
GSE23295	6935	3089	3846
GSE24747	4011	2723	1288
GSE34053	2230	954	1276
GSE38049	1038	512	526
AVERAGE	3178	1628	1550

Table 4.2. Summary of differential analysis

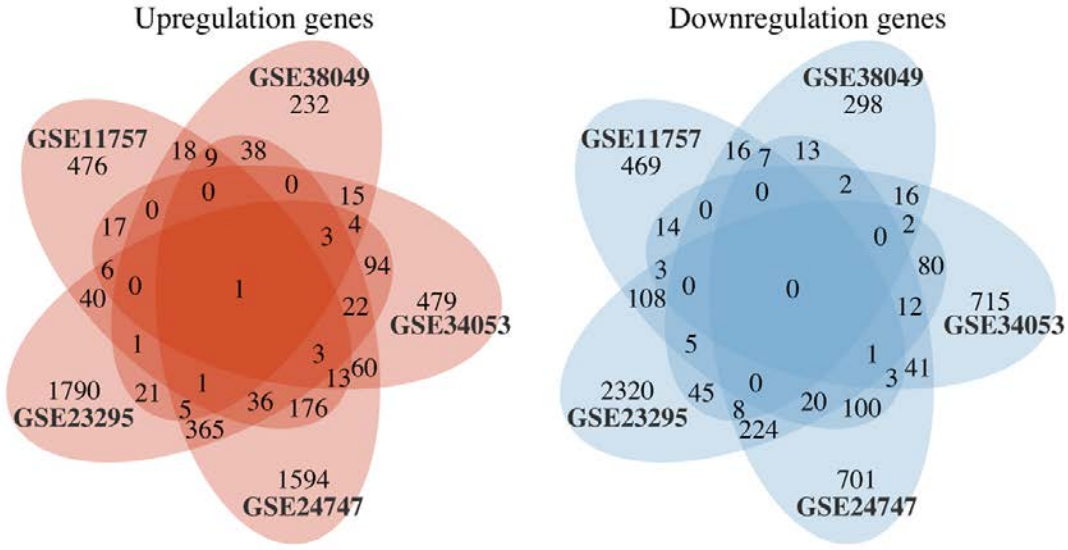

Figure 4.2 Venn Diagrams Of Differentially Regulated Genes*. Each circle represents a GEO dataset. The number in each intersecting region represents the number of overlapping genes.*

4.4.3 Metabolomic Profiling

The gene and pathway enrichment analyses suggest that metabolic reprogramming may be a signature of CD133+ CCICs. To validate this hypothesis, we FACS sorted pure CD133+ and CD133- populations from patient-derived CRC lines we have previously published (Bu, Chen et al. 2013) and performed unbiased, high-resolution metabolomics to measure metabolite levels in triplicate samples using LC-MS. Differential analysis identified 54 metabolites that were differentially expressed in a statistically significant way (P-value < 0.05), among which 28 metabolites were upregulated in CD133+ CCICs and 26 metabolites were downregulated in CD133+ CCICs. The list of differential expressed metabolites is summarized in Table 4. 3.

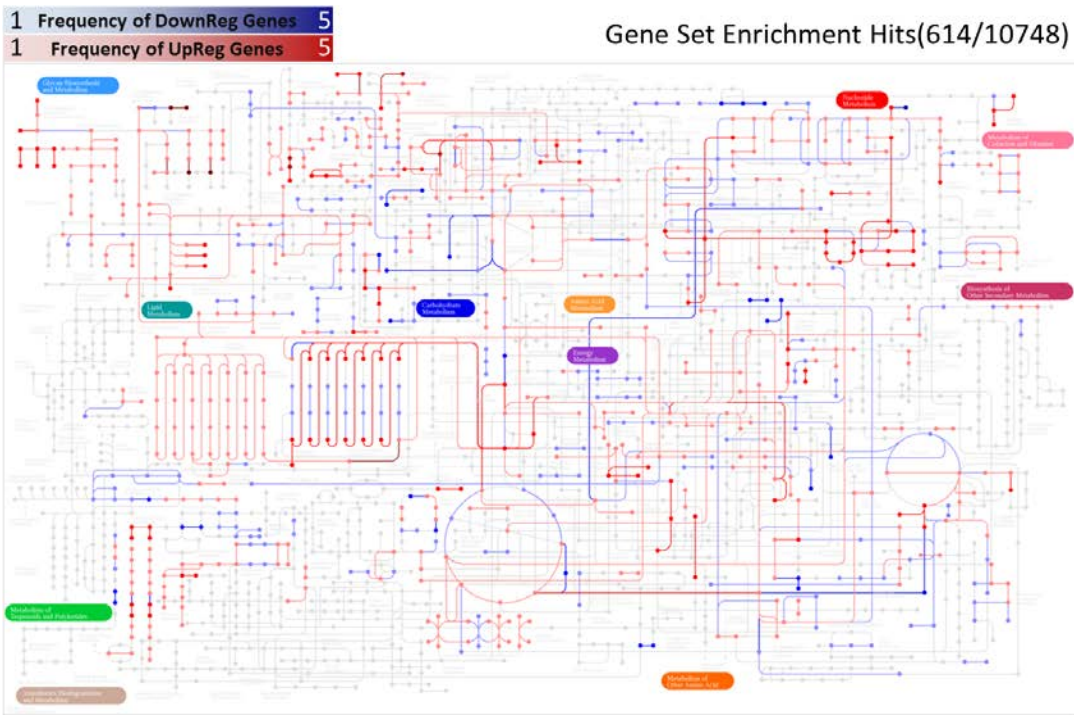

Figure 4.3 A Global Metabolic Map Showing Metabolic Alterations In CD133+ Ceils. *Nodes represent metabolites, and lines represent enzymatic reactions. Red color refers to significantly upregulated enzymetic genes, and blue color refers to significantly downregulated enzymetic genes. Color saturation reprents the frequency of the gene across GEO datasets, from 5 (darkest) to 1 (lightest).*

54 differentially expressed metabolites (p-value < 0.05)	
Upregulated Metabolites (28 metabolites)	Downregulated Metabolites (26 metabolites)
fructose-16-bisphosphate	serine
inosine	adenine
Phosphorylcholine	betaine aldehyde
UTP	2-keto-isovalerate
CDP-ethanolamine	sarcosine
malate	2-hydroxygluterate
ATP	Atrolactic acid
dGTP	Phenyllactic acid
S-methyl-5-thioadenosine	hydroxyphenylpyruvate
orotate	aspartate
uridine	Pyroglutamic acid
Maleic acid	histidine
octulose-monophosphate (O8P-O1P)	folate
NAD+	2-Isopropylmalic acid
glutathione disulfide	glycolate
4-aminobutyrate	phenylpyruvate
dimethylglycine	Hydroxyisocaproic acid
S-adenosyl-L-methionine	glucono-D-lactone
UDP-N-acetyl-glucosamine	Pyridoxamine
citrulline	Ascorbic acid
aconitate	N-acetyl-glutamine
ADP	acetoacetate
dGDP	sn-glycerol-3-phosphate
citrate-isocitrate	Pyrophosphate
betaine	6-phospho-D-glucono-15-lactone
3-phosphoglycerate	2,3-dihydroxybenzoic acid
alanine	
a-ketoglutarate	

Table 4.3 List Of Significantly-Differential Metabolites

4.4.4 Integrated Transcriptomic And Metabolomic Network Analysis

Above transcriptomic and metabolomic analyses suggest that metabolic pathways are altered in CD133+ CCICs across different CRC backgrounds. To investigate the connections between CCIC transcriptome and metabolome, we performed integrated KEGG pathway analysis on the list of differential genes and metabolites. The analysis identified carbohydrate metabolism (glycolysis, the TCA cycle) and cysteine and methionine metabolism as consistently altered in CCICs, with highly altered enzyme and metabolite levels (Figures 4, 5).

In most cells, glycolysis converts glucose into pyruvate, which then enters the TCA cycle. Compared to CD133- CRC cells, major glycolysis enzymes PGK1, BPGM, and ENO1 are significantly downregulated in CD133+ CCICs, indicating suppressed upstream activities (Figure 4.4). Moreover, ACSS1 (Acyl-CoA Synthetase Short-chain family member 1), a mitochondrial acetyl-CoA synthetase enzyme that catalyzes acetate to acetyl-CoA, is significantly upregulated in CD133+ CCICs, which potentially convert more upstream acetate into acetyl-CoA. On the other hand, downstream reactions to catalyze acetyl-CoA into malonyl-CoA and acetoacetyl-CoA are suppressed, hence forcing the extra acetyl-CoA to enter the TCA cycle. Consistently, the upstream metabolites in the TCA-cycle, i.e., citrate, aconitate, isocitrate, and α-ketoglutarate, are highly accumulated in CD133+ CCICs. At the end point of the TCA cycle, significantly upregulated PCK1 and PCK2 form a positive feedback loop to further facilitate the conversion of oxaloacetate into acetyl-CoA to fuel the TCA cycle. It has been shown that reprogramming of energy metabolism is a hallmark of pluripotent stem cells reprogram (Shyh-Chang, Zheng et al. 2011, Zhang, Nuebel et al. 2012). Stem cells influence epigenetic regulation such as histone acetylation and histone/DNA demethylation by controlling intermediate metabolite substrates Acetyl-CoA and α-ketoglutarate (Zhang, Nuebel et al. 2012, Johnson, Warmoes et al. 2013). Therefore, altered energy metabolism and elevated Acetyl-CoA and α-ketoglutarate levels may explain some of the stem cell-like phenotypes observed in CD133+ CCICs.

Another consistently altered metabolic pathway is cysteine and methionine metabolism (Figure 4.5). In this pathway, enzyme CBS (Cystathionine-β-Synthase) combines homocycteine and serine to generate cystationine and subsequently CTH catalyzes cystationine into cysteine. Both CBS and CTH are significantly upregulated in CD133+ CCICs. Interestingly, cysteine has been reported to regulate neural stem cells through the CBS/H_2S pathway(Wang, Liu et al. 2013). In methionine metabolism, DNMT1/3L, SRM, AMD1, and MTAP, downstream enzymes that catalyze S-AdenosylMethionine (SAM), are significantly downregulated in CD133+ CCICs. The metabolomics data confirm that the downregulated enzymatic reactions lead to accumulation of SAM in CD133+ CCICs. Among the downregulated enzymes, DNMT1/3L is an important DNA methyltransferase that catalyzes the transfer of methyl groups

from SAM to DNA. Therefore, altered methionine metabolism might impact DNA methylation in CD133+ CCICs.

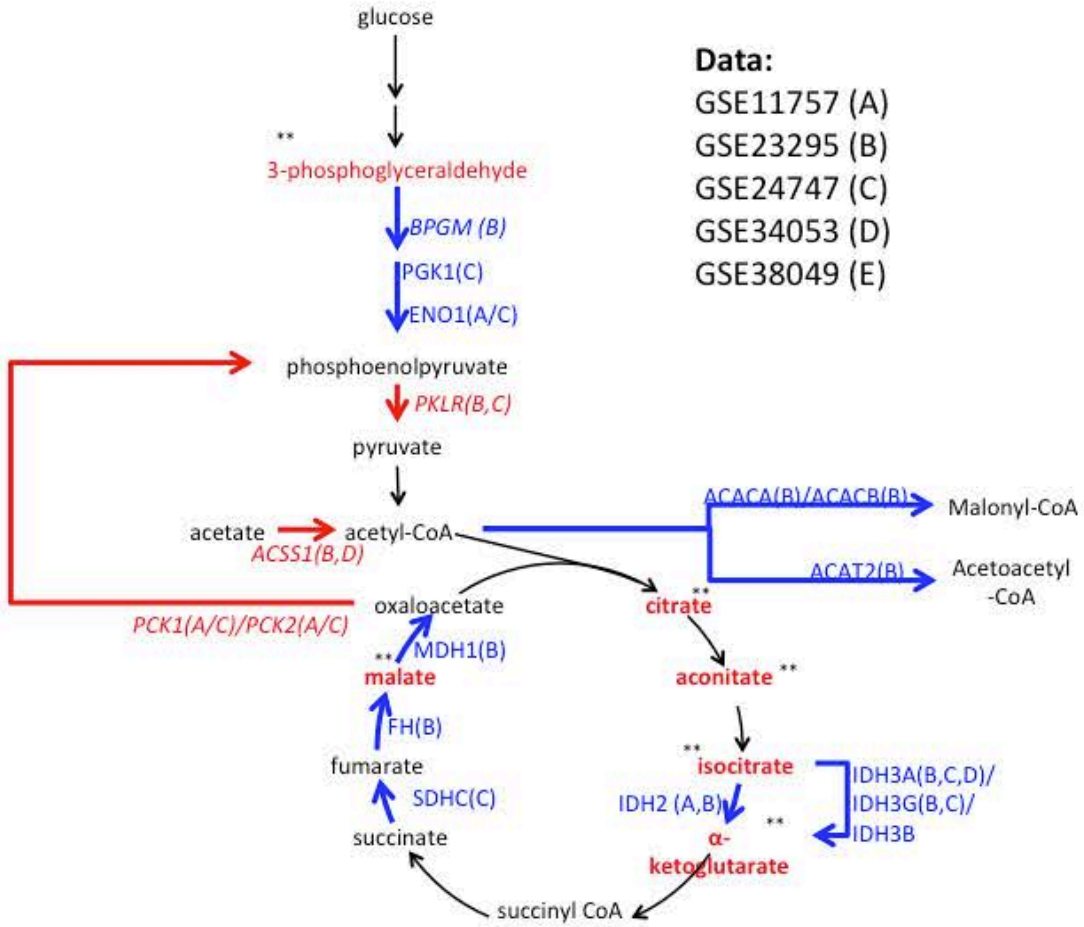

Figure 4.4 Altered Carbohydrate Metabolism In CCIC. *Arrows represent metabolic flows regulated by marked metabolic enzymes. Metabolites are shown as nodes. Upregulated genes and metabolites are shown in red, downregulated genes and metabolites are shown in blue.*

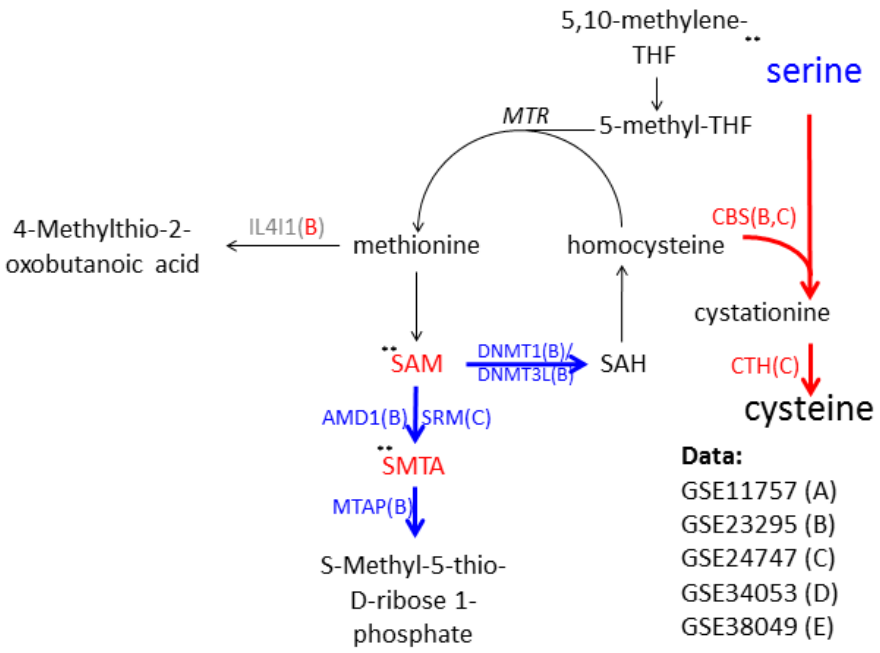

Figure 4.5 Altered Cysteine And Methionine Metabolism In CCIC*. The Annotation Is Consistent With That Of Figure4.*

4.5 Discussion

CD133+ CCICs from different CRC tumors are likely to have diverse mechanisms. However, by perform system-level transcriptomic and metabolomic analyses on various CRC sources, we identified a distinct metabolic signature of CD133+ CCICs that involve glycolysis, the TCA cycle, and cysteine/methionine metabolism. The metabolite substrates involved in epigenetic regulations are highly altered, suggesting a potential epigenetic link. RNA-seq, metabolic flux analysis (MFA), and functional assays are currently being performed to further establish such links. The identified metabolic signature provides insights into reported stem cell-like properties of CD133+ CCICs. The involved metabolic enzymes and metabolites may provide biomarkers for CRC diagnosis and prognosis. New CRC treatments may also target them to suppress CCICs in the tumor population to reduce the risk of relapse and metastasis.

REFERENCES

Barrett, T., S. E. Wilhite, P. Ledoux, C. Evangelista, I. F. Kim, M. Tomashevsky, K. A. Marshall, K. H. Phillippy, P. M. Sherman, M. Holko, A. Yefanov, H. Lee, N. Zhang, C. L. Robertson, N. Serova, S. Davis and A. Soboleva (2013). "NCBI GEO: archive for functional genomics data sets--update." Nucleic acids research **41**(Database issue): D991-995.

Bu, P., K. Y. Chen, J. H. Chen, L. Wang, J. Walters, Y. J. Shin, J. P. Goerger, J. Sun, M. Witherspoon, N. Rakhilin, J. Li, H. Yang, J. Milsom, S. Lee, W. Zipfel, M. M. Jin, Z. H. Gumus, S. M. Lipkin and X. Shen (2013). "A microRNA miR-34a-regulated bimodal switch targets Notch in colon cancer stem cells." Cell Stem Cell **12**(5): 602-615.

Chao, C., J. R. Carmical, K. L. Ives, T. G. Wood, J. F. Aronson, G. A. Gomez, C. D. Djukom and M. R. Hellmich (2012). "CD133+ colon cancer cells are more interactive with the tumor microenvironment than CD133- cells." Lab Invest **92**(3): 420-436.

Chen, H. and P. C. Boutros (2011). "VennDiagram: a package for the generation of highly-customizable Venn and Euler diagrams in R." BMC bioinformatics **12**: 35-35.

Davis, J. W. (2007). Bioinformatics and Computational Biology Solutions Using R and Bioconductor.

Gentleman, R. C., V. J. Carey, D. M. Bates, B. Bolstad, M. Dettling, S. Dudoit, B. Ellis, L. Gautier, Y. Ge, J. Gentry, K. Hornik, T. Hothorn, W. Huber, S. Iacus, R. Irizarry, F. Leisch, C. Li, M. Maechler, A. J. Rossini, G. Sawitzki, C. Smith, G. Smyth, L. Tierney, J. Y. H. Yang and J. Zhang (2004). "Bioconductor: open software development for computational biology and bioinformatics." Genome biology **5**: R80-R80.

Jaksch, M., J. Múnera, R. Bajpai, A. Terskikh and R. G. Oshima (2008). "Cell cycle-dependent variation of a CD133 epitope in human embryonic stem cell, colon cancer, and melanoma cell lines." Cancer research **68**: 7882-7886.

Johnson, C., M. O. Warmoes, X. Shen and J. W. Locasale (2013). Epigenetics and cancer metabolism. Cancer Letters.

Kanehisa, M., S. Goto, S. Kawashima, Y. Okuno and M. Hattori (2004). "The KEGG resource for deciphering the genome." Nucleic acids research **32**(Database issue): D277-280.

Medema, J. P. (2013). "Cancer stem cells: the challenges ahead." Nature cell biology **15**(4): 338-344.

O'Brien, C. A., A. Pollett, S. Gallinger and J. E. Dick (2007). "A human colon cancer cell capable of initiating tumour growth in immunodeficient mice." Nature **445**: 106-110.

Ren, F., W. Q. Sheng and X. Du (2013). "CD133: a cancer stem cells marker, is used in colorectal cancers." World J Gastroenterol **19**(17): 2603-2611.

Ricci-Vitiani, L., D. G. Lombardi, E. Pilozzi, M. Biffoni, M. Todaro, C. Peschle and R. De Maria (2007). "Identification and expansion of human colon-cancer-initiating cells." Nature **445**(7123): 111-115.

Shyh-Chang, N., Y. Zheng, J. W. Locasale and L. C. Cantley (2011). "Human pluripotent stem cells decouple respiration from energy production." The EMBO journal **30**(24): 4851-4852.

Subramanian, A., P. Tamayo, V. K. Mootha, S. Mukherjee, B. L. Ebert, M. A. Gillette, A. Paulovich, S. L. Pomeroy, T. R. Golub, E. S. Lander and J. P. Mesirov (2005). "Gene set enrichment analysis: a knowledge-based approach for interpreting genome-wide expression profiles." Proceedings of the National Academy of Sciences of the United States of America **102**(43): 15545-15550.

Wang, Z., D. Liu, F. Wang, Q. Zhang, Z. Du, J. Zhan, Q. Yuan, E.-A. Ling and A. Hao (2013). "L-cysteine promotes the proliferation and differentiation of neural stem cells via the CBS/H(2)S pathway." Neuroscience.

Zhang, J., E. Nuebel, G. Q. Daley, C. M. Koehler and M. A. Teitell (2012). "Metabolic regulation in pluripotent stem cells during reprogramming and self-renewal." Cell stem cell **11**(5): 589-595.

CHAPTER 5

DYNAMIC REGULATION OF INTESTINAL STEM CELL NICHE RECOVERY IN REAL-TIME

5.1 Summary

The stem cell niche regulates tissue homeostasis and regeneration. Yet, how precisely the niche replaces lost cells and recovers from damage remains largely unknown. Here, we developed a systems biology approach combining *in vivo* laser ablation followed by chronic imaging and *in silico* dynamic models to study this spatiotemporal process in the intestinal epithelium. We ablated individual stem or Paneth cells in the mouse intestinal crypt with high-precision photodisruption using a femtosecond laser, and monitored the *in vivo* dynamics of intestinal niche recovery in real-time, stabilized by a surgically implanted 3D-printed scaffold. The niche recovers immediately after cell loss by rearranging stem/Paneth cell patterns rather than waiting for new cell division to fill the vacancy. Distinct from classic lateral inhibition, intestinal stem cells employ a unique positive feedback mechanism via direct Notch1 binding to sustain the niche. Inactivation of the positive feedback by CRISPR/Cas9 mutation disrupts the niche pattern, limits self-renewal, and renders the niche incapable of recovery in organoids. Dynamical system analysis and agent-based multiscale stochastic modeling demonstrated that this regulation scheme enhances the robustness of Notch-mediated patterning when cell turnover rate is high. This study highlights a systems approach that integrates *in vivo*, *in vitro*, and *in silico* models coupled with technology of precise perturbation to comprehend spatiotemporal regulation of mammalian tissue.

5.2 Introduction

The stem cell niche provides a spatial environment to regulate stem cell self-renewal and differentiation(Lander, Kimble et al. 2012). Some mammalian tissues, especially regenerative ones, rely on stem cell niches rather than asymmetric division to control the number of proliferative stem cells. Remarkably, the niche often has the ability to recover from damaged cells and restore homeostasis. However, we know very little of this process and its underlying control mechanism.

One prominent example is the stem cell niche at the base of the intestinal crypt. In the niche, self-renewing LGR5+ crypt base columnar (CBC) cells and lysozyme-secreting Paneth cells form a mosaic pattern(Barker, van Es et al. 2007, Sato, van Es et al. 2010). As proliferative intestinal stem cells (ISCs), CBCs divide symmetrically, compete with each other in a neutral drift process, and regenerate the intestinal epithelium in 3 to 5 days(Lopez-Garcia, Klein et al. 2010, Snippert, van der Flier et al. 2010). Remarkably, the stem cell niche is capable of recovering from radiation or chemical damages(Buczacki, Zecchini et al. 2013, Metcalfe, Kljavin et al. 2014).

5.3 Material And Methods

Antibodies

Primary Antibody	Supplier	Catalog Number	Dilution*
anti-ATOH1	Abcam	ab137534	1:1000 (WB)
anti-β-ACTIN	Abcam	ab6276	1:4000 (WB)
Anti-CD24 (APC)	Abcam	ab51535	1:500 (FC)
Anti-DLL1	Abcam	ab85346	1:500 (WB)
Anti-DLL4	Abcam	ab7280	1:1000 (WB)
Anti-EPHB2	R&D Systems	AF467	1:1000 (FC)
Anti-EpCAM (FITC)	Abcam	ab8666	1:500 (FC)
Anti-GFP	Abcam	ab5450	1:200 (IF)
Anti-HES1	Abcam	ab108937	1:1000 (WB)
Anti-HES5	Santa Cruz Biotechnology	sc-25395	1:500 (WB)
Anti-JAG1	Santa Cruz Biotechnology	sc-6011	1:500 (WB)
Anti-LYSOZYME	Abcam	ab108508	1:100 (IF)
Anti-(human)NICD	R&D Systems	AF3647	1:200 (ChIP)
Anti-(mouse)NICD	Cell Signaling	4147	1:200 (ChIP)
Anti-NOTCH1	Santa Cruz Biotechnology	sc-9170	1:1000 (WB)

Anti-NOTCH2	Santa Cruz Biotechnology	sc-32346	1:1000 (WB)
Anti-OLFM4	Sino Biological Inc.	11639-MM12-50	1:1000 (FC)

***Application: IF: (Immunofluorescence); WB: (Western Blotting); FC: (Flow Cytometry)**

Mouse strains

LGR5-EGFP mice on a mixed 129/C57BL/6 background and Rosa26-CAG-LSL-tdTomato-WPRE mice on a mixed 129/C57BL/6 background were purchased from The Jackson laboratory. Notch1-CreERT2 knock-in (KI) mice, Notch2-CreERT2 KI mice, and Rosa26-NICD-IRES-YFP KI mice were a generous give from Dr. **Spyros Artavanis-Tsakona**'s laboratory at Harvard University. Subsequently, we generated an inducible Notch1 reporter mouse strain (Notch1-CreERT2 KI x Rosa26-CAG-LSL-tdTomato-WPRE) and an inducible Notch2 reporter mouse strain (Notch2-CreERT2 KI x Rosa26-CAG-LSL-tdTomato-WPRE). We also generated a LGR5-EGFP-CreERT2 x Rosa26-NICD-IRES-YFP KI mouse strain for inducible NICD overexpression (NICD-OE). Genotyping was performed using the following PCR primer pairs for Notch1 (Forward: ATAGGAACTTCAAAATGTCGCG; Reverse: CACACTTCCAGCGTCTTTGG), Notch2: (Forward: ATAGGAACTTCAAAATGTCGCG; Reverse: CCCAACGGTGCCAAAAGAGC), and NICD: (Forward: CTTCACACCCCTCATG ATTGC; Reverse: GCAATCGGTCCATGTGATCC). The thermocyling profile used for PCR amplification is described as follows: 95°C (5 min)/[95°C (30 sec), 60°C (30 sec), 72°C (60 sec)] for 35 cycles/72°C (10 min). Notch1 and Notch2 reporter mice were induced with 75 mg/kg Tamoxifen by i.p. injection. The LGR5-EGFP-CreERT2 x Rosa26-NICD-IRES-YFP KI mouse strain was treated daily with 75 mg/kg Tamoxifen (i.p. injection) for 8 consecutive days to induce Cre enzyme activity and NICD-OE phenotype.

Abdominal window

Abdominal window were surgically implanted on LGR5-EGFP mice for imaging and laser ablation studies. At the beginning of surgery, animals received an anticholinergic (atropine) to assist in keeping the airways clear of fluid build-up. Body temperature was kept at 37°C using a heating blanket controlled by a rectal thermometer (50-7053; Harvard Apparatus, Holliston, MA, USA). All areas to be incised were cleaned and shaved with #40 clippers, sterilized with 70% ethanol, swabbed with betadine, and were

numbed with a subcutaneous injection of bupivacaine (0.125%). Dexamethasone (0.1mg/ml) and Ketopropane (2.0 mg/ml) were administered i.p. to help recovery after surgery. Eyes were covered with veterinary eye ointment to prevent drying. The animals were hydrated with subcutaneous injections of 5% glucose in saline for isotonic fluid replacement. Abdominal skin was removed in circular shape to implant commercially available window frame (12 mm in inner diameter, APJ trading, CA). Outer edge of the window was covered by skin with tissue glue (Loctite 406, Henkel). Muscular layer of inner circle was incised by scissor to expose small intestine directly. 3D printed insert (RPL lab, Cornell University) was sutured to the skin to be placed under the small intestine loop and a portion of small intestine was position on top of the insert. Window was secured by 12 mm cover glass with a retaining ring to keep physiological environment intact. All experiments were performed in accordance with the ethical and care guidelines established by the Research Animal Resource Center and Institutional Animal Care and Use Committee of Cornell University.

***In vivo* Two Photon Excited Fluorescent Microscopy**

Animals with abdominal window were imaged using a custom-built two-photon excited fluorescent (2PEF) microscope with four simultaneous fluorescent detection channels. All animals were anesthetized with isoflurane during the imaging time and monitored by physiological condition. Texas-red dextran (Molecular Weight: 70,000; Thermo Fisher Scientific. NY) was administered through retro-orbital injection to visualize vasculature. Images were acquired using a Ti:Sapphire laser (Chameleon; Coherent, Santa Clara, CA), a central wavelength at 880 nm. A X20 1.0 numerical aperture (NA) water-immersion microscope objective and X4 0.28 NA objective lens (Zeiss, Thornwood, NY) were used for all imaging. A 494-nm bandpass filter with 41-nm bandwidth and a 641-nm bandpass filter with a 75-nm bandwidth were used for detecting green fluorescent protein (GFP) and Texas-red dextran dye, respectively. Image series were acquired before and after laser ablation, and three dimensional (3D) image stacks with 1 um spacing in the axial direction were acquired through the entire imaging session. All images were processed using ImageJ. The raw stack was separated into four channels, and each channel was color-coded accordingly. The image frames containing abrupt movement from respiration or peristalsis were

deleted and the stack has re-aligned by using Stackreg(Thevenaz, Ruttimann et al. 1998). Z-projection was used for final image presentation to incorporate the 3D structure. The average z-axis in each image is 5-10 um.

Femtosecond Laser Photodisruption

Selective disruption of cellular contact was performed using a low-repetition-rate, high-pulse-energy Ti:Sapphire regenerative amplifier with 100-fs pulse duration, 1-kHz repetition rate, and 800-nm central wavelength (Legend-USP; Coherent, Santa Clara, CA). A polarizing beamsplitter cube was used to introduce this beam into the 2PEF microscope so that the pulses were focused at the center of the imaging field and in the 2PEF imaging plane, enabling real-time monitoring of recovery process. Laser energy incident on the cells was controlled by neutral density filters, and a fast mechanical shutter limited the number of pulses incident on each cell. Laser energy to remove a single cell did not exceed 100 nJ.

***In vivo* Notch Signaling Inhibition**

DBZ (Syncom, Netherlands), a small molecule gamma-secretase inhibitor, was locally injected into the submucosal layer of the small intestine through the implanted abdominal window on mice. Each animal was anesthetized with isoflurorane to inject DBZ. DBZ was dissolved in DMSO at final concentration of 30 uM. Animals were pre-treated with DBZ (15 umol/kg) for 2 hours before ablation to inhibit Notch signaling.

Murine Intestinal Crypt Isolation and Organoid Culture

8-week-old LGR5-EGFP or LGR5-EGFP/NICE-OE mice were sacrificed to establish intestinal organoid culture. Briefly, small intestines were harvested, flushed with $Ca2^{+/}Mg^{2+}$-free PBS to remove debris, and opened up longitudinally to expose luminal surface. A glass coverslip was then gently applied to scrape off villi, and the tissue was cut into 2-3 mm fragments. Intestinal tissues were then washed again with cold PBS and incubated with 2.0mM EDTA for 45 minutes on a rocking platform at 4°C. EDTA solution was then decanted without disturbing settled intestinal fragments and replaced with cold PBS. In order to release intestinal crypts in solution, a 10 mL pipette was used to vigorously agitate tissues. The supernatant was collected and this process was repeated several times to harvest multiple fractions. The

crypt fractions were then centrifuged at 6,000 RPM for 5 minutes. Based on microscopic examination, the appropriate enriched crypt fractions were pooled and centrifuged again to obtain a crypt-containing pellet. Advanced DMEM/F12 (Life Technologies) containing Glutamax (Life Technologies) was used to resuspend the cell pellet and subsequently a 40um filter was used to purify crypts. Next, single cell dissociation was achieved by incubating purified crypt solution at 37°C with 0.8 KU/ml DNase (Sigma), 10 uM ROCK pathway inhibitor, Y-27632 (Sigma), and 1 mg/mL Trypsin-EDTA (Invitrogen) for 30 minutes. Single cells were then passed again though a 40um filter and resuspended in cold PBS with 0.5% BSA for FACS analysis to collect LGR5-EGFP+ intestinal stem cells (ISCs), which are also called crypt base columnar (CBC) cells.

Single LGR5-EGFP+ CBCs were suspended in Matrigel (BD Biosciences) at a concentration of 1000 cells or crypts/mL and 50ul Matrigel drops were seeded per well on pre-warmed 24-well plates. Matrigel polymerization occurred at 37°C for 10 minutes, and was followed by the addition of complete media to each well. ISC media included the following: Advanced DMEM/F12 supplemented with Glutamax, 10mM HEPES (Life Technologies), N2 (Life Technologies), B27 without vitamin A (Life Technologies), and 1 uM N-acetylcysteine (Sigma). Growth factors were freshly prepared each passage in an ISC media solution containing 50ng/mL EGF (Life Technologies), 100ng/mL Noggin (Peprotech), and 10% R-SPONDIN1 conditioned media (generated in house). The addition of growth factors occurred every 2 days and the media was fully replaced every 4 days. Organoids were passaged once per week at a ratio of 1:4 by removing organoids from Matrigel with ice-cold PBS. Next, organoids were incubated on ice for 10 minutes followed by mechanical disruption, centrifugation, and resuspension in fresh Matrigel.

For *in vitro* studies, organoids derived from single LGR5-EGFP ISCs were treated with one of the following: DMSO or 10uM DAPT (EMD Millipore) added to the media for 48 hours (Sikandar, Pate et al. 2010), or 1uM JAG-1 (AnaSpec) embedded in Matrigel for 48 hours (Takeda, Jain et al. 2011). EDTA was added to ISC media (for a final concentration of 0.5mM EDTA) to treat organoids for 4 hours. Subsequently, organoids were harvested and analyzed by FACS to isolate LGR5-EGFP cells and Paneth cells for RT-PCR or protein analysis. FACS was conducted using a Beckman Coulter flow cytometer

with a 40um filter. Data analysis was performed using FlowJo software to gate populations according to 7-AAD viability, and forward and side scattering. Cutoff thresholds were provided by unstained ISCs and single stained ISCs when using multiple fluorochromes in order to achieve appropriate compensation.

CRISPR/Cas9 genomic editing

The procedure for CRISPR/Cas9-mediated transfection in mouse ISC organoids has been previously described (Schwank, Koo et al. 2013). Briefly, guide RNA (gRNA) sequences were designed by Optimized CRISPR Design tool (http://crispr.mit.edu), and CRISPR/Cas9 plasmids including gRNA sequences were purchased from GenScript. For murine experiments gRNAs targeting the NICD binding motif on Notch1 included the following: gRNA1: (TACATGCATGGAAGGTGCGT) or gRNA2: (GTACATGCATGGAAGGTGCG) and were cloned into a pGS-gRNA-Cas9-Puro vector backbone. A pGS-CAS9-PURO only vector (no gRNA) was used as a control. Single sorted LGR5-EGFP+ ISCs were transfected using Lipofectamine-2000 (Life Technologies) according to the manufacturer's instructions. Briefly, 4uL Lipofectamine-2000 (diluted in 50uL Opti-MEM) and 2ug of CRISPR/Cas9 plasmids (diluted in 50uL Opti-MEM) were mixed 1:1: and incubated for 5 minutes at room temperature. Lipofectamine/DNA complexes were then added to single LGR5-EGFP+ ISCs (50uL/well) in a 24-well plate, which was subsequently centrifuged for 1 hour and incubated at 37C for 4 hours. ISCs were then resuspended in Matrigel and overlaid with ISC media (as prepared above) and supplemented with Y-27632 for 48 hours. Next, transfected ISCs were selected in media (without R-SPONDIN) containing 300ng/uL Puromycin for 72 hours. Selection media was then replaced with ISC media and organoids were monitored for 15 days followed by FACS analysis or co-immunofluorescence. Individual CRISPR/Cas9-mutated organoid clones were also harvested and lysed for DNA extraction using a QIAmp DNA Mini kit (Qiagen: 51304) according to the manufacturer's instructions. Subsequently, the NICD binding site on mouse Notch1 was amplified by PCR using the following primers (Forward: AGAAGAGAAGACAGGAGAAGGA and Reverse: GAAGCCACTGACTTTCCTAGAG) and analyzed by Sanger sequencing to visualize mutations. CRISPR/Cas9-mutated organoids derived from single

transfected LGR5-EGFP ISCs were also treated for 48 hours with DAPT or JAG-1 (as described earlier) before harvesting cells for FACS to isolate LGR5-EGFP+ cells for RT-PCR analysis.

In order to study Notch signaling dynamics, a RBPJk-dsRed reporter on a pGA981-6 vector backbone (Addgene #47683) was transfected into single wild-type or CRISPR/Cas9-mutated sorted LGR5-EGFP ISCs using Lipofectamine-2000 according to the protocol described above. ISCs were then treated for 48 hours with 10uM DAPT or 1uM JAG-1 and analyzed by microscopy and flow cytometry for LGR5-EGFP and RBPJk-dsRed expression.

Mouse organoids derived from single wild-type or CRISPR/Cas9-mutated ISCs were also subjected to single cell multi-photon laser ablation. Single cells in wild-type organoids were targeted based on LGR5-EGFP expression. CRISPR/Cas9-mutated organoids were incubated with Hoechst-33342 dye (Life Technologies) to target single cells. The organoid imaging and laser ablation were performed using ZEISS Inverted LSM880 (i880) laser scanning confocal microscope with full confocal and multiphoton capability. The i880 system is integrated with a heated chamber with CO_2 and humidity regulation. The temperature was controlled at 37°C, and concentration of CO_2 was kept at 5% through the imaging periods. A X10 0.3 NA objective lens was used for imaging, and 780nm 2-photon laser was used for targeting single-cell ablation. Time-lapse imaging series was used to analyze organoid dynamics pre- and post-ablation.

Isolation of Single Cells from Human Colonic Tissue

Approval for this research protocol was obtained from IRB committees at Weill Cornell Medical College and NY Presbyterian Hospital. Patients undergoing colorectal surgery provided written informed consent for use of human tissues. Material was derived from proximal colonic tissue during surgical biopsies. The procedure for isolation of colonic stem cells and organoid culture are previously described (Jung, Sato et al. 2011). Briefly, colonic specimens were collected and incubated in Advanced DMEM/F12 supplemented with gentamycin (Life Technologies) and fungizone (Life Technologies). Extraneous muscular and sub-mucosal layers were removed from colonic mucosa. The tissue was cut into 1 cm fragments and incubated with 8mM EDTA for 1 hour on a rocking platform at 37°C followed by a 45

minute incubation at 4°C. The supernatant was replaced with Advanced DMEM/F12 supplemented with Glutamax, HEPES, and 5% FBS. Vigorous shaking released crypts, which were collected in several fractions. Crypt fractions were then centrifuged (400 RPM, 5 minutes) and visualized by microscopy to determine which enriched fractions to combine. Subsequently, pooled crypt fractions were centrifuged and resuspended in Advanced DMEM/F12 supplemented with Glutamax, HEPES, N-2, B-27 without vitamin A, 1 mM N-Acetyl-L-cysteine, Nicotinamide (Sigma), 10 **μ**M Y-27632, 2.5 **μ**M PGE2 (Sigma), 0.5 mg/ml Dispase (BD Biosciences), and 0.8 KU/ml DNAse I. Cells were then incubated for 15 min at 37°C followed by mechanical disruption and passage of cell solution through 40um filter to obtain a single cell suspension.

Human Colon Organoid Culture

Single human colon cells were stained with EPHB2 (conjugated to PE), OLFM4 (conjugated to APC), EpCAM-FITC and 7-AAD according to standard protocols and were suspended in cold PBS with 0.5% BSA for FACS analysis. FlowJo software was used to gate populations according to 7-AAD viability, and forward and side scattering. Cutoff thresholds were provided by unstained ISCs and single stained ISCs when using multiple fluorochromes in order to achieve appropriate compensation. $EPHB2^{high}OLFM4^{high}$ colon stem cells were harvested, and subjected to lipotransfection of CRISPR/Cas9 plasmids using lipofectamine-2000 in a similar method as described earlier for mouse ISCs. CRISPR/Cas9 gRNAs targeting the NICD binding motif of human Notch1 (cloned into a pGS-gRNA-Cas9-Puro vector backbone) were designed and ordered from Genscript with the following inserted gRNA sequences: (gRNA1: TGCTTTTGGGGGATCCGCGT, gRNA2: CACTGCGGGAATTTCCCACG). A pGS-CAS9-PURO only vector (no gRNA) was used as a control. Transfected human colon stem cells were selected in medium lacking WNT-3A, and R-SPONDIN1 and containing Y-27632 and 300 ng/ul puromycin for 48 hours.

Subsequently, transfected cells were suspended in Matrigel, and overlaid with human colon stem cell medium containing Advanced DMEM/F12 supplemented with Glutamax, HEPES, N-2, B-27 without vitamin A, 1 mM N-Acetyl-L-cysteine, Nicotinamide, PGE2, Y-27632, human Noggin (Peprotech),

human EGF (Life Technologies), Gastrin (Sigma), TGF-ß type I Receptor inhibitor A83-01 (Tocris), P38 inhibitor SB202190 (Sigma-Aldrich), WNT3A-conditioned media (generated in house) and R-SPONDIN1 conditioned medium (generated in house) (Jung, Sato et al. 2011). For organoid culture, full medium was replaced every 2 days. Transfected organoids were monitored for 14 days and then harvested and analyzed by FACS to isolate EPHB2^{high}OLFM4^{high} colon stem cells for RT-PCR and protein analysis. Individual CRISPR/Cas9-mutated organoid clones were also harvested and lysed for DNA extraction using a QIAmp DNA Mini kit (Qiagen: 51304) according to the manufacturer's instructions. Subsequently, the NICD binding site on human Notch1 was amplified by PCR and analyzed by Sanger sequencing to visualize mutations.

Quantitative RT-PCR and Protein Analysis

Total RNA from mouse ISCs or human colon stem cells was extracted using a Qiagen RNeasy Plus kit. Subsequently, isolated RNA was reverse transcribed to cDNA using ABI Taqman Reverse Transcription kit (Applied Biosystems). ABI Taqman Master mix and ABI Prism HT7900 were used to run quantitative real-time PCR. Taqman primers (ABI) purchased from Life Technologies were used for the following mouse genes: Notch1 (Product ID: Mm00627185_m1), Notch2 (Product ID: Mm00803077_m1), Hes1 (Product ID: Mm01342805_m1), Hes5 (Product ID: Mm00439311_g1), Dll1 (Product ID: Mm01279269_m1), Dll4 (Product ID: Mm00444619_m1), Jag1 (Product ID: Mm00496902_m1), Atoh1 (Product ID: Mm00476035_s1), Lgr5 (Product ID: Mm00438890_m1). Human Taqman primers purchased from Life Technologies include: Notch1 (Product ID: Hs01062014_m1), Notch2 (Product ID: Hs01050702_m1), Hes1 (Product ID: Hs00172878_m1), Hes5 (Product ID: Hs01387463_g1), Lgr5 (Product ID: Hs00969422_m1), and Olfm4 (Product ID: Hs00197437_m1). RT-PCR analysis represents the average of three independent experiments normalized to GAPDH expression. Error bars designate S.E.M. Protein extraction from mouse ISCs or human colon stem cells and western blotting were performed as previously described. β-actin was used as a control for normalization (Pan, Sikandar et al. 2008).

ChIP-PCR

Mouse intestinal and human colonic organoids were harvested and ChIP-PCR was performed according to manufacturer's instructions (EMD Millipore: 17-408). Briefly, normal rabbit IgG was used as a negative control while rabbit anti-Acetyl Histone H3 was used as a positive control for immunoprecipitation (IP). Subsequently, primer pairs specific for human or mouse GAPDH sequences were for positive PCR controls. Following IP using anti-mouse NICD, PCR primers (Forward: AGATGAAGGTGGAGCATGTG, Reverse: TTTTCCCACGGCCTAGAAG) were used for amplification of Notch1. Similarly, for ChIP assays involving anti-human NICD, PCR primers (Forward: ACTAGGTGTCACCAAAGTGC, Reverse: CATGACCATCTTGGCCTCTC) were used to amplify Notch1. Sanger sequencing was used to validate NICD binding motif on Notch1 for PCR products. Subsequently, ChIP-qPCR analyses were performed according to the manufacturer's instructions (ActiveMotif: 53029).

Immunofluorescence

Intestinal tissues from Tamoxifen-induced Notch1- and Notch2- (tdTomato) reporter mice were harvested at various time points, fixed with 4% PFA, snap-frozen in O.C.T, cryo-sectioned and visualized on a Zeiss LSM 510 laser scanning confocal microscope. DAPI was used as a nuclear counterstain. For *in vitro* imaging, wild-type or CRISPR/Cas9-mutated intestinal organoids derived from LGR5-EGFP mice were embedded in Matrigel on glass chamber slides. Cells were fixed for 15 minutes at room temperature using 4% PFA and rinsed three times with PBS. 0.2% Triton X-100 was used for permeabilization of cell membranes. Next, cells were incubated in a serum-free blocking solution (Dako) for 30 minutes. For co-immunofluorescence staining, an antibody diluent solution (Dako) was used to prepare primary and secondary antibodies. Primary antibodies were added overnight at room temperature followed by application of Alexa-flour 488/555 secondary antibodies for 1 hour. Organoids were visualized using Lysosyme (LYZ) and LGR5 (detected by GFP) expression. DAPI (Life Technologies) was as a nuclear counterstain on a Zeiss LSM 510 laser scanning confocal microscope using an Apo 40Å~ 1.40 oil objective.

Statistical Analysis

The data is displayed as mean ± S.E.M. Statistical comparisons between two groups was made using Student t-test. $P < 0.05$ was used to establish statistical significance.

Computational Modeling

The deterministic model was constructed and simulated in Matlab, and the systems dynamics analysis was solved by numerical optimization in Matlab. The 3D stochastic crypt model was designed and simulated based on the Glazier-Graner-Hogeweg (GGH) computational model using Compucell3D(Swat, Thomas et al. 2012). A supporting layer covered by a single-cell layer of epithelial cells was designed to mimic the finger-like shape of intestine crypts. All *in silico* epithelial cells inherited an effective energy function programmed in the CGH's cell-lattice configuration to have the desired cell prosperities, behaviors, and interactions. The epithelial cells were programmed to possess the essential cellular prosperities including: 1. cell growth, 2. cell divisions, 3. cell-cell adhesion, and 4. anoikis (when epithelial cells detach from supporting layers). In addition, a module of SBML (Systems Biology Markup Language) solver was applied to integrate the Notch signaling models (LI, PFLI) programmed in SBML(Hucka, Finney et al. 2003) format to every epithelial cell at the bottom of the crypt. Notch signaling and stochastic cellular dynamics were simulated simultaneously in the combined model. A Notch signaling threshold was assigned to determine $Notch^{high}$ (stem) cells and $Notch^{low}$ (Paneth) cells at the crypt bottom. $Notch^{high}$ cells were programmed to actively grow and divide when their cell volume reached division threshold, while $Notch^{low}$ cells were programmed to neither grew nor divide to mimic differentiated Paneth cells. These cells naturally migrate upward to leave the bottom of the crypt with the force generated by the growing and dividing cells at the crypt base. R was used to analyze and plot the statistical results.

5.4 Result

5.4.1 In Vivo Imaging And Laser Ablation of Crypt Base

To understand how the niche spatiotemporally maintains homeostasis, we need to observe its actions *in vivo*. An abdominal window for intravital microscopy has been previously demonstrated, and the organ of interest was glued to the coverslip on the window for imaging (Ritsma, Steller et al. 2012, Ritsma,

Ellenbroek et al. 2014). Because adherence by glue often causes substantial inflammation, lethal intestinal obstruction, and detachment from the window due to intestinal peristalsis, we replaced the glue with a 3D printed, biocompatible scaffold insert, which was designed to stabilize the intestine and minimize its movement without blocking its motility functions (Fig. 5.1a). The scaffold was first sutured to the skin, and a portion of the small intestine was then positioned beneath the abdominal window. The mice live normally for months carrying the window and scaffold. Furthermore, replacing the glue with the scaffold allowed us to design an openable window, through which staining dye and small molecule inhibitors could be locally administered throughout the experiment (Fig. 5.1b). Vasculature was labeled with an injection of FITC or Texas-red dextran. These vessels were stable over weeks, enabling them to be used as a roadmap to identify and image the same areas repeatedly (Supplementary Fig. S5.1a). Imaging LGR5-EGFP mice(Barker, van Es et al. 2007) showed the mosaic stem cell niche pattern at the crypt base, where LGR5+ CBCs fluoresce green while Paneth cells appear dark (Fig. 5.1c). This LGR5-GFP pattern in the niche appears to be stable, with little change after a day (Supplementary Fig. S5.1b).

To understand how precisely the niche is regulated, we wanted to observe its response to loss of individual cells. This level of spatial specificity is difficult to achieve by current methods of radiation, chemical treatment, or genetic ablation, which either cause massive damage or wipe out entire lineages. We therefore designed and built a custom two-photon excited fluorescence (2PEF) microscope integrated with a low-repetition-rate, high-pulse-energy femtosecond (fs) laser, which is capable of penetrating the intestinal wall to reach the epithelium facing the lumen (Fig. 5.1d). In order to ablate a cell of choice, one or two 50-fs pulses is delivered from a Ti:Sapphire regenerative amplifier (800-nm wavelength, 1-kHz repetition rate) to the target while the surrounding region is continuously monitored. Incident pulse energy is adjusted to provide an estimated 50-100 nJ at the focus. Because the damage is mediated by an electron-ion plasma formed by nonlinear optical absorption in a process called photodisruption, there is very little thermal energy deposited(Schaffer, Nishimura et al. 2002). As a result, the damage is largely confined to the focal volume(Nishimura, Schaffer et al. 2006) (Supplementary Fig.S1c).

We redesigned the abdominal frame to install an openable window as aforementioned. This new capability enabled us to locally administer Hoechst dye through the window to stain cell nuclei, and then close the window for imaging and laser ablation. We first targeted an LGR5-EGFP+ CBC in the intestinal stem cell niche. The GFP signal of the targeted cell quickly dissipated, while GFP signals from neighboring CBCs remain unperturbed. The nucleus of the targeted cell disappeared between 10-30 minutes (Fig. 5.1e). Disappearance of the nucleus was also observed when a Paneth cell was targeted by the laser (Supplementary Fig. S5.1d). The nuclear and LGR5-EGFP pattern remains stable in untargeted crypts (Supplementary Fig. S5.1e).

5.4.2 Niche Cells Rearrange After Ablation

We previously expected that the void created by ablation of a CBC would be later filled by division of a neighboring CBC, which takes 24~48 hours to complete(Barker, van Es et al. 2007). This expectation arose from an assumption that the mosaic CBC/Panetch cell pattern is largely fixed based on a "blueprint" provided by the underlying lamina propria. However, time-lapse images after ablation suggest that the niche is rather dynamic, with adjacent CBCs expanding and surrounding cells rearranging within an hour (Fig. 5.1e). In contrast, niches in neighboring crypts without laser ablation remain unperturbed, confirming that the dynamic rearrangement was in response to the loss of the ablated cell (Supplementary Fig. S5.1f).

A more systematic ablation/imaging study found that cells in proximity consistently rearrange to fill the void after ablation of a CBC or Paneth cell, and the mosaic configuration is somewhat restored after an hour or two. With further adjustments, the niche appears normal a day later, although the pattern does not look identical to the one before ablation. (Fig. 5.1f, Supplementary Fig.S5.1g). Remarkably, the niche also reshuffles rather quickly to restore the spatial configuration even when multiple CBCs or Paneth cells are ablated (Fig. 5.1f). A day later, the niche again appears normal but different from the one before ablation, suggesting that its configuration does not rely on a fixed blueprint –rather—it probably depends on local cell-cell contact and communication.

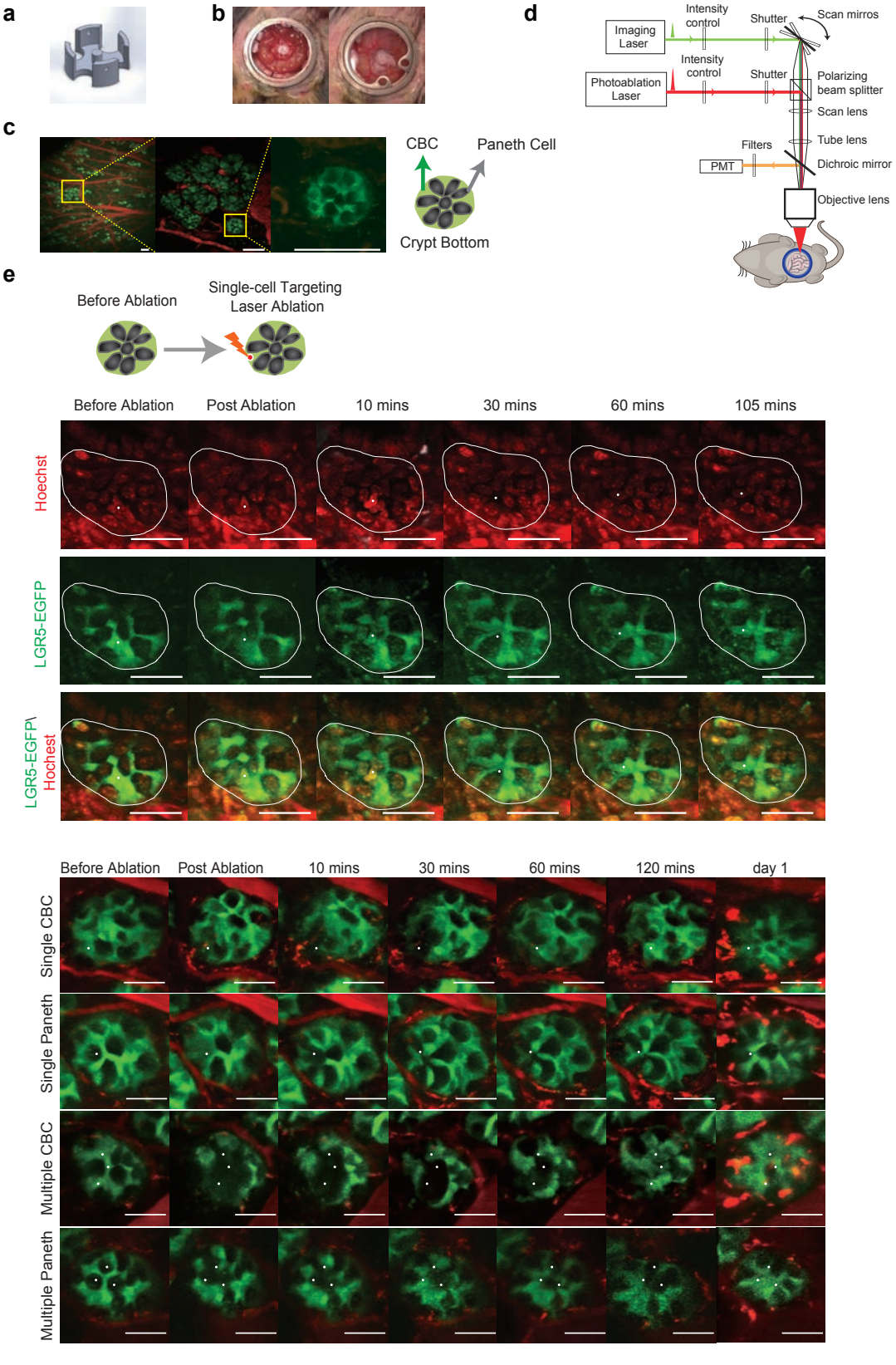
a
b
c
d
e
f
CBC
Paneth Cell
Crypt Bottom
Imaging Laser
Intensity control
Shutter
Scan mirros
Photoablation Laser
Polarizing beam splitter
Scan lens
Filters
Tube lens
PMT
Dichroic mirror
Objective lens
Before Ablation
Single-cell Targeting Laser Ablation
Post Ablation
10 mins
30 mins
60 mins
105 mins
Hoechst
LGR5-EGFP
LGR5-EGFP\ Hochest
120 mins
day 1
Single CBC
Single Paneth
Multiple CBC
Multiple Paneth

Figure 5.1. Imaging And Laser Ablation Of The Intestinal Stem Cell Niche.

(a) *Design of the 3-D printed intestinal scaffold.* ***(b)*** *Images of an open (left) and a closed (right) abdominal window.* ***(c)*** *Representative images of crypts and vasculature at low (left), intermediate (middle) and high (right) magnification. Green, CBCs in LGR5-EGFP mice. Red, vasculature labeled by Texas-red dextran. Yellow, field of view magnified in each subsequent panel. Also shown is a cartoon of a crypt bottom. (Scale bar: left: 150 μm, middle, right: 50 μm).* ***(d)*** *Schematic illustrating the in vivo multiphoton imaging and laser ablation setup.* ***(e)*** *Time-lapse images following laser ablation. Nuclei were stained by Hoechst dye. GFP signal in the ablated cell dissipated right away, and the nucleus of the ablated cell disappeared between 10 and 30 minutes. White dot marks the target position of laser focus. Scale bar: 30 μm.* ***(f)*** *Time-lapse series following laser ablation of single or multiple CBCs or Paneth cells. Crypts were continuously monitored for 2 hours (120 minutes) post ablation, and imaged again after approximately 24 hours. Green, GFP signaling from LGR5+ CBCs. Red, vasculature labeled by Texas-red dextran. White dots mark the target positions of laser focus. Scale bar: 30 μm.*

5.4.3 Notch Signaling In The Niche

Paneth cells provide niche factors including epidermal growth factor (EGF), Wnt ligands (WNT3A), Notch ligands, and bone morphogenetic protein (BMP) inhibitor Noggin to support CBC stem cell self-renewal, while pericryptal stromal cells underneath the niche also supply additional Wnt ligands (WNT2B)(Barker 2014). Regulation of the niche is certainly a concerted effort involving various such signaling pathways. For proof-of-principle, we first focused on the role of Notch signaling, a juxtacrine signaling pathway linked to developmental patterning(Artavanis-Tsakonas, Rand et al. 1999, Kopan and Ilagan 2009). Notch signaling is mediated through direct cell-to-cell contact of membrane-bound Notch ligands on one cell and trans-membrane Notch receptors on adjacent cells. The extracellular domain of Notch receptors binds Notch ligands, which activates receptor cleavage that releases the Notch receptor intracellular domain (NICD) to translocate to the nucleus. NICD interacts with the DNA-binding protein RBPJk to activate expression of downstream genes, such as the HES family transcription factors.

Notch signaling is essential for intestinal stem cell self-renewal and crypt homeostasis (Fre, Huyghe et al. 2005, van der Flier and Clevers 2009). Among Notch receptors, inhibition of both Notch1 and Notch2 completely depletes proliferative stem/progenitor cells(Riccio, van Gijn et al. 2008). Inhibition of Notch1 alone is sufficient to cause a defective intestinal phenotype, while inhibition of Notch2 alone causes no significant phenotype(Wu, Cain-Hom et al. 2010). Notch3 and Notch4 are not expressed in the intestinal epithelium(Fre, Hannezo et al. 2011). Among Notch ligands, DLL1 and DLL4 are essential and function redundantly, and inactivation of both causes loss of stem and progenitor cells; in contrast, JAG1 is not essential(Pellegrinet, Rodilla et al. 2011).

To examine the effect of Notch inhibition on the niche in real-time, DBZ, a γ-secretase inhibitor that prevents Notch receptor cleavage, was locally injected into the submucosal layer of the target intestinal region through the openable window prior to imaging. DBZ steadily degraded GFP signals in CBCs and blurred the pattern until GFP signals were hardly detectable in the niche 24 hours later, while the vasculature remained largely intact (Supplementary Fig. S5.1h, S5.1i). Therefore, Notch signaling is important for maintaining the LGR5-EGFP pattern in the niche.

5.4.4 Notch Lateral Inhibition And Positive Feedback

In the niche, Paneth cells express lysozyme and CD24(Sato, van Es et al. 2010) (Fig. 5.2a). Using an established protocol(Sato, van Es et al. 2010), we isolated LGR5-EGFP+ CBCs and CD24+ Paneth cells from mouse intestinal organoid culture (Supplementary Fig. S5.2a). Immunofluorescence (IF) confirmed that the sorted CD24+ Paneth cells express lysozyme (Supplementary Fig. S5.2b). Notch receptors (Notch1, Notch2) and signaling effectors (Hes1, Hes5) are enriched in CBCs, while Notch ligands (Dll1, Dll4, Jag1) and the secretory lineage regulator, Atoh1(Yang, Bermingham et al. 2001), are enriched in Paneth cells (Fig. 5.2b). Inhibition of Notch receptor cleavage by the γ-secretase inhibitor DAPT significantly up-regulated ligand expression, indicating that activated Notch signaling suppresses ligand expression (Fig. 5.2c, d). This is consistent with classic lateral inhibition (LI), where ligands on a ‘sender’ cell (in this case, Paneth cell) activate receptors on a ‘receiver’ cell (in this case, CBC), which, in turn, suppresses ligand expression in the receiver cell(Collier, Monk et al. 1996). This intercellular feedback

scheme causes bifurcation between adjacent cells, resulting in two opposite Notch signaling states (Fig. 5.2e).

Additionally, Notch activation by recombinant JAG1(Yamamura, Yamamura et al. 2014) or EDTA(Rand, Grimm et al. 2000) significantly increased receptor (Notch1/2) expression, while DAPT significantly reduced receptor expression (Fig. 5.2c, d). This suggests the existence of a positive feedback loop, where activated Notch receptors up-regulate their own expression (Fig. 5.2e). To validate that the positive feedback loop acts via NICD, the cleaved and activated intracellular domain from the Notch1 receptor, we crossed a LGR5-EGFP strain with a Rosa26-YFP-NICD strain(Fre, Hannezo et al. 2011) to generate a Tamoxifen-inducible LGR5-EGFP-CreERT2 x Rosa26-YFP-NICD (NICD-OE) mouse strain. In derived organoids, Tamoxifen-induced NICD up-regulated Notch receptor expression, while DAPT suppressed receptor and up-regulated Notch ligand expression (Supplementary Fig. S5.2c, S5.2d). Therefore, NICD activates expression of Notch receptors, forming a positive autoregulation loop.

5.4.5 NICD Directly Activates Notch1 Transcription

Although both Notch1 and Notch2 form positive autoregulation, Notch1 has a stronger response than Notch2 (Fig. 5.2d and Supplementary Fig. S5.2c). This is consistent with previous reports showing that Notch1 and Notch2 are somewhat functionally redundant, but Notch1 is more critical to stem cell self-renewal and crypt homeostasis while Notch2 is dispensable(Wu 2010). To delineate how Notch1 and Notch2 correlate with CBC functions in the niche, we performed lineage tracing using Tamoxifen-inducible $Notch1^{CreER}$ x $ROSA26^{tdTomato}$ and $Notch2^{CreER}$ x $ROSA26^{tdTomato}$ transgenic mouse reporter strains(Fre, Hannezo et al. 2011, Oh, Lobry et al. 2013). After induction, labeled Notch1+ cells showed a similar pattern that largely overlaps with CBCs in the niche (Fig. 5.2f). From Day 1 to Day 3, marked progeny of Notch1+ cells expanded out of the niche and overtook the trans-amplifying (TA) progenitor compartments; by Day 30, the marked clones of the original Notch1+ cells replaced the entire epithelium (Fig. 5.2g, Supplementary Fig. S5.2e). In contrast, labeled Notch2+ cells and their clones were much fewer and more sporadic (Supplementary Fig. S5.2e). These lineage tracing experiments confirmed that Notch1 are more active in CBCs and more critical to crypt regeneration than Notch2, which is consistent

with previous findings(Wu 2010, Fre, Hannezo et al. 2011, Pellegrinet, Rodilla et al. 2011, Oh, Lobry et al. 2013).

We analyzed the LICR ChIP-Seq dataset of mouse small intestinal cells from ENCODE using the UCSC genome browser(Consortium 2012) to investigate regulation of Notch1 and Notch2 transcription. The 2nd intron region of the Notch1 gene is highly enriched with enhancer Histone marks H3K4me1 and H3K27ac(Hon, Hawkins et al. 2009, Bonn, Zinzen et al. 2012, Shlyueva, Stampfel et al. 2014), while no such regions were found in the Notch2 sequence (Supplementary Fig. S5.3a). Computational analysis of this region with MotifMap(Wang, Zang et al. 2014) predicted a putative binding motif for RBPJk, the DNA-binding protein that forms an effector complex with NICD to activate Notch signaling. A unique 8 base pair sequence (TTCCCACG, Chr2: 26,349,981-26,349,988) was identified (Fig. 5.3a). ChIP-PCR shows that NICD binds to this sequence in CBCs, and the binding was enhanced by JAG1 activation of receptors and suppressed by DAPT inhibition of receptor cleavage (Fig. 5.3b). Similarly, ChIP-PCR analysis of Tamoxifen-induced NICD-OE intestinal cells (from NICD-OE mice) also showed elevated NICD binding compared to uninduced control (Supplementary Fig. S5.3b). Therefore, the NICD/RBPJk complex interacts with this sequence motif.

We next designed CRISPR-Cas9 vectors targeting the NICD binding sequence (Supplementary Fig. S5.3c). CRISPR/Cas9 vectors with specific guide RNAs (gRNAs) were transfected into single LGR5-EGFP CBCs, which were subsequently propagated as organoids. Sequencing results indicate the presence of indels in the target NICD binding region formed through Non-Homologous End Joining (NHEJ) (Supplementary Fig. S5.3d). The mutated binding motif significantly reduced NICD binding compared to the empty vector (EV) control in CBCs sorted from organoids treated with DMSO (control), JAG1, or DAPT, according to ChIP-qPCR (Supplementary Fig. S5.3e). The mutations also significantly decreased Notch1 transcript levels measured by RT-qPCR (Supplementary Fig. S5.3f) and NICD levels measured by Western blot (Supplementary Fig. S5.3g). Expression levels of Notch signaling components (Notch1, Notch2, Hes1, Hes5) and LGR5 all decreased in CRISPR/Cas9-targeted cells with the mutated binding motif (Supplementary Fig. S5.3h). Taken together, the data suggest that, when Notch receptors are

activated, the resulting NICD/RBPJk complex bind to the Notch1 gene and enhances its transcription, hence producing more Notch1 receptors and forming a positive feedback in stem cells.

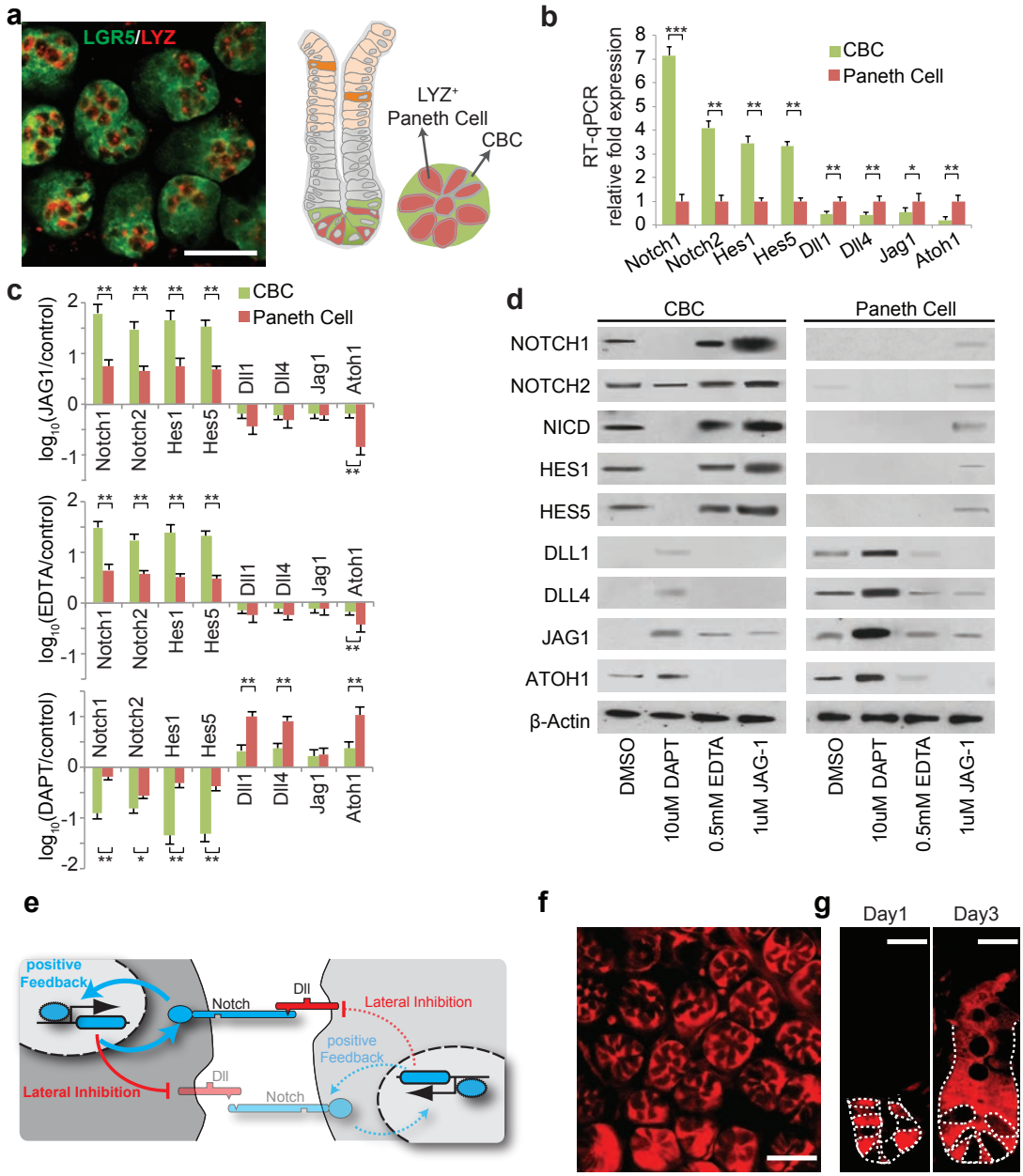

Figure 5.2. Notch Signaling In Niche Cells.

(a) *Left: Cross-sectional view of murine intestinal crypt bottoms with co-immunofluorescence (co-IF) showing intermingled LGR5-EGFP+ (green) CBCs and lysozyme+ (LYZ, red) Paneth cells. Scale bar: 50*

μm. Right: schematic illustration of a niche pattern in both longitudinal and cross sectional views of a crypt. ***(b)*** *RT-qPCR quantification of Notch signaling components in CBC and Paneth cell populations. The experiment was performed in triplicate and presented mean ± S.E.M. (***, p=0.001, **, p = 0.01, *, p=0.05; Student t-test).* ***(c)*** *RT-qPCR quantification of Notch signaling components in CBCs and Paneth cell populations after organoids were treated with JAG1 (top), EDTA (middle) or DAPT (bottom). The experiments were performed in triplicate and presented mean ± S.E.M. (**, p = 0.01, *, p=0.05; Student t-test).* ***(d)*** *Western blot analysis of Notch signaling components from conditions described in (c). Actin was used as a loading control.* ***(e)*** *Schematic illustration of lateral inhibition and positive feedback between neighboring cells. Transparent colors and dotted lines represent low expression/activity levels.* ***(f)*** *Representative IF image indicating Notch1 expression (red) in intestinal crypt bottoms of Tamoxifen-induced Notch1^{CreER} x Rosa26^{tdTomato} mice. Scale bar: 50 μm.* ***(g)*** *Representative IF images of intestinal crypts showing progeny of Notch1+ cells 1 day (left) and 3 days (right) after Tamoxifen induction in Notch1^{CreER} x Rosa26^{tdTomato} mice. Scale bar: 20 μm.*

5.4.6 Positive Feedback Is Critical To Self-Renewal, Niche Homeostasis And Recovery

To our knowledge, this positive feedback (PF) mechanism via direct NICD binding to the Notch1 gene has not yet been reported in other systems, despite extensive studies of Notch signaling. This raises the question as to its role in the stem cell niche and intestinal homeostasis. CRISPR mutation of the binding motif (PF KO) reduced colony-forming efficiency and growth rate of intestinal organoids markedly (Fig. 5.3c, 5.3d). Furthermore, the mutation significantly reduced the ratio of CBC to Paneth cells in the niche (Fig. 5.3c, 5.3e, Supplementary Fig. S5.3i).

Next, to understand how this positive feedback influences Notch signaling and cell fate, we transfected sorted LGR5-EGFP+ CBCs with an RBPJk-dsRED reporter as an indicator of Notch activity and grew them into organoids, followed by FACS analysis and time-lapse microscopy. Notch activation by JAG1 treatment hardly increased the Notch^{high}/LGR5^{high} (dsRed^{high}/GFP^{high}) CBC population in PF KO organoids in contrast to the empty vector control. On the other hand, Notch inhibition by DAPT depleted

Notch^{high}/LGR5^{high} CBCs more thoroughly in PF KO organoids than the empty vector control (Fig. 5.3f, Supplementary Fig. S5.4a). Therefore, the positive feedback amplifies the effect of Notch activation for stem cell renewal, and helps prolong stem cell fate when Notch signaling is disrupted.

We next investigated the role of the Notch1 positive feedback in maintaining the integrity of the CBC/Paneth cell niche in organoids using single-cell laser ablation. LGR5+ cells located in the budding arms of wild-type or PF KO organoids were selected for laser ablation. After ablation, we observed reorganization and recovery of the mosaic LGR5-EGFP pattern within 4 hours, and the pattern was still sustained after 10 hours in wild-type organoids (Fig. 5.3g, Supplementary Fig. S5.4b; Supplementary Movie 1). In contrast, PF KO organoids started with fewer LGR5-EGFP CBCs with dimmer signals, and was unable to recover from ablation of a single LGR5-EGFP CBC; strikingly, surrounding cells lost cell-cell attachments and the targeted budding arm eventually collapsed (Fig. 5.3g, Supplementary Fig. S5.4b; Supplementary Movie 2). These data demonstrate that direct Notch1 PF promotes stem cell self-renewal, maintains the mosaic niche configuration, and regulates its recovery.

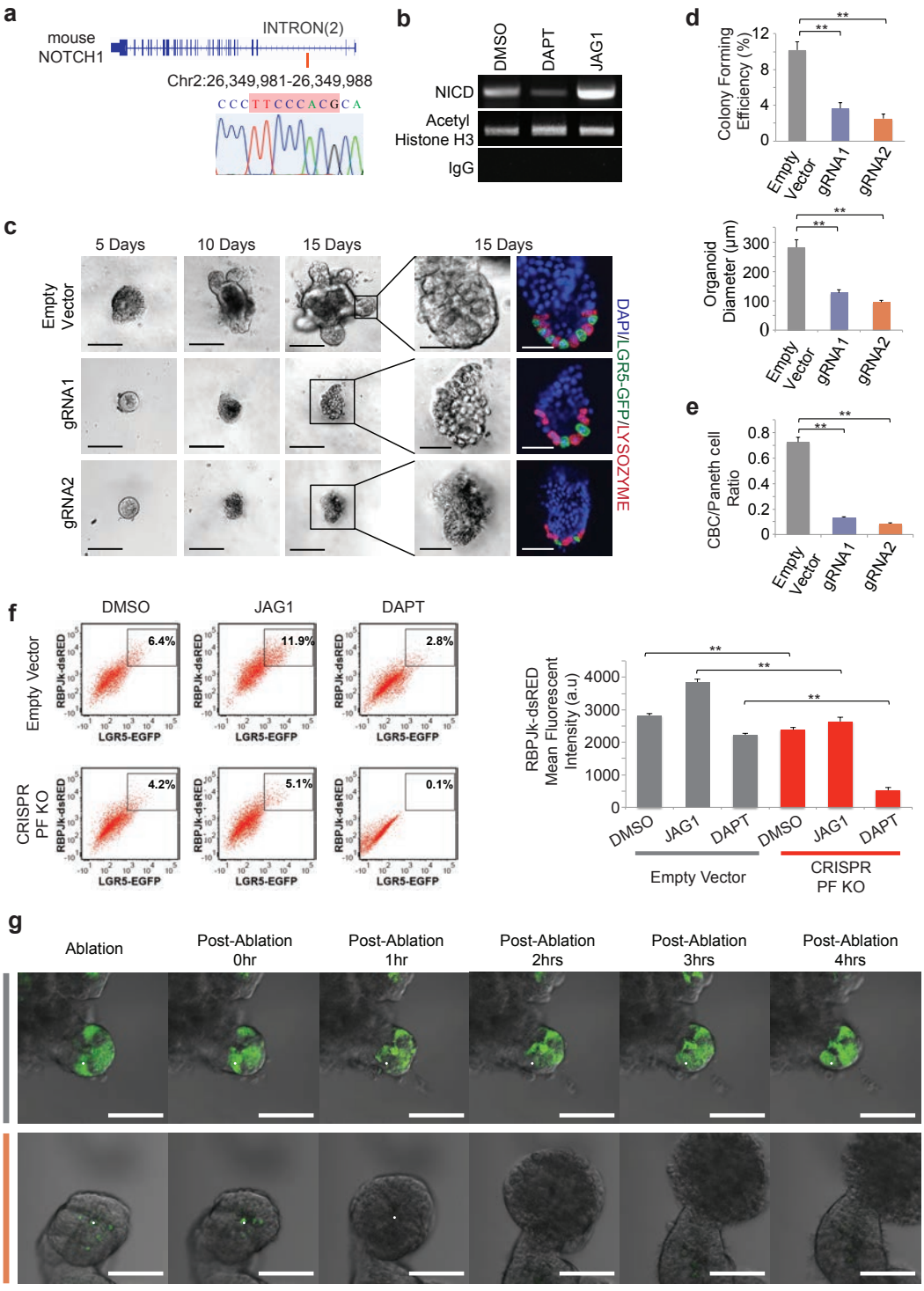

Figure 5.3. Notch1 Positive Feedback.

(a) *Top: Predicted sequence and location of putative NICD/RBPJk binding motif on Notch1. Bottom: Sequence and chromatogram of NICD binding motif in mouse Notch1 following ChIP-PCR from LGR5-*

EGFP+ CBCs. ***(b)*** *Agarose gel analysis of ChIP-PCR products from LGR5-EGFP+ CBCs validating NICD binding to the motif in Notch1 sequence. LGR5-EGFP+ CBCs were sorted from organoids treated with DMSO, DAPT or JAG1.* ***(c)*** *Single LGR5-EGFP+ CBCs were transfected with either an empty vector (control) or CRISPR/Cas9 gRNAs. Shown are representative brightfield images over 15 days and co-IF images indicating LGR5-EGFP (green) and LYZ (red) expression with DAPI nuclear staining. Scale bar represents 100 µm in low magnification and 25 µm in high magnification images, respectively.* ***(d)*** *Single LGR5-EGFP CBCs were transfected with either an empty vector (control) or CRISPR/Cas9 gRNAs. Top: Colony forming efficiency measured after 5 days. Quantitative analysis calculated from 1000 cells/replicated. The experiment was performed in triplicate and presented mean ± S.E.M. (**, p = 0.01; Student t-test). Bottom: Quantitative comparison of organoid diameters after 15 days. The experiment was performed in triplicate and presented mean ± S.E.M. (**, p = 0.01; Student t-test).* ***(e)*** *Single LGR5-EGFP ISCs were transfected with either an empty vector (control) or CRISPR/Cas9 gRNAs. Ratio of LGR5-EGFP+ CBCs/LYZ+ Paneth cells as determined by FACS analysis after 15 days. The experiment was performed in triplicate and presented mean ± S.E.M. (**, p = 0.01; Student t-test).* ***(f)*** *Single empty vector control or CRISPR/Cas9-postive feedback knockout (PF KO) LGR5-EGFP+ CBCs were transfected with an RBPJk-dsRed reporter construct and grown into organoids, which were subsequently treated with DMSO, DAPT or JAG1 for 48 hours. Left: Representative FACS plots for RBPJk-dsRED and LGR5-EGFP expression indicating a gated double positive fraction for each condition. Right: Mean fluorescence intensity (MFI) of RBPJk-dsRed expression. The experiment was performed in triplicate and presented mean ± S.E.M. (**, p = 0.01; Student t-test).* ***(g)*** *Wild-type or CRISPR/Cas9 PF KO CBCs propagated as organoids were subjected to single cell laser ablation. Shown are representative images pre- and post-ablation for 4 hours. White dots mark the target position of laser focus. Green: LGR5-EGFP. Scale bar: 50 µm.*

5.4.7 The Notch1 PF Motif Is Conserved In Human Colon Organoids

Like their mouse counterparts, human intestinal and colon epithelia also contain LGR5+ CBCs and are highly regenerative. A similar computational analysis of the human genome identified an analogous NICD/RBPJk binding region (TTCCCACG, Chr9: 139,425,108-139,425,115) located on the 2nd intron of the human Notch1 sequence (Fig. 5.4a), which also showed high enrichment of H3K4me1 and H3K27ac enhancer chromatin marks in several human cell lines (Supplementary Fig. S5.5a). We then derived human colon organoids using normal colon tissue in surgically resected specimens from colorectal cancer (CRC) patients(Sato, Stange et al. 2011). ChIP-PCR validated NICD binding on the predicted sequence (Fig. 5.4b) in human colon stem cells marked by EPHB2^{high}OLFM4^{high} expression(Jung, Sato et al. 2011). Consistent with mouse CBCs, NICD binding to the motif was suppressed by DAPT and enhanced by JAG1 treatment. We then designed CRISPR-Cas9 vectors to mutate the NICD/RBPJk binding motif in human colon stem cells (Supplementary Fig. S5.5b, S5.5c). ChIP-qPCR validated that the CRISPR/Cas9-mediated mutation reduced NICD binding to the motif in all three conditions (DMSO, JAG1, and DAPT), and prevented JAG1 treatment from increasing NICD binding (Supplementary Fig. S5.5d). Suppression of the Notch1 PF by the mutations (PF KO) significantly reduced organoid-forming efficiency, size of organoids, and the percentage of EPHB2^{high}OLFM4^{high} colon stem cells compared to empty vector control (Fig. 5.4c, 5.4d, 5.4e, Supplementary Fig. S5.5e). The epithelial cell identity of the EPHB2^{high}OLFM4^{high} cells was validated by their EpCAM expression (Supplementary Fig. S5.5e). Without the signal-amplifying Notch1 PF, colon stem cells had lower Notch1 transcript levels (Fig. 5.4f). Mutated colon stem cells also had lower expression levels of NICD, other Notch signaling components, and human colon stem cell markers (LGR5 and OLFM4) (Fig. 5.4g, 5.4h). In summary, the Notch1 PF promotes both mouse intestinal and human colon stem cells by amplifying and sustaining receptor activation.

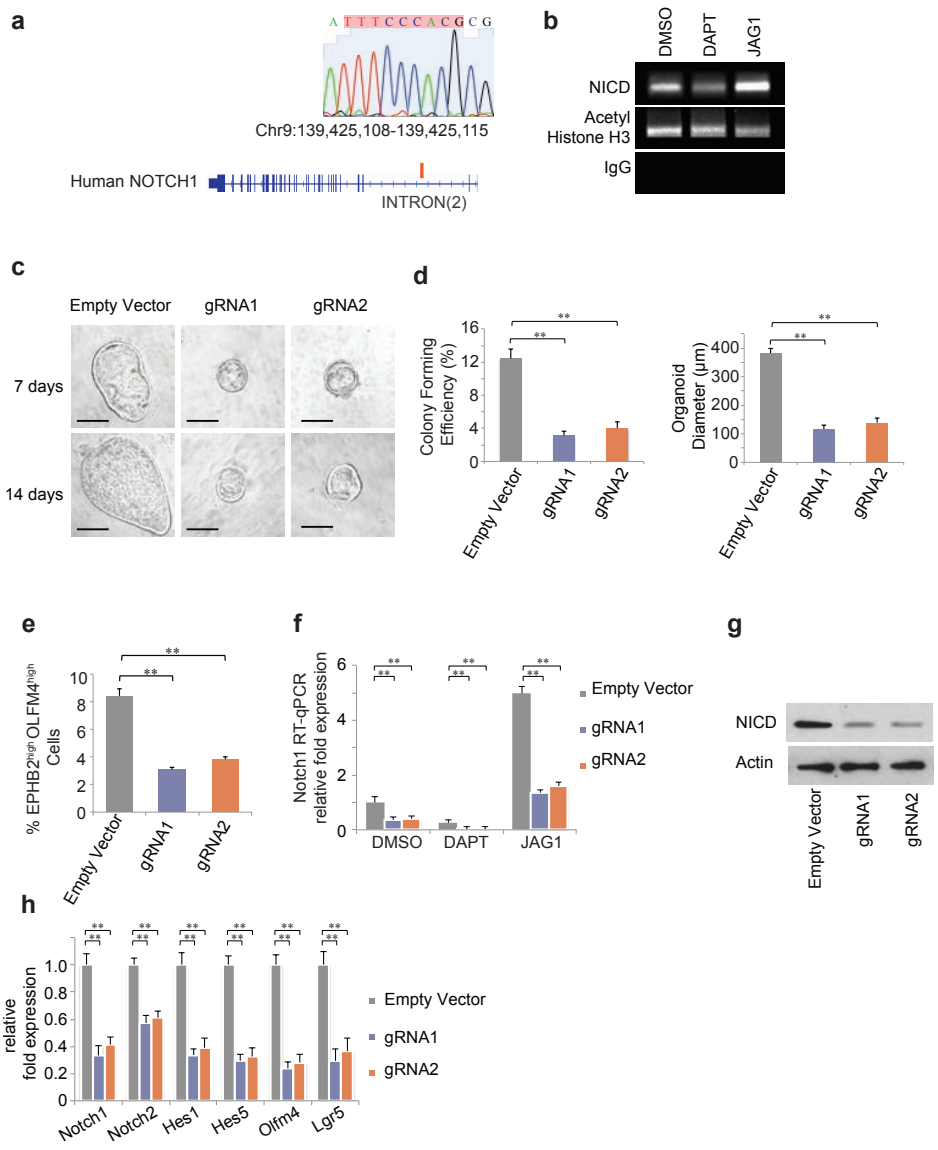

Figure 5.4. Notch1 Positive Feedback Is Conserved In Human Colon Organoids.

(a) *Top: Sequence and chromatogram of NICD binding motif to human Notch1 following ChIP-PCR from EPHB2^{high}OLFM4^{high} colon stem cells. Bottom: Predicted sequence and location of putative NICD binding motif on human Notch1.* ***(b)*** *Agarose gel analysis of ChIP-PCR products indicating active binding of NICD to the motif in Notch1 sequence in EPHB2^{high}OLFM4^{high} colon stem cells treated with DMSO, DAPT, or JAG1.* ***(c)*** *Representative brightfield images of organoids derived from single EPHB2^{high}OLFM4^{high} colon stem cells transfected with either an empty vector control or CRISPR/Cas9 gRNAs after 7 days (top panel) and 14 days (bottom panel). Scale bar represents 50 μm.* ***(d)*** *Single*

*$EPHB2^{high}OLFM4^{high}$ human colon stem cells were transfected with either an empty vector control or CRISPR/Cas9 gRNAs. Left: Colony forming efficiency measured after 7 days. Quantitative analysis calculated from 1000 cells/replicated. The experiment was performed in triplicate and presented mean ± S.E.M. (**, p = 0.01; Student t-test). Right: Quantitative comparison of organoid diameters after 14 days for each condition. The experiment was performed in triplicate and presented mean ± S.E.M. (**, p = 0.01; Student t-test).* ***(e)*** *Percentage of $EPHB2^{high}OLFM4^{high}$ stem cells based on FACS analysis for each condition described in (d) after 14 days. The experiment was performed in triplicate and presented mean ± S.E.M. (**, p = 0.01; Student t-test).* ***(f)*** *RT-PCR measurements indicating NOTCH1 expression in $EPHB2^{high}OLFM4^{high}$ colon stem cells transfected with either an empty vector control or CRISPR/Cas9 gRNAs and subsequently treated with DMSO, DAPT or JAG1. The experiment was performed in triplicate and presented mean ± S.E.M. (**, p = 0.01; Student t-test).* ***(g)*** *Single $EPHB2^{high}OLFM4^{high}$ colon stem cells were transfected with either an empty vector control or CRISPR/Cas9 gRNAs. Shown is Western blot analysis for NICD expression in sorted $EPHB2^{high}OLFM4^{high}$ colon stem cells from each condition. Actin was used as a loading control.* ***(h)*** *RT-PCR measurements indicating Notch1/2, Hes1/5, Olfm4, and Lgr5 expression in $EPHB2^{high}OLFM4^{high}$ colon stem cells for each condition described in (g). The experiment was performed in triplicate and presented mean ± S.E.M. (**, p = 0.01; Student t-test).*

5.4.8 Notch1 PF Enhances Robustness of Dynamic Stem Cell Niche

However, it is not clear how Notch1 positive feedback (PF) contributes to the dynamic regulation of the niche in space and time. It seems that lateral inhibition (LI) alone should be sufficient for generating such patterns as it did for other developmental patterning(Collier, Monk et al. 1996). To understand the underlying control principle of Notch signaling in the intestinal niche, we constructed single-, pair-, and multi-cell mathematical models to analyze LI with and without PF (Supplementary Information).

We first analyzed Notch response to external ligands in a single cell as an input-output function. In LI, external ligands activate receptors and Notch signaling, which in turn suppresses internal ligand expression. Hence, increasing levels of external ligands leads to a monotonic decrease of internal ligands (Fig. 5.5a, Supplementary Fig. S5.6a). The addition of the Notch positive feedback to LI (PFLI) causes

bifurcation and generates a more switch-like response with hysteresis (Fig. 5.5a, Supplementary Fig. S5.6b).

Pair-cell analysis suggests that both LI and PFLI could achieve intercellular bistability, with two neighboring cells settling in opposite ($Notch^{high}$ vs. $Notch^{low}$) states. Nevertheless, PFLI is much more robust in generating bistability than LI alone, and is less dependent on cooperativity (hill coefficient) of the reactions (Fig. 5.5b, Supplementary Fig. S5.6c, S5.6d).

Next, we used the Maximum Lyapunov Exponent (MLE) to analyze the stability of patterning in multicellular systems(Sprinzak, Lakhanpal et al. 2011). PFLI is able to maintain stable patterns over a much wider parameter range than LI, especially when cooperativity of reaction is low, suggesting that PFLI is a more robust patterning mechanism (Fig. 5.5c). We then scaled up the pair-cell model to a multicellular model with stationary cells surrounding each other to explore Notch patterning dynamics. In steady state analysis, both LI and PFLI can generate stable mosaic patterns with varying levels of Notch signaling and ligands (Supplementary Fig. S5.7a). However, dynamic simulations from an initial homogeneous state suggest that PFLI reaches the steady-state pattern much faster than LI by speeding up divergence of individual cell signaling states (Fig. 5.5d). Taken together, the analyses suggest that PFLI increases robustness, stability, and speed of Notch-mediated patterning.

These properties are not necessarily critical to largely stationary patterns with low cellular turnovers. However, they could be important for the intestinal stem cell niche, which is very dynamic with rapid cell division and migration that regenerate the entire epithelium every 3~5 days. We therefore constructed a multiscale, agent-based stochastic model using CompuCell3D(Swat, Thomas et al. 2012). The model takes into consideration the three-dimensional structure of the crypt, cell growth, division, migration, and cell-cell physical contact (Fig. 5.5e, see Methods). Notch signaling is only modeled in the niche at the base of the crypt, while cells above the niche are simply pushed upwards with no specific assumptions made about their properties. This model does not attempt to capture every aspect of the crypt, which involves many signaling pathways and cell types. Rather, it is solely designed to test how cell division and migration in the niche would affect PFLI- vs. LI-mediated Notch patterning.

As expected, PFLI generates bimodality in niche cells with regard to Notch signaling (NICD) levels (Supplementary Fig. S5.7b). When the strength of the PF is reduced, the ratio of $NICD^{high}$ to $NICD^{low}$ cells as well as NICD levels in the $NICD^{high}$ population decrease (Supplementary Fig. S5.7b), consistent with our experimental observation that CRISPR/Cas9-mutated PF KO organoids have lower CBC/Paneth cell ratio, and those CBCs have weaker signals (Fig. 5.3c, 5.3e-5.3g, Supplementary Fig. S5.3f-S5.3i).

However, can the Notch signaling pattern be maintained by LI alone if we simply change its parameters to increase Notch signaling levels? In other words, is the PF's role limited to enhancing Notch signaling levels, or is PFLI an inherently different control scheme from LI? To address this, we readjusted the maximum Notch transcription rate in the LI model, so that LI and PFLI have equivalent Notch signaling levels. Indeed, both LI and PFLI can generate mosaic Notch signaling patterns when cell proliferation rate is slow (Fig. 5.5e). We then gradually increased the proliferation rate inside the niche, which led to increased rates of cell division, migration, and anoikis (Supplementary Fig. S7c). PFLI is still able to maintain bimodality and binary patterns with higher turnover rate in the niche, whereas LI starts to show less bimodality and more blurred pattern (Fig. 5.5e). Therefore, PFLI is a more robust control motif than LI when the pattern is highly dynamic with a lot of cell turnover. The discovery of the direct Notch1 PF in the intestinal niche is probably not a coincidence; rather, it may be an evolutionary response to the unique regulatory challenges of the highly regenerative intestinal epithelium.

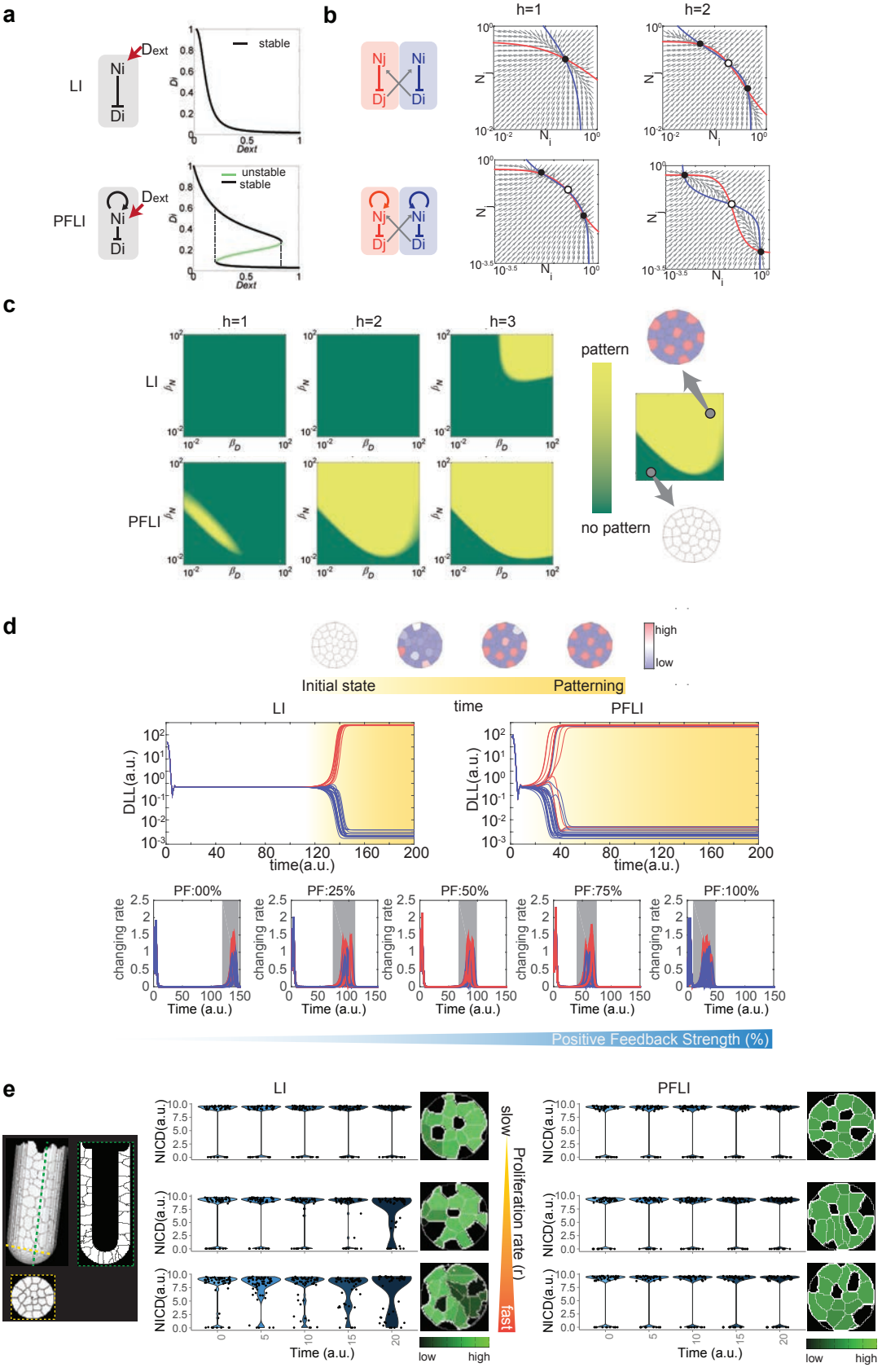
a
LI
Ni
Di
Dext
stable
PFLI
unstable
stable
b
h=1
h=2
Nj
Dj
c
h=1
h=2
h=3
LI
PFLI
pattern
no pattern
d
Initial state
Patterning
high
low
time
LI
PFLI
DLL(a.u.)
time(a.u.)
PF:00%
PF:25%
PF:50%
PF:75%
PF:100%
changing rate
Time (a.u.)
Positive Feedback Strength (%)
e
LI
PFLI
NICD(a.u.)
Time (a.u.)
slow
Proliferation rate (r)
fast
low
high

Figure 5.5. Computational Analysis Of Notch Patterning With Lateral Inhibition And Positive Feedback.

(a) *Dynamic analysis of the single-cell Notch signaling model. Internal Dll (D_i) vs. external Dll (D_{ext}) protein levels are plotted. Lateral inhibition (LI) exhibits monostable behavior (top panel) while Notch positive feedback + LI (PFLI) exhibits bifurcation (bottom panel) in response to external Notch activation.* ***(b)*** *Phase portraits of the pair-cell Notch signaling model. LI (top panel) requires higher cooperativity (Hill coefficient, h) than PFLI (bottom panel) to generate bistability. Lines: nullclines; solid dots: stable steady states; hollow dots: unstable steady states.* ***(c)*** *Multi-cell Maximum Lyapunov Exponents (MLE) analysis of LI-only (top) or PFLI (bottom) circuits spanning parameters of production rates of Notch and Dll with varying degrees of cooperativity (h). Yellow regions (positive MLE values) represent states with patterning and green regions (negative MLE values) represent states without patterning. PFLI generates patterns over a broader parameter range than LI.* ***(d)*** *Multi-cellular simulation of Notch signaling models showing DLL levels from initially homogeneous unstable steady states to heterogeneous stable steady states (top panel). Middle-left panel: representative simulation of LI. Middle-right panel: representative simulation of PFLI. Bottom panel shows the change rates of DLLs levels during patterning with varying relative strength of positive feedback. Red: signaling dynamics of cells reaching high steady states. Blue: signaling dynamics of cells reaching low steady states. Grey: patterning transition period from homogeneous steady states to heterogeneous steady state.* ***(e)*** *Analysis of a stochastic crypt model integrated with Notch signaling simulation. Left: Structure of the crypt model. Right: representative violin plots indicating NICD level dynamics at crypt bottom with varying turnover rates. Shown also are corresponding representative simulated patterns of NICD levels in crypt bottoms. PFLI shows stronger NICD bimodality and binary patterns than LI when turnover rates become higher.*

5.5 Discussion

The stem cell niche is a dynamic environment that controls regeneration and homeostasis of the tissue. However, it is notoriously difficult to study spatiotemporal regulation of biological systems involving intercellular communication and feedback. Here, we demonstrate that integration of *in vivo*, *in vitro*, and *in silico* models coupled with precise methods of physical and genomic perturbation (laser ablation, CRISPR) provides a way to unravel some of the "design principles" underlying such systems.

By designing and surgically implanting a 3D-printed intestinal scaffold and an openable abdominal window, coupled with a low-repetition-rate, high-pulse-energy femtosecond (fs) laser, we studied how the intestinal stem cell niche recovers from cell ablation *in vivo*. Instead of having a fixed blueprint, the mosaic CBC/Paneth cell pattern in the niche is rather fluidic and can spatially readjust upon damage. We then characterized Notch signaling in the niche, and discovered a direct positive feedback, in which NICD cleaved from activated receptors directly activates Notch1 receptor expression. This positive feedback is active in mouse intestinal and colon epithelial cells, and its silencing by CRISPR/Cas9 mutation reduced CBC/Paneth cell ratio, limited self-renewal, and deprived organoids of the ability to recover from cell ablation. Dynamical systems analysis and multiscale stochastic simulation further revealed that, compared to LI, PFLI enhances robustness of the spatiotemporal Notch signaling pattern, especially in the presence of perturbation and turnover.

Biological systems such as the stem cell niche are known to be robust. They work most of the time, capable of accommodating different conditions and recovering from mistakes and damages. Control theory would predict that they rely on additional mechanisms such as feedback to enhance their regulation. However, conventional assays seldom reveal such intricacies. The importance of these "safeguard" mechanisms is often revealed only when systems are perturbed.

Here, precise laser ablation highlights the flexibility of the niche regulation. Further investigation shows that control motifs like PFLI and LI can appear similar in steady-state conditions, but display different dynamic properties that can have important implications to a rapidly regenerative tissue like the intestinal epithelium.

The direct Notch1 PF seems to be an evolutionary response to the challenges of regulating intestinal and colon epithelium, since it has not been reported in other tissues or model systems such as *Drosophila* and *C. elegans* despite extensive study of Notch. Nonetheless, it is also likely that the direct PF is a widely conserved mechanism that simply awaits discovery in other systems. In that case, it will be interesting to see whether the existence of PF is associated with the rate of tissue regeneration.

Notch signaling is certainly not the only mechanism responsible for niche pattern. Other signaling pathways like developmental (Wnt, BMP, EGFR, Hedgehog), chemokine, and mechanotransduction pathways likely reinforce or crosstalk with Notch to regulate the niche collectively. An integrated approach that takes dynamics into account may help unravel the intricate control scheme of the stem cell niche.

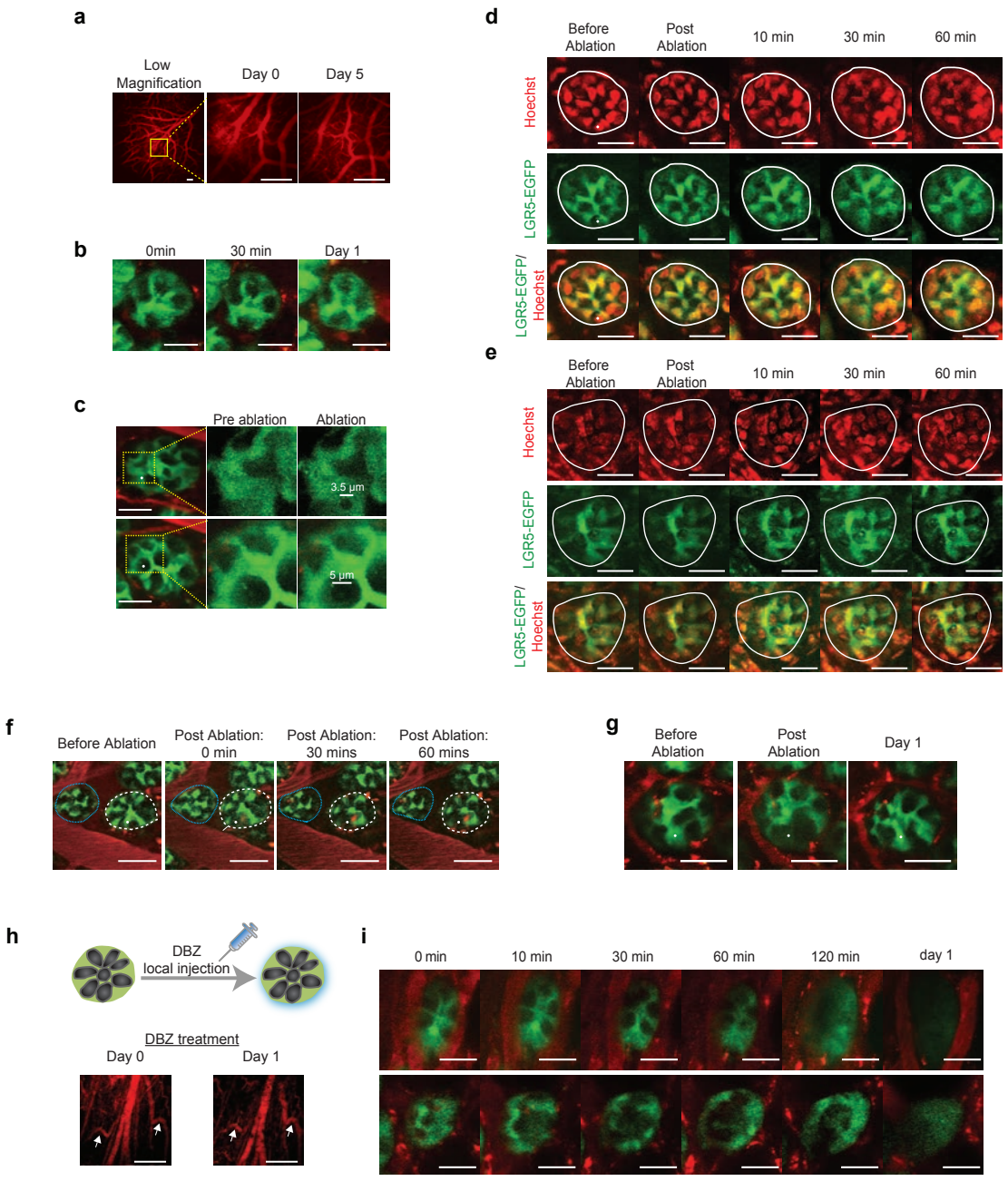

Supplementary Figure S5.1. In vivo imaging and laser ablation. *(a) Intestinal vasculature imaged through abdominal window. The vasculature remains largely unchanged after 5 days. Scale bar: 150 μm. (b) Time-lapse images showing the LGR5-EGFP pattern largely unchanged. Scale bar: 30 μm. (c) Laser ablation created focal damage on the targeted cells. Top: ablation on a LGR5-EGFP+ CBC. Bottom: ablation on a Paneth cell. The bars in the high magnificent images show the diameter of the focal damage*

generated by ablation. White dot marks the position of laser focus. Scale bar: 40 μm in low magnification images. (d) Time-lapse images following laser ablation on a Paneth cell. The nucleus of the ablated Paneth cell disappeared between 30 and 60 minutes. Nuclei were stained by Hoechst dye. White dot marks the target position of laser focus. Scale bar: 30 μm. (e) Time-lapse images of a control crypt without ablation. The LGR5-EGFP+ CBCs and Paneth cells remain unchanged during the imaging period. Nuclei were stained by Hoechst dye. White dot marks the target position of laser focus. Scale bar: 30 μm (f) Time-lapse images following laser ablation showing targeted niche undergoing rearrangement while adjacent untargeted niche remains unchanged. White dot marks the position of laser focus. Scale bar: 40 μm. (g) Representative time-lapse series following laser ablation of LGR5-EGFP+ CBC showing crypt base pattern the next day. White dot marks the target position of laser focus. Scale bar: 20 μm. (h) Vasculature labeled by Texas-red dextran (red) remained largely unchanged after DBZ treatment. Scale bar: 150 μm. (i) Time-series images starting at 2 hours after local injection of Notch inhibitor DBZ via the openable abdominal window. Two independent series are presented in top and bottom panels, respectively. Green, LGR5-EGFP; Red, Texas-red dextran labeled vasculature. Scale bar: 30 μm.

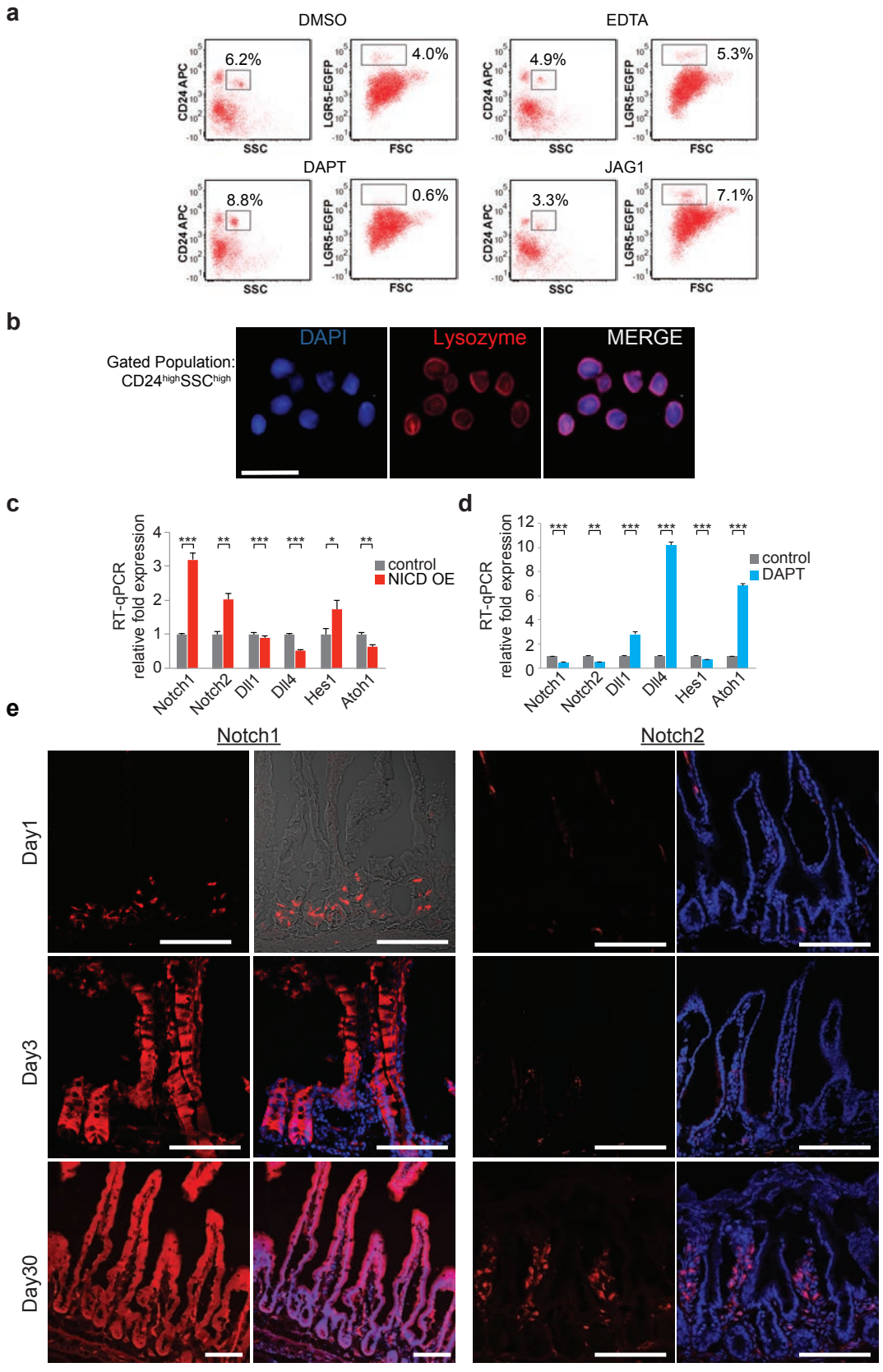
a
DMSO
EDTA
DAPT
JAG1
6.2%
4.0%
4.9%
5.3%
8.8%
0.6%
3.3%
7.1%
CD24 APC
SSC
LGR5-EGFP
FSC
b
Gated Population:
CD24highSSChigh
DAPI
Lysozyme
MERGE
c
RT-qPCR
relative fold expression
control
NICD OE
Notch1
Notch2
Dll1
Dll4
Hes1
Atoh1
d
RT-qPCR
relative fold expression
control
DAPT
e
Notch1
Notch2
Day1
Day3
Day30

Supplementary Figure S5.2. Notch levels in niche cells. (a) *Representative FACS plots of organoids treated with DMSO, JAG1, EDTA or DAPT for 48 hours, including gated analysis to isolate* $CD24^{high}/SSC^{high}$ *Paneth cells and LGR5-EGFP+ CBCs according to an established protocol*[3]. ***(b)*** *Immunofluorescent (IF) image of sorted* $CD24^{high}/SSC^{high}$ *cells showing expression of Paneth cell-specific marker Lysozyme (red). DAPI labels nuclei and scale bar represents 50 µm.* ***(c)*** *Organoids extracted from LGR5-EGFP x CreERT2/Rosa26-YFP-NICD mice were treated with Tamoxifen to induce NICD overexpression (NICD-OE). Shown is RT-qPCR quantification of Notch levels. The experiment was performed in triplicate and presented mean ± S.E.M. (*, p=0.05; **, p = 0.01; ***, p=0.001, Student t-test).* ***(d)*** *RT-qPCR measurements of Notch levels with DMSO or DAPT treatment. The experiment was performed in triplicate and presented mean ± S.E.M. (**, p = 0.01; ***, p=0.001, Student t-test).* ***(e)*** *Representative IF images of intestinal tissue derived from Tamoxifen-induced Notch1-CreERT2 KI x Rosa26-tdTomato-WPRE mice (left) and Notch2-CreERT2 KI x Rosa26-tdTomato-WPRE mice (right). Shown are images from 1 day, 3 days, and 30 days post-Tamoxifen induction. Notch1/2 IF (red). DAPI labels nuclei and scale bar represents 100 µm.*

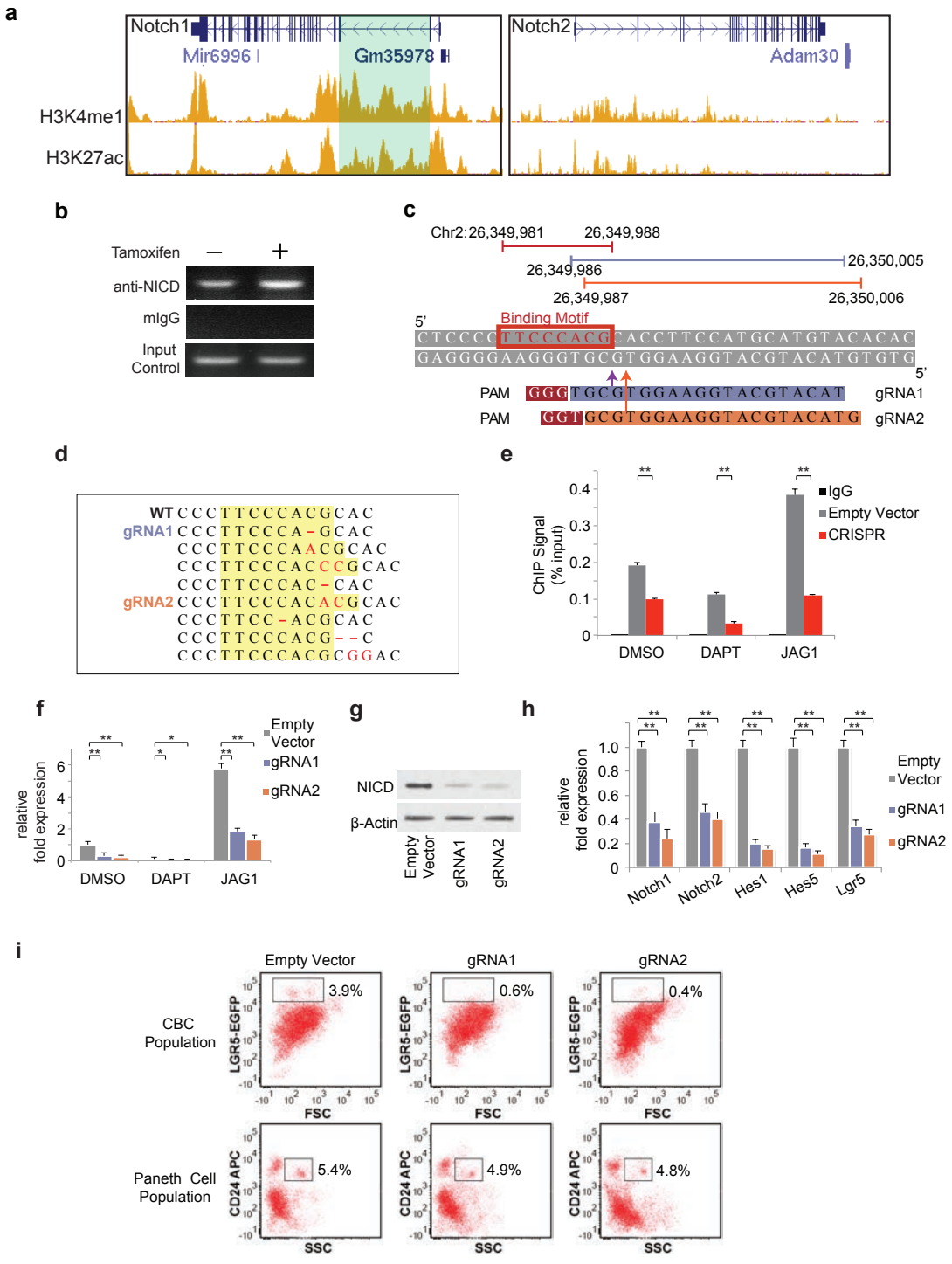

Supplementary Figure S5.3. Notch 1 positive feedback in mouse intestine. (a) *ChIP-Seq signal of LICR Histone tracks (H3K4me1 and H3K27ac) on mouse small intestine cells from ENCODE at UCSC Genome Browser. Left: H3K4me1 (top) and H3K27ac (bottom) occupancy related to Notch1. Right:*

H3K4me1 (top) and H3K27ac (bottom) occupancy related to Notch2. ***(b)*** *Organoids extracted from LGR5-EGFP x CreERT2/Rosa26-YFP-NICD mice were treated with Tamoxifen to induce NICD overexpression (NICD-OE). Shown is agarose gel analysis of ChIP-PCR products to validate active NICD binding on Notch1.* ***(c)*** *Design of gRNAs for CRISPR/Cas9 mutagenesis to target the putative NICD/RBPJk binding motif on mouse Notch1 sequence.* ***(d)*** *Representative sequences from selected organoid clones transfected with CRISPR/Cas9 gRNAs showing indel mutations in the targeted region of the mouse NICD binding motif.* ***(e)*** *LGR5-EGFP+ CBCs were transfected with either an empty vector control or CRISPR/Cas9 gRNA and subsequently treated with DMSO, DAPT or JAG1. Shown is ChIP-qPCR analysis of Notch1, indicating enrichment with NICD antibody compared with IgG control. The experiment was performed in triplicate and presented mean ± S.E.M. (**, p = 0.01; Student t-test).* ***(f)*** *RT-PCR measurements indicating Notch1 expression in LGR5-EGFP+ CBCs transfected with either an empty vector control or CRISPR/Cas9 gRNAs and subsequently treated with DMSO, DAPT or JAG1. The experiment was performed in triplicate and presented mean ± S.E.M. (*, p=0.05, **, p = 0.01; Student t-test).* ***(g)*** *Single LGR5-EGFP+ CBCs were transfected with either an empty vector control or CRISPR/Cas9 gRNAs and propagated as organoids. Shown is Western blot analysis for NICD expression in sorted LGR5-EGFP+ CBCs from each condition. Actin was used as a loading control.* ***(h)*** *RT-PCR measurements indicating Notch1/2, Hes1/5, and Lgr5 expression in LGR5-EGFP+ ISCs for each condition described in (f). The experiment was performed in triplicate and presented mean ± S.E.M. (**, p = 0.01; Student t-test).* ***(i)*** *Single LGR5-EGFP+ CBCs were transfected with either an empty vector control or CRISPR/Cas9 gRNAs and propagated as organoids for 15 days. Shown are representative FACS plots for each condition including gated analysis to isolate* $CD24^{high}/SSC^{high}$ *Paneth cells and LGR5-EGFP+ ISCs.*

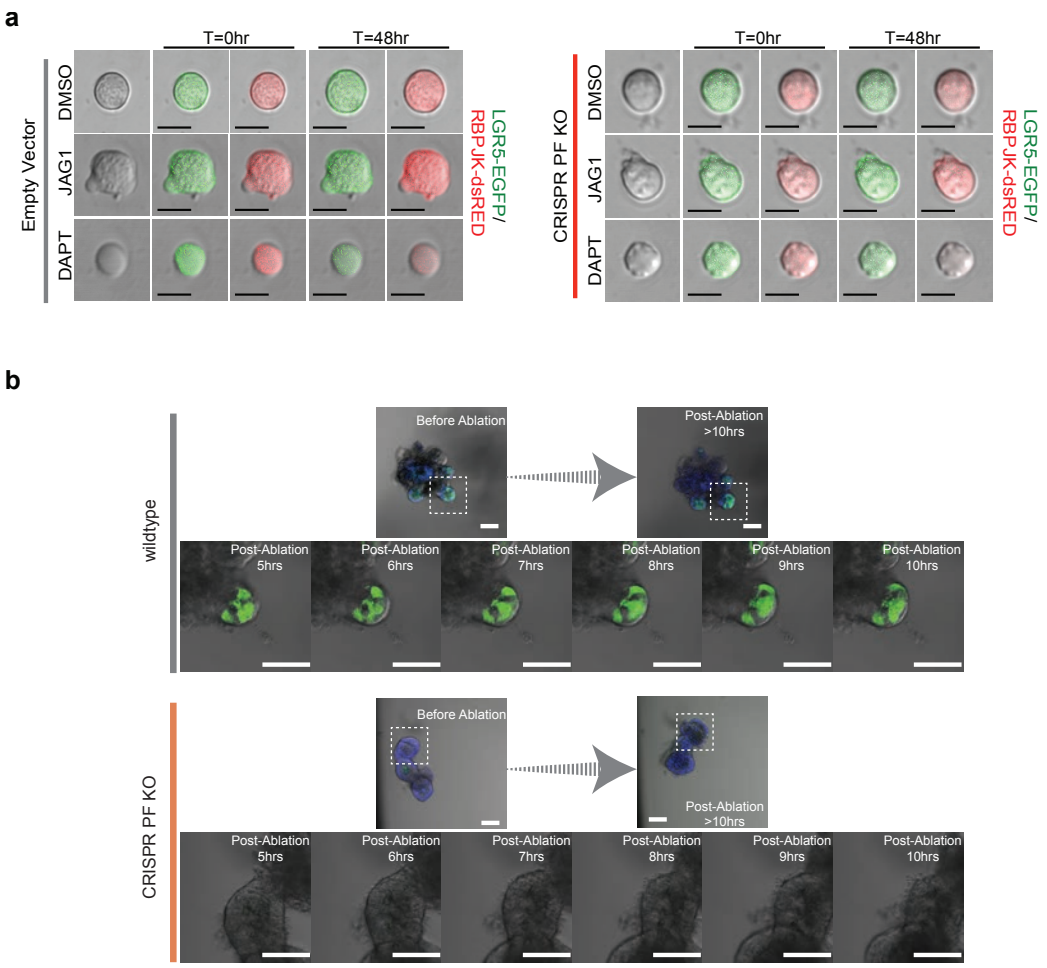

Supplementary Figure S5.4. Disruption of Notch1 positive feedback. (a) *Single empty vector (control) containing cells or CRISPR/Cas9-mutated LGR5-EGFP+ CBCs were transfected with a RBPJk-dsRed reporter construct and subsequently treated with DMSO, DAPT or JAG1 for 48 hours. Shown are representative images indicating LGR5-EGFP (green) and RBPJk-dsRed (red) expression for each condition.* ***(b)*** *Wild-type (top) or CRISPR/Cas9 gRNA-transfected (bottom) CBCs propagated as organoids were subjected to single cell laser ablation. Shown are representative images of whole organoids pre-ablation and 10 hours post-ablation, and magnified time-lapse images of the targeted budding region from 5 hours to 10 hours post-ablation. LGR5-EGFP (green). Hoescht dye (blue) labels nuclei and scale bar represents 50 µm.*

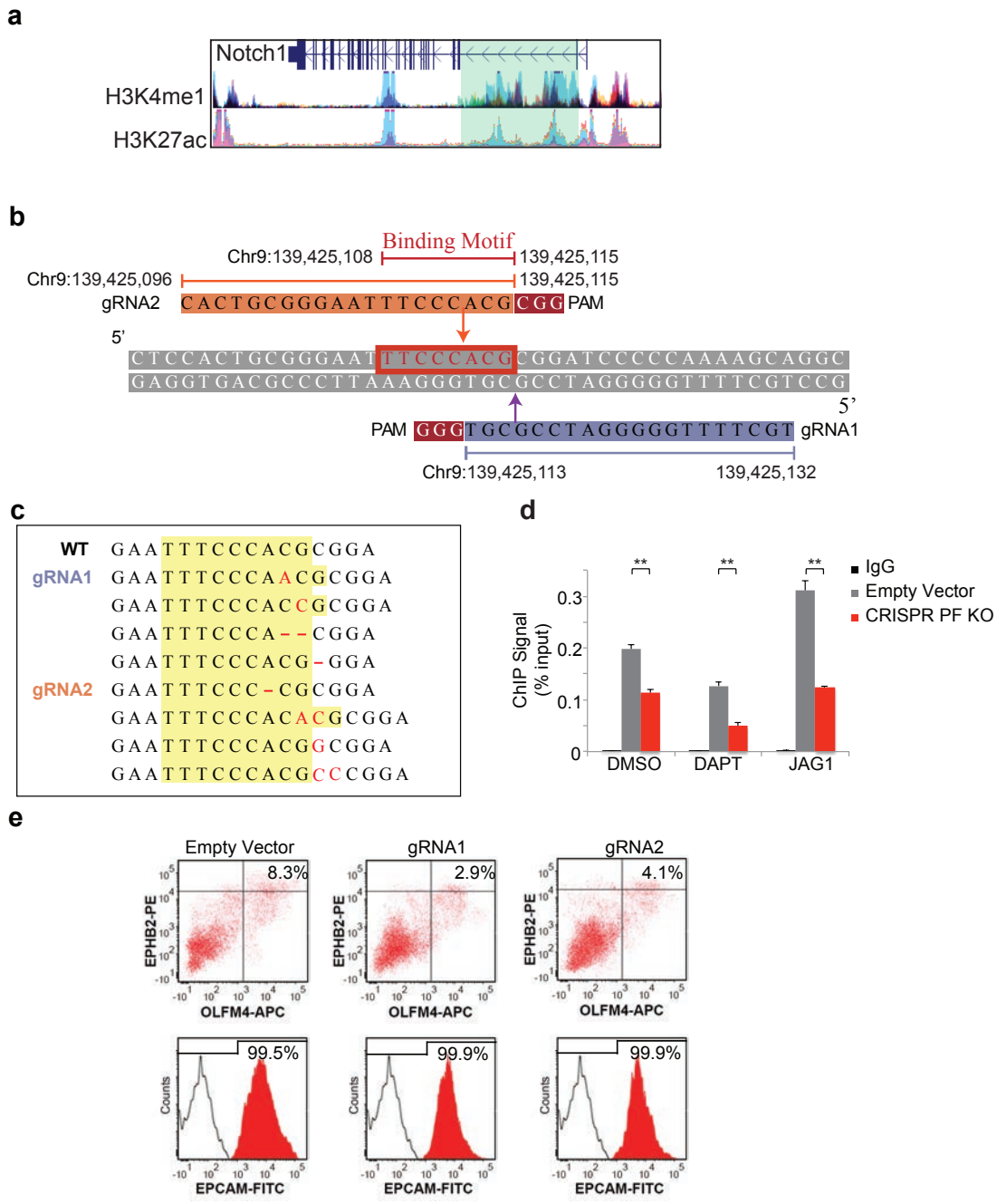

Supplementary Figure S5.5. Notch 1 positive feedback in human colon stem cells. (a) *ChIP-Seq signal of H3K4me1 (top) and H3K27ac (bottom) occupancy related to human Notch1 on 7 human cell lines from ENCODE at UCSC Genome Browser.* ***(b)*** *Design of gRNAs for CRISPR/Cas9 mutagenesis to target the putative NICD/RBPJk binding motif on human Notch1.* ***(c)*** *Single EPHB2^{high}OLFM4^{high} colon stem cells were transfected with either an empty vector control or CRISPR/Cas9 gRNAs. Shown are*

representative sequences from selected clones with indel mutations in the targeted region of the human NICD binding motif. ***(d)*** *EPHB2^{high}OLFM4^{high} colon stem cells were transfected with either an empty vector control or CRISPR/Cas9 gRNA and subsequently treated with DMSO, DAPT or JAG1. Shown is ChIP-qPCR analysis of Notch1, indicating enrichment with NICD antibody compared with IgG control. The experiment was performed in triplicate and presented mean ± S.E.M. (**, p = 0.01; Student t-test).* ***(e)*** *Single EPHB2^{high}OLFM4^{high} colon stem cells were transfected with either an empty vector control or CRISPR/Cas9 gRNAs and cultured as organoids for 14 days. Top: Representative FACS plots for EPHB2 and OLFM4 expression and the percentage of EPHB2^{high}OLFM4^{high} stem cells for each condition. Bottom: FACS histograms indicating expression for the epithelial-specific cell marker EpCAM in the EPHB2^{high}OLFM4^{high} subset of cells for each condition.*

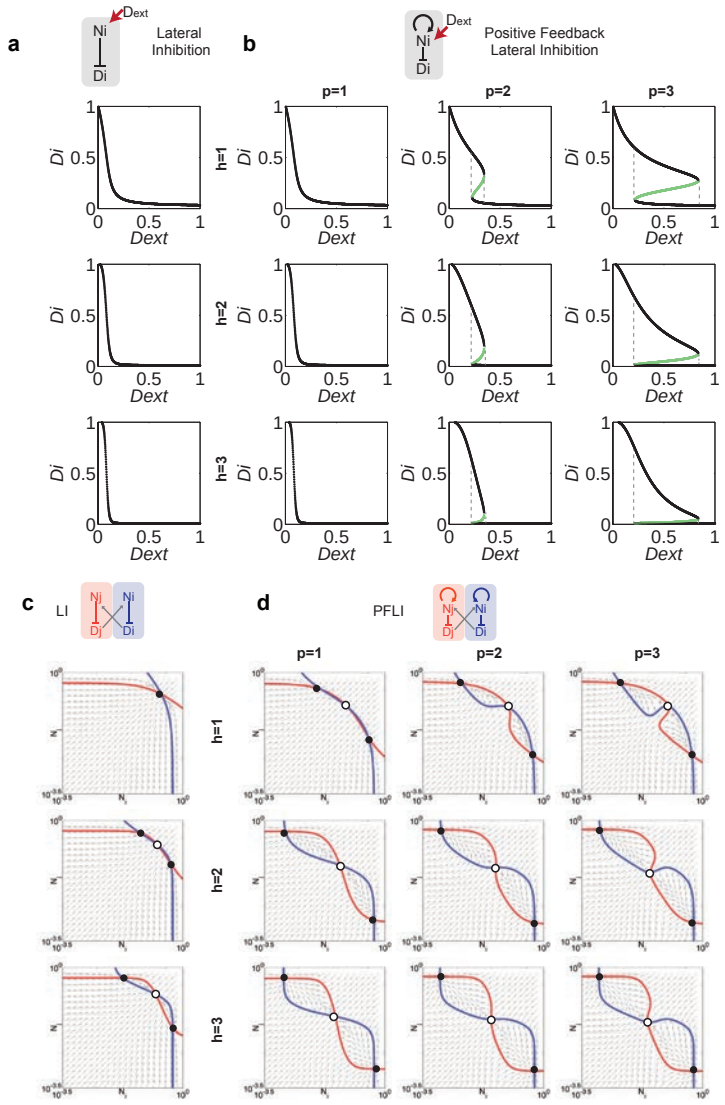

Supplementary Figure S5.6. Bistability of LI vs. PFLI. (a) *Dynamic analysis of the single-cell LI model. Internal Dll (Di) vs. external Dll (Dext) protein levels are plotted.* ***(b)*** *Dynamic analysis of the single-cell PFLI model. Internal Dll (Di) vs. external Dll (Dext) protein levels are plotted.* ***(c)*** *Phase portraits of the pair-cell LI model. h, Hill coefficient representing cooperativity of LI reaction.* ***(d)*** *Phase portraits of the pair-cell PFLI model. h, Hill coefficient representing cooperativity of LI reaction. p, Hill coefficient representing cooperativity of the Notch positive feedback.*

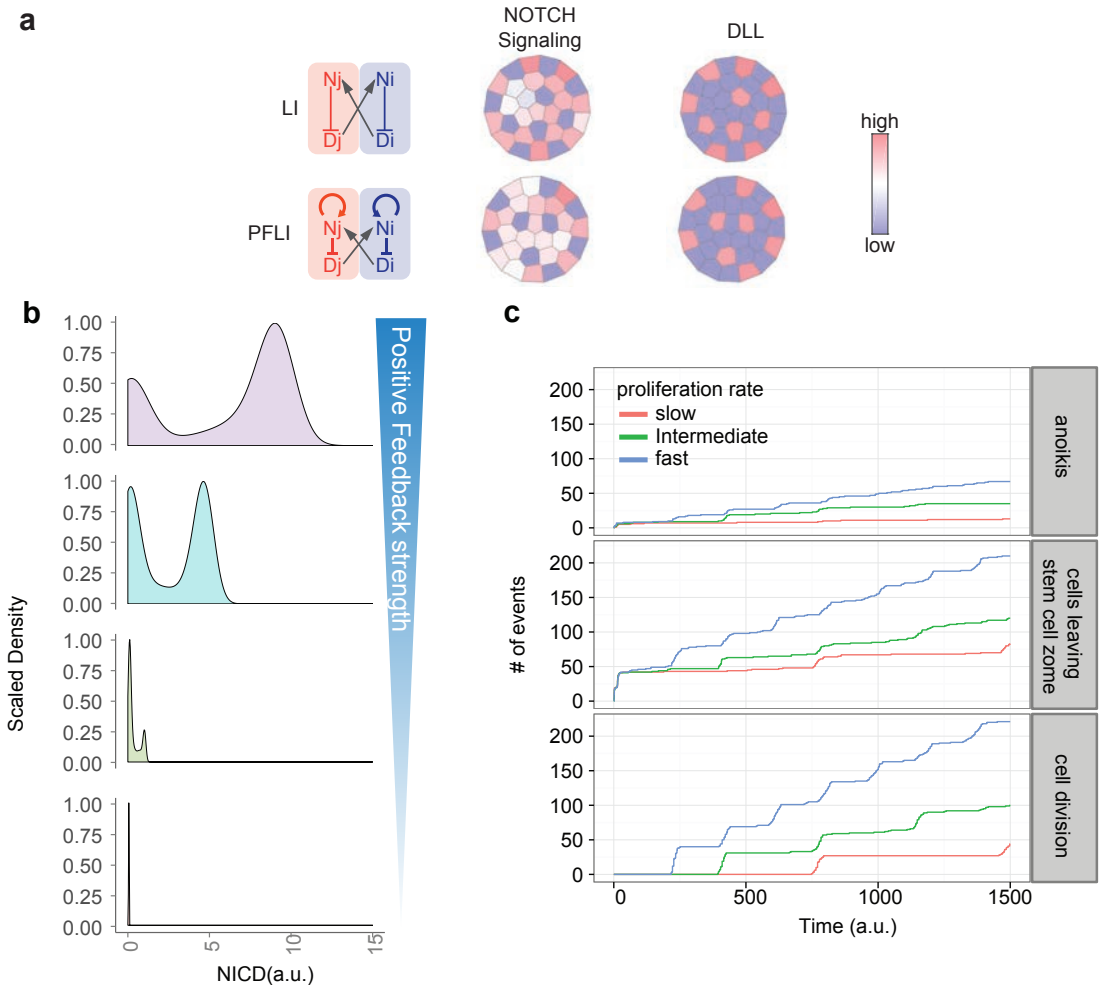

Supplementary Figure S5.7. Multicellular patterning simulation. ***(a)*** *Deterministic multi-cellular simulation of Notch expression patterns with LI and PFLI circuitry.* ***(b)*** *Representative density plots of NICD distribution in the multiscale, stochastic model with gradual suppression of Notch positive feedback.* ***(c)*** *Simulated stochastic cellular events (anoikis, cells leaving stem cell zone, and cell division) with increasing cell proliferation rates.*

REFERENCES

Artavanis-Tsakonas, S., M. D. Rand and R. J. Lake (1999). "Notch signaling: cell fate control and signal integration in development." Science **284**(5415): 770-776.

Barker, N. (2014). "Adult intestinal stem cells: critical drivers of epithelial homeostasis and regeneration." Nat Rev Mol Cell Biol **15**(1): 19-33.

Barker, N., J. H. van Es, J. Kuipers, P. Kujala, M. van den Born, M. Cozijnsen, A. Haegebarth, J. Korving, H. Begthel, P. J. Peters and H. Clevers (2007). "Identification of stem cells in small intestine and colon by marker gene Lgr5." Nature **449**(7165): 1003-1007.

Bonn, S., R. P. Zinzen, C. Girardot, E. H. Gustafson, A. Perez-Gonzalez, N. Delhomme, Y. Ghavi-Helm, B. Wilczynski, A. Riddell and E. E. Furlong (2012). "Tissue-specific analysis of chromatin state identifies temporal signatures of enhancer activity during embryonic development." Nat Genet **44**(2): 148-156.

Buczacki, S. J., H. I. Zecchini, A. M. Nicholson, R. Russell, L. Vermeulen, R. Kemp and D. J. Winton (2013). "Intestinal label-retaining cells are secretory precursors expressing Lgr5." Nature **495**(7439): 65-69.

Collier, J. R., N. A. Monk, P. K. Maini and J. H. Lewis (1996). "Pattern formation by lateral inhibition with feedback: a mathematical model of delta-notch intercellular signalling." J Theor Biol **183**(4): 429-446.

Consortium, E. P. (2012). "An integrated encyclopedia of DNA elements in the human genome." Nature **489**(7414): 57-74.

Fre, S., E. Hannezo, S. Sale, M. Huyghe, D. Lafkas, H. Kissel, A. Louvi, J. Greve, D. Louvard and S. Artavanis-Tsakonas (2011). "Notch lineages and activity in intestinal stem cells determined by a new set of knock-in mice." PLoS One **6**(10): e25785.

Fre, S., M. Huyghe, P. Mourikis, S. Robine, D. Louvard and S. Artavanis-Tsakonas (2005). "Notch signals control the fate of immature progenitor cells in the intestine." Nature **435**(7044): 964-968.

Hon, G. C., R. D. Hawkins and B. Ren (2009). "Predictive chromatin signatures in the mammalian genome." Hum Mol Genet **18**(R2): R195-201.

Hucka, M., A. Finney, H. M. Sauro, H. Bolouri, J. C. Doyle, H. Kitano, A. P. Arkin, B. J. Bornstein, D. Bray, A. Cornish-Bowden, A. A. Cuellar, S. Dronov, E. D. Gilles, M. Ginkel, V. Gor, Goryanin, II, W. J. Hedley, T. C. Hodgman, J. H. Hofmeyr, P. J. Hunter, N. S. Juty, J. L. Kasberger, A. Kremling, U. Kummer, N. Le Novere, L. M. Loew, D. Lucio, P. Mendes, E. Minch, E. D. Mjolsness, Y. Nakayama, M. R. Nelson, P. F. Nielsen, T. Sakurada, J. C. Schaff, B. E. Shapiro, T. S. Shimizu, H. D. Spence, J. Stelling, K. Takahashi, M. Tomita, J. Wagner, J. Wang and S. Forum (2003). "The systems biology markup language (SBML): a medium for representation and exchange of biochemical network models." Bioinformatics **19**(4): 524-531.

Jung, P., T. Sato, A. Merlos-Suarez, F. M. Barriga, M. Iglesias, D. Rossell, H. Auer, M. Gallardo, M. A. Blasco, E. Sancho, H. Clevers and E. Batlle (2011). "Isolation and in vitro expansion of human colonic stem cells." Nat Med **17**(10): 1225-1227.

Kopan, R. and M. X. Ilagan (2009). "The canonical Notch signaling pathway: unfolding the activation mechanism." Cell **137**(2): 216-233.

Lander, A. D., J. Kimble, H. Clevers, E. Fuchs, D. Montarras, M. Buckingham, A. L. Calof, A. Trumpp and T. Oskarsson (2012). "What does the concept of the stem cell niche really mean today?" BMC Biol **10**: 19.

Lopez-Garcia, C., A. M. Klein, B. D. Simons and D. J. Winton (2010). "Intestinal stem cell replacement follows a pattern of neutral drift." Science **330**(6005): 822-825.

Metcalfe, C., N. M. Kljavin, R. Ybarra and F. J. de Sauvage (2014). "Lgr5+ stem cells are indispensable for radiation-induced intestinal regeneration." Cell Stem Cell **14**(2): 149-159.

Nishimura, N., C. B. Schaffer, B. Friedman, P. S. Tsai, P. D. Lyden and D. Kleinfeld (2006). "Targeted insult to subsurface cortical blood vessels using ultrashort laser pulses: three models of stroke." Nature Methods **3**(2): 99-108.

Oh, P., C. Lobry, J. Gao, A. Tikhonova, E. Loizou, J. Manent, B. van Handel, S. Ibrahim, J. Greve, H. Mikkola, S. Artavanis-Tsakonas and I. Aifantis (2013). "In vivo mapping of notch pathway activity in normal and stress hematopoiesis." Cell Stem Cell **13**(2): 190-204.

Pan, Z., S. Sikandar, M. Witherspoon, D. Dizon, T. Nguyen, K. Benirschke, C. Wiley, P. Vrana and S. M. Lipkin (2008). "Impaired placental trophoblast lineage differentiation in Alkbh1(-/-) mice." Dev Dyn **237**(2): 316-327.

Pellegrinet, L., V. Rodilla, Z. Liu, S. Chen, U. Koch, L. Espinosa, K. H. Kaestner, R. Kopan, J. Lewis and F. Radtke (2011). "Dll1- and dll4-mediated notch signaling are required for homeostasis of intestinal stem cells." Gastroenterology **140**(4): 1230-1240 e1231-1237.

Rand, M. D., L. M. Grimm, S. Artavanis-Tsakonas, V. Patriub, S. C. Blacklow, J. Sklar and J. C. Aster (2000). "Calcium depletion dissociates and activates heterodimeric notch receptors." Mol Cell Biol **20**(5): 1825-1835.

Riccio, O., M. E. van Gijn, A. C. Bezdek, L. Pellegrinet, J. H. van Es, U. Zimber-Strobl, L. J. Strobl, T. Honjo, H. Clevers and F. Radtke (2008). "Loss of intestinal crypt progenitor cells owing to inactivation of both Notch1 and Notch2 is accompanied by derepression of CDK inhibitors p27Kip1 and p57Kip2." EMBO Rep **9**(4): 377-383.

Ritsma, L., S. I. Ellenbroek, A. Zomer, H. J. Snippert, F. J. de Sauvage, B. D. Simons, H. Clevers and J. van Rheenen (2014). "Intestinal crypt homeostasis revealed at single-stem-cell level by in vivo live imaging." Nature **507**(7492): 362-365.

Ritsma, L., E. J. Steller, E. Beerling, C. J. Loomans, A. Zomer, C. Gerlach, N. Vrisekoop, D. Seinstra, L. van Gurp, R. Schafer, D. A. Raats, A. de Graaff, T. N. Schumacher, E. J. de Koning, I. H. Rinkes, O. Kranenburg and J. van Rheenen (2012). "Intravital microscopy through an abdominal imaging window reveals a pre-micrometastasis stage during liver metastasis." Sci Transl Med **4**(158): 158ra145.

Sato, T., D. E. Stange, M. Ferrante, R. G. Vries, J. H. Van Es, S. Van den Brink, W. J. Van Houdt, A. Pronk, J. Van Gorp, P. D. Siersema and H. Clevers (2011). "Long-term expansion of epithelial organoids from human colon, adenoma, adenocarcinoma, and Barrett's epithelium." Gastroenterology **141**(5): 1762-1772.

Sato, T., J. H. van Es, H. J. Snippert, D. E. Stange, R. G. Vries, M. van den Born, N. Barker, N. F. Shroyer, M. van de Wetering and H. Clevers (2010). "Paneth cells constitute the niche for Lgr5 stem cells in intestinal crypts." Nature.

Schaffer, C. B., N. Nishimura, E. N. Glezer, A. M. T. Kim and E. Mazur (2002). "Dynamics of femtosecond laser-induced breakdown in water from femtoseconds to microseconds." Optics Express **10**(3): 196-203.

Schwank, G., B. K. Koo, V. Sasselli, J. F. Dekkers, I. Heo, T. Demircan, N. Sasaki, S. Boymans, E. Cuppen, C. K. van der Ent, E. E. Nieuwenhuis, J. M. Beekman and H. Clevers (2013). "Functional repair of CFTR by CRISPR/Cas9 in intestinal stem cell organoids of cystic fibrosis patients." Cell Stem Cell **13**(6): 653-658.

Shlyueva, D., G. Stampfel and A. Stark (2014). "Transcriptional enhancers: from properties to genome-wide predictions." Nat Rev Genet **15**(4): 272-286.

Sikandar, S. S., K. T. Pate, S. Anderson, D. Dizon, R. A. Edwards, M. L. Waterman and S. M. Lipkin (2010). "NOTCH signaling is required for formation and self-renewal of tumor-initiating cells and for repression of secretory cell differentiation in colon cancer." Cancer Res **70**(4): 1469-1478.

Snippert, H. J., L. G. van der Flier, T. Sato, J. H. van Es, M. van den Born, C. Kroon-Veenboer, N. Barker, A. M. Klein, J. van Rheenen, B. D. Simons and H. Clevers (2010). "Intestinal crypt homeostasis results from neutral competition between symmetrically dividing Lgr5 stem cells." Cell **143**(1): 134-144.

Sprinzak, D., A. Lakhanpal, L. Lebon, J. Garcia-Ojalvo and M. B. Elowitz (2011). "Mutual inactivation of notch receptors and ligands facilitates developmental patterning." PLoS computational biology **7**(6): e1002069-e1002069.

Swat, M. H., G. L. Thomas, J. M. Belmonte, A. Shirinifard, D. Hmeljak and J. A. Glazier (2012). "Multi-scale modeling of tissues using CompuCell3D." Methods Cell Biol **110**: 325-366.

Takeda, N., R. Jain, M. R. LeBoeuf, Q. Wang, M. M. Lu and J. A. Epstein (2011). "Interconversion between intestinal stem cell populations in distinct niches." Science **334**(6061): 1420-1424.

Thevenaz, P., U. E. Ruttimann and M. Unser (1998). "A pyramid approach to subpixel registration based on intensity." IEEE Trans Image Process **7**(1): 27-41.

van der Flier, L. G. and H. Clevers (2009). "Stem cells, self-renewal, and differentiation in the intestinal epithelium." Annu Rev Physiol **71**: 241-260.

Wang, H., C. Zang, L. Taing, K. L. Arnett, Y. J. Wong, W. S. Pear, S. C. Blacklow, X. S. Liu and J. C. Aster (2014). "NOTCH1-RBPJ complexes drive target gene expression through dynamic interactions with superenhancers." Proc Natl Acad Sci U S A **111**(2): 705-710.

Wu, C., Cain-Hom*, L, Hagenbeek T. et al & Siebel, C. (2010). " Therapeutic antibody targeting of individual Notch receptors." Nature **464**(15 April): doi:10.1038.

Wu, Y., C. Cain-Hom, L. Choy, T. J. Hagenbeek, G. P. de Leon, Y. Chen, D. Finkle, R. Venook, X. Wu, J. Ridgway, D. Schahin-Reed, G. J. Dow, A. Shelton, S. Stawicki, R. J. Watts, J. Zhang, R. Choy, P. Howard, L. Kadyk, M. Yan, J. Zha, C. A. Callahan, S. G. Hymowitz and C. W. Siebel (2010). "Therapeutic antibody targeting of individual Notch receptors." Nature **464**(7291): 1052-1057.

Yamamura, H., A. Yamamura, E. A. Ko, N. M. Pohl, K. A. Smith, A. Zeifman, F. L. Powell, P. A. Thistlethwaite and J. X. Yuan (2014). "Activation of Notch signaling by short-term treatment with Jagged-1 enhances store-operated Ca(2+) entry in human pulmonary arterial smooth muscle cells." Am J Physiol Cell Physiol **306**(9): C871-878.

Yang, Q., N. A. Bermingham, M. J. Finegold and H. Y. Zoghbi (2001). "Requirement of Math1 for Secretory Cell Lineage Commitment in the Mouse Intestine." Science **294**(5549): 2155-2158.

CHAPTER 6

DISCUSSIONS

6.1 miR-34a Regulation On Colon Cancer Stem Cell Division

Our studies showed that CCSC division is highly regulated by miR-34a, and its versatile threshold response generates the bimodal distribution of CCSCs (Bu, Chen et al. 2013). CCSCs favor symmetric division of CCSCs-CCSCs when miR-34a level is reduced, which results in less asymmetric division and more CCSC daughter cells and non-CCSC daughter cells. In contrast, when miR-34a levels increase, the frequency of symmetric division of CCSCs and asymmetric division reduces, which leading to less CCSCs daughter cells and non-CCSCs daughter cells. Since CCSCs has higher proliferative potential than non-CCSCs, inhibiting miR-34a leads to higher proliferation as well as self-renewal while overexpressing miR-34a results in less tumorigenesis. To maintain asymmetric division, miR-34a should be precisely controlled: excess or diminished miR-34a could both reduce the frequency of asymmetric division of CCSCs.

Our computational modeling also confirms that the miR-34a regulation is versatile to exhibit a "threshold response" to fine-tune CCSCs during division. This versatility of miR-34a regulation then results in bimodal distribution of CCSCs and non-CCSCs due to the dynamic control of CCSCs division. In addition, the distribution of CCSCs has a dynamic response to the levels of miR-34a, and mi-34a shows versatile multicellular distribution regulation to balance the CCSC population from a unimodal to a bimodal distribution.

6.2 miR-34a Regulated Incoherent Feedforward Loop Exhibit Distinct Bimodality

Interestingly, despite the versatile "threshold response" that miR-34a exhibits to regulate CCSCs division, miR-34a does not work alone on the cell division regulation. In addition to miR-34a, here we show that the microRNA cell fate determinant miR-34a and canonical protein cell fate determinant Numb synergize to regulate self-renewal vs. differentiation of early-stage CCSC. miR-34a directly suppresses Numb to form an IFFL, which generates a robust binary switch response from Notch. This switch enhances bimodality of the population and separates CCSCs from non-CCSCs. Undermining this switch via Numb

knockdown degrades bimodality and gives rise to an intermediate population of cells that have more ambiguous and plastic cell fate. We further showed that this cell fate determination switch likely provides a safeguard against excessive ISC self-renewal and proliferation in normal tissues. This safeguard mechanism can be triggered during tissue regeneration and repair after inflammation-induced damage, and its inactivation by miR-34a deletion exacerbates Lgr5+ ISC proliferation. The miR-34a-mediated asymmetric division is active in early-stage CCSCs, likely triggered by their excessive proliferation, and is eventually subverted by miR-34a silencing in late-stage CCSCs.

6.3 CCSCs Show Globally Altered Transcriptomics And Metabolomics Profiles.

CCSCs and non-CCSCs have been showed to behave very differently. CCSCs are more proliferative and tumorigenic, while non-CCSCs are less proliferative and could not efficiently form tumors in the xenograft experiments. There are several CCSC markers developed to label CCSCs in colorectal cancer cells and isolate them from the non-CCSCs. Here, we used different microarray data from various colon cancer cell lines, and combined this information with transcriptomic data and metabolomic measurements to globally understand reprograming of CCSCs at the transcriptional and metabolic levels (Chen, Liu et al. 2014). The integrative analysis suggests that the metabolic reprogramming is prominent in CCSCs compared to non-CCSCS. The pathway analysis further highlights the highly reprogrammed glycolysis, the citric acid (TCA) cycle, and cysteine and methionine metabolism. Additionally, the metabolites α-ketoglutarate (α-KG) and S-AdenosylMethionine (SAM) are highly altered as the relevant enzymatic genes. This implies the potential reprogrammed transcriptomic and metabolomics profiles of CCSCs that might lead to global epigenetic alteration (DNA methylation/demethylation and acetylation) with the relevant metabolites (α-KG and SAM)(Johnson, Warmoes et al. 2013). To further comprehensively understand the altered link between transcriptomics, metabolomics and epigenetics, future RNA-Seq, metabolomics, and Bisulfate sequencing analyses are possible extensions to elucidate greater complexity.

6.4 Notch1 Positive Feedback Is Essential To Intestine Stem Cell Niche

In these studies, we have shown that miR-34a regulation on CCSC division results in the control of a heterogeneous population of colorectal cancer cells. In the normal intestine, the tightly controlled stem

cell niche also plays a critical role in maintaining the tissue homeostasis of crypts. Here, using our novel optic approach to locally target single cells in the stem cell niche of intestinal crypts reveals the importance of the stem cell niche bearing a robust intestinal stem cell (ISCs) and Paneth cell pattern. The compact stem cell/Paneth cell pattern could recover rapidly after laser ablation targeting a single cell in the stem cell niche. Moreover, the dynamic tracking of the vanishing stem cell/Paneth cell pattern with local administration of DBZ, a Notch signaling inhibitor, suggests that the Notch signaling is essential to maintain the stable stem cell/Paneth cell pattern. Computationally and experimentally, we discovered the novel Notch1 positive feedback that is essential and critical to control intestinal stem cell self-renewal and regeneration. *In vitro* laser ablation on mouse-derived organoids further validates that the Notch1 positive feedback is important to maintain the robust stem cell/Paneth cell pattern recovery. In addition to the mouse genome, the Notch1 positive feedback is a conserved motif that can be found in human colon stem cells as well. Our computational modeling explains the robustness and stability of cell fate bifurcation from single-cell, pair-cell, to multi-cell dynamic analysis due to the Notch positive feedback. The speed analysis and multi-scale crypt modeling shows that Notch1 positive feedback exhibits rapid patterning response that helps the intestinal crypt to maintain a stable heterogeneous population of stem cells and Paneth cells even when the stem cell niche is highly proliferative. In addition, the discovered Notch1 2nd intron is shown to have strong signal of histone marks for enhancer activity. The super-enhancer has been identified in other stem cells and shown to be essential to stem cell lineage commitment and plasticity (Di Micco, Fontanals-Cirera et al. 2014, Adam, Yang et al. 2015). The high enhancer activity region on Notch1 2nd intron could potentially be the genomic location to understand the crosstalk between Notch and other important transcriptional factors and investigate whether there is a super-enhancer in intestinal stem cells.

Combining these studies, we showed that stem cell division and the stem cell niche are critical to dynamic homeostatic regulation in both normal tissue and tumors. The genetic motif could serve as an extra safeguard to ensure a better bimodal switch or a more robust control mechanism to balance the stem cell niche, in which both transcriptional regulation and posttranscriptional regulation could play critical roles.

REFERENCES

Adam, R. C., H. Yang, S. Rockowitz, S. B. Larsen, M. Nikolova, D. S. Oristian, L. Polak, M. Kadaja, A. Asare, D. Zheng and E. Fuchs (2015). "Pioneer factors govern super-enhancer dynamics in stem cell plasticity and lineage choice." Nature **521**(7552): 366-370.

Bu, P., K. Y. Chen, J. H. Chen, L. Wang, J. Walters, Y. J. Shin, J. P. Goerger, J. Sun, M. Witherspoon, N. Rakhilin, J. Li, H. Yang, J. Milsom, S. Lee, W. Zipfel, M. M. Jin, Z. H. Gumus, S. M. Lipkin and X. Shen (2013). "A microRNA miR-34a-regulated bimodal switch targets Notch in colon cancer stem cells." Cell Stem Cell **12**(5): 602-615.

Chen, K. Y., X. Liu, P. Bu, C. S. Lin, N. Rakhilin, J. W. Locasale and X. Shen (2014). "A metabolic signature of colon cancer initiating cells." Conf Proc IEEE Eng Med Biol Soc **2014**: 4759-4762.

Di Micco, R., B. Fontanals-Cirera, V. Low, P. Ntziachristos, S. K. Yuen, C. D. Lovell, I. Dolgalev, Y. Yonekubo, G. Zhang, E. Rusinova, G. Gerona-Navarro, M. Canamero, M. Ohlmeyer, I. Aifantis, M. M. Zhou, A. Tsirigos and E. Hernando (2014). "Control of embryonic stem cell identity by BRD4-dependent transcriptional elongation of super-enhancer-associated pluripotency genes." Cell Rep **9**(1): 234-247.

Johnson, C., M. O. Warmoes, X. Shen and J. W. Locasale (2013). Epigenetics and cancer metabolism. Cancer Letters.

Adam, R. C., H. Yang, S. Rockowitz, S. B. Larsen, M. Nikolova, D. S. Oristian, L. Polak, M. Kadaja, A. Asare, D. Zheng and E. Fuchs (2015). "Pioneer factors govern super-enhancer dynamics in stem cell plasticity and lineage choice." Nature **521**(7552): 366-370.

Bu, P., K. Y. Chen, J. H. Chen, L. Wang, J. Walters, Y. J. Shin, J. P. Goerger, J. Sun, M. Witherspoon, N. Rakhilin, J. Li, H. Yang, J. Milsom, S. Lee, W. Zipfel, M. M. Jin, Z. H. Gumus, S. M. Lipkin and X. Shen (2013). "A microRNA miR-34a-regulated bimodal switch targets Notch in colon cancer stem cells." Cell Stem Cell **12**(5): 602-615.

Chen, K. Y., X. Liu, P. Bu, C. S. Lin, N. Rakhilin, J. W. Locasale and X. Shen (2014). "A metabolic signature of colon cancer initiating cells." Conf Proc IEEE Eng Med Biol Soc **2014**: 4759-4762.

Di Micco, R., B. Fontanals-Cirera, V. Low, P. Ntziachristos, S. K. Yuen, C. D. Lovell, I. Dolgalev, Y. Yonekubo, G. Zhang, E. Rusinova, G. Gerona-Navarro, M. Canamero, M. Ohlmeyer, I. Aifantis, M. M. Zhou, A. Tsirigos and E. Hernando (2014). "Control of embryonic stem cell identity by BRD4-dependent transcriptional elongation of super-enhancer-associated pluripotency genes." Cell Rep **9**(1): 234-247.

Johnson, C., M. O. Warmoes, X. Shen and J. W. Locasale (2013). Epigenetics and cancer metabolism. Cancer Letters.

Adam, R. C., H. Yang, S. Rockowitz, S. B. Larsen, M. Nikolova, D. S. Oristian, L. Polak, M. Kadaja, A. Asare, D. Zheng and E. Fuchs (2015). "Pioneer factors govern super-enhancer dynamics in stem cell plasticity and lineage choice." Nature **521**(7552): 366-370.

Bu, P., K. Y. Chen, J. H. Chen, L. Wang, J. Walters, Y. J. Shin, J. P. Goerger, J. Sun, M. Witherspoon, N. Rakhilin, J. Li, H. Yang, J. Milsom, S. Lee, W. Zipfel, M. M. Jin, Z. H. Gumus, S. M. Lipkin and X. Shen (2013). "A microRNA miR-34a-regulated bimodal switch targets Notch in colon cancer stem cells." Cell Stem Cell **12**(5): 602-615.

Chen, K. Y., X. Liu, P. Bu, C. S. Lin, N. Rakhilin, J. W. Locasale and X. Shen (2014). "A metabolic signature of colon cancer initiating cells." Conf Proc IEEE Eng Med Biol Soc **2014**: 4759-4762.

Di Micco, R., B. Fontanals-Cirera, V. Low, P. Ntziachristos, S. K. Yuen, C. D. Lovell, I. Dolgalev, Y. Yonekubo, G. Zhang, E. Rusinova, G. Gerona-Navarro, M. Canamero, M. Ohlmeyer, I. Aifantis, M. M. Zhou, A. Tsirigos and E. Hernando (2014). "Control of embryonic stem cell identity by BRD4-dependent transcriptional elongation of super-enhancer-associated pluripotency genes." Cell Rep **9**(1): 234-247.

Adam, R. C., H. Yang, S. Rockowitz, S. B. Larsen, M. Nikolova, D. S. Oristian, L. Polak, M. Kadaja, A. Asare, D. Zheng and E. Fuchs (2015). "Pioneer factors govern super-enhancer dynamics in stem cell plasticity and lineage choice." Nature **521**(7552): 366-370.

Bu, P., K. Y. Chen, J. H. Chen, L. Wang, J. Walters, Y. J. Shin, J. P. Goerger, J. Sun, M. Witherspoon, N. Rakhilin, J. Li, H. Yang, J. Milsom, S. Lee, W. Zipfel, M. M. Jin, Z. H. Gumus, S. M. Lipkin and X. Shen (2013). "A microRNA miR-34a-regulated bimodal switch targets Notch in colon cancer stem cells." Cell Stem Cell **12**(5): 602-615.

Di Micco, R., B. Fontanals-Cirera, V. Low, P. Ntziachristos, S. K. Yuen, C. D. Lovell, I. Dolgalev, Y. Yonekubo, G. Zhang, E. Rusinova, G. Gerona-Navarro, M. Canamero, M. Ohlmeyer, I. Aifantis, M. M. Zhou, A. Tsirigos and E. Hernando (2014). "Control of embryonic stem cell identity by BRD4-dependent transcriptional elongation of super-enhancer-associated pluripotency genes." Cell Rep **9**(1): 234-247.

Adam, R. C., H. Yang, S. Rockowitz, S. B. Larsen, M. Nikolova, D. S. Oristian, L. Polak, M. Kadaja, A. Asare, D. Zheng and E. Fuchs (2015). "Pioneer factors govern super-enhancer dynamics in stem cell plasticity and lineage choice." Nature **521**(7552): 366-370.

Di Micco, R., B. Fontanals-Cirera, V. Low, P. Ntziachristos, S. K. Yuen, C. D. Lovell, I. Dolgalev, Y. Yonekubo, G. Zhang, E. Rusinova, G. Gerona-Navarro, M. Canamero, M. Ohlmeyer, I. Aifantis, M. M. Zhou, A. Tsirigos and E. Hernando (2014). "Control of embryonic stem cell identity by BRD4-dependent transcriptional elongation of super-enhancer-associated pluripotency genes." Cell Rep **9**(1): 234-247.

Adam, R. C., H. Yang, S. Rockowitz, S. B. Larsen, M. Nikolova, D. S. Oristian, L. Polak, M. Kadaja, A. Asare, D. Zheng and E. Fuchs (2015). "Pioneer factors govern super-enhancer dynamics in stem cell plasticity and lineage choice." Nature **521**(7552): 366-370.

CHAPTER 7

FUTURE DIRECTIONS

7.1 Versatile Dynamics of miR-34a Regulation

In Chapter 2, our studies showed that miR-34a induced threshold response that, in turn, generates a bimodal distribution of CCSCs (Bu, Chen et al. 2013). In addition, as discussed in Chapter 3, we showed that a miR-34a-regulated incoherent feedforward loop is able to exhibit an ultra-sensitive response to generate a stronger bimodal distribution. These dynamic responses make microRNA regulation suitable to control stem cell fate decisions. However, microRNA regulation could be even more versatile. MiR-34a has been known to be the direct transcriptional target of p53, a well-known tumor suppressor (Chang, Wentzel et al. 2007). P53 has been quantitatively characterized to exhibit repeated pulses when cells response to DNA damage (Lev Bar-Or, Maya et al. 2000, Batchelor, Loewer et al. 2011, Purvis, Karhohs et al. 2012). As a direct target of P53, miR-34a subsequently targets the important cell fate decision maker, Notch. This signal transduction link raises the question about whether p53 pulsation could affect Notch-mediated cell fate determination and make it unstable. In our preliminary computational analysis, we characterized that the threshold response from miR-34a regulation could potentially filter out upstream noise. Intuitively, when the p53 pulse is strong enough to drive high expression of miR-34a, the dynamical pulse will not get passed downstream to Notch due to the threshold effect, and this will prevent Notch from unwanted dynamical variation. In our preliminary simulation, we used a periodic p53 signal to simulate the repeated pulses induced from DNA damage (Figure 7.1), and dynamically tracked signal transduction. Due to signal transduction, there are different time delays (Δt_1, Δt_2) between different signal stages. In addition, within the dynamically oscillatory ranges of p53, miR-34a regulation could disrupt the oscillatory response (here, we show that the target only responds to the other half of the oscillatory p53 signals when it is low). In addition, the oscillation filtering effect depends on the strength of the mutual sequestration (the number of binding sites and affinity to bind to the target). When mutual sequestration is weak, the target still responds to the full oscillatory upstream p53 signals, and it stays at a high level. The upstream oscillation will be disrupted more significantly when the strength of mutual sequestration

becomes stronger (Figure 7.2). In addition, the time delay between p53 signals and target Notch signals through miR-34a regulation also helps filter out high-frequency noise (Figure 7.3).

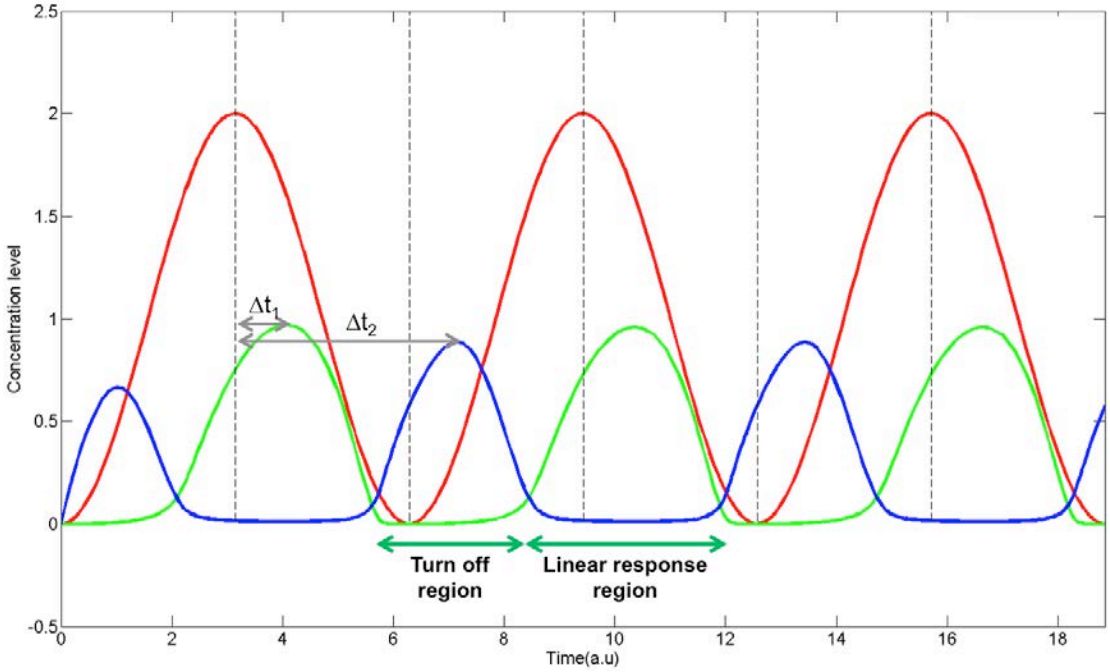

Figure 7.1. Dynamic analysis of P53, miR-34a, and Notch. *Here, a periodic oscillation is used to simulate the repeated pulses of p53 induced by DNA damage. Red: p53, Green: miR-34a, Blue: target* $Notch_{mRNA}$.

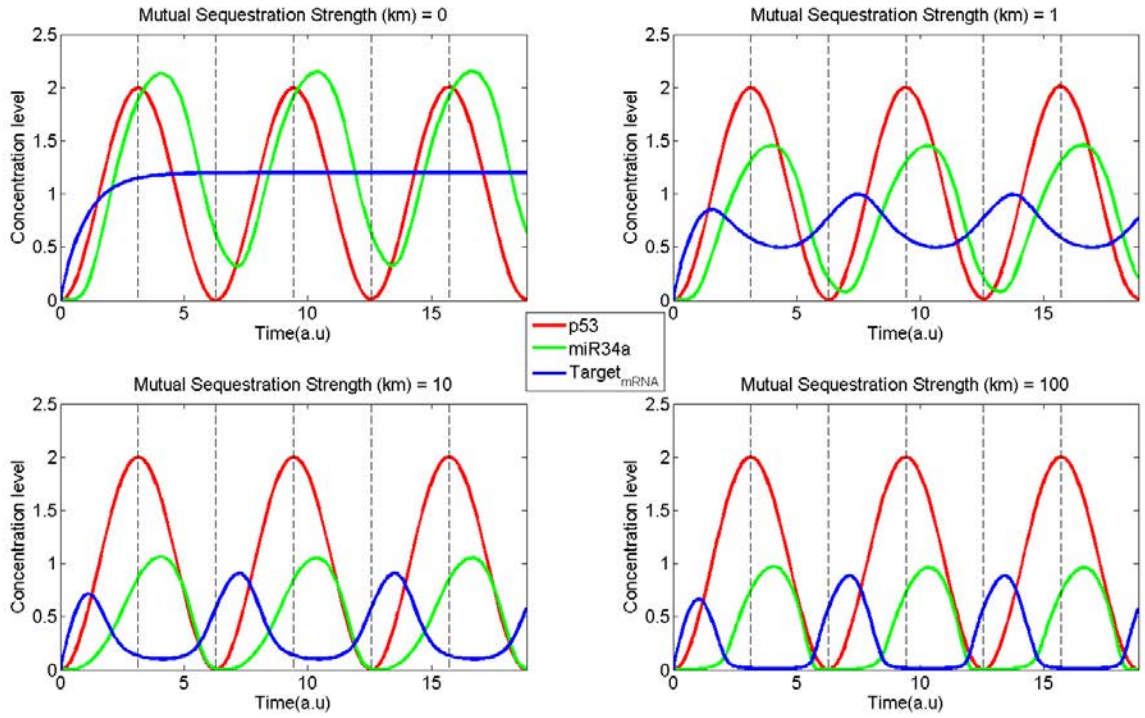

Figure 7.2 Dynamic simulation of miR-34a regulation. *The red lines represents repeated pulses of P53 signals, and green line refers to miR-34a responses. The blue lines are the target Notch mRNA. The strength of mutual sequestration is varied from 0 to 100 to simulate the disruption of repeated pulses due to miR-34a regulation.*

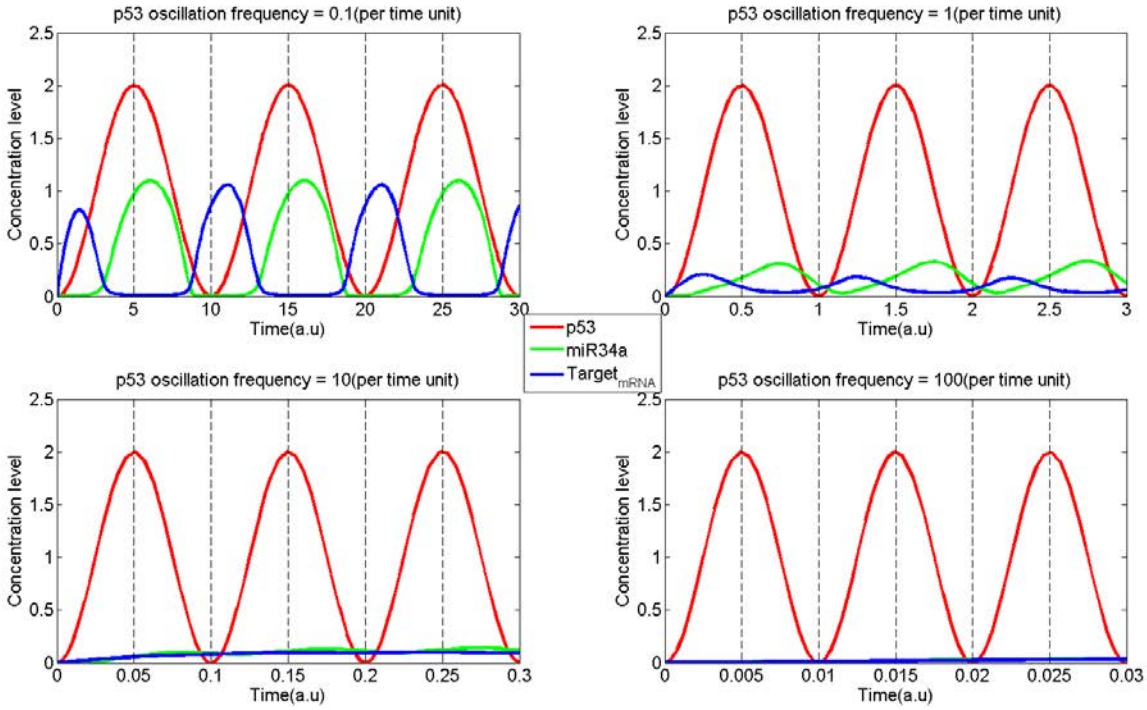

Figure 7.3 miR-34a regulation acts as low-pass filter*. The red lines represents repeated pulses of p53 signals, and green line refers to miR-34a responses. The blue lines are the target Notch mRNA. The frequency of p53 pulses is varied from 0.1 to 100 to simulate the oscillation filtering due to miR-34a regulation.*

Moreover, in Chapter 3, we showed that miR-34a, Numb, and Notch form an incoherent feedforward loop (iFFL) that is able to induce an ultra-sensitive response. This miR-34a regulated iFFL is more versatile than exhibiting an ultrasensitive response alone. By adjusting the regulatory strength of direct (miR-34a --| Notch) and indirect (miR-34a --| Numb --| Notch) paths of iFFL, Notch shows different non-linear responses to miR-34a levels (Figure 7.4). When the regulation strength of the indirect arm (miR34a--| NUMB--| NOTCH) is much stronger than direct arm (miR34a --| NOTCH), the increasing miR-34a levels will cause suppression of NUMB, which releases NOTCH from degradation by binding to NUMB and increases expression levels. The direct arm functions to stabilize responses at low and high levels of miR34a, and make the Notch response increasingly monotonic and ultra-sensitive. When the regulation strength of the direct arm increases, Notch levels initially increase, but non-monotonically drop in

response to higher miR-34a levels when miR-34a inhibition on NOTCH starts to take over the regulation. If the direct arm is much stronger than the indirect arm, the total NOTCH response to miR-34a levels becomes a monotonically decreasing and ultra-sensitive function as the miR-34a inhibition on NOTCH plays a major role.

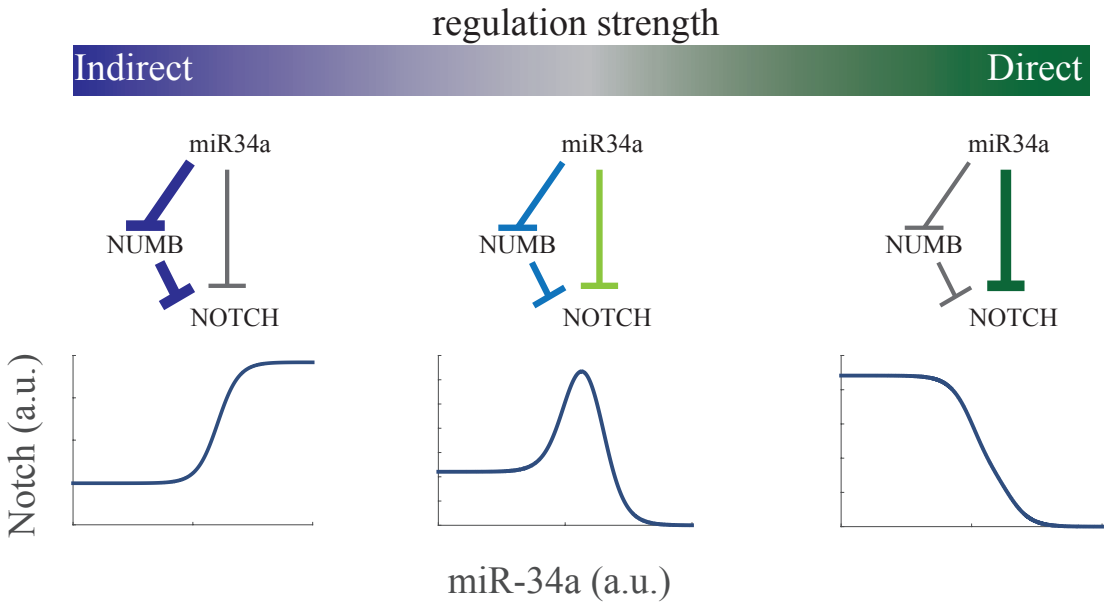

Figure 7.4 miR-34a regulated incoherent feedforward loop shows a versatile response*. Notch can show a monotonically increasing 2-step response, a non-monotonic response, and eventually a decreasing 2-step response when the strength of the iFFL changes from a stronger indirect path to a stronger direct path.*

In our study, we identified that the miR-34a regulated iFFL exhibits an ultrasensitive decreasing response, and this response is associated with the bimodal distribution of Notch signaling in CCSCs. It will be interesting to know if any other microRNA-regulated iFFLs exhibit different regulatory responses in other organisms or other cell types.

7.2 Notch Mutual Inhibition in Intestine Stem Cells

Our studies of the intestinal stem cell niche identified an intercellular circuitry including Notch lateral inhibition and a novel Notch1 positive feedback, and both of which comprise transcriptional regulation. In

Notch signaling, a post-translational interaction between the ligands and receptors on the same cell, called mutual inhibition, has been reported to directly inactivate Notch signaling (Klein, Brennan et al. 1997, Miller, Lyons et al. 2009). Mutual inhibition has also been dynamically characterized as an ultra-sensitive switch inducing sharper Notch signaling activation (Sprinzak, Lakhanpal et al. 2010). However, this post-translational regulation has never been clearly identified in intestinal cells yet. We infected Dll1 and Dll4 overexpression constructs into intestinal cells, and cultured the cells as organoids. The preliminary data suggests that, when the Dll1 and Dll4 levels increase, the protein levels of Notch1 and Notch2 decrease (Figure 7.5), which is consistent with the existence of Notch mutual inhibition.

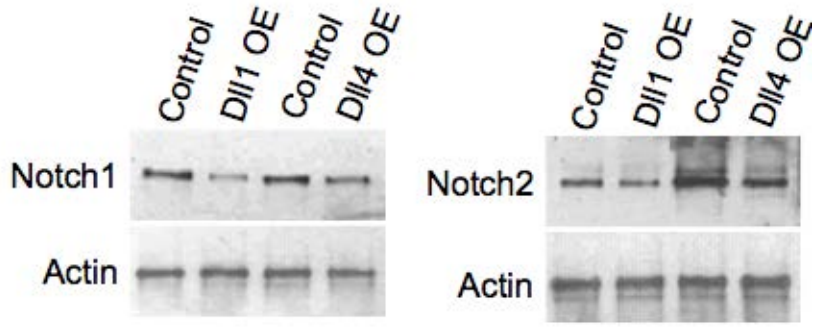

Figure 7.5 *Western blot of Notch1 and Notch2 with Dll1 and Dll4 overexpression in the intestinal organoids.*

This result suggests that, in addition to Notch1 positive feedback and lateral inhibition, the post-translational regulation could also play a role regulating intestinal stem cells. As mentioned, the intestinal epithelium is one of the fastest regenerative tissues, as it is replaced every 3-5 days. The quantitatively characterized ultrasensitive response and fast patterning speed of Notch mutual inhibition (Sprinzak, Lakhanpal et al. 2010, Sprinzak, Lakhanpal et al. 2011) might be an interesting angle to study how mutual inhibition could contribute to maintaining stem cell functions in the fast regenerative intestinal tissue.

7.3 Super Enhancer on Intestine Stem Cells

Based on our analysis of ChIP-Seq datasets, Notch1 2nd to 4th exons were shown to have strong signals of histone marks for enhancer activity. The super-enhancer has been identified in other stem cells and shown to be essential to stem cell lineage commitment and plasticity (Di Micco, Fontanals-Cirera et al. 2014,

Adam, Yang et al. 2015). However, it is still not clear whether and how super enhancers may regulate intestinal stem cells. The high enhancer activity region on Notch1 covers several million base pairs, and there are numerous binding sites to various transcription factors. This region could potentially be the genomic location to understand the crosstalk between Notch and other important transcriptional factors and investigate whether there is a super-enhancer in intestinal stem cells. In addition to Notch1, the other important genes that regulates intestinal stem cells, e.g. β-catenin, Dll1, Dll4, Hes1, and Hes5, also show high histone marks signals. More in-depth analysis on this highly occupied region might reveal more transcriptional links to complex genetic networks that govern intestinal stem cell functions.

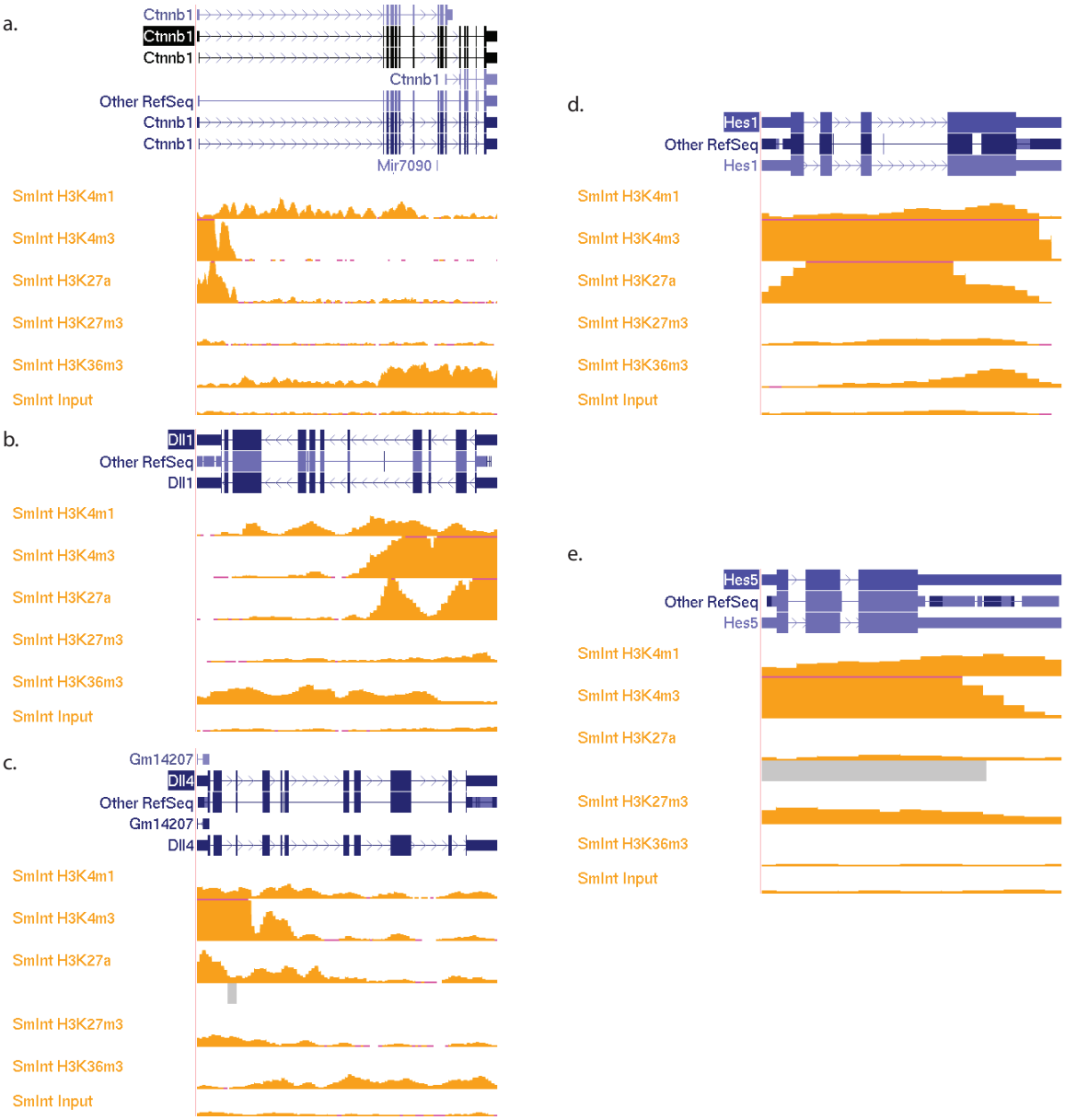

Figure 7.6 ChIP-Seq signals of histone marks H3K4m1, H3K4m3, H3K27ac, H3K27m3, and H3K36m3 in intestinal cells*. a) histone signals on β-catenin, b) Dll1, c) Dll4, d)Hes1, and e) Hes5.*

REFERENCES

Adam, R. C., H. Yang, S. Rockowitz, S. B. Larsen, M. Nikolova, D. S. Oristian, L. Polak, M. Kadaja, A. Asare, D. Zheng and E. Fuchs (2015). "Pioneer factors govern super-enhancer dynamics in stem cell plasticity and lineage choice." Nature **521**(7552): 366-370.

Batchelor, E., A. Loewer, C. Mock and G. Lahav (2011). "Stimulus-dependent dynamics of p53 in single cells." Mol Syst Biol **7**: 488.

Bu, P., K. Y. Chen, J. H. Chen, L. Wang, J. Walters, Y. J. Shin, J. P. Goerger, J. Sun, M. Witherspoon, N. Rakhilin, J. Li, H. Yang, J. Milsom, S. Lee, W. Zipfel, M. M. Jin, Z. H. Gumus, S. M. Lipkin and X. Shen (2013). "A microRNA miR-34a-regulated bimodal switch targets Notch in colon cancer stem cells." Cell Stem Cell **12**(5): 602-615.

Chang, T. C., E. A. Wentzel, O. A. Kent, K. Ramachandran, M. Mullendore, K. H. Lee, G. Feldmann, M. Yamakuchi, M. Ferlito, C. J. Lowenstein, D. E. Arking, M. A. Beer, A. Maitra and J. T. Mendell (2007). "Transactivation of miR-34a by p53 broadly influences gene expression and promotes apoptosis." Mol Cell **26**(5): 745-752.

Di Micco, R., B. Fontanals-Cirera, V. Low, P. Ntziachristos, S. K. Yuen, C. D. Lovell, I. Dolgalev, Y. Yonekubo, G. Zhang, E. Rusinova, G. Gerona-Navarro, M. Canamero, M. Ohlmeyer, I. Aifantis, M. M. Zhou, A. Tsirigos and E. Hernando (2014). "Control of embryonic stem cell identity by BRD4-dependent transcriptional elongation of super-enhancer-associated pluripotency genes." Cell Rep **9**(1): 234-247.

Klein, T., K. Brennan and A. M. Arias (1997). "An intrinsic dominant negative activity of serrate that is modulated during wing development in Drosophila." Dev Biol **189**(1): 123-134.

Lev Bar-Or, R., R. Maya, L. A. Segel, U. Alon, A. J. Levine and M. Oren (2000). "Generation of oscillations by the p53-Mdm2 feedback loop: a theoretical and experimental study." Proc Natl Acad Sci U S A **97**(21): 11250-11255.

Miller, A. C., E. L. Lyons and T. G. Herman (2009). "cis-Inhibition of Notch by endogenous Delta biases the outcome of lateral inhibition." Curr Biol **19**(16): 1378-1383.

Purvis, J. E., K. W. Karhohs, C. Mock, E. Batchelor, A. Loewer and G. Lahav (2012). "p53 dynamics control cell fate." Science **336**(6087): 1440-1444.

Sprinzak, D., A. Lakhanpal, L. Lebon, J. Garcia-Ojalvo and M. B. Elowitz (2011). "Mutual inactivation of notch receptors and ligands facilitates developmental patterning." PLoS computational biology **7**(6): e1002069-e1002069.

Sprinzak, D., A. Lakhanpal, L. Lebon, L. A. Santat, M. E. Fontes, G. A. Anderson, J. Garcia-Ojalvo and M. B. Elowitz (2010). "Cis-interactions between Notch and Delta generate mutually exclusive signalling states." Nature **465**(7294): 86-90.

APPENDIX1

COMPUTATIONAL MODELING OF THE MIR-34A/NUMB/NOTCH IFFL

A1.1 Deterministic model

We expanded our previously published miR-34a-Notch model(Bu, Chen et al. 2013) to incorporate interactions between miR-34a, Numb, and Notch, based on microRNA regulation models from other papers(Levine, Ben Jacob et al. 2007, Khanin and Vinciotti 2008, Mukherji, Ebert et al. 2011, Osella, Bosia et al. 2011, Riba, Bosia et al. 2014). The ordinary differential equation (ODE) based model was used to simulate the behaviors of the IFFL:

$$\frac{d[miR34a]}{dt} = b_1 - a_1[miR34a] - r_1[miR34a][Notch_{mRNA}] - r_2[miR34a][Numb_{mRNA}]$$
$$\frac{d[Notch_{mRNA}]}{dt} = b_2 - a_2[Notch_{mRNA}] - r_1[miR34a][Notch_{mRNA}]$$
$$\frac{d[NOTCH]}{dt} = b_3[Notch_{mRNA}] - a_3[NOTCH] - r_3[NUMB][NOTCH]$$
$$\frac{d[Numb_{mRNA}]}{dt} = b_4 - a_4[Numb_{mRNA}] - r_2[miR34a][Numb_{mRNA}]$$
$$\frac{d[NUMB]}{dt} = b_5[NUMB_{mRNA}] - a_5[NUMB]$$

where

[*x*]: number of molecule of species: miR-34a, Notch mRNA, NOTCH, Numb mRNA, and NUMB

b_s: transcription/ translation rates

a_s: degradation rates

$r_{1,2}$: reaction rates of miR34a binding on $Notch_{mRNA}$ and $Numb_{mRNA}$ respectively.

r_3: reaction rate of Numb inhibition on Notch

For simplicity, the ODEs were transformed into dimensionless equations with parameters: $\tau \equiv t_0 t, miR \equiv \frac{miR34a}{miR_0}, Nm \equiv \frac{Notch_{mRNA}}{Nm_0}, N \equiv \frac{NOTCH}{N_0}, Num \equiv \frac{Numb_{mRNA}}{Num_0}, Nu \equiv \frac{NUMB}{Nu_0}, miR_0 \equiv Num_0 \equiv Nm_0$

The new dimensionless ODEs are shown as:

$$\frac{d[miR34a]}{d\tau} = \beta_1 - \alpha_1[miR34a] - \gamma_1[miR34a][Notch_{mRNA}] - \gamma_2[miR34a][Numb_{mRNA}]$$
$$\frac{d[Notch_{mRNA}]}{d\tau} = \beta_2 - \alpha_2[Notch_{mRNA}] - \gamma_1[miR34a][Notch_{mRNA}]$$
$$\frac{d[NOTCH]}{d\tau} = \beta_3[Notch_{mRNA}] - \alpha_3[NOTCH] - \gamma_3[NUMB][NOTCH]$$
$$\frac{d[Numb_{mRNA}]}{d\tau} = \beta_4 - \alpha_4[Numb_{mRNA}] - \gamma_2[miR34a][Numb_{mRNA}]$$
$$\frac{d[NUMB]}{d\tau} = \beta_5[NUMB_{mRNA}] - \alpha_5[NUMB]$$

where $\beta_1 \equiv \frac{b_1}{miR_0 t_0}, \beta_2 \equiv \frac{b_2}{Nm_0 t_0}, \beta_3 \equiv \frac{b_3 Nm_0}{N_0 t_0}, \beta_4 \equiv \frac{b_4}{Num_0 t_0}, \beta_5 \equiv \frac{b_5 Num_0}{Nu_0 t_0}, \alpha_1 \equiv \frac{a_1}{t_0}, \alpha_2 \equiv \frac{a_2}{t_0}, \alpha_3 \equiv \frac{a_3}{t_0}, \alpha_4 \equiv \frac{a_4}{t_0}, \alpha_5 \equiv \frac{a_5}{t_0}, \gamma_1 \equiv \frac{r_1 miR_0}{t_0}, \gamma_2 \equiv \frac{r_2 miR_0}{t_0}, r_3 \equiv \frac{r_3 Nu_0}{t_0}$

Parameter values used for Fig. 3.2d:

IFFL: β_1= various, β_2= 360, β_3= 0.0112, β_4=400, β_5=0.0008, α_1=0.002, α_2= 0.027, α_3= 0.02, α_4= 0.009, α_5=0.002, γ_1=6x10^{-5}, γ_2=2x10^{-5}, γ_3=10^{-5}

NumbKD: β_1=various, β_2= .018, β_3= 29.38, α_1= 0.4, α_2= 0.027, α_3= 0.002, γ_1=6x10^{-5}

Parameter values used for Supplemental Fig. S3.2:

β_1= various, β_2= 360, β_3= 0.0112, β_4=400, β_5=0.0008, α_1=0.002, α_2= 0.027, α_3= 0.02, α_4= 0.009, α_5=0.002, γ_1=[4.2x10^{-6}~2.4x10^{-4}], γ_2=[4x10^{-6}~2.8x10^{-5}], γ_3=10^{-5}

A1.2 Stochastic simulation

Stochastic simulations were performed using the stochastic solver, stochastic simulation algorithm (SSA), in the Matlab (MathWork®) toolbox SimBology with the reactions listed below:

Reaction	Parameter

1.	Transcription of miR-34a	b_1
2.	Degradation of miR-34a	a_1
3.	miR-34a binding on Notch mRNA	r_1
4.	miR-34a binding on Numb mRNA	r_2
5.	Transcription of Notch mRNA	b_2
6.	Degradation of Notch mRNA	a_2
7.	Translation of Notch	b_3
8.	Degradation of Notch	a_3
9.	Transcription of Numb mRNA	b_4
10.	Degradation of Numb mRNA	a_4
11.	Translation of Numb	b_5
12.	Degradation of Numb	a_5
13.	Numb inhibition on Notch	r_3

Based on previous FACS measurement of induced miR-34a(Bu, Chen et al. 2013), we applied a stochastic transfer function $f(x) = kx(1 \pm \xi\%)$ to model miR-34a induction, where x refers to the number of molecules, k refers to the signal intensity coefficient, and ξ denotes the variation of signal intensity. Stochastic simulations were run to reach steady states determined by deterministic simulations, and levels were sampled at the same time point for statistics.

Parameter values used for Fig. 3.2e:

IFFL: b_1= various, b_2= 360, b_3= 0.0112, b_4=400, b_5=0.0008, a_1= 0.002, a_2= 0.027, a_3= 0.02, a_4= 0.009, a_5=0.002, r_1=6x10^{-5}, r_2= 2x10^{-5}, r_3=1x10^{-5}, k=1, ξ=20

NUMB KD: b_1= various, b_2= 1.8, b_3= 0.0113, a_1= 0.002, a_2= 0.027, a_3= 0.02, r_1=6x10^{-5}, k=1, ξ=20

REFERENCE

Bu, P., K. Y. Chen, J. H. Chen, L. Wang, J. Walters, Y. J. Shin, J. P. Goerger, J. Sun, M. Witherspoon, N. Rakhilin, J. Li, H. Yang, J. Milsom, S. Lee, W. Zipfel, M. M. Jin, Z. H. Gumus, S. M. Lipkin and X. Shen (2013). "A microRNA miR-34a-regulated bimodal switch targets Notch in colon cancer stem cells." Cell Stem Cell **12**(5): 602-615.

Khanin, R. and V. Vinciotti (2008). "Computational modeling of post-transcriptional gene regulation by microRNAs." J Comput Biol **15**(3): 305-316.

Levine, E., E. Ben Jacob and H. Levine (2007). "Target-specific and global effectors in gene regulation by MicroRNA." Biophys J **93**(11): L52-54.

Mukherji, S., M. S. Ebert, G. X. Zheng, J. S. Tsang, P. A. Sharp and A. van Oudenaarden (2011). "MicroRNAs can generate thresholds in target gene expression." Nat Genet **43**(9): 854-859.

Osella, M., C. Bosia, D. Cora and M. Caselle (2011). "The role of incoherent microRNA-mediated feedforward loops in noise buffering." PLoS Comput Biol **7**(3): e1001101.

Riba, A., C. Bosia, M. El Baroudi, L. Ollino and M. Caselle (2014). "A combination of transcriptional and microRNA regulation improves the stability of the relative concentrations of target genes." PLoS Comput Biol **10**(2): e1003490.

APPENDIX2

ODES MODELS OF NOTCH SIGNALING CIRCUITS

A2.1: MATHEMATICAL MODEL

The mathematical model of Notch signaling includes 3 types of regulations: (1) trans-activation of Notch receptor by external ligand (TA), (2) lateral Inhibition (LI), and (3) positive feedback (PF). Transcriptional activation is modeled by Hill function $(x, k, p) = \frac{x^p}{k^p + x^p}$, and transcriptional suppression is modeled by Hill function $\delta(x, k, h) = \frac{k^h}{k^h + x^h}$, where x refers to the regulator, k refers to the saturation coefficient, and h is the hill coefficient. Below are the ODE equations:

$$\dot{Notch}_{mRNA_i} = \beta_{n0} + \beta_n \cdot \sigma\left(k_t \cdot NOTCH_i\langle DLL_j\rangle, k_p, p\right) - \alpha_n \cdot Notch_{mRNA_i}$$

$$\dot{NOTCH}_i = \beta_N \cdot Notch_{mRNA_i} - \alpha_N \cdot NOTCH_i - k_t \cdot N \quad TCH_i\langle DLL_j\rangle$$

$$\dot{Dll}_{mRNA_i} = \beta_{d0} + \beta_d \cdot \delta\left(k_t \cdot NOTCH_i\langle DLL_j\rangle, k_d, h\right) - \alpha_d \cdot Dll_{mRNA_i}$$

$$\dot{DLL}_i = \beta_D \cdot Dll_{mRNA_i} - \alpha_D DLL_i - k_t \cdot \langle NOTCH_j\rangle DLL_i$$

$$\dot{R}_i = k_t NOTCH_i\langle DLL_j\rangle - \alpha_R R_i$$

where $Notch_{mRNA}$, *NOTCH*, Dll_{mRNA}, *DLL, and R* refer to the expression level of Notch mRNA, NOTCH receptor, Dll mRNA, DLL ligand, and cleaved NICD (activated Notch signaling), respectively. The annotation i and j refer to cell j adjacent to cell i. β_s denote the synthesis rates (transcription rates for mRNAs and translation rates for protein), while α_s denote the degradation rates. $\langle X_j\rangle_i$ is the average expression of X from the neighboring *j* cells of cell *i*. k_t is the reaction rate of trans-activation. β_{1_0} and β_{3_0} are the basal transcriptional rates of $Notch_{mRNA}$ and Dll_{mRNA}. By changing the ratios of $\beta_n/(\beta_{n0} + \beta_n)$ and $\beta_d/(\beta_{d0} + \beta_d)$, we can adjust the regulatory strength of LI and PF.

A2.2: Dimensionless Analysis

For simplicity, we transform the equations into dimensionless equations with dimensionless parameters: $\tau \equiv t_0 t, Nm \equiv \frac{Notch_{mRNA}}{Nm_0}, N \equiv \frac{NOTCH}{N_0}, Dm \equiv \frac{Dll_{mRNA}}{Dm_0}, D \equiv \frac{DLL}{D_0}, R \equiv \frac{R}{R_0}, N_0 = D_0 = R_0 \equiv \frac{t_0}{k_t}$.

Model 1:

$$\dot{Nm_i} = \beta_{n0} + \beta_n \cdot \sigma\big(NOTCH_i\langle DLL_j\rangle, k_p, p\big) - \alpha_n \cdot Nm_i$$

$$\dot{N_i} = \beta_N \cdot Nm_i - \alpha_N \cdot N_i - N_i\langle D_j\rangle$$

$$\dot{Dm_i} = \beta_{d0} + \beta_d \cdot \delta\big(NOTCH_i\langle DLL_j\rangle, k_d, h\big) - \alpha_d \cdot Dm_i$$

$$\dot{D_i} = \beta_D \cdot Dm_i - \alpha_D \cdot D_i - \langle N_j\rangle D_i$$

$$\dot{R_i} = NOTCH_i\langle DLL_j\rangle - \alpha_R R_i$$

Where $\beta_{n0} \equiv \frac{\beta_{n0}}{t_0 \cdot Nm_0}, \beta_n \equiv \frac{\beta_n}{t_0 \cdot Nm_0}, \beta_N \equiv \frac{\beta_N \cdot Nm_0}{t_0 \cdot N_0}, \beta_{d0} \equiv \frac{\beta_{d0}}{t_0 \cdot Dm_0}, \beta_d \equiv \frac{\beta_d}{t_0 \cdot Dm_0}, \beta_D \equiv \frac{\beta_D \cdot Dm_0}{t_0 \cdot D_0}, \alpha_n \equiv \frac{\alpha_n}{t_0}, \alpha_N \equiv \frac{\alpha_N}{t_0}, \alpha_d \equiv \frac{\alpha_d}{t_0}, \alpha_D \equiv \frac{\alpha_D}{t_0}, \alpha_R \equiv \frac{\alpha_R}{t_0}, k_p \equiv \frac{k_p}{k_t \cdot N_0 \cdot D_0}, k_d \equiv \frac{k_d}{k_t \cdot N_0 \cdot D_0}$.

To modulate the relative strength of the transcriptional regulations (LI, PF), we rescaled the ratios of basal transcriptional rates and regulated transcriptional rates as: $S_{PF} \equiv \frac{\beta_n}{\beta_{n0}+\beta_n}, S_{LI} \equiv \frac{\beta_d}{\beta_{d0}+\beta_d}$, and maximum transcriptional rate as: $_{nm} = (\beta_{n0} + \beta_n), \beta_{dm} = (\beta_{d0} + \beta_d)$, where $0 \le S_{PF}, S_{LI} \le 1$. A new set of equations can be shown as:

Model 2:

$$\dot{Nm_i} = \beta_{nm}\big[(1 - S_{PF}) + S_{PF} \cdot \sigma\big(NOTCH_i\langle DLL_j\rangle, k_p, p\big)\big] - \alpha_n \cdot Nm_i$$

$$\dot{N_i} = \beta_N \cdot Nm_i - \alpha_N \cdot N_i - N_i\langle D_j\rangle$$

$$\dot{Dm_i} = \beta_{dm}\big[(1 - S_{LI}) + S_{LI} \cdot \delta\big(NOTCH_i\langle DLL_j\rangle, k_d, h\big)\big] - \alpha_d \cdot Dm_i$$

$$\dot{D_i} = \beta_D \cdot Dm_i - \alpha_D \cdot D_i - \langle N_j\rangle D_i$$

$$\dot{R_i} = N_i\langle D_j\rangle - \alpha_R R_i$$

A2.3: Dimension Reduction

First, we assume the time scale for mRNA is much faster than proteins, so quasi-steady state method is applied to reduce the mRNA species in the equations:

Set $\dot{Nm_i} = 0,\ \dot{Dm_i} = 0$

$$Nm_i{}^* = \frac{\beta_{nm}}{\alpha_n}\left[(1 - S_{PF}) + S_{PF} \cdot \sigma\left(NOTCH_i\langle DLL_j\rangle, k_p, p\right)\right],$$

$$Dm_i{}^* = \frac{\beta_{dm}}{\alpha_d}\left[(1 - S_{LI}) + S_{LI} \cdot \delta\left(NOTCH_i\langle DLL_j\rangle, k_d, h\right)\right]$$

replace $[Nm_i, Dm_i]$ with $[Nm_i{}^*, Dm_i{}^*]$ in $\dot{N}_i$ and $\dot{D}_i$ respectively, and set $\beta_N = \beta_N \frac{\beta_{nm}}{\alpha_n}$, $\beta_D = \beta_D \frac{\beta_{dm}}{\alpha_d}$. A simple protein model can be shown as:

Model 3:

$$\dot{N}_i = \beta_N \cdot \left[(1 - S_{PF}) + S_{PF} \cdot \sigma\left(NOTCH_i\langle DLL_j\rangle, k_p, p\right)\right] - \alpha_N \cdot N_i - N_i\langle D_j\rangle$$

$$\dot{D}_i = \beta_D \cdot \left[(1 - S_{LI}) + S_{LI} \cdot \delta\left(NOTCH_i\langle DLL_j\rangle, k_d, h\right)\right] - \alpha_D \cdot D_i - \langle N_j\rangle D_i$$

$$\dot{R}_i = N_i\langle D_j\rangle - \alpha_R R_i$$

A2.4: Parameter Table

Figure	Model	Parameters
Figure 5.5a (LI)	Model 1	β_{n0}= 1, β_{d0}= 0.01, β_n= 0, β_d= 1, β_N= 1, β_D= 1,α_n= 1, α_d= 1, α_N= 1, α_D= 1, k_d= 0.1, h= 1
Figure 5.5a (PFLI)	Model 1	β_{n0}= 0.04, β_{d0}= 0.01, β_n= 1, β_d= 1, β_N= 1, β_D= 1,α_n= 1, α_d= 1, α_N= 1, α_D= 1 , k_p= 0.01, k_d= 0.1, h= 1, p= 3
Figure 5.5b (LI)	Model 1	β_{n0}= 1, β_{d0}= 0.01, β_n= 0, β_d= 1, β_N= 1, β_D= 1, α_n= 1, α_d= 1, α_N= 1, α_D= 1, k_d= 0.1, h= [1-2]
Figure 5.5b (PFLI)	Model 1	β_{n0}= 0.1, β_{d0}= 0.01, β_n= 1, β_d= 1, β_N= 1, β_D= 1,α_n= 1, α_d= 1, α_N= 1, α_D= 1 , k_p= 0.0774, k_d= 0.0167, h= [1-2], p= 1
Figure 5.5c (LI)	Model 1	β_{n0}= 10^{-2}-10^{2}, β_{d0}=10^{-5}, β_n=0, β_d= 10^{-2}-10^{2}, β_N= 1, β_D= 1,α_n= 1, α_d= 1, α_N= 1, α_D= 1, k_d= 0.1778, h= [1-3]
Figure 5.5c (PFLI)	Model 1	β_{n0}= 10^{-5}, β_{d0}=10^{-5}, β_n= 10^{-2}-10^{2}, β_d= 10^{-2}-10^{2}, β_N= 1, β_D= 1,α_n= 1, α_d= 1, α_N= 1, α_D= 1, k_p= 0.0774, k_d= 0.0167, h= [1-3], p= 1
Figure 5.5d	Model 1	β_{nm}=10, S_{PF}=0-1, β_{dm} =100, S_{LI}=1, β_N= 1, β_D= 1, α_n= 1, α_d= 1, α_N= 1, α_D= 1 , k_p= various, k_d= various, h= 3, p= 3
Figure 5.5e (LI)	Model 3	β_N= 10, S_{PF}=0, β_D=100, S_{LI}= 1,α_n= 1, α_d= 1, α_N= 1, α_D= 1, α_R = 1, k_d= 0.1778, h= 3
Figure 5.5e (PFLI)	Model 3	β_N= 10, S_{PF}=1, β_{D0}= 0, β_D= 100,α_n= 1, α_d= 1, α_N= 1, α_D= 1, α_R = 1, k_n=0.0042, k_d= 0.015, h= 3, p=3
Figure S5.6a (LI)	Model 1	β_{n0}= 1, β_{d0}= 0.0100, β_n= 0, β_d= 1, β_N= 1, β_D= 1,α_n= 1, α_d= 1, α_N= 1, α_D= 1,k_d= 0.1,h= [1-3]
Figure S5.6b (PFLI)	Model 1	β_{n0}= 0.04, β_{d0}= 0.01, β_n= 1, β_d= 1, β_N= 1, β_D= 1,α_n= 1, α_d= 1, α_N= 1, α_D= 1 , k_p= 0.01, k_d= 0.1,h= [1-3],p= [1-3]
Figure S5.6c (LI)	Model 1	β_{n0}= 1, β_{d0}= 0.0100, β_n= 0, β_d= 1, β_N= 1, β_D= 1,α_n= 1, α_d= 1, α_N= 1, α_D= 1,k_d= 0.1,h= [1-3]
Figure S5.6d (PFLI)	Model 1	β_{n0}= 0.1, β_{d0}= 0.01, β_n= 1, β_d= 1, β_N= 1, β_D= 1,α_n= 1, α_d= 1, α_N= 1, α_D= 1 , k_p= 0.0774, k_d= 0.0167, h= [1-3], p= [1-3]
Figure S5.6a	Model 1	β_{nm}=10, S_{PF}=0-1, β_{dm} =100, S_{LI}=1, β_N= 1, β_D= 1, α_n= 1, α_d= 1, α_N= 1, α_D= 1 , k_p= various, k_d= various, h= 3, p= 3
Figure S5.7a	Model 3	β_{N0}= 0.1, $\beta_{N'}$=[0.1,1,5,10], β_{D0}= 0, $\beta_{D'}$= 100,α_n= 1, α_d= 1, α_N= 1, α_D= 1, α_R = 1, k_n=0.0042, k_d= 0.015, h= 3, p=3, β_{N0}= β_N(1- S_{PF}), $\beta_{N'}$= β_N(S_{PF}), β_{D0}= β_D(1- S_{LI}), $\beta_{D'}$= β_D(S_{LI})
Figure S5.7b	Model 3	β_{n0}= 10^{-5}, β_{d0}= 10^{-5}, β_n= 5, β_d= 5, β_N= 1, β_D= 1,α_n= 1, α_d= 1, α_N= 1, α_D= 1 ,k_p= 0.0115, k_d= 0.015,h= 3,p= 1